

Integrated Theoretical and Transient Kinetic Investigation of Catalytic Materials for the Selective Synthesis of Hydrogen and Aromatic Hydrocarbons

by

Hari Narayanan Rangarajan Thirumalai

A dissertation submitted to the Department of Chemical and Biomolecular
Engineering

Cullen College of Engineering

in partial fulfillment of the requirements for the degree of

Doctor of Philosophy

in Chemical Engineering

Chair of Committee: Prof. Lars. C. Grabow

Committee Member: Prof. Michael P. Harold

Committee Member: Prof. Jeffrey D. Rimer

Committee Member: Prof. Steven Baldelli

Committee Member: Dr. Javier Guzman

University of Houston

December 2019

Copyright 2019, Hari Narayanan Rangarajan Thirumalai

Acknowledgements

A cliché, yet relevant quote that epitomizes my gratitude to the many people who had played a role in guiding me to where I am today comes from the home webpage of most graduate students' browsers, *Google Scholar* — *Stand on the Shoulders of Giants!*.

In chronological order, I want to start by thanking my *family* - my parents and my sister. I have had the absolute privilege of being able to pursue my ambitions without any distractions and responsibilities due to the incredible perseverance and determination of my father and mother. I have never had to look elsewhere for role models and the dedication that I have had to put in to finish my Ph.D. is testament to what they have instilled in me over the years. My sister Harini, was, is and always will be my partner in crime and my best friend. Our bubbly, meaningless, often deep and insightful and other times stupid and nonsensical conversations were priceless in keeping me afloat during the difficult periods. Her innate ability to understand my worries and insecurities and her reassurance that everything will work out in the end was priceless.

I came to Carnegie Mellon University as a wide-eyed, naive and ambitious student who wasn't really sure of what path to take. Thankfully, I had a charismatic *giant* rooting for me in Professor John Kitchin. I want to thank him for putting up with my incessant interruptions while he was working in his office. But more important, I owe him for giving me the space to learn and to grow as a graduate student and for instilling in me the appreciation for scripting, organization, methodology and attention to detail. A special mention goes out to my first ever mentor, Jacob Boes, who taught me everything I needed to get into graduate

school. Carnegie Mellon was an amazing experience overall, and for that I have to thank my roommates and friends, Samji Samira, Keshav Rangan, Arpita Iddya and Siddharth Deshpande, all of whom are pursuing their own Ph.D's elsewhere. The curriculum in school squeezed us to our bones, but looking forward to doing fun (sometimes wild) things with these guys made it easy.

My life at the University of Houston has been a blur, an incredibly fulfilling experience, primarily due to the *giant* named Professor Lars Grabow. He has been a colleague, a father-figure, a friend and a mentor and has influenced me to the extent that it cannot be put into words. Quite simply, thank you Lars for having my back and looking out for me and reaffirming your belief in my work. Thank you for allowing me to do cutting-edge computational research and at the same time, open up decades-old vacuum pumps and reactors. Thank you for letting me go on a life-changing research trip to Europe. I am indeed privileged to call you my boss! Special thanks to the wonderful Grabow group and especially, Sashank, Quan, Juan Manuel and Karun. Your companionship has had a profound impact on my development and if I have never said it out to you in person, please do consider this acknowledgment as a token of my appreciation. It takes a village of *giants* to raise a child and I want to acknowledge two individuals, Nicolette Solano and Gerald Blosser, for fun conversations and making life at the University of Houston easy. Gerald - that rum cake at 9 am in the morning was the best cake I have ever eaten!

A late, but extremely important entrant to my life is Poorvi. The last few months have been tough, but would have been significantly worse if not for you. Thank you for being there always and I can't wait to spend the rest of my life with you!

Abstract

Metal-exchanged zeolites are emerging as catalytic materials containing isolated metal centers that perform chemical transformation with high activity and selectivity to desired products. While there exist very successfully commercialized examples, for instance Cu-SSZ-13 for automotive emissions applications, much is unknown about metal sites in zeolites. Thus, statistical analyses of energetic quantities obtained from density functional theory (DFT) simulations of various zeolite models were performed for the activation of methane as probe hydrocarbon species. A comprehensive error analysis overwhelmingly shows that the identity and type of metal species in the zeolite determines the reactivity rather than the zeolite framework properties. Statistical distributions were used to identify and validate other metals that would theoretically function as catalysts for methane activation.

Insights gained from the investigation of a diverse set of metal-exchanged zeolites were applied in understanding the mechanisms by which Ag-ZSM-5 enhances the selective formation of aromatic hydrocarbons from ethylene. Silver sites in the zeolite were experimentally and computationally characterized as Ag cations. Transient pulsing experiments using the temporal analysis of products (TAP) reactor and exploration of reaction mechanisms using DFT reveal that silver sites catalyze dehydrogenation and hydrogen-transfer pathways and accelerate the accumulation of aromatic hydrocarbon forming precursors. The cause for the enhancement of these chemistries arises from the synergistic Brønsted–Lewis acid character of the zeolite.

The TAP technique was used to understand the finer aspects of the methy-

lation of toluene to xylene, both important aromatic hydrocarbons. Pulse responses of reactants and products provide insights on competitive adsorption inside the zeolite, with methanol and methanol-based intermediates of finite lifetime identified as being crucial to the process of methylation. Typically in industry, hydrocarbon conversion processes using zeolites include co-feeds of hydrogen that are usually obtained from methane steam-reforming, a highly capital and energy intensive process. The search for hydrogen production avenues that do not rely on fossil resources has led to a surge of research devoted to electrocatalytic processes. This dissertation also explores the surface science of electrocatalytic hydrogen production over novel metal-phosphide surfaces. Density functional theory calculations reveal that metal-rich surface sites catalyze hydrogen evolution, as opposed to accepted notions that phosphorous-rich sites are the active sites.

Table of Contents

Acknowledgements	iii
Abstract	v
Table of Contents	vii
List of Tables	xi
List of Figures	xii
1. Introduction	1
1.1. Catalysis in Everyday Life	1
1.2. Zeolite Catalysts	5
1.3. Hydrocarbon Conversion in Zeolite Catalysts	8
1.4. Outline of this Dissertation	11
2. Methods	12
2.1. Density Functional Theory	12
2.2. Temporal Analysis of Products	17
2.2.1. Background	17
2.2.2. Overview of Set Up	22
2.2.3. Differential High Vacuum Pumping System	24
2.2.4. Quadropole Mass Spectrometer	25
2.2.5. Microreactor	26
2.2.6. Pulsing Setup and Manifold	27

2.2.7. Feed Preparation Section	28
2.2.8. Data Acquisition and Processing	31
3. Quantification and Statistical Analysis of Errors Related to the Approximate Description of Active Site Models in Metal-exchanged Zeolites	36
3.1. Introduction	36
3.2. Computational Methods	40
3.3. Results and Discussion	44
3.3.1. Lewis Acid Sites	44
3.3.2. Preferred Activation Pathways	49
3.3.3. Trends in CH ₄ Activation	54
3.3.4. Factors Affecting the Reactivity of Lewis Acids towards CH ₄ Activation	59
3.3.5. Statistical Analysis of Error Ensembles	63
3.4. Conclusions	69
4. Bifunctional Lewis and Brønsted Acid sites In Ag-H-ZSM-5 Catalysts for Ethylene Dimerization and Aromatization	72
4.1. Introduction	72
4.2. Experimental Methods	75
4.2.1. Temporal Analysis of Products Experiments	75
4.2.2. UV-Vis Spectroscopy	78
4.2.3. X-Ray Absorption Spectroscopy	80
4.3. Density Functional Theory Calculations	81
4.4. Results and Discussion	83
4.4.1. Characterization of Active Sites	83
4.4.2. Evaluation of Catalytic Activity	94
4.5. Conclusions	119

5. Toluene Alkylation with Methanol over H-ZSM-5 Catalysts: Insights from Transient Pulsing Experiments	120
5.1. Introduction	120
5.2. Experimental Methods	123
5.2.1. Materials	123
5.2.2. Experimental Setup and Procedures	123
5.3. Results and Discussion	126
5.4. Conclusions	138
 6. Effects of Catalyst Phase on the Hydrogen Evolution Reaction of Water Splitting: Preparation of Phase-pure Films of FeP, Fe₂P, and Fe₃P and their Relative Catalytic Activities	 140
6.1. Introduction	141
6.2. Experimental and Computational Methods	143
6.2.1. Growth of FeP, Fe ₂ P and Fe ₃ P Crystals	143
6.2.2. Growth of Thin Films on Substrate	144
6.2.3. Characterization	145
6.2.4. Electrochemical measurements	146
6.2.5. Density Functional Theory Calculations	147
6.3. Results and Discussion	152
6.3.1. MOCVD Growth of Phase Pure Thin Films of FeP and Fe ₂ P .	152
6.3.2. Film Characterization	155
6.3.3. Catalytic Activity of the Iron Phosphide Films	158
6.3.4. Insights from density functional theory (DFT) calculations . .	162
6.4. Conclusions	168

7. Perspectives and Scope for Future Work	170
7.1. Statistical Analysis of Model Errors in Metal-exchanged Zeolite Models for Hydrocarbon Activation	170
7.2. Computational Modeling and Transient Kinetics of Hydrocarbon Conversion over Zeolite Catalysts	171
References	173
Appendix A. Quantification and Statistical Analysis of Errors Related to the Approximate Description of Active Site Models in Metal-exchanged Zeolites	207
Appendix B. Effects of Catalyst Phase on the Hydrogen Evolution Reaction of Water Splitting: Preparation of Phase-pure Films of FeP, Fe₂P, and Fe₃P and their Relative Catalytic Activities	222

List of Tables

2.1. Calibration factors for gases monitored as reactants and products over the course of all TAP experiments performed.	33
2.2. Fragmentation ratios for all hydrocarbons measured in TAP experiments performed in this dissertation.	35
3.1. Metal-exchange candidates, active sites and pathways for CH ₄ activation on (Al × 1) models.	50
3.2. Metal-exchange candidates, active sites and pathways for CH ₄ activation on (Al × 2) models.	50
3.3. Activation energies and energies of reaction (in parentheses) for CH ₄ activation pathways on various active sites in the 5T cluster models and ZSM-5 periodic unit cells.	52
3.4. Probabilities P(M1 > M2) for metal M1 showing a lower activation energy barrier for CH ₄ dissociation than metal M2.	67
4.1. The coefficient matrix of relative signals at overlapping <i>m/z</i> ratios. .	77
4.2. Ag K-edge ex-situ XANES edge energies of Ag ₂ O and Ag _x -ZSM-5 samples (x=0.08, 0.46) measured at ambient conditions.	88
4.3. Parameters obtained from EXAFS-fits to FT-EXAFS of Ag _x -ZSM-5 (x=0.08, 0.46) and Ag ₂ O samples at ambient conditions.	90
6.1. Bulk unit cells and optimized lattice parameters of Fe ₃ P, Fe ₂ P and FeP	149

List of Figures

1.1. Photo of fertilizer test showing the improvement of yield, 1919. Adapted from BASF	2
1.2. Volkswagen 'dieselgate' scandal. Graphic on the Volkswagen emissions cheating scandal. Adapted from Yahoo News	3
1.3. Structures of four selected zeolites (from top to bottom: faujasite or zeolites X, Y; zeolite ZSM-12; zeolite ZSM-5 or silicalite-1; zeolite Theta-1 or ZSM-22) and their micropore systems and dimensions. ¹ .	5
1.4. Schematic representation of the types of shape selectivity exhibited by zeolites. Taken from the work of Davis. ²	7
1.5. Postulated mechanism for methane aromatization on Mo/ZSM-5 catalysts showing the roles of the Mo–C sites and the Brønsted acid sites in the zeolite. ³	9
2.1. Stages of the catalyst development program.	18
2.2. Pressure–materials diagram indicating the position of various approaches to investigate mechanisms and kinetics of heterogeneously catalyzed reactions. ⁴	19
2.3. Conceptual comparison of key components of (a) molecular beam scattering experiment and (b) TAP experiment. Adapted from the work of Gleaves. ⁵	20
2.4. The temporal analysis of products (TAP-1) reactor at the University of Houston.	22

2.5. Schematic of the TAP-1 setup without the feed preparation and mixing section included.	23
2.6. A typical pulse response obtained from a TAP experiment.	25
2.7. The quartz microreactor showing the catalyst loaded in a thin-zone configuration ⁶ between two beds of silica	26
2.8. The reactor chamber of the TAP-1 reactor showing the pulse valve manifold and the microreactor housing.	27
2.9. Piping and instrumentation diagram the liquid feed setup.	29
2.10. Piping and instrumentation diagram for lines A and B in the feed preparation section.	30
2.11. Screenshot of the TAPSoft data acquisition software used to perform typical experiments with the TAP-1 reactor.	31
3.1. Illustration of the combination of ensembles of different models, i.e. 5T (red), $2 \times 5T$ (blue), ZSM-22 (green) and ZSM-5 (magenta). . . .	42
3.2. The ZSM-5 periodic cell with the straight [010] and sinusoidal [100] channels (shaded in brown). The T-12 site at the intersection of the two channels is enlarged and forms the basis of the 5T-cluster used in this work.	44
3.3. Geometries of acid sites in zeolite models of different complexity considered in this study.	45
3.4. Representative geometries of active Lewis acid site models used in this study.	47
3.5. Calculated potential energy diagrams for CH ₄ activation pathways on 5T cluster models for (a) Ag ⁺ and (b) [CuOH] ⁺ Lewis acid sites. Competing pathways are distinguished by color.	53

3.6.	Energies of reaction ΔE_{rxn} (solid circles) and activation barriers E_a (crosses) for the activation of CH_4 on Lewis acids in $(\text{Al} \times 1)$ models in (a) and $(\text{Al} \times 2)$ models in (b).	57
3.7.	Parity plot comparing the energies of reaction (solid dots) and activation (crosses) of isolated Lewis acids in $(\text{Al} \times 1)$ models and in the presence of a proximal Brønsted acid in $(\text{Al} \times 2)$ models.	59
3.8.	Parity plot comparing the energies of reaction (solid dots) and activation (crosses) of isolated Lewis acids in $(\text{Al} \times 1)$ models and in the presence of a proximal Brønsted acid in $(\text{Al} \times 2)$ models.	61
3.9.	Boxplots comparing the E_a ensembles for CH_4 activation over Lewis acids in periodic SSZ-13 and combined ensembles using descriptive statistics.	64
3.10.	Boxplots comparing the E_a ensembles for cluster models and periodic cells.	66
4.1.	UV-Visible spectra collected at 27 °C for various Ag-ZSM-5 samples ($\text{SAR} \sim 12$) for various Ag loadings (Ag/Al) in a) and for different methods of synthesis (indicated in the legend) of $\text{Ag}_{0.25}$ -ZSM-5 in b).	84
4.2.	Computed UV-Vis spectra of five Ag-SSZ-13 zeolite models, i.e. Ag-SSZ-13 (blue), Ag-H-SSZ-13 $_{\text{Al} \times 2}$ (red), Hydrated Ag-SSZ-13+ H_2O (cyan), AgH-SSZ-13 (gold) and clustered Ag ₃ -H-SSZ-13 (green).	85
4.3.	Normalized Ag K-edge X-ray absorption near edge spectra (XANES) for Ag-ZSM-5 samples collected ex-situ at ambient conditions.	88
4.4.	Fourier transforms of k^2 -weighted EXAFS spectra of $\text{Ag}_{0.08}$ -ZSM-5, $\text{Ag}_{0.46}$ -ZSM-5, Ag_2O and Ag foil collected at ambient conditions.	89
4.5.	TPD spectra for quartz (brown), H-ZSM-5 (blue), $\text{Ag}_{0.08}$ -ZSM-5 (orange), $\text{Ag}_{0.25}$ -ZSM-5 (green) and $\text{Ag}_{0.48}$ -ZSM-5 (red) for temperature ramps of 5 °C/min.	91

4.6.	Free energies of adsorption of H ₂ O ($\Delta G_{\text{ads,H}_2\text{O}}$) in the vicinity of the Brønsted and Lewis acid sites in H-ZSM-5 (black) and Ag-ZSM-5 (blue) periodic cell models as a function of the number of molecules adsorbed.	93
4.7.	Height-normalized pulse responses for ethylene ($m/z = 28$) exiting the microreactor for various catalyst samples (color indicated in the legend). Inset depicts the mean residence time (τ) for ethylene pulses.	95
4.8.	Height normalized ethylene (helium in inset) pulse responses exiting the microreactor for H-ZSM-5, Ag _{0.08} -Na-ZSM-5 and the Ag-H-Na-ZSM-5 physical mixtures (colors indicated in the figure legend).	97
4.9.	a) Binding energies in eV of olefins and paraffins to Ag ⁺ (blue) and H ⁺ (black). Visualizations of the π -bonded geometries through which ethylene and 1-butene bind to b) Ag ⁺ and c) H ⁺ acid sites in a ZSM-5 periodic cell.	98
4.10.	a) Height-normalized pulse responses for α -olefins and paraffins (inset). b) depicts the mean residence times of the pulses in a) as a function of carbon number for α -olefins in black and for alkanes in red.	100
4.11.	Conversion and uptake (X) as a function of pulses. Colors refer to catalysts indicated in the figure legend.	101
4.12.	a) Percentage yields for 100 ethylene/helium pulsed over 10 mg of H-ZSM-5 at 400 °C. b) charts the yields of 1,3-butadiene and hydrogen as a function of pulse admitted.	102

4.13. Gibbs free energy diagram for the activation and oligomerization of ethylene for H-ZSM-5 with the Brønsted acid site located at the T-12 site in a ZSM-5 periodic unit cell. Annotations in black indicate the absolute energy of stable intermediate states while those in red indicate the activation energy barriers relative to the previous stable state.	104
4.14. Visualizations of the initial (IS), transition (TS) and final states (FS) for intermediate steps in the activation and oligomerization of ethylene on H-ZSM-5.	105
4.15. Initial, transition and final state geometries sampled in the dehydrogenation of 1-butene to 1,3-butadiene. Reaction steps are given in the annotations above each structure.	106
4.16. Percentage product yields obtained for 100 pulses of ethylene/helium admitted to 10 mg of Ag _{0.08} -Na-ZSM-5 at 400 °C.	107
4.17. Free energy diagrams (T = 400 °C and P = 101325 Pa) for a) the deprotonation mechanism and b) the metallacycle mechanism for the dimerization of ethylene.	109
4.18. Depictions of the intermediate states sampled as part of the deprotonation pathway. The figures for IS through FS3 in the first row visualize geometries along the sinusoidal channel of ZSM-5. Figures for FS3 through FS6 visualize geometries along the straight channel (second row) and the sinusoidal channel (third row) of ZSM-5. . . .	110
4.19. Visualizations of the initial, transition and final states for the a) reverse deprotonation mechanism as seen through the sinusoidal channel and b) the internal hydrogen transfer mechanism seen through the straight channel.	112

4.20. The initial, transition and final states sampled while modeling the metallacycle mechanism for the dimerization of ethylene to 1-butene. The figures are annotated according to those introduced in Figure 4.17 b	114
4.21. Yields for butenes (1-C ₄ H ₈ , 2-C ₄ H ₈), 1,3-butadiene (C ₄ H ₆), propene (C ₃ H ₈) and methane (CH ₄) obtained over for 100 ethylene/helium pulses admitted into microreactor.	115
4.22. Height normalized averaged pulses for 1(2)-butene in a and 1,3-butadiene in b. The inset in a) shows the development of the peak-shoulder feature over the first 20 butene pulses recorded over H-ZSM-5	117
5.1. Representative descriptions of a) pump-probe experiments and b) saturation experiments performed in this work.	126
5.2. (a) Moles of toluene pulsed in (∇) and moles retained in the zeolite (\bigcirc) and b) Percentage product yields for benzene and xylene obtained while saturating the ZSM-5 catalyst with toluene (1×10^{-6} moles/pulse).	127
5.3. a) Methanol conversion profiles obtained as a function of methanol/helium pulse number for a H-ZSM-5 catalyst sample saturated <i>a priori</i> with toluene. b) percentage product yields obtained per mole of methanol consumed.	129
5.4. a) Height-normalized averaged pulse responses for toluene corrected for overlapping fragments of xylene and b) height-normalized pulse responses for xylene.	130
5.5. Signals of unreacted toluene collected while saturated H-ZSM-5. . .	130

5.6.	a) Methanol conversion and moles of water as a function of pulses and b) height normalized pulse responses for unreacted methanol and water detected at the MS.	132
5.7.	a) Percentage product yields per mole of toluene consumed when toluene is pulsed into H-ZSM-5 saturated with methanol <i>a priori</i> and b) Height-normalized averaged pulse responses for toluene, xylene and water.	133
5.8.	Height normalized averaged pulse responses for water collected from all saturation experiments performed in this work.	135
5.9.	Percentage product yields of a) xylene and b) benzene per mole of toluene consumed. The trends indicated by the green cross marks (×) are obtained from an experiment in which a methanol pulse probes a toluene pump pulse.	136
6.1.	The deposition apparatus. X and Y parameters for each deposition can be found in Table B.1.	144
6.2.	Regular grid of 100 H atoms fixed in their (x, y) cartesian coordinates on the Fe ₃ P(100) surface.	150
6.3.	Structures of the molecular precursors 1-4 used for the synthesis of FeP, Fe ₂ P and Fe ₃ P in this work.	152
6.4.	(A) Crystal Structure of the major component of 3 (R,R isomer). (B) Major component of 3 viewed down the P–P bond (C) Minor Component of 3 viewed down the P–bond. Thermal ellipsoids are given at 50% probability.	155
6.5.	XRD, XPS, and XPS-Depth Profile of FeP on Quartz; A) XRD, B) Surface XPS Spectra, C) XPS Depth Profile, D) Interior XPS Spectra. Peaks denoted by * in the XRD pattern arise from the substrate. . . .	156

6.6.	XRD, XPS, and XPS-Depth Profile of Fe_2P on Quartz; A) XRD, B) Surface XPS Spectra, C) XPS Depth Profile, D) Interior XPS Spectra.	157
6.7.	SEM images of FeP (A) and (D), Fe_2P (B) and (E), and Fe_3P (C) and (F) on FTO.	158
6.8.	Electrochemical characterization. (A) Polarization curves. (B) Corresponding Tafel slopes. (C) Charge transfer Tafel slopes. (D) Half of the current density differences as a function of scan rate.	159
6.9.	Contours of H binding strength on the surfaces of a) Fe_3P (100); b) Fe_2P (100); and c) $\text{FeP}_{\text{Fe-t}}$ (011). Fe atoms are depicted with thick boundaries, while P atoms are depicted with thin boundaries.	164
6.10.	Coverage-dependent, differential Gibbs free binding energy for seven distinct Fe_xP models with different stoichiometry or termination. . .	166

1. Introduction

1.1. Catalysis in Everyday Life

The International Union of Pure and Applied Chemistry (IUPAC's) Gold book defines a catalyst as *a substance that increases the rate of a reaction without modifying the overall standard Gibbs energy change in the reaction*. The catalyst is both a reactant and product of a chemical reaction. Catalysis can be classified as homogeneous, in which only one phase (solid, liquid or gas) is involved, and heterogeneous catalysis, in which the reaction occurs at or near an interface between phases. Heterogeneous catalysis is extremely important in the world order because it enables selective large-scale production of important chemicals. Catalysis has a hand in $\sim 35\%$ of the world's GDP with solid catalysts responsible for production of $\sim 90\%$ of chemicals (by volume). The socio-economic impact of catalysis on society is immense can be seen in two examples, one in the twentieth and the other in the twenty first century.

Nitrogen is a critical requirement for plants to perform photosynthesis and without nitrogen, there would be no photosynthesis, and thus insufficient food production. The lack of "bioavailability" of atmospheric nitrogen limits its utilization by plants, except in certain leguminous plants with nitrogen-fixing bacteria in their root nodules. This is in part attributed to the extremely strong bond that connects the nitrogen atoms. At the time, scientific research into improving agricultural output zeroed in on the use of fertilizers to improve crop yield by supplementing their growth with synthetic nitrogen. The effect of fertilizer on crop growth is seen in Figure 1.1. In the late 1800's and early 1900's, scientists,

mainly chemists, began looking for ways to develop fertilizers by artificially fixing nitrogen the way legumes do in their roots. On July 2, 1909, Fritz Haber demonstrated the continuous production of liquid ammonia from the reaction of nitrogen and hydrogen in a hot iron tube under high pressure catalyzed by osmium metal catalyst. This process was later modified to become an industrial process to make fertilizers by Carl Bosch and commercialized by BASF in 1913.⁷

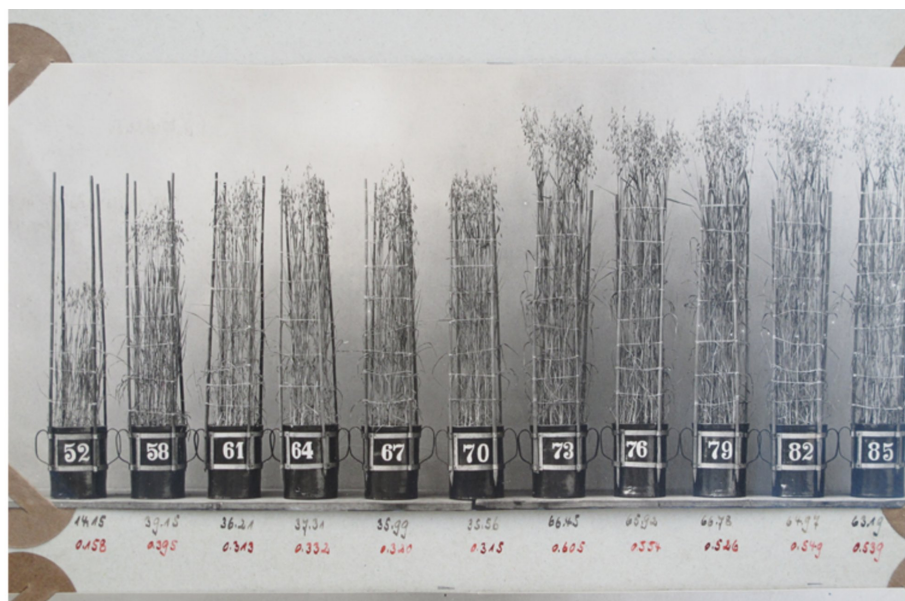


Figure 1.1. Photo of fertilizer test showing the improvement of yield, 1919. Adapted from [BASF](#).

The Haber-Bosch process is considered to be one of the most important technological advances of the 20th century. A study by the SLAC National Accelerator Laboratory (part of the U.S. Department of Energy) in 2013 summarizes the societal impact of the process - *"Roughly 1 to 2 percent of the world's annual energy supply is utilized to produce more than 500 million tons of nitrogen fertilizer, which is believed to sustain about 40 percent of the world's 7 billion people. Approximately half of the protein in today's humans originated with nitrogen fixed through the Haber-Bosch process."*

A more recent example that highlighted the importance, although in a neg-

ative connotation, of heterogeneous catalysis to society. The development of internal spark and compressed ignition engines that permit the controlled combustion of fuel with air have helped drive society forward, literally and figuratively. Engines typically produce total combustion products such as CO_2 and H_2O and some partial combustion products such as CO and unburned hydrocarbons (HC). High temperatures ($> 800^\circ\text{C}$) are attained during the combustion process and result in the gas-phase oxidation of nitrogen with air to form poisonous NO_x (NO , NO_2 and N_2O) species.⁸

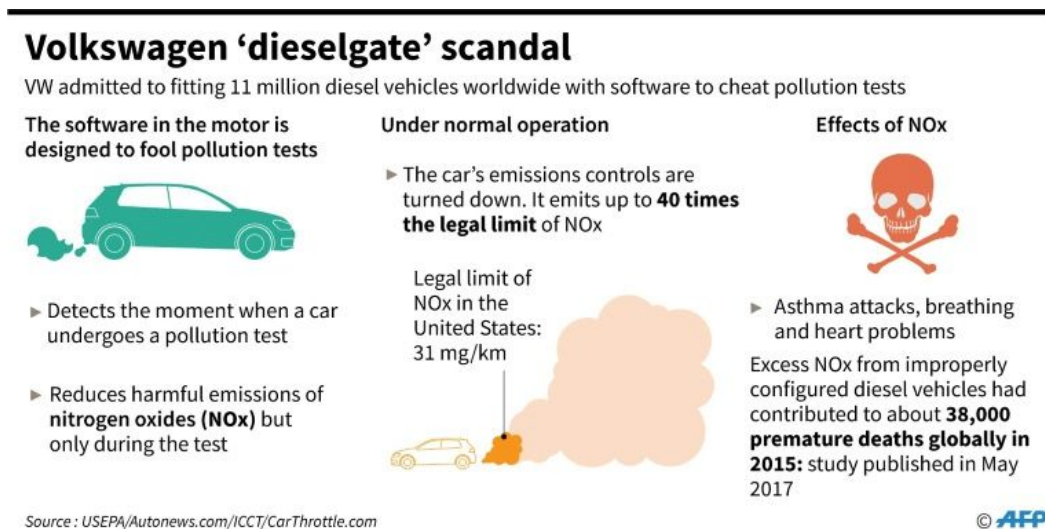


Figure 1.2. Volkswagen 'dieselgate' scandal. Graphic on the Volkswagen emissions cheating scandal. Adapted from [Yahoo News](#).

Catalysts in automotive catalytic converters render these noxious gases harmless by converting, for example, CO to CO_2 and NO_x to N_2 and H_2O . The functioning of these catalysts is critical to the well-being of humans and is rightly termed as a matter of life and death.⁹ A recent report suggests that tens of thousands of premature deaths per year could be avoided if catalytic converters functioned on-road as designed.¹⁰ In May 2014, investigators discovered the systematic installation and use of 'defeat-devices' in cars produced by Volkswagen.¹¹ An excellent graphic depicting the scandal is shown in Figure 1.2. Fines, litigation

and class-action lawsuits were estimated to have cost Volkswagen US \$6.4 billion but more importantly, underscores the importance of heterogeneous catalysis in everyday life.

1.2. Zeolite Catalysts

Zeolites are naturally occurring microporous aluminosilicate minerals that were first discovered in 1756. Commonly found zeolite minerals are faujasite, mordenite, offrerite, ferrierite, erionite and chabazite. The naturally occurring forms were not suitable for catalytic applications due to the presence of impurities. It was only with the advent of synthetic zeolites, specifically the syntheses of zeolite A and zeolite X¹² that really initiated the large-scale use of zeolites as adsorbents and catalysts. Zeolites X and Y were first used commercially in the fluid catalytic cracking (FCC) of heavy petroleum distillates in 1962 and ever since, their use has exponentially increased. These new catalysts resulted in a significant increase in the yield of gasoline, the most valuable product from FCC plants and in general showed orders of magnitude more activity than the previously used amorphous silica-alumina catalysts.¹

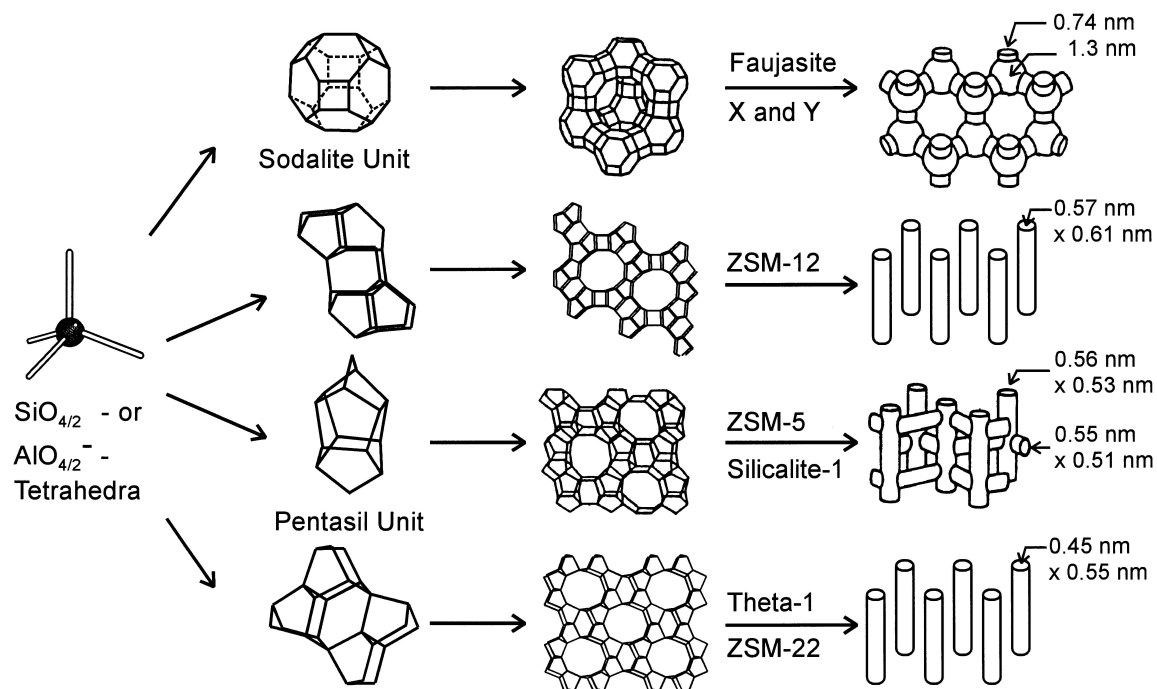


Figure 1.3. Structures of four selected zeolites (from top to bottom: faujasite or zeolites X, Y; zeolite ZSM-12; zeolite ZSM-5 or silicalite-1; zeolite Theta-1 or ZSM-22) and their micropore systems and dimensions.¹

In a zeolite framework, silicon atoms known as T-sites generally prefer to form four bonds with neighboring oxygen atoms in a tetrahedral geometry as an SiO_4 unit. These are known as the primary building units of zeolites. Specific geometric combinations of primary building units give rise to the formation of distinct secondary building units, which on three-dimensional replication form a zeolite framework. The structural components of zeolites for some commonly used zeolites are given in Figure 1.3. However, an SiO_4 unit in a framework is neutral because each oxygen atom bridges two T-sites. Thus, a defect-free or silicious zeolite framework is charge-neutral and not reactive. If an aluminum atom is tetrahedrally coordinated to four oxygen atoms and is connected to another T-site to form an aluminosilicate framework, there is a negative charge associated with each aluminum atom that can be balanced by a moiety of charge +1. This negative charge is often referred to as the active site in zeolite catalysis, with the species compensating this charge defect lending either Brønsted or Lewis acid character to the active site. Protons as charge-balancing species are most commonly encountered in zeolites. The exchange of cations into the pores of the zeolite is a relatively newer field of research with Cu-CHA commercialized in automotive catalytic converters for the selective catalytic conversion of NO_x species.^{13–15}

The use of zeolite catalysts revolutionized processes in industry in part due to the large enhancement in turnover at excellent selectivities to desired products. Zeolite catalysts share important properties with their predecessors in the industry, the amorphous silica-alumina systems, in exhibiting acidic properties due to the presence of Lewis and Brønsted acid sites. However, they also bring unique features to the table such as their strictly uniform pore diameters and pore widths in the order of molecular dimensions. The surface acidity is among the most important properties of zeolites with respect to their use as catalysts. It is a manifestation of a number of individual characteristics such as the nature of the

acid sites (Brønsted vs Lewis acidity), the density or concentration of acid sites, their strength and lastly, their location within the framework of the zeolite.

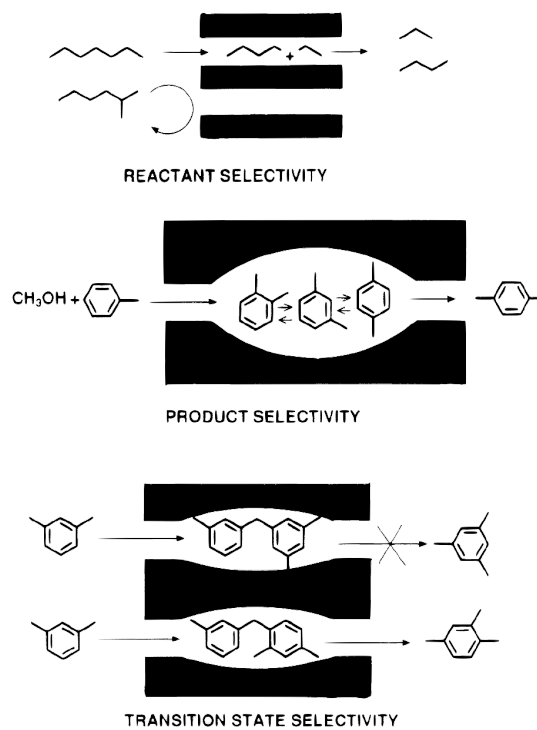


Figure 1.4. Schematic representation of the types of shape selectivity exhibited by zeolites. Taken from the work of Davis.²

The excellent selectivity to desirable products afforded by zeolite catalysts is attributed to its shape-selective properties and is summarized in Figure 1.4. Weisz and Frillette at the Mobil Oil Company (now ExxonMobil) coined the term "shape selective catalysis" in the 1950s when they discovered that only molecules that could diffuse through an LTA-type zeolite were catalytically converted. This effect was attributed to a combination of transport effects and the unique effects of the interaction of molecules and zeolite surfaces in the same order of magnitude.¹⁶

1.3. Hydrocarbon Conversion in Zeolite Catalysts

The confluence of zeolite acidity and shape selectivity have seen the use of zeolites in various many fields and more recently, there is considerable research being devoted to the use of zeolites in the conversion of natural gas feed stocks (mainly methane) to value-added products such as aromatics through a process known as dehydroaromatization. The reader is referred to the works of Spivey and Hutchings,³ Schwach and Bao¹⁷ and Kosinov and Hensen¹⁸ for excellent reviews of the latest concepts and research published in the field of methane dehydroaromatization.

The discovery of massive shale-gas deposits in various locations across the world has incentivized the search for catalysts that can enable the direct utilization of methane and other light hydrocarbons. One of the first major breakthroughs in this chemistry was the commercialization of the UOP CYCLAR process in which showed that ZSM-5 zeolites were effective for the conversion of propane and higher alkanes to aromatic chemicals, benzene, toluene and xylene.¹⁹ Molybdenum-exchanged ZSM-5 catalysts are the most promising catalysts for the conversion of methane to aromatics and is the subject of rigorous research efforts.

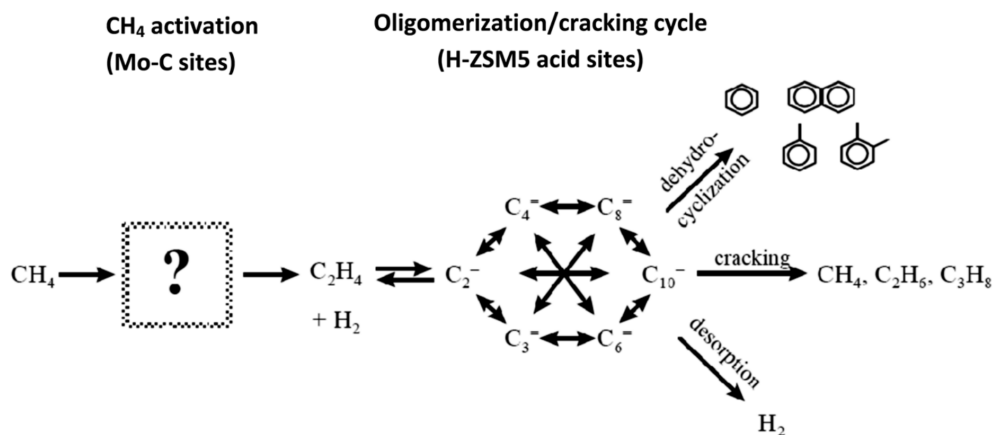


Figure 1.5. Postulated mechanism for methane aromatization on Mo/ZSM-5 catalysts showing the roles of the Mo-C sites and the Brønsted acid sites in the zeolite.³

For the conversion of methane, various moieties of molybdenum are exchanged into the zeolite to form a *bifunctional catalyst*. The acidity offered by the Brønsted acid and the Mo based Lewis acids work in conjunction with the shape-selective properties of ZSM-5 to enable this reaction. The Mo site is said to activate methane and enable the formation of the C–C bond by forming ethylene (C₂H₄) that is then oligomerized to benzene on the Brønsted acid sites.^{20,21} As with most hydrocarbon conversion mechanisms over zeolitic active sites, there is considerable uncertainty on the nature and type of intermediates that precede the formation of the final products. A schematic describing the conversion of methane at aromatics is given in Figure 1.5. Comparison can be made between the methane dehydroaromatization and the chemistry of the conversion of methanol to olefins over H-ZSM-5.^{22,23} There is consensus that long-lived carbonaceous species within the zeolitic pores, known as the hydrocarbon-pool act as a catalyst on which the methanol is converted to ethene as a primary product through autocatalytic mechanisms.

Overall, methane dehydroaromatization consists of a number of competing

sub-chemistries, each of which is complicated to study independently. Some of these chemistries are depicted in Figure 1.5 and include oligomerization, cracking, hydrogen-transfer, cyclization, dehydrogenation, isomerization to name a few. Additionally, once the aromatic species begin to form, disproportionation and alkylation chemistries are also initiated. While most of these chemistries are acid-catalyzed, the exact role and function of various zeolite characteristics introduced previously are still in question. For the case of Mo/H-ZSM-5, the chemistry is complicated by the presence of a diverse set of active metal-carbide motifs under reaction conditions that catalyze various mechanisms and pathways.^{24,25} A simplifying factor in the use of metal-exchanged zeolites for methane conversion to aromatics is the use of monovalent metals such as silver. Ag-ZSM-5 catalysts have been tested for various hydrocarbon conversions reactions and show promise as dehydroaromatization catalysts.²⁶⁻²⁹ The attractiveness of using Ag-ZSM-5 as a catalyst to understand the fundamental mechanisms that drive methane dehydroaromatization chemistries is due to the ease and control of its synthesis, and the relatively fewer number of active sites that exist under reaction conditions.

1.4. Outline of this Dissertation

The major focus of this dissertation is to investigate and understand the mechanisms and pathways that underlie the dehydroaromatization of ethylene to aromatics using a combination of transient pulsing experiments using the temporal analysis of products (TAP) technique and atomistic simulations using electronic structure theory in the guise of density functional theory (DFT). A cursory introduction to DFT is provided in chapter 2, section 2.1 and an in-depth description of the TAP reactor, data acquisition and processing is given in section 2.2. Next, a DFT-based statistical analysis of various metal-exchanged zeolite models was performed to evaluate the effects of various factors such as metal identity, framework, model description on the thermodynamics and kinetics of methane activation. The methods used and results of this investigation are given in chapter 3. Perspectives obtained from studying a diverse set of metal-exchanged zeolites were used in understanding the origin of the enhanced selectivity to aromatic hydrocarbons for Ag-ZSM-5 compared to H-ZSM-5 using an integrated approach of experimental and computational characterization, plug-flow and TAP experiments and computational modeling using DFT in chapter 4. Other types of TAP experiments were performed in chapter 5 to study the methylation of toluene, with focus on understanding the acid catalyzed mechanisms that take place inside the pores of H-ZSM-5. Finally, to address the frequent use of hydrogen co-feeds in hydrocarbon conversion processes using zeolites, chapter 6 outlines the computational efforts in rationalizing the enhanced electrocatalytic evolution of hydrogen exhibited by iron phosphide catalysts.

2. Methods

2.1. Density Functional Theory

Atomistic simulations, especially those employing density functional theory (DFT) becoming an increasingly important part of materials science today. A great variety of approaches and implementations have been developed that have strived to ease its applicability for the specialists and novices alike. The fundamental atomistic principles that govern the structural and functional behavior of materials are surprisingly simple. Atomic nuclei can be treated as classical particles of known mass and positive charge and electrons are treated as particles of spin one half, thus obeying the Pauli exclusion principle. Their contributions to kinetic behavior can then be calculated by quantum mechanics. The main interactions within the system are electrodynamic in nature with attractive and repulsive interactions governed by Coulomb's law. These fundamental principles make it conceptually possible to predict and rationalize the diverse physical and chemical properties of matter such as the structure and stability of molecules, crystalline phases, the mechanical properties of metals and alloys, the optoelectronic properties of semiconductors, the magnetic properties of transition metals, and so on.

The DFT approach is quite general in the sense that it is applicable to all atoms of the periodic table, with special considerations taken into account for heavier elements such as third row transition metals, rare-earths, and actinides. The range and variety of materials under investigation is almost all-encompassing. This approach can be used for metallic, covalent, and ionic bonds. The answers that are derivative of this approach are broad and include quantities

that are experimentally measurable such as densities of states, magnetic moments, and energy level transitions. Additionally, the theoretical aspect of the approach also enables the realization of quantities that are not experimentally accessible, such as, in-layer bond-length relaxations and formal charges. These properties are still important in understanding the properties of a given material. When direct comparisons are afforded, the density functional theory approach provides powerful methods to test theoretical calculations and eventually to improve them, bringing them even closer to their experimental benchmarks. In particular, DFT calculations have seen much success in evaluating the properties of metallic condensed systems. An excellent example that is relevant to the ideas implemented in this dissertation is the first-principles investigation of ammonia synthesis in heterogeneous catalytic systems.³⁰

A comprehensive overview of DFT is beyond the scope of this chapter as in-depth reviews are easily found in the literature.^{31,32} Texts relevant to computational catalysis and the general applicability of density functional theory to understand catalytic systems are also numerous in number.^{33,34} Instead, this chapter is intended to provide a useful starting point for a non-expert to understand and use DFT appropriately and consequently, better interpret results and conclusions proposed in this dissertation.

The Schrödinger equation is the fundamental equation of physics for describing quantum mechanical behavior. Also called the Schrödinger wave equation, it is a partial differential equation that describes how the wavefunction of a physical system evolves over time.³⁵ It was postulated in 1926 by Erwin Schrödinger for which he later shared the Nobel prize with Paul A. M. Dirac in 1933. The wave function seemed promising as it contained all of the information available about a system.

The wave equation is a highly-coupled many-body eigenvalue problem

given by the equation

$$H\psi = E\psi, \quad (2.1)$$

where H is a Hamiltonian operator and ψ is a set of solutions or eigenstates of the Hamiltonian. The full interaction Hamiltonian can be expanded for a typical chemical system consisting of N electrons interacting with M nuclei and is given by

$$\left[-\frac{\hbar^2}{2m} \sum_{i=1}^N \nabla_i^2 + \sum_{i=1}^N V(\mathbf{r}_i) + \sum_{i=1}^N \sum_{j<i}^N U(\mathbf{r}_i, \mathbf{r}_j) \right] \psi = E\psi. \quad (2.2)$$

The first term in the Hamiltonian is the net kinetic energy of all N electrons; the second term quantifies the cumulative Coulombic interactions all N electrons and the net electric field of all M nuclei, and the last term is the inter-electronic interaction. The wavefunction ψ is an abstract quantity and is related to a physically observable property called the electron density $n(\mathbf{r})$, which is the probability of finding an electron in a fixed space $d\mathbf{r}$. For a system with N electrons with electronic spin ω , $n(\mathbf{r})$ is related to the wavefunction ψ as,

$$n(\mathbf{r}) = N \int \psi^*(\mathbf{r}_1, \dots, \mathbf{r}_N, \omega_1, \dots, \omega_N) \psi(\mathbf{r}_1, \dots, \mathbf{r}_N, \omega_1, \dots, \omega_N) d\mathbf{r}_1 d\omega_1 \dots d\mathbf{r}_N d\omega_N. \quad (2.3)$$

The wavefunction in Schrödinger equation ψ depends on the spatial coordinates (x_i, y_i, z_i) of N electrons and the M nuclei, i.e. $\psi(r_1, \dots, r_N, R_1, \dots, R_M)$. Unfortunately, most practical systems of interest consist of many interacting electrons, and the effort required to find solutions to the wave equation increases exponentially with the number of electrons limiting its use to systems with a small number of relevant electrons N .

The exact solution of the Schrödinger equation or the wave-function method has been extremely successful in studying the properties of small molecules. However, this method unsuitable for studies of large, extended solids such as

catalytic surfaces and supported nanoparticles. This difficulty was recognized by Paul Dirac in 1929, when he wrote "The underlying physical laws necessary for the mathematical theory of a large part of physics and the whole of chemistry are thus completely known, and the difficulty is only that the application of these laws leads to equations much too complicated to be soluble".³⁶

The insurmountability of obtaining solutions to the full Schrödinger equation led to multi-pronged efforts by various researchers to find creative methods based on iterative numerical schemes based on well-founded theories. The widespread use of DFT as an approximate solution to the wave equation is in part due to the fundamental breakthrough achieved by Hohenberg and Kohn³⁷ in 1964 who postulated that *"The ground-state energy E_0 obtained from Schrödinger's equation is a unique functional of the electron density $N(r)$."* and *"The electron density $N(r)$ that minimizes the energy of the overall functional is the true electron density corresponding to the full solution of the Schrödinger's equation."*

The next major development followed in 1965, when Kohn and Sham showed that the problem of many interacting electrons in an external potential can be mapped exactly to a set of N noninteracting electrons in an effective external potential $V_{ext}(r)$ resulting in a set of self-consistent, single particle equations known as the Kohn-Sham (KS) equations.^{38,39} Accordingly, it was shown that the ground state electron density $n_0(r)$ minimizes the functional

$$E[n] = F[n] + \int n(\mathbf{r})V_{ext}(\mathbf{r})d\mathbf{r}, \quad (2.4)$$

where $F[n]$ is the universal functional of n . Finally, the Kohn-Sham equations are

written as

$$\left(\frac{1}{2} \nabla^2 + v_{eff}(\mathbf{r}) - \epsilon_j \right) \varphi(\mathbf{r}) = \epsilon_j \varphi(\mathbf{r}), \text{ with} \quad (2.5)$$

$$v_{eff}(\mathbf{r}) = v(\mathbf{r}) + \int \frac{n(\mathbf{r}')}{|\mathbf{r} - \mathbf{r}'|} d\mathbf{r}' + v_{xc}(\mathbf{r}). \quad (2.6)$$

where $v(\mathbf{r})$ is the external potential and $v_{xc}(\mathbf{r})$ is the exchange-correlation potential, that depends on the entire density function. If the exchange-correlation energy functional is known, Equation 2.6 is exact. However, the exact form of the exchange-correlation energy functional is not known and is today, subject to rigorous research. In the meantime, various approximations for the exchange-correlation functional have been proposed, of which the most common types are the Local Density Approximation (LDA) and the Generalized Gradient Approximation (GGA). All density functional theory calculations in this dissertation employ the BEEF-vdW exchange-correlation functional, a fitted semi-empirical functional that utilizes finite contributions of exchange energy from the LDA and GGA approximation and non-local correlation energy from the vdW-DF2 van der Waals functional.⁴⁰

Therefore, Equation 2.6 requires a known electron density $n(\mathbf{r})$ to define the effective potential term $v_{eff}(\mathbf{r})$. If $\varphi(\mathbf{r})$ corresponds to the j^{th} KS orbital of energy ϵ_j , then the ground state electron density $n_0(\mathbf{r})$ is given by

$$n_0(\mathbf{r}) = \sum_{j=1}^N |\varphi_j(\mathbf{r})|^2. \quad (2.7)$$

An initial guess of $\varphi_j(\mathbf{r})$ is used to compute the electron density in Equation 2.7, which can then be used to define the effective potential $v_{eff}(\mathbf{r})$ in Equation 2.6. This equation is then solved for $\varphi_j(\mathbf{r})$ iteratively until the $\varphi_j(\mathbf{r})$ resulting from the KS equations (Equation 2.5) are equal to $\varphi_j(\mathbf{r})$ calculated initially in Equation 2.7,

yielding self-consistent solutions. Finally, the ground state energy is given by

$$E = \sum_j \epsilon_j + E_{xc}[n(\mathbf{r})] - \int v_{xc}(\mathbf{r})n(\mathbf{r})d\mathbf{r} - \frac{1}{2} \int \frac{n(\mathbf{r})n(\mathbf{r}')}{|\mathbf{r} - \mathbf{r}'|}d\mathbf{r}'d\mathbf{r}, \quad (2.8)$$

where $E_{xc}[n(\mathbf{r})]$ is the exchange-correlation energy functional.

This ground state energy is an arbitrary quantity that describes the stability of the initially considered configuration of M nuclei and N atoms. Atomic simulation packages such as VASP, Quantum Espresso, GPAW, NWChem that are built around the fundamental theorems of DFT expand its applicability into automatically obtaining more useful information of interest. For instance, the most commonly run calculations are those to obtain the ground state structure and energy of a known configuration of atoms. In such a calculation, an initial guess of electron density is defined from the cartesian coordinates and elements provided through the approximation of core electrons of the atoms by means of pseudopotentials. This electron density is self-consistently minimized to obtain the ground state density, and by extension, the ground state energy of that configuration. Structure optimization algorithms utilize the energy iteratively alter the configuration of atoms to minimize the DFT energy until the ground state structure is attained, commonly referred to as the "*relaxed structure*".

2.2. Temporal Analysis of Products

2.2.1. Background

The TAP technique was invented by John Gleaves and coworkers while at Monsanto in 1988 and serves to bridge the materials gap and partially, the pressure gap between UHV surface science and high-pressure catalytic experiments.⁴¹ Before getting into the specifics of the TAP reactor, a brief overview of

the motivation behind using this unique technique within the relevance of catalytic experiments is provided.

Historically, catalyst design, development and refinement is based on time-consuming trial and error Edisonian approaches, in most cases leading to an incremental improvement in catalyst performance. The reason behind the slow progress can be largely attributed to an incomplete understanding of the fundamental reaction mechanisms and kinetics. This information is crucial in the catalyst development program, shown in figure Figure 2.1, to accelerate the identification of promising catalysts in the primary screening phase and the eventual scale up of the catalytic process to an industry scale.⁴

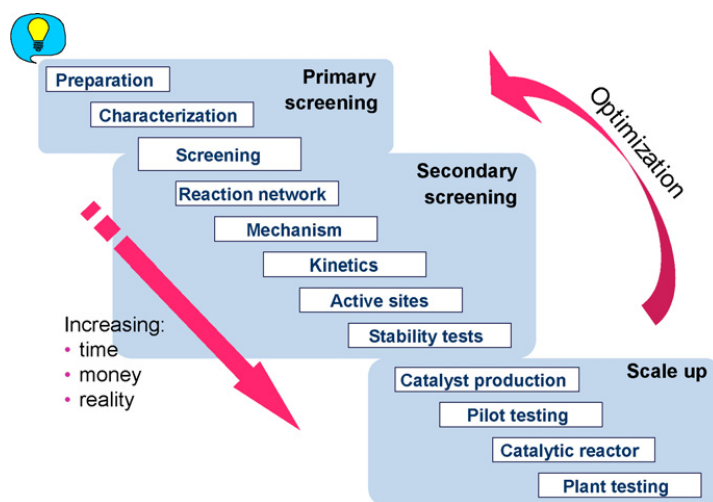


Figure 2.1. Stages of the catalyst development program.

Traditional steady-state flow catalytic experiments have been successfully used to understand and decipher complex catalytic phenomena for decades, but are sometimes a victim of their own simplicity. For instance, the lack of molecular detail due to low time resolution eventually lead to kinetic modeling that consist of lumped parameters that provide an integrated description of the catalyst by rationalizing the global behavior of the system.⁴² Over the years, several attempts have been made to enable a deeper understanding of the molecular phenomena

that govern catalytic processes through surface science techniques. A standard approach would be to synthesize a well-defined model surface, characterize it with atomic precision and then subject it to catalytic reactions.⁴³ An example of such an approach would be modulated molecular beam experiments performed under controlled ultra-high vacuum conditions at well-defined catalytic centers. Quantum chemical modeling techniques have also made significant progress and are able to provide measures of thermodynamics and kinetics that drive chemical transformations. However, a major drawback of the fundamental knowledge gained from these advanced techniques is the inability to extrapolate concepts to an industrial process, commonly referred to as the pressure and material gap in concepts. A visualization of various techniques for investigation catalytic reactions and their positions with respect to the pressure and material gap provided in Figure 2.2.

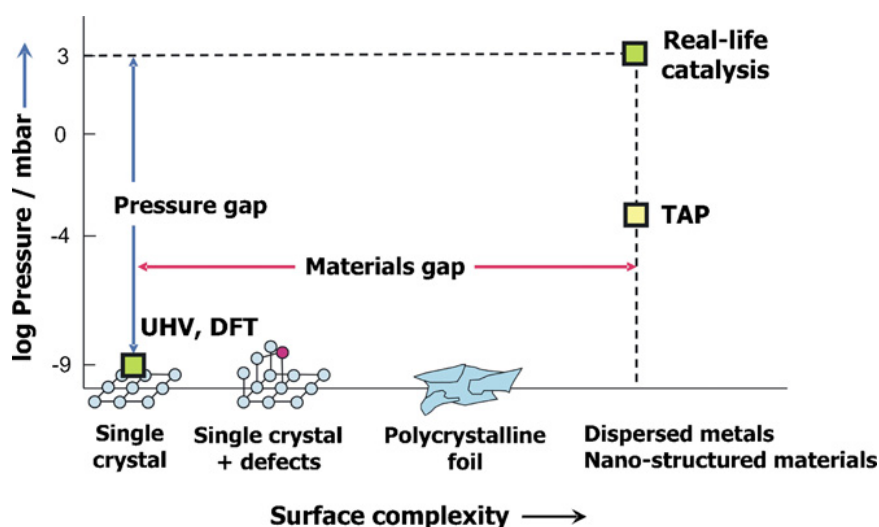


Figure 2.2. Pressure-materials diagram indicating the position of various approaches to investigate mechanisms and kinetics of heterogeneously catalyzed reactions.⁴

Transient methods are alternative strategies that can be used to overcome the deficiencies of traditional mechanistic studies. Testing under transient conditions removes mean field approximations that contribute heavily to the global

behavior of the catalyst, and with precise control can characterize the dynamic reactions as individual reaction steps. Transients (reactants) are fed into the system while perturbing more measures of state, i.e. pressure, temperature, composition, and flow rate.⁴⁴ The temporal analysis of products (TAP) reactor falls under this category of transient techniques. The main advantage of the TAP technique is the sub-millisecond time resolution it affords and it enables the study of mechanisms, kinetics, and transport phenomena of heterogeneously catalyzed gas–solid reactions at a high level of precision and accuracy.

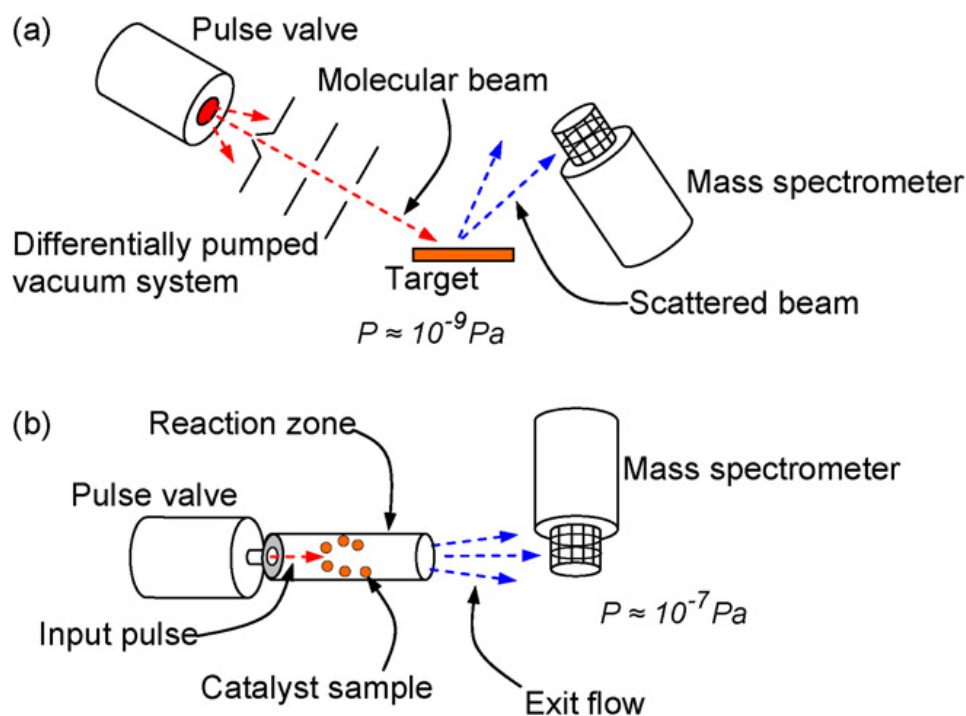


Figure 2.3. Conceptual comparison of key components of (a) molecular beam scattering experiment and (b) TAP experiment. Adapted from the work of Gleaves.⁵

In the bigger picture, the overall advantages of the TAP technique are best illustrated in Figure 2.2. A diverse set of catalyst samples ranging from well-defined model surfaces to washcoated monoliths to nanoparticles supported on metal oxides can be studied. Additionally, the upper limits of pressure attained at the catalyst bed are approximately in the order of 1 mbar, which is still 9 orders

of magnitude higher than pressures typically associated with ultra-high vacuum (UHV) surface science experiments. An excellent comparison of a representative molecular-beam scattering experiment, a UHV technique with the TAP is given in Figure 2.3. The TAP technique also offers a middle-ground to compare transient kinetic information to knowledge derived from atomistic simulations using density functional theory (DFT), offering the possibility of a TAP-guided exploration of reaction pathways and mechanisms.

2.2.2. Overview of Set Up

All transient experiments referred to in this work were performed on the temporal analysis of products (TAP-1) reactor at the University of Houston and is pictured in Figure 2.4. In simple terms, the functioning of a typical TAP experiment is illustrated in Figure 2.3 b. A narrow pulse consisting of 10^{-10} – 10^{-6} moles of reactant is admitted into the reactor. Unreacted reactants and products formed elute from the microreactor and are monitored and quantified by the quadrupole mass spectrometer. An overview of the key components of the reactor follows.

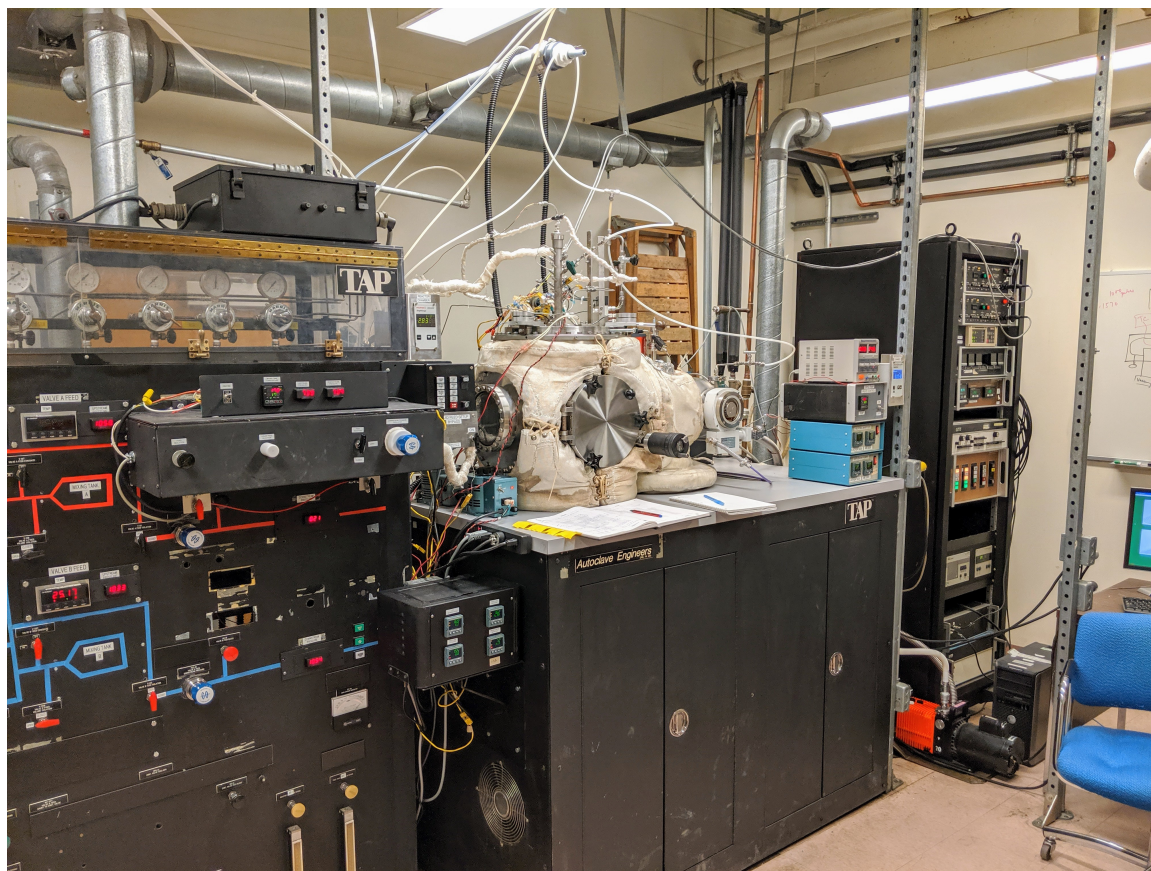
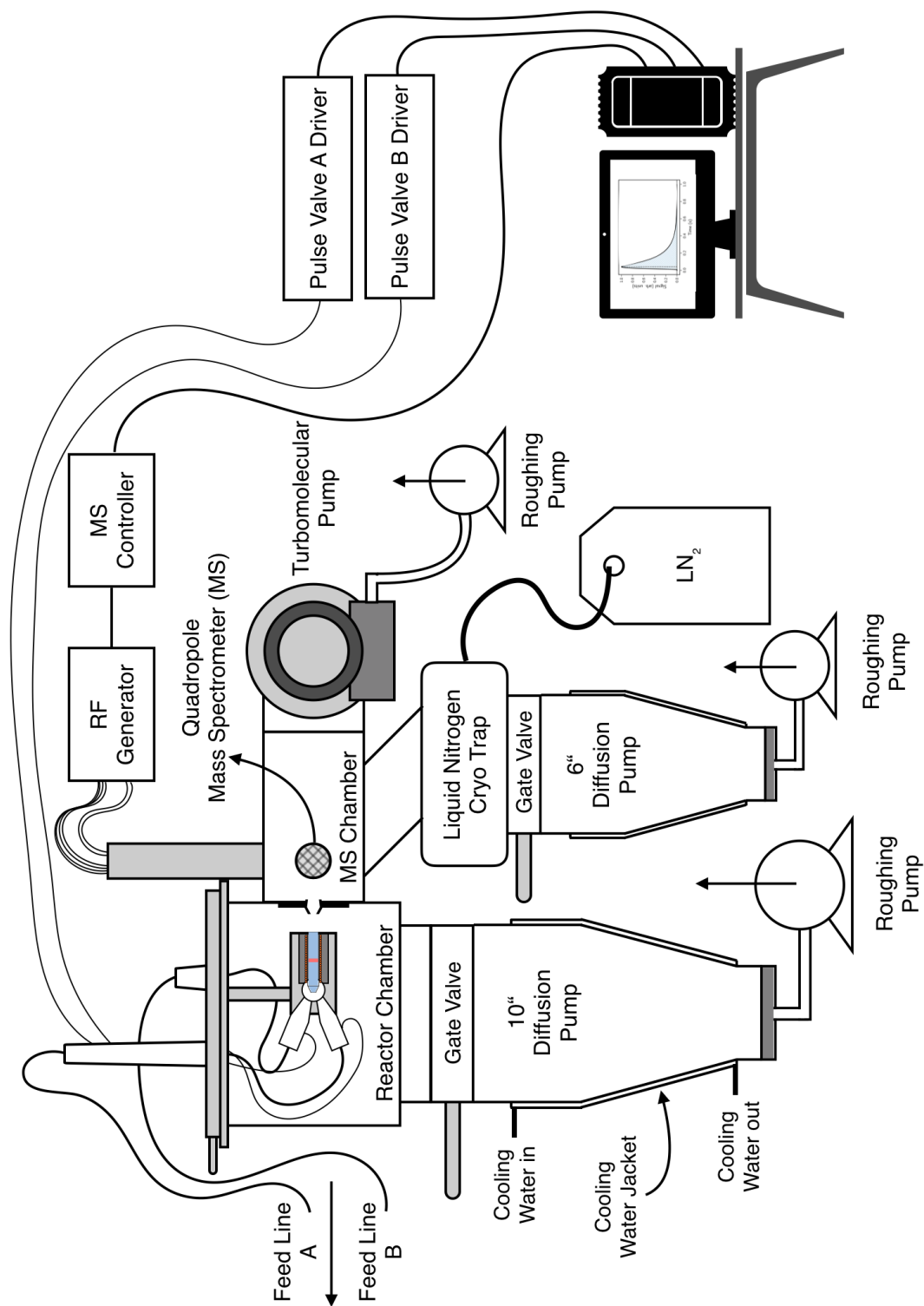


Figure 2.4. The temporal analysis of products (TAP-1) reactor at the University of Houston.

The main components of the TAP setup are the differential high vacuum pumping system, the mass spectrometer, the microreactor, a pulsing setup and the feed preparation and mixing section. The schematic of the TAP setup is shown in

Figure 2.5



Temporal Analysis of Products (TAP-1) Schematic

Figure 2.5. Schematic of the TAP-1 setup without the feed preparation and mixing section included.

2.2.3. Differential High Vacuum Pumping System

The TAP reactor is operated under high-vacuum regimes of pressure and is differentially pumped to ensure that the diffusing gases from the microreactor outlet are in the form of a molecular beam. The MS chamber is at lower pressures than the reactor chamber and this is achieved by a combination of pumps. The chamber is pumped down to pressures of 10^{-6} torr by a multi-stage Pfeiffer-Balzers TPH 510 turbomolecular pump and an Alcatel roughing pump. Higher vacuums are attained with the help of the Varian VHS6 6" oil diffusion pump and a higher capacity Alcatel roughing pump. Cooling water is circulated in the jacket that surrounds the external surface of the pump to prevent overheating. To ensure that the mass spectrometer and its vicinity are not contaminated by oil vapors from the diffusion pump, a cryo trap is filled with liquid nitrogen and maintained at temperatures under -165°C . The MS chamber is also kept at a temperature of 225°C to keep the oils from condensing on the chamber walls and the ultimate pressure attained at full pumping capacity is $\sim 4 \times 10^{-8}$ torr.

The reactor chamber typically operated at pressures in the order of 10^{-6} torr to allow of the differential pumping system to work optimally and ensure the rapid diffusion of the molecular beam from the microreactor to the mass spectrometer. The chamber is pumped down to high-vacuum with the help of a multi stage Varian VHS10 10" oil diffusion pump and a high-capacity Alcatel roughing pump. The pump is kept under optimal operating conditions by circulating cooling water in the jacket surrounding the external surface of the pump. This chamber is also kept heated at 225°C to prevent oil condensation on the inner walls of the chamber. The pressures of both chambers are monitored by Pfeiffer PKR251 cold cathode full range gauges.

The vacuum system is designed such that all chambers can be isolated from each other, as well as from the pumps. The diffusion pumps can be brought off

line by actuating pneumatic gate valves, and the reactor and the MS chambers can be isolated from each other by a manual shutter. These components are visualized in Figure 2.5. Once an experiment is complete, the reactor chamber is isolated from its diffusion pump and the MS chamber and vented to atmospheric pressure to access the microreactor. This way, the mass spectrometer is continuously under high vacuum and can be kept under stable conditions of operation for many months.

2.2.4. Quadropole Mass Spectrometer

A UTI 100C quadropole mass spectrometer is positioned in the MS chamber in the direction of the molecular beam of gases diffusing out of the microreactor such that its axis and reflector assembly are perpendicular to the director of gas diffusion. It measures the signal of a pre-set mass-to-charge ratio (m/z) as an analog voltage as a function of time. A typical *Pulse Response* is shown in Figure 2.6.

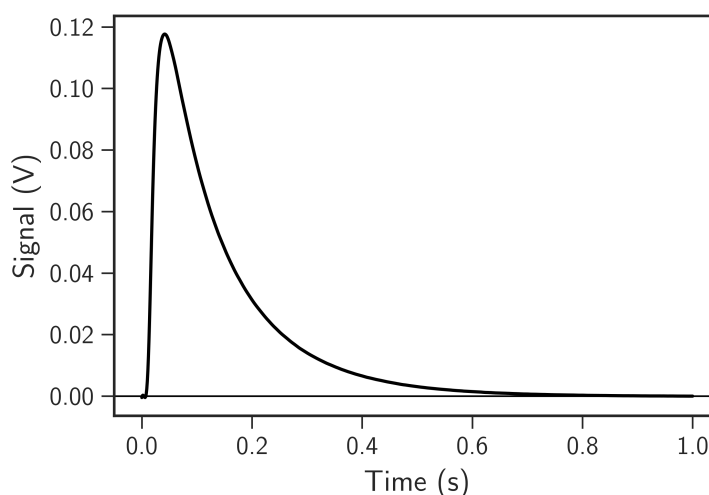


Figure 2.6. A typical pulse response obtained from a TAP experiment.

The mass spectrometer can measure m/z ratios ranging from 0 to 300 with

a resolution of 0.1, and is typically set up to measure the signal of one ratio at a time. The resolution of data collection can be as high as 10000 data points per second of data collection. Calibrations experiments with pure gases or in inert gas mixtures can be performed to equate MS signals to molar quantities through the calculation of calibration factors. Finally, experiments are set up such that the MS switches from one m/z ratio to the next as pulsing of reactants is initiated. For example, if eight ratios are to be monitored, the pulse response for the first ratio will be measured for the 1st, 9th, 17th pulse and so on.

2.2.5. Microreactor

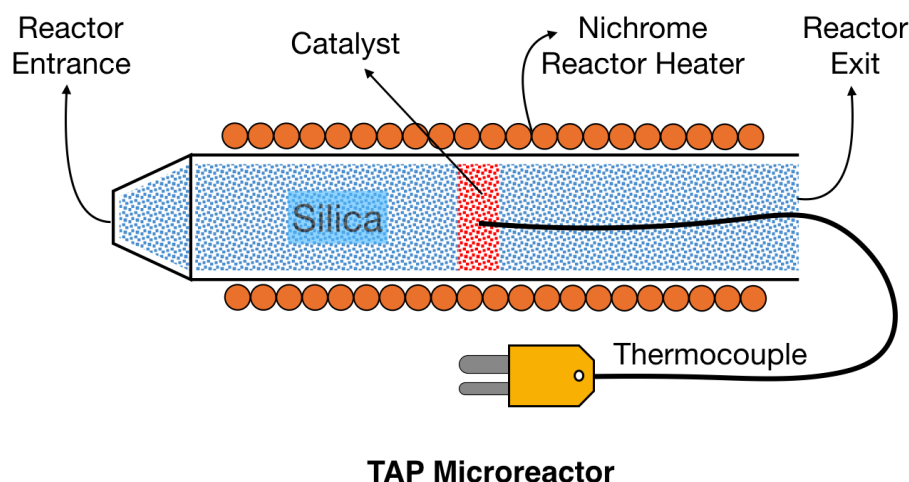


Figure 2.7. The quartz microreactor showing the catalyst loaded in a thin-zone configuration⁶ between two beds of silica

A schematic visualization of a TAP microreactor is shown in Figure 2.7. The reactor is made out of quartz tubes of ID=4 mm and OD=6mm and can be heated up to 600 °C. The reactor, minus the tapered end is ~53 mm long and seals at both ends with appropriately sized O-rings. It is housed in the pulse valve manifold and is surrounded by coiled nichrome resistance wire (Omega). The temperature of the reactor is measured and controlled by a K-type thermocouple (Omega) that

is connected to a PID temperature controller (Eurotherm). This controller can be programmed for specific ramps, temperatures and dwell times as is required by the experimenter.

2.2.6. Pulsing Setup and Manifold

As introduced in the previous section, the microreactor is housed in the pulse valve manifold where the reactant entrance seals against the pin-hole of the zero volume chamber (see Figure 2.8) with an O-ring. Two pulse valves (Parker-Hannifin) are mounted onto the manifold such that they directly feed the zero volume chamber. The pressure differential of the system will then ensure that the reactants pulsed in diffuse through the reactor and finally into the MS chamber. The entire set up in the reactor chamber is shown in Figure 2.8.

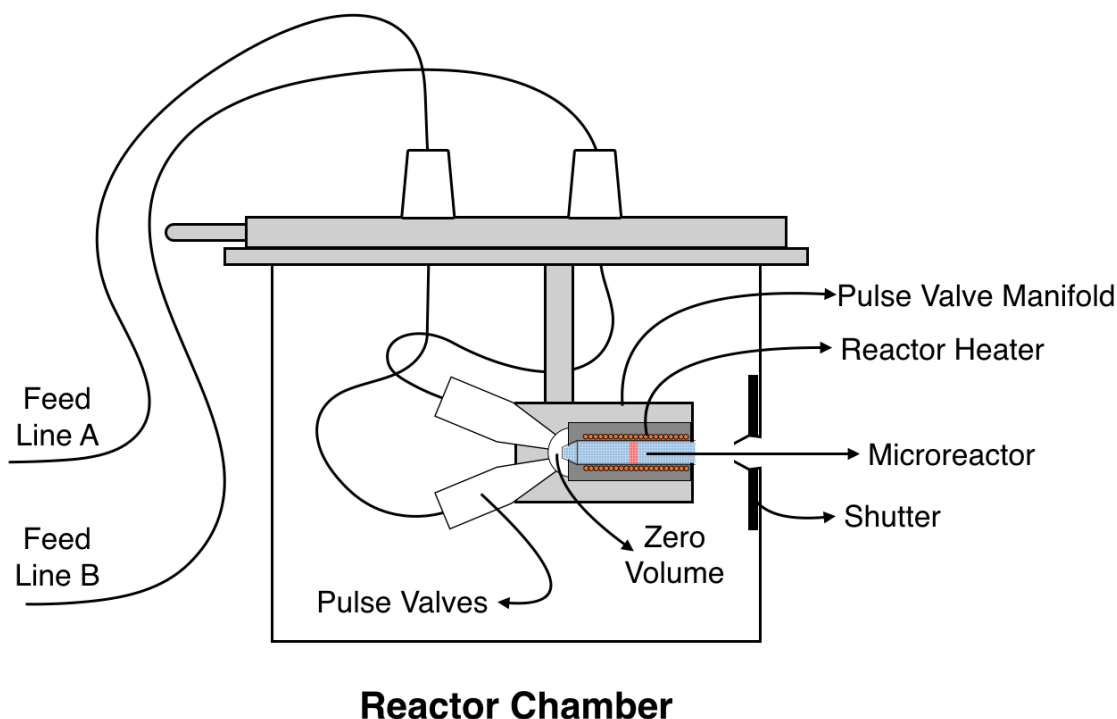


Figure 2.8. The reactor chamber of the TAP-1 reactor showing the pulse valve manifold and the microreactor housing.

The pulse valves are set up to be normally closed and open when an external pulse of current activates its electromagnetic coils. External, independently connected pulse valve driver apparatus (seen in Figure 2.5) are configured such that a 100 V pulse of current is sent at pre-set times to open the reactor. The duration of the pulse corresponds to the opening time of the pulse valves and the time separation between two pulses determines the pulse spacing. The opening times are set manually on the pulse valve drivers and typically range from 200–600 μ s. The pulse spacing is controlled by the data acquisition software which synchronizes pulsing with signal collected from the mass spectrometer.

2.2.7. Feed Preparation Section

Reactant gas mixtures of known proportions are prepared in this section. The feed lines are designed such that each of line A and B can carry of mixture that contains 9 component gases. A detailed schematic of the feed preparation section is given in Figure 2.10. Mixtures in mixing tanks A and B by admitting one component gas at a time. The partial pressure of the gases contained in the mixing tanks are measured by a Setra Model 280 pressure transducer. Once a pre-determined mixture of gases has been prepared upstream, the mixture is admitted downstream by means of the ball valve labeled "Downstream Open/Close". The pressure of the gas downstream is controlled by a pressure regulator that can be tuned manually based on the requirements of the experiment. The entire chamber can be evacuated by a Varian SD200 vacuum pump.

Latest upgrades to the feed preparation section allow for the injection of liquids and to prepare mixtures of gases that are liquids at ambient conditions. Liquids are injected through a leak-proof septum into the mixing tanks. The rest of the design remains the same as that of the original feed preparation section, but include for temperature-controlled heating trace cables and tapes to prevent

condensation of the vaporized liquid mixtures. The use of liquid mixtures have also necessitated the need to keep the pulse valve manifold at elevated temperatures. An aluminum block with insertion heaters (Watlow) in pre-drilled holes was machined to enclose the entire manifold and the pulse valves. The manifold is kept at a constant temperature of 110 °C. The schematic detailing the inclusion of upgrades for the handling of liquids is given in Figure 2.9

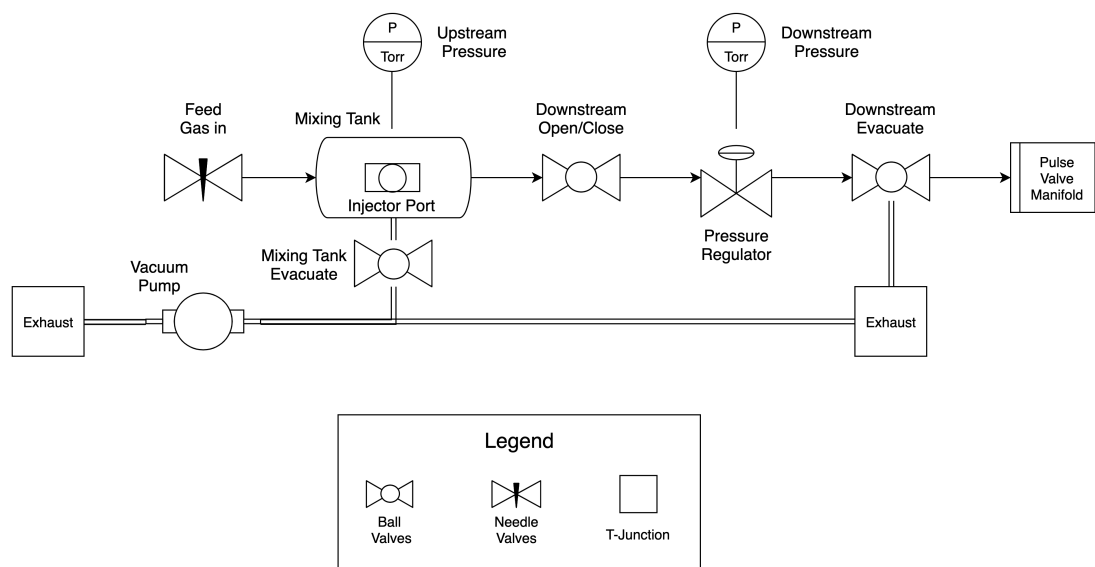


Figure 2.9. Piping and instrumentation diagram the liquid feed setup.

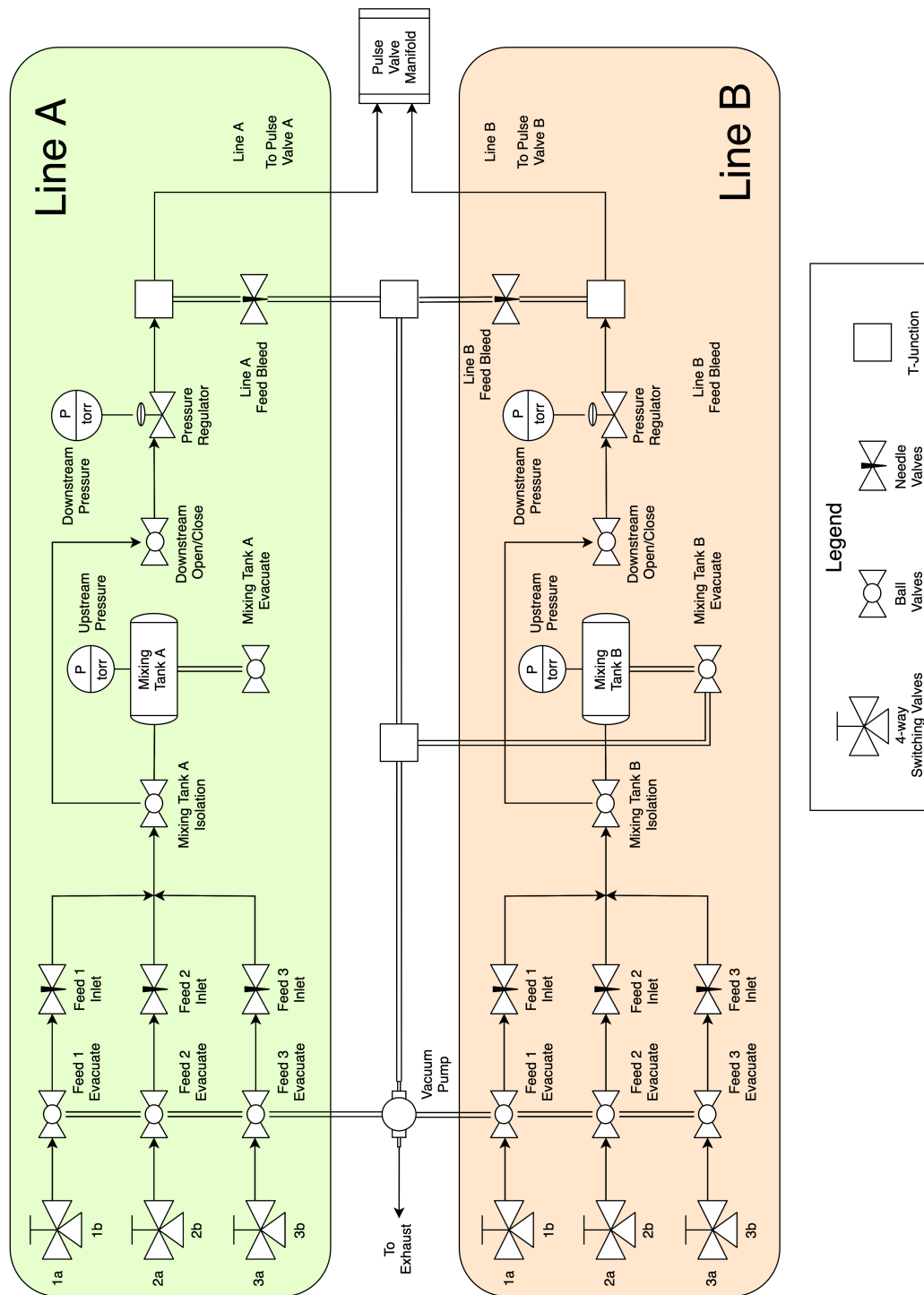


Figure 2.10. Piping and instrumentation diagram for lines A and B in the feed preparation section.

2.2.8. Data Acquisition and Processing

Data Acquisition

Data acquisition and control of TAP experiments were done with the TAPSoft application developed for the TAP-1 reactor. Various functions available in the program allow an experimenter to perform a sweep scan, transient and scope experiments. A sweep scan is used to record the background signal in the MS chamber. A typical scan is shown in the inset of Figure 2.11. The major peaks recorded are those of water ($m/z \sim 18$), nitrogen ($m/z \sim 28$), oxygen ($m/z \sim 32$). Transient experiments are initialized for data collection in the TAP mode. Using this program requires the user to set up typical experimental metrics such as choice of pulse valve, pulse spacing, collection time, AMUs or m/z ratios to be collected, MS gain for each AMU, amongst other options. A temperature program module is also available for the user to set ramp rates, dwell times, temperature levels and so on.

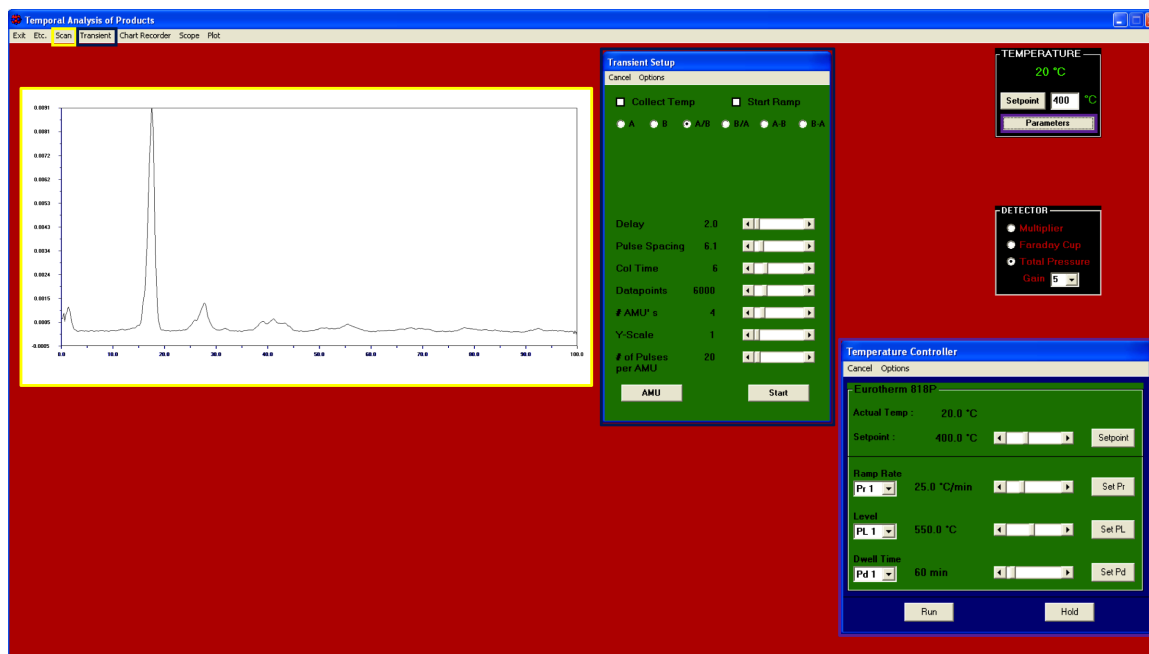


Figure 2.11. Screenshot of the TAPSoft data acquisition software used to perform typical experiments with the TAP-1 reactor.

Data Processing

TAP experiments generate a large quantity of data, with 1000 data points recorded per second of data per AMU recorded. To efficiently process and analyze TAP data, an in-house python package, TAPPy is being developed in collaboration with the TAP Group led by Dr. Rebecca Fushimi at the Idaho National Laboratory, Idaho Falls, Idaho.⁴⁵

The data recorded is saved in ASCII text files by TAPSoft. Measurements for each pulse response are extracted and baseline corrected. Since pulse data is collected till the signal for the corresponding AMU attains its flat baseline, they can be easily baseline-corrected with the average value of the flat portion of the pulse response. Then, pulse responses are smoothed to improve the signal-to-noise ratio. The Savitzky-Golay smoothing filter is used because this moving filter technique best preserves the physical characteristics of the pulse response. However, care was taken to not overly smooth the response. All of the original and post-processed data was stored in python-accessible dictionaries stored in pickle files. These dictionaries are data-structures based on key-value concepts where indexing of the data-structure is done through keys. The zeroth moments of pulse responses are calculated using the Simpson's Rule module provided by python's SciPy module.

Calibration

Calibration experiments must be performed over inert reactor beds to be able to convert the signal measured at the MS into molar quantities. These experiments are important to characterize and identify system specific differences that arise due to fluctuations in the functioning of the mass spectrometer. A finite number of pulses N at a pre-determined AMU are recorded while pure gas or gas/inert mixtures are being pulsed in from a fixed volume. The pressure drop

Table 2.1. Calibration factors for gases monitored as reactants and products over the course of all TAP experiments performed.

Gas	Peak AMU	c.f ($\frac{moles}{V.s}$)
He	4	2.41E-05
H ₂	2	9.58E-06
CH ₄	16	1.78E-06
H ₂ O	18	5.61E-05
C ₂ H ₄	28	1.20E-06
C ₂ H ₆	28	3.87E-06
C ₃ H ₆	41	1.20E-06
C ₃ H ₈	29	8.75E-07
C ₄ H ₆	39	4.06E-06
C ₄ H ₈	41	8.15E-07
C ₄ H ₁₀	42	6.40E-07
C ₆ H ₆	78	3.66E-07

ΔP of the fixed volume V held at a temperature T at the end of the experiments is noted and the number of moles pulsed in is calculated according to

$$n = \frac{\Delta P \times V}{R \times T}, \quad (2.9)$$

where R is the universal gas constant. Therefore, n moles of gas was measured at the mass spectrometer as the product of the average zeroth moment A (area under the pulse response) and the total number of pulses N . Finally, the calibration factor $c.f_{gas}$ is calculated as

$$c.f_{gas} = \frac{n}{N \times A}. \quad (2.10)$$

The calibration factors of all gases subjected to calibration experiments are given in Table 2.1.

Hydrocarbon Fragments and Defragmentation

A common set of difficulties encountered while working with mass spectrometry and hydrocarbons is the presence of mass fragments at lower m/z ratios or AMUs due to the ionization of higher hydrocarbons at the MS filaments. Table 2.2 succinctly describes the problem of interfering fragments, for example, at an m/z ratio of 28. The signal measured at this ratio will consist of contributions from propene, (C_3H_6), propane (C_3H_8), 1,3-butadiene (C_4H_6), 1(2)-butene (C_4H_8), butane, (C_4H_{10}) and benzene (C_6H_6).

Assuming that the total area measured at a particular m/z ratio is a linear combination of fragments, a system of linear equations can be set up to obtain a measure of areas/moles that correspond to a pure component and is given as

$$\overline{\overline{A}}.\overline{x} = \overline{b}, \text{ with} \quad (2.11)$$

$$\begin{bmatrix} 1.0000 & 0.7784 & 0.5850 & 0.3091 & 0.0000 & 0.0905 \\ 0.0223 & 1.0000 & 0.0100 & 0.1414 & 0.0000 & 0.0000 \\ 0.0010 & 0.2451 & 1.0000 & 0.5115 & 0.0000 & 0.0000 \\ 0.0003 & 0.1986 & 0.0039 & 1.0000 & 0.0000 & 0.0000 \\ 0.0039 & 0.0000 & 0.0092 & 0.0000 & 1.0000 & 0.0000 \\ 0.0073 & 0.0027 & 0.0085 & 0.0044 & 0.0067 & 1.0000 \end{bmatrix} \cdot \begin{bmatrix} C_2H_4 \\ C_3H_8 \\ C_4H_6 \\ C_4H_8 \\ CH_4 \\ H_2 \end{bmatrix} = \begin{bmatrix} a_{28} \\ a_{29} \\ a_{39} \\ a_{41} \\ a_{16} \\ a_2 \end{bmatrix} \cdot \quad (2.12)$$

Table 2.2. Fragmentation ratios for all hydrocarbons measured in TAP experiments performed in this dissertation.

Gas	2	4	16	28	29	39	41	78
H ₂	1	0	0	0.0905	0	0	0	0
He	0.0021	1	0	0.02	0	0	0	0
CH ₄	0.0067	0	1	0	0	0	0	0
C ₂ H ₄	0.005	0.0003	0	1	0.0223	0	0	0
C ₃ H ₈	0.0027	0.0001	0	0.7784	1	0.2451	0.1986	0
C ₄ H ₆	0.0085	0	0.0092	0.585	0.01	1	0.0039	0
C ₄ H ₈	0.0044	0	0	0.3091	0.1414	0.5115	1	0
C ₆ H ₆	0.0023	0	0.0014	0.0263	0.0006	0.2115	0.0008	1

In many experiments, the signal-to-noise ratios for certain product m/z ratios are quite low due to a small amount of product exiting the microreactor. The sinusoidal noise of MS signals and subtle changes induced due to smoothing often results in solutions to Equation 2.11 and Equation 2.12 that quantify a negative measures of area. Due to the unphysical nature of negative areas/moles, the system of linear equations for each pulse was solved as a constrained optimization problem. The solutions were constrained to be zero or greater and the system was set up as a non-linear least squares minimization problem. The linear equations problem is re-written as

$$y = \bar{\bar{A}}.\bar{x} - \bar{b}, \quad (2.13)$$

and the optimization problem is set up and given as

$$\min |y^2 = (\bar{\bar{A}}.\bar{x} - \bar{b})^2| \quad S.T \quad y_0 \in [0, \infty]. \quad (2.14)$$

3. Quantification and Statistical Analysis of Errors Related to the Approximate Description of Active Site Models in Metal-exchanged Zeolites

This chapter was reproduced from ChemCatChem, Volume 11, 2019, *Quantification and Statistical Analysis of Errors Related to the Approximate Description of Active Site Models in Metal-exchanged Zeolites*, Pages 5055-5067.

3.1. Introduction

Zeolites consist of microporous aluminosilicate networks and have been successfully used in industrial applications such as ion exchangers, molecular sieves and catalysts. Brønsted acid zeolites have been extensively studied and are used commercially in fluid catalytic cracking (FCC), aromatic isomerization and alkylation and in the methanol to olefins (MTO) process.^{46–49} More recently, metal-exchanged zeolites with Lewis acid functionality have extended the application range of zeolites to the selective catalytic reduction (SCR) in automotive emission control^{14,50} and have potential for other emerging applications in hydrocarbon upgrade. For instance, the conversion of methane to methanol can occur

over Cu-exchanged SSZ-13, where extra-framework Cu Lewis acid sites catalyze the difficult C–H bond activation step.⁵¹ Similarly, reports of catalytic testing of Ag–Y, Ag–A and Ag–ZSM-5 show activity for non-oxidative coupling (NOC) of methane with ethylene with a methane conversion of 2-13% in the temperature range of 623-673 K, and with a product selectivity of over 20% to propylene.^{52,53} Mo-exchanged zeolites have also been reported to be active for NOC of methane with $\sim 10\%$ methane conversion at 673 K. These materials are also known to catalyze the dehydroaromatization (DHA) of methane to selectively form benzene at low methane conversions of 7-8%.²⁴ Hsieh and coworkers have shown that exchanging 8% of the Brønsted acid sites of H-ZSM-5 increases the selectivity to aromatics from 15% to $\sim 60\%$ during DHA of ethylene.²⁹ Cu-, Zn-, Ga- and Fe-exchanged zeolites are known to catalyze reactions such as the partial oxidation of methane to methanol,^{54,55} dehydrogenation of light alkanes,^{56–58} and decomposition of N₂O to N₂ and O₂,^{59–61} respectively. Overall, these selected examples demonstrate that metal-exchanged zeolites offer the potential to convert readily available methane to value-added products.

The problem of activating and functionalizing methane and other small alkanes has occupied the minds of researchers in academia and industry alike. This interest is motivated by methane's feedstock potential and gained traction with the ongoing discovery of large shale gas and natural gas reservoirs in the United States and many other parts of the world.⁶² The activation of methane presents itself as a difficult problem to solve due to its intrinsic properties. Large enthalpies of both homo- and heterolytic cleavage of the C – H bond, low electron affinity, large ionization energy and limited polarizability of methane render this molecule unsuitable for typical redox or acid-base chemistry.⁶³ Consequently, the use of methane has remained limited to electricity generation (combustion) and conversion to syngas, a mixture of CO and H₂ using steam reforming.⁶⁴ To realize

the full potential of this underutilized feedstock, there is a need to develop economically viable catalytic processes for methane upgrade to higher value chemicals. Oxidative upgrade to products such as methanol or oxidative coupling to ethane are attractive because the processes are thermodynamically favorable. However, they suffer from low selectivity, with the complete oxidation of methane to CO_2 as the favored product. Conversely, non-oxidative coupling of methane, while highly selective, has a large energy requirement.⁶⁵ Exploratory investigations into the applicability of metal-exchanged zeolites for methane upgrade are encouraging, but rely generally on time-consuming Edisonian trial-and-error approaches. Modern design strategies for supported metal catalysts commonly employ computational screening to accelerate materials discovery, but such strategies have not yet been established for metal-exchanged zeolites.

Atomic-level information on active site structures and reaction mechanisms is crucial in the design and optimization of the catalyst. Theoretical chemistry under the guise of density functional theory (DFT) or other levels of theory can be used to obtain much of this information.^{66,67} Historically, zeolites have been modeled with DFT as smaller cluster models, which serve to approximate the zeolite framework in a minimalistic manner, while describing the Lewis acid site with the requisite complexity. These smaller clusters, while being computationally inexpensive, ineffectively describe the long range crystal potential and confinement effects of periodic zeolitic systems.⁶⁸ The advent of more powerful computers supports attempts to close the gap between computational models and the real material, and the use of periodic cells to obtain electronic and structural information pertaining to a model with a complete physical description has evolved as state-of-the-art.^{25,69–74}

To advance the predictive capabilities for the design of metal-exchanged zeolites, there is a growing need to develop an improved understanding of structure-

performance relationships of Brønsted and Lewis acid sites in zeolites.⁷⁵ Application of DFT is especially appealing when it can be used to guide the selection of a potential metal-exchanged zeolite through a computational screening protocol,⁷⁶ which can provide an estimate of desired properties of the zeolite. The incorporation of van der Waals (vdW) interactions^{73,77,78} within the pores of a zeolite further improve the physical description of zeolite models.

In this work, we develop a screening study that transcends the variations in physical description of zeolite cluster models and periodic cells in Lewis acid zeolites. To this end, we investigate the activation of a probe hydrocarbon, methane (CH_4), assumed to be the rate determining step in NOC and DHA of methane to higher hydrocarbons,²⁴ on different metal-exchanged zeolite models ranging from a small 5T cluster, a larger $2 \times 5\text{T}$ cluster, ZSM-22 and ZSM-5 periodic unit cells. The selected metal-exchange candidates are commonly encountered in literature, i.e. Ag, Cu, Zn, Fe, Pd and Mo. Li and Na were included as additional monovalent cations. Sampling different active site configurations and relevant activation pathways for CH_4 in various zeolite models provides for an initial understanding of the critical active site features leading to catalytic activity. We propose a hierarchy of factors that determine the catalytic activity of metal-exchanged zeolite models on the basis of uncertainty quantification and statistical analyses. We find that the identity of the extra-framework metal primarily determines the thermodynamics and intrinsic kinetics of CH_4 activation, whereas the framework type is of secondary importance. This observation was validated by comparing the independent error distribution for metal-exchanged CHA with the parent distribution consisting of data from 5T, $2 \times 5\text{T}$, ZSM-22, and ZSM-5 models. Our bottom-up approach of combining CH_4 activation error distributions to provide statistically meaningful measures of Lewis acid reactivity is a computationally inexpensive method of screening various metal-exchange candidates for specific

probe reactions. These results enable a better understanding of the structure-activity relationships that characterize the catalytic behavior of metal-exchanged zeolites and aid the development of more efficient screening methodologies that contribute to the rational design of metal-exchanged zeolites.

3.2. Computational Methods

Density functional theory (DFT) calculations were performed using the Vienna Ab-initio Simulation Package (VASP)^{79–82} and interfaced through the Atomic Simulation Environment (ASE).⁸³ The projector augmented wave (PAW) method⁸⁴ and the Bayesian error estimation functional (BEEF–vdW)⁴⁰ were used to solve the Kohn-Sham equations. This functional has been shown to quantitatively describe van der Waals interactions as well as reaction kinetics in zeolite pores.⁷⁸ All calculations were performed with a plane wave cutoff energy of 540 eV, a Gaussian smearing of $k_B T = 0.1$ eV and the Brillouin-zone was sampled at the Γ -point. The gas phase reference energy of CH_4 was computed with the same parameters, except with a smaller smearing width of $k_B T = 0.01$ eV and dipole corrections enabled in all directions. Model geometries including transition states were optimized until the residual force on each atom converged to 0.05 eV/Å or less. Transition state structures and energies were obtained by using the climbing image nudged elastic band method (CI-NEB)⁸⁵ and subsequently refined using the Dimer method to the same level of geometric convergence.⁸⁶ The energy of reaction ΔE_{rxn} and activation energy barrier E_a for the dissociation of CH_4 on a zeolite model are calculated using

$$\Delta E_{rxn} = E_{Z,FS} - E_{IS} \text{ and} \quad (3.1)$$

$$E_a = E_{Z,TS} - E_{IS}. \quad (3.2)$$

The BEEF-vdW energy ensemble quantifies a range of energies that can be expected from a typical DFT calculation. This is done by using a generalized gradient approximation (GGA) functional that has been slightly perturbed from its original formulation. Simultaneously, it is also pinned down in its description of the physics that underlies a model by being fit to a number of training data sets. It utilizes a set of trained perturbation coefficients to vary contributions from various exchange functional formulations to calculate an error ensemble. The mean of this ensemble quantifies the energy of the system. This error ensemble is an array of 2000 energies, and provides a systematic procedure to calculate the uncertainty and error associated with the use of GGA functionals in DFT calculations.^{40,87} These errors can then be used to assign a statistical measure of confidence in how accurately a DFT predicted energy describes the actual energy of a system. The error ensemble for ΔE_{rxn} and E_a corresponding to each pathway was calculated using

$$\Delta[E]_{rxn} = [E]_{Z,FS} - [E]_{IS} \text{ and} \quad (3.3)$$

$$[E]_a = [E]_{Z,TS} - [E]_{IS}. \quad (3.4)$$

The error ensembles can be combined based on the method described by Deshpande and coworkers.⁸⁷ An illustration depicting the combination of error ensembles $[E]_{x,i}$ where $x \in \{\Delta E_{rxn}, E_a\}$ and $i \in \{5T, 2 \times 5T, ZSM-22, ZSM-5\}$ is given in Figure 3.1. The resulting histogram in Figure 3.1 c was then re-centered at $\langle\langle[E]_i\rangle\rangle$ to yield a resampled histogram in Figure 3.1 d). Its (μ, σ) quantifies the mean and average standard error of the distribution. Additionally, the histogram was normalized such that the area bound by it is unity, and subsequently, a probability density function (PDF) was fit to the data. Comparisons of random variables defined by these functions or distributions enable further analysis

of these error distributions with techniques from a statistician's toolbox such as descriptive statistics.

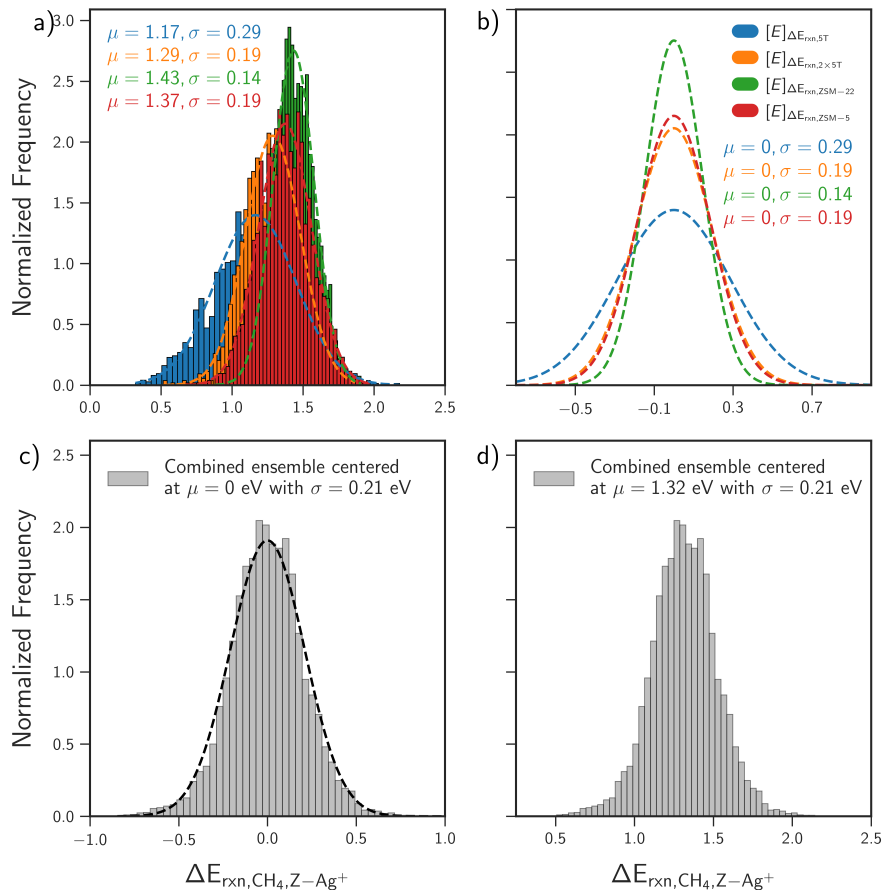


Figure 3.1. Illustration of the combination of ensembles of different models, i.e. 5T (red), $2 \times 5\text{T}$ (blue), ZSM-22 (green) and ZSM-5 (magenta).

Finally, the error ensembles relating to the activation of CH_4 on various active site motifs of a metal were combined, normalized and fit to probability density functions (PDFs) $f_{M1}(x)$, $f_{M2}(x)$, $f_{M3}(x)$, ... where M1, M2 are Ag, Cu etc. These non-normal PDFs are converted into independent continuous random

variables X_{M1}, X_{M2}, \dots such that

$$P(X_{M1}) = \int_{x_{min}}^x f_{M1}(x)dx; \quad \int_{x_{min}}^{x_{max}} f_{M1}(x)dx = 1; \quad X_{M1} \in [x_{min}, x_{max}] \text{ and} \quad (3.5)$$

$$P(X_{M2}) = \int_{x_{min}}^x f_{M2}(x)dx; \quad \int_{x_{min}}^{x_{max}} f_{M2}(x)dx = 1; \quad X_{M2} \in [x_{min}, x_{max}]. \quad (3.6)$$

Under the assumption that CH_4 activation is a rate determining step, a favorable metal exchange candidate will have a lower activation barrier. Therefore, the probability that candidate M1 is the favored Lewis acid over M2 can be calculated as $P[X_{M1} < X_{M2}]$ as defined by

$$P[X_{M1} < X_{M2}] = \int_{y=x_{min}}^{y=x_{max}} \int_{x=x_{min}}^x f_{M1}(x)f_{M2}(y) dx dy. \quad (3.7)$$

Elucidation and application of all statistical techniques that have been implemented in this analysis are provided in the Appendix.

3.3. Results and Discussion

3.3.1. Lewis Acid Sites

The simplest zeolite model used in this study was the 5T-cluster, where T is either a Si or Al atom forming a TO_4 tetrahedral site. It was constructed as a minimum representation of a T-12 site in a periodic ZSM-5 unit-cell and is depicted in Figure 3.2 and Figure 3.3 a. An anionic site was created by replacing the central Si with an Al atom and adding cationic charge balancing species. The terminal Si atoms in this model were saturated with H atoms, and the resulting SiH_3 groups were fixed to mimic the rigidity of the extended MFI zeolite framework. These cluster models were then centered in a box of dimensions $16 \text{ \AA} \times 16 \text{ \AA} \times 16 \text{ \AA}$ to minimize interactions between periodically repeated images. Dipole corrections along all lattice vectors were included in the calculations to account for any spurious dipole moments that may arise in these isolated cluster models. Additionally, to investigate the effect of cluster termination, the terminal Si atoms were saturated with OH groups instead of H atoms (Figure 3.3 b). The same constraints and model parameters as those previously specified were applied for the 5T-OH clusters.

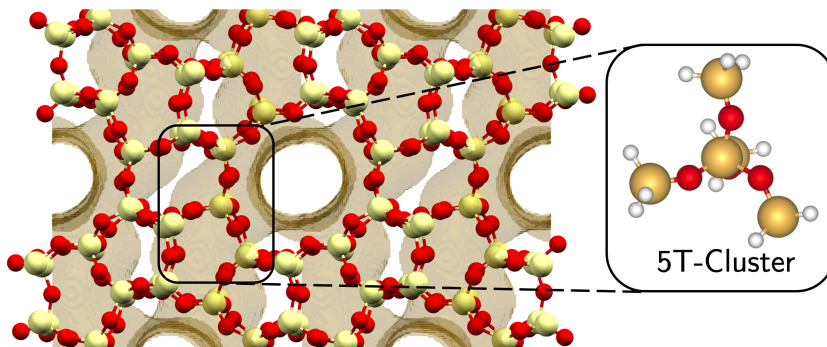


Figure 3.2. The ZSM-5 periodic cell with the straight [010] and sinusoidal [100] channels (shaded in brown). The T-12 site at the intersection of the two channels is enlarged and forms the basis of the 5T-cluster used in this work.

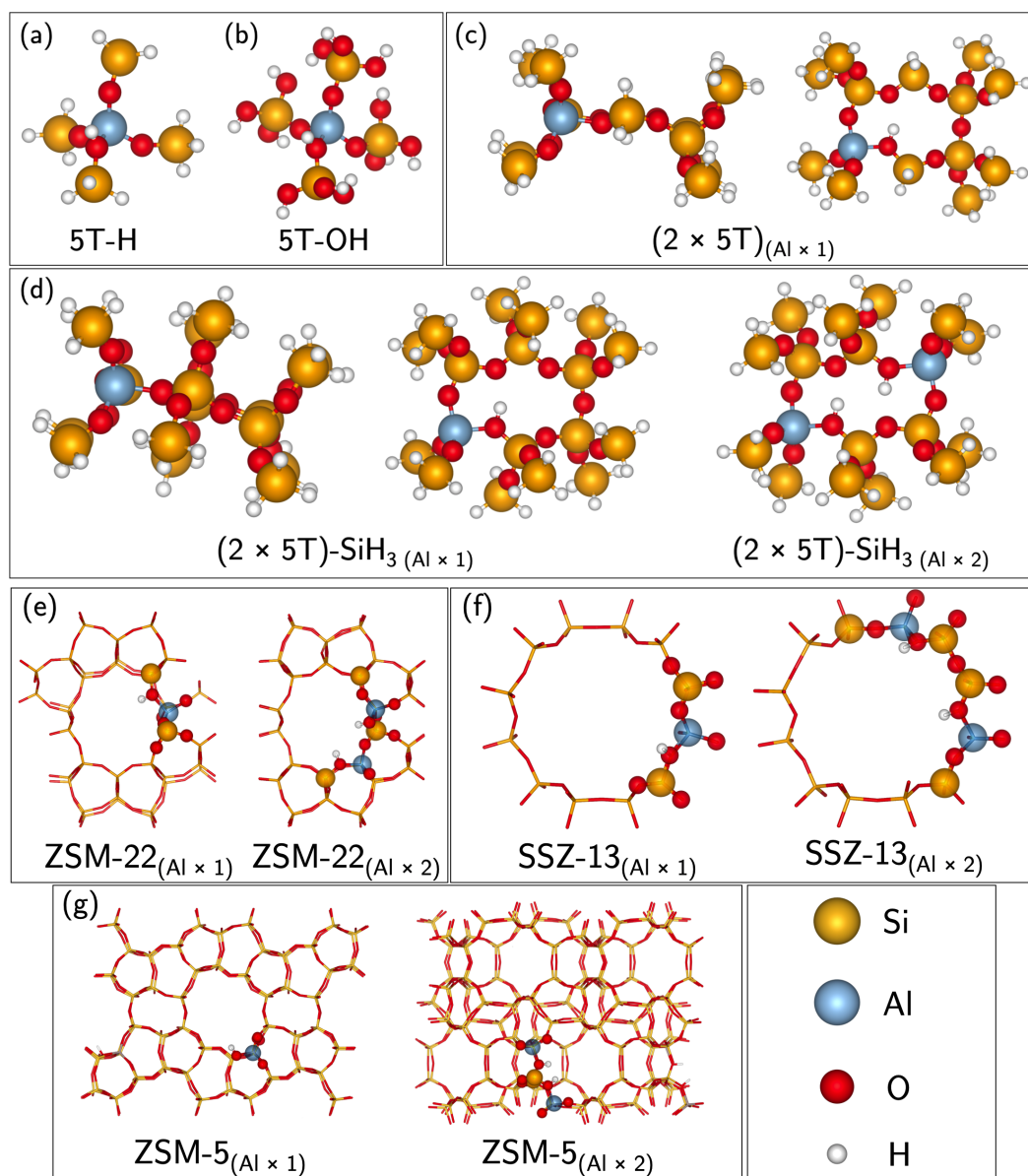


Figure 3.3. Geometries of acid sites in zeolite models of different complexity considered in this study.

The 5T cluster models have a single anionic site and thus, cannot be used to model more complex active sites that may form between paired anionic sites. Therefore, a larger $(2 \times 5T)$ model, consisting of two 5T-clusters forming a 6-membered ring (MR), a ubiquitously encountered feature in various zeolite morphologies, was constructed. This $(2 \times 5T)$ cluster model is shown in Figure 3.3 c and is sufficiently large to accommodate commonly postulated active sites for

multivalent cations that require the presence of two Al anionic sites in close proximity. Analogous to the 5T-H cluster models, the terminal SiH_3 species were constrained and the interconnecting SiH_2 species were allowed to relax, minimizing destabilization of adsorbates due to strain and other steric factors. Replacement of one or two Si atoms leads to the formation of $(\text{Al} \times 1)$ and $(\text{Al} \times 2)$ models, respectively, which were centered in a box of dimensions $20 \text{ \AA} \times 20 \text{ \AA} \times 20 \text{ \AA}$. These $(2 \times 5\text{T})$ clusters were expanded by replacing the H atoms of the interconnecting SiH_2 species with OSiH_3 groups, as shown in Figure 3.3 d.

The next model chosen for our study was the ZSM-22 periodic unit cell. ZSM-22 (TON framework) is a small pore zeolite that consists of 24 TO_4 tetrahedra per unit cell. It has four unique T-sites with non-interconnecting channels which are linear, unidirectional and one-dimensional with 10 MR openings.⁸⁸ This model choice represents a logical progression in model complexity and size from the $(2 \times 5\text{T})$ clusters, while incorporating zeolitic features such as channels, periodicity and long range order into the model. The ZSM-22 unit cell was obtained from the International Zeolite Association (IZA) database and was optimized for use with the BEEF-vdW functional and other chosen calculation parameters by optimizing the cell volume, keeping the shape of the orthorhombic unit cell fixed. This resulted in optimized cell lattice constants of $a = 14.19 \text{ \AA}$, $b = 17.94 \text{ \AA}$ and $c = 5.29 \text{ \AA}$, in good agreement with experimental lattice parameters.⁸⁹ The unit cell was repeated twice in the c -direction to ensure that adsorbates are sufficiently separated under periodic boundary conditions. The Si atom at the T-1 site was replaced with an Al to create an anionic site, which was then charge balanced by extraframework cationic species, thus forming isolated acid site models [ZSM-22-(Al \times 1)]. Paired anionic site models [ZSM-22-(Al \times 2)] were constructed by substituting a second nearest neighbor T-2 Si atom. This anionic site pair was used in all calculations pertaining to this model. The geometries of the isolated

acid site and paired acid site models are depicted in Figure 3.3 e.

The activation of methane was also investigated on Lewis acids bound to anionic sites in the SSZ-13 periodic unit cell. SSZ-13 (CHA framework) is a small pore zeolite⁹⁰ with 3-dimensional interconnected pores. A single symmetry-distinct T-site among 4, 6, and 8 MR rings that form cages of ~ 8 Å in diameter.⁵⁰ The SSZ-13 lattice constants were optimized in a hexagonal unit cell using the same procedure as described for ZSM-22 and were found to be $a = b = 13.68$ Å and $c = 14.9$ Å. These values are in good agreement with those obtained in experimental and other theoretical investigations.⁷⁴ For all subsequent calculations we chose a rhombohedral unit cell containing 12 TO_4 tetrahedra,⁹¹ and the location of Al substituted framework T sites for (Al \times 1) and (Al \times 2) models were adopted from the detailed investigation into the nature of active sites in Cu-SSZ-13 under SCR conditions by Paolucci and coworkers.⁵⁰ The two SSZ-13 models are visualized in Figure 3.3 f.

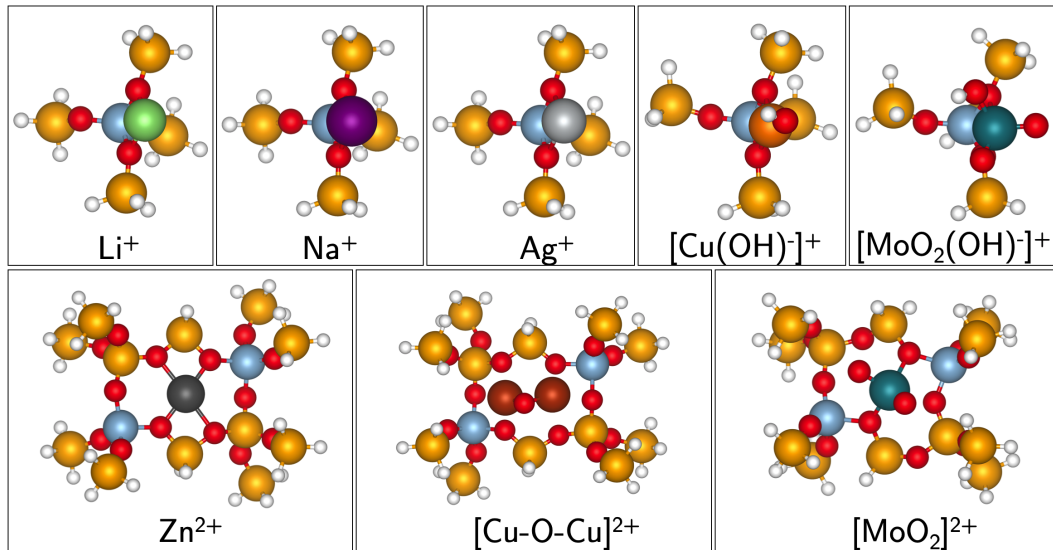


Figure 3.4. Representative geometries of active Lewis acid site models used in this study.

The largest and most complex model used was the ZSM-5 periodic unit cell with 288 TO_4 primary building units. ZSM-5 (MFI framework) is a three-

dimensional medium pore zeolite with intersecting channels defined by 10 MR rings. The unit cell geometry was optimized for use with the BEEF-vdW functional using the same procedure as described for ZSM-22 and SSZ-13 unit cells resulting in optimized unit cell dimensions of $a = 20.26$, $b = 19.91$ and $c = 13.26$, closely agreeing with experimentally determined lattice parameters.⁹² The activation and subsequent dissociation of methane was modeled to occur at the T-12 site and Figure 3.2 visualizes this site as a 5T cluster model at the intersection of the straight and sinusoidal. Al was introduced into the framework at this site, thus forming ZSM-5-(Al \times 1) models. The location of the second anionic site was chosen to be the T-4 site in the sinusoidal channel such that the separation of the framework atoms was similar to that in the cluster models. The geometries of active species at this site exhibit similar binding characteristics as those obtained for other zeolite models. The acid pair (Al \times 2) is also in proximity to the channel intersection, as seen in Figure 3.3 g, and provides unconstrained access to the active species.

Methane activation was studied over metal-exchanged zeolite models that span a spectrum of complexity and model accuracy. The acid sites in each model are charge compensated by cationic species, which are also the preferred sites for CH₄ activation. The metal centers for active sites in (Al \times 1) models were chosen such that they possess a residual charge of +1, sufficient to balance the negative charge on the framework Al atom. On (Al \times 2) models, the second anionic site could play the role of a spectator as a Brønsted acid, or take part in active site formation, thus requiring species with a residual charge of +1 or +2. Of the metal-exchange candidates reported in literature, we chose Ag, Cu, Zn, Fe, Pd and Mo based species. Methane activation was also modeled on Brønsted acid and on analogous monovalent Li- and Na-exchanged zeolite models. Visual representations of all Lewis acid geometries are provided in Figure 3.4.

3.3.2. Preferred Activation Pathways

The dissociative adsorption of CH_4 was first modeled at Lewis acid sites in various zeolite models with a single Al anionic site ($\text{Al} \times 1$). Despite the simplicity of CH_4 as reactant, mechanistic details of its activation vary with active site identities and depend on the number of anionic sites and the oxidation state of the metal cation. A non-exhaustive summary of possible mechanisms is presented in Table 3.1 and Table 3.2.

Extra-framework cations with oxidation state +1 can compensate the charge imbalance at a single Al anionic site. This category includes H^+ and the monovalent Lewis acids (Li^+ , Na^+ , Ag^+). The active site for Ag-ZSM-5 for hydrocarbon upgrade has been characterized to be in the form of Ag^+ cations^{26,93} or Ag_n clusters.^{94,95} While the presence of Ag clusters cannot be ruled out without further investigation, we chose Ag^+ as the active site. Li^+ and Na^+ cations are also assumed to be analogous monovalent active sites.

Among the divalent metal cations (Cu^{2+} , Zn^{2+} , Fe^{2+} and Pd^{2+}), the identity of Cu species has been subject to the most significant body of work. Bell and coworkers proposed $[\text{CuOH}]^+$ and Cu^{2+} models,⁹⁶ while O_2 bridged Cu-pairs and $[\text{Cu-O-Cu}]^{2+}$ were reported by Schoonheydt and Sels.^{54,55,97} These geometries were confirmed in a computational investigation by Vilella and Studt⁹⁸ and in the work of Yoshizawa et al.⁹⁹ Zeolite models with extra-framework Zn have been extensively studied by van Santen and coworkers,^{58,100,101} and the active sites reported are structurally identical to those reported for Cu-exchanged zeolites. Similar active sites have been reported for Fe-exchanged zeolites by van Santen^{102,103} and Bell.^{60,61,104} Based on these results, $[\text{MOH}]^+$ for ($\text{Al} \times 1$) models and $[\text{MOH}]^+$, M^{2+} and $[\text{M-O-M}]^{2+}$ for ($\text{Al} \times 2$) models were chosen as active sites, with $\text{M} \in \{\text{Cu}, \text{Zn}, \text{Fe} \text{ \& } \text{Pd}\}$.

Table 3.1. Metal-exchange candidates, active sites and pathways for CH₄ activation on (Al × 1) models.












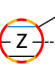




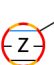







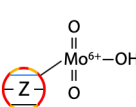
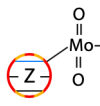
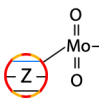
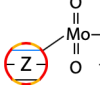









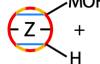
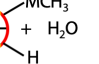

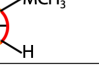


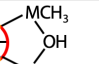



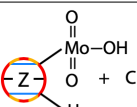
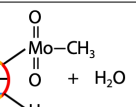

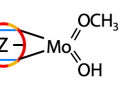
Extraframework Species	CH ₄ Activation Pathways
 H 	P1  + CH ₄ →  + H ₂
 Li  Na  Ag 	P1  + CH ₄ →  MH P2  + CH ₄ →  MCH ₃
 Cu  Zn  Fe  Pd 	P1  + CH ₄ →  + H ₂ P2  + CH ₄ →  + H ₂ O P3  + CH ₄ →  + CH ₃ OH
 Mo 	P1  + CH ₄ →  + H ₂ P2  + CH ₄ →  + H ₂ O

Table 3.2. Metal-exchange candidates, active sites and pathways for CH₄ activation on (Al × 2) models.

Extraframework Species	CH ₄ Activation Pathways
 Cu  Zn  Fe  Pd    	 + CH ₄ →  + H ₂ O  + CH ₄ → 
	 + CH ₄ → 
  	 + CH ₄ →  + H ₂ O  + CH ₄ → 

Mo-exchanged active sites with Mo⁶⁺ centers were also included, because

of their known activity towards the dehydroaromatization of CH₄ to benzene.^{105,106} Although the as-synthesized form of Mo-exchanged zeolites consist of MoO_x species, they are reduced to MoC_y after an induction period and the active form towards the dissociation of CH₄ was reported to be MoC_y species by Iglesia and coworkers.¹⁰⁷ In contrast, the work of Wachs and Podkolzin^{24,25} confirms that [MoO₂OH]⁺ and [MoO₂]²⁺ are the active sites in the presence of one anionic Al site (Al × 1) and higher anionic site concentrations (Al × 2), respectively. To avoid the complexity of phase transition and possible formation of mixed oxy-carbide species, we limit our investigation to the pure oxide motifs proposed as active sites by Wachs and Podkolzin.

Among the monovalent species, protons are most commonly encountered in zeolites. Brønsted acid zeolites have been subject to many experimental and computational studies for various reactions such as methanol to hydrocarbons (MTH)^{108–113} and methanol to dimethyl ether (DME),^{114,115} and serve as reference for C-H bond activation on other zeolitic active sites. As seen in Table 3.1, the predominant dissociation pathway for CH₄ on a Brønsted acid site forms a framework-bound methoxy species and H₂ gas. The calculated barrier for this reaction is excessively large at 4.18 eV on the 5T cluster model and 4.01 eV on the ZSM-5 periodic unit cell. In agreement with the work of Hsieh and coworkers, we can conclude that Brønsted acid sites are inactive for CH₄ activation.²⁹ In contrast, Lewis acid sites have known CH₄ activation ability, but the preferred activation pathway may vary with the metal, its oxidation state and local environment.

Silver, with a commonly found oxidation state of +1, can balance the acid site of a zeolite as an Ag⁺ cation and has known activity for C–H bond activation. Over Ag⁺ in a 5T cluster model, P2 or the *alkyl pathway* is preferred, forming a Brønsted acid site and a loosely bound AgCH₃ upon CH₄ dissociation. The activation barrier (E_a) and the reaction energy (ΔE_{rxn}) for this pathway were found

to be 1.69 and 1.18 eV, respectively. Concurrently, Ag^+ in ZSM-5 also prefers to activate CH_4 through P2, with an E_a of 1.62 eV and ΔE_{rxn} of 1.38 eV, respectively. This preference agrees with the simulations performed by Ding and coworkers;¹¹⁶ however, NMR studies on Ag-ZSM-5 and other theoretical investigations on cluster models suggest that P1, or the *carbenium* pathway, is preferred.^{93,117,118} The activation of CH_4 through P1 showed an E_a of 3.56 and 3.72 eV for the 5T cluster model and ZSM-5, respectively.

Table 3.3. Activation energies and energies of reaction (in parentheses) for CH_4 activation pathways on various active sites in the 5T cluster models and ZSM-5 periodic unit cells.

Pathway	Model	Monovalent			Divalent			Hexavalent
		Li^+	Na^+	Ag^+	Cu^{2+}	Zn^{2+}	Fe^{2+}	Mo^{6+}
P1	5T	4.90	4.95	3.56	3.22	4.77	4.93	4.48
		(-3.80)	(-3.90)	(-1.87)	(-1.08)	(-1.38)	(-1.16)	(-1.04)
	ZSM-5	6.35	6.46	3.72	3.46	4.63	4.31	3.62
		(-3.80)	(-4.02)	(-1.93)	(-0.84)	(-1.23)	(-2.47)	(-0.79)
P2	5T	-	-	1.69	1.35	1.60	1.68	2.62
		(-3.37)	(-3.36)	(-1.18)	(-0.44)	(-0.2)	(-0.97)	(-1.09)
	ZSM-5	-	-	1.62	1.03	1.51	1.59	2.07
		(-3.33)	(-3.55)	(-1.38)	(-0.07)	(-0.12)	(-0.67)	(-1.17)
P3	5T				2.98	3.75	2.90	
					(-1.55)	(-1.23)	(-2.23)	
	ZSM-5				2.78	3.30	2.56	
					(-0.52)	(-0.22)	(-1.07)	

Given the unfavorable energetics of P1, P2 was chosen as the preferred pathway for CH_4 activation on Ag-zeolites for all subsequent calculations. For the other monovalent cations Li^+ and Na^+ , our calculations on 5T clusters and ZSM-5 periodic cells show that both Li^+ and Na^+ catalyzed CH_4 dissociations occur with ΔE_{rxn} of 3.37 and 3.36 eV on the 5T cluster models and 3.33 and 3.55 eV on the ZSM-5 periodic cells, respectively. Transition state searches yielded no

saddle-points for this mechanism. The alternative pathway P1 is slightly more endothermic but well-defined transition states could be located resulting in E_a of 4.90 and 4.95 eV for Li^+ and Na^+ on the 5T cluster models and 6.35 and 6.46 eV on the ZSM-5 periodic cells, respectively. The high activation energy barrier is indicative of the poisoning effect of these alkali metal cations in their lack of activity towards CH_4 activation.¹¹⁹ Therefore, Li- and Na- exchanged zeolite models are omitted from detailed discussions.

Table 3.3 summarizes the results for possible activation pathways for CH_4 activation over the Lewis acids on the 5T cluster models and ZSM-5 periodic unit cells. The results for Ag^+ and $[\text{CuOH}]^+$ on the 5T cluster models are visualized as a potential energy diagram in Figure 3.5 a and b. We note that the energetic differences between the preferred and unfavorable pathways are large, such that the model complexity, i.e. 5T cluster versus periodic ZSM-5, has no impact on the determination of the dominant mechanism. All initial, transition, and final states for these dissociation pathways are depicted in Table A.1.

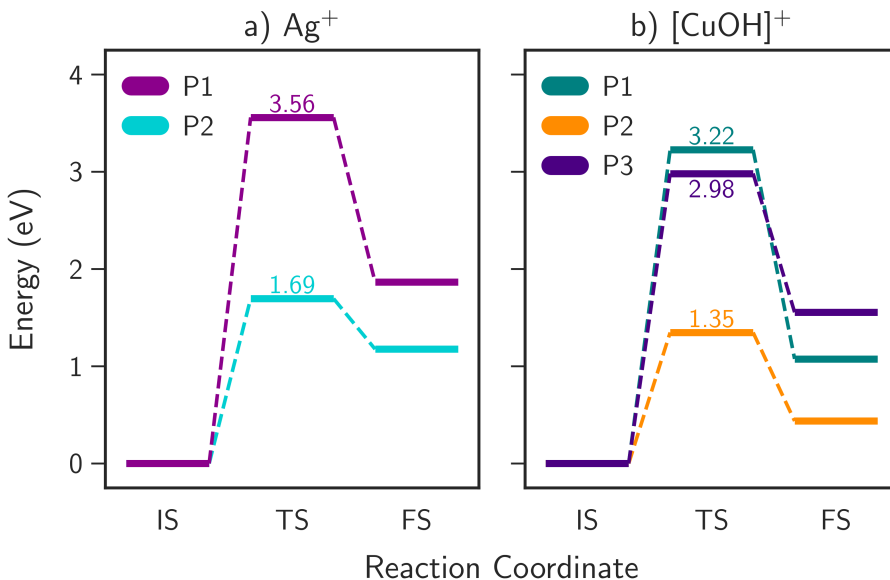


Figure 3.5. Calculated potential energy diagrams for CH_4 activation pathways on 5T cluster models for (a) Ag^+ and (b) $[\text{CuOH}]^+$ Lewis acid sites. Competing pathways are distinguished by color.

The Lewis acid sites for divalent M^{2+} metals (Cu, Zn, Fe) were modeled as $[MOH]^+$ with a residual charge of +1. This active site motif is consistent with the characterization of Cu species at isolated acid sites in SSZ-13.¹⁴ Three pathways of activation forming H_2 (P1), H_2O (P2) and CH_3OH (P3) were considered as potential mechanisms for CH_4 activation and are shown in Table 3.1 and Table A.1. Our results show a consistent preference for P2 on $[CuOH]^+$, $[ZnOH]^+$ and $[FeOH]^+$ on the 5T cluster model and the ZSM-5 periodic cells, with the Lewis acid site forming an $M-CH_3$ species and eliminating a residual H_2O molecule. The barriers for the activation for $[CuOH]^+$, $[ZnOH]^+$, and $[FeOH]^+$ were found to be 1.35, 1.60 and 1.68 eV on the 5T cluster models and 1.03, 1.51 and 1.59 eV on ZSM-5, respectively. These modest barriers are substantially lower than those of the other pathways considered and therefore, P2 is considered to be the preferred pathway for CH_4 activation on $[MOH]^+$ Lewis acid sites for all other zeolite models.

Hexavalent Mo-based Lewis acid species were modeled as $[MoO_2OH]^+$ to compensate the negative framework charge. Two pathways for the dissociation of CH_4 are summarized in Table 3.1: pathway P1 forming MoO_2OCH_3 and H_2 , and pathway P2 forming MoO_2CH_3 and H_2O . Activation barriers for both pathways indicate that P2 is preferred, with an activation barrier of ~ 1.8 eV lower than that for P1 for the 5T cluster model. This preference is also maintained for ZSM-5.

3.3.3. Trends in CH_4 Activation

The preferred CH_4 activation pathways on isolated acid sites summarized in Table 3.1 and Table 3.3 have in common that they form $M-CH_3$ and $O-H$ bonds, or eliminate H_2O , if applicable. The large barriers exhibited by pathways involving the formation of H_2 or CH_3OH suggest that these mechanisms are unlikely to occur. This observation applies to simple 5T cluster models and complex ZSM-5 periodic unit cells, such that only the preferred pathway for each Lewis acid site

was modeled for the active site representation of intermediate complexity, i.e. $(2 \times 5T)-(Al \times 1)$ and ZSM-22- $(Al \times 1)$. A summary of the energies of reaction (ΔE_{rxn}) and activation (E_a) for the preferred pathway on each Lewis acid site on $(Al \times 1)$ zeolite models is shown in Figure 3.6 and tabulated in Table A.2. A cursory analysis of these data suggests that the smaller zeolite models, i.e., 5T and $2 \times 5T$, are effectively able to capture trends in CH_4 activation energetics over Lewis acid sites at isolated active sites $(Al \times 1)$ in larger and more complex periodic cells, such as ZSM-22 and ZSM-5. Ag substituted models appear to show similar energies across all models, with ΔE_{rxn} and E_a varying within ~ 0.1 eV. The $[MOH]^+$ class of Lewis acids follows a general trend of decreasing ΔE_{rxn} and E_a with increasing model complexity, presumably caused by stronger stabilization of reaction intermediates and products by van der Waals (vdW) interactions.

Expanding our investigation to include active sites with higher Al anionic site concentrations $(Al \times 2)$ also reveals that a general trend in Lewis acid site reactivity is retained, irrespective of model choice or complexity. The energies of reaction and activation barriers for all Lewis acid motifs modeled on $(Al \times 2)$ models are given in Table A.3 and the overall trends are visualized in Figure 3.6 b. We chose CH_4 dissociation pathways consistent with the preferred formation of M- CH_3 and O-H bonds, and/or H_2O elimination. The corresponding initial, transition, and final states for all mechanisms on $(Al \times 2)$ models are recorded in Table A.4. The active site motifs considered for divalent metals, i.e. M^{2+} , $[M-O-M]^{2+}$ and $[MOH]^+$ and hexavalent $[MoO_2]^{2+}$ and $[MoO_2OH]^+$, generally appear to activate CH_4 more favorably with increasing model complexity. The M^{2+} Lewis acids behave as outliers on the $(2 \times 5T)-(Al \times 2)$ cluster, with energies E_a of 1.61, 1.48 and 1.73 eV for Cu^{2+} , Zn^{2+} and Fe^{2+} , compared to 0.84, 0.72 and 1.15 eV obtained on ZSM-5- $(Al \times 2)$. We can partially attribute the model discrepancies to steric effects originating from artificial constraints imposed on the

$2 \times 5T$ cluster model. Manifestation of these steric effects occur as dipole artifacts in zeolite models. The periodic cells of ZSM-22 and ZSM-5 are able to delocalize the dipole moment at the anionic site more effectively than the $(2 \times 5T)$ cluster model. The increased stabilization of reaction intermediates (Table 3.2) results in significantly reduced energies of reaction and activation barriers. A detailed discussion on these model discrepancies and their effects on zeolite reactivity is given in section A. Given these model artifacts, the $M^{2+}-(2 \times 5T)$ Lewis acids have been excluded from the general trend lines in Figure 3.6 b.

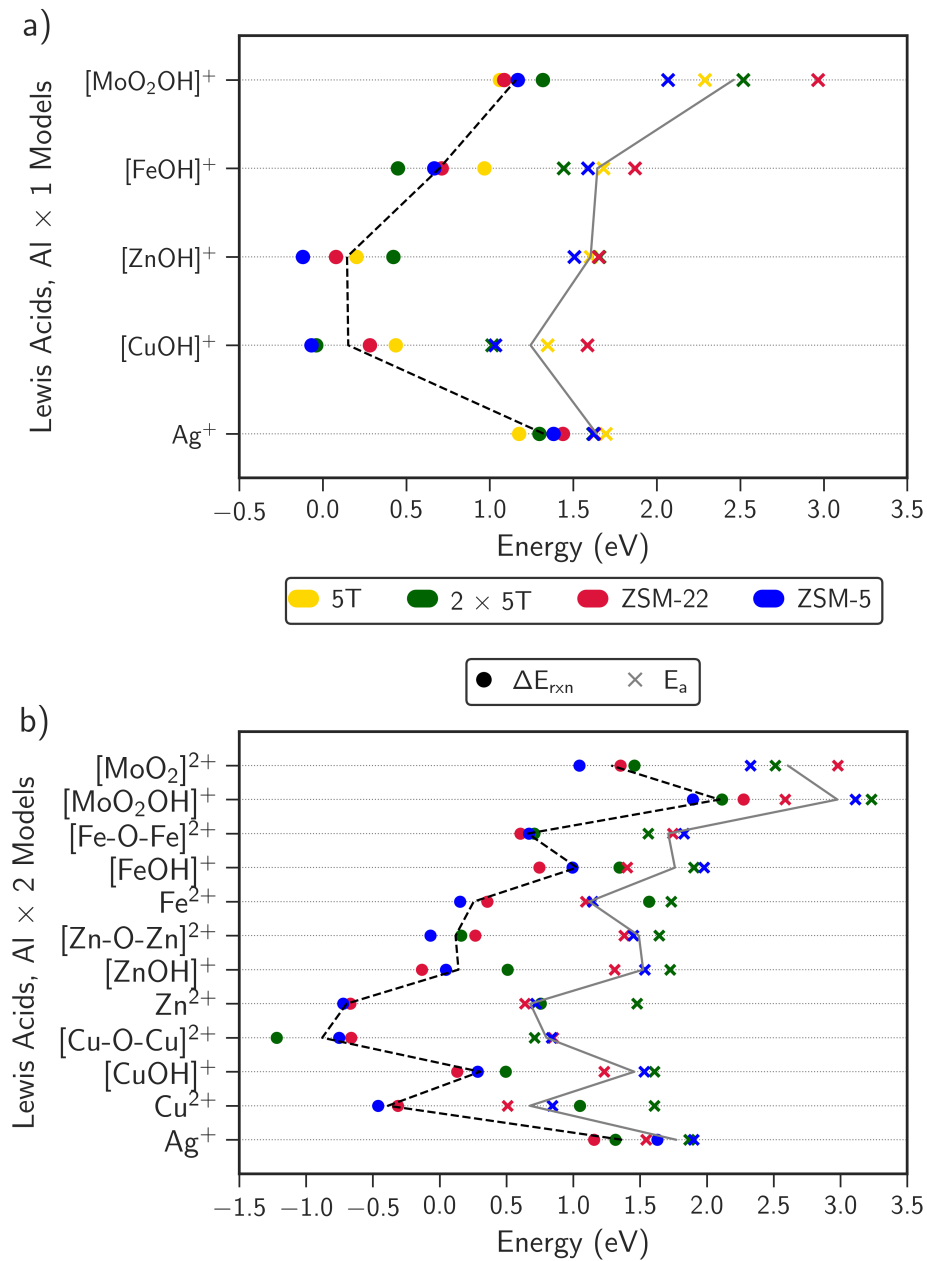


Figure 3.6. Energies of reaction ΔE_{rxn} (solid circles) and activation barriers E_a (crosses) for the activation of CH_4 on Lewis acids in $(\text{Al} \times 1)$ models in (a) and $(\text{Al} \times 2)$ models in (b).

Lewis acid sites of divalent metals were also modeled as an $[\text{M-O-M}]^{2+}$ motif, bonded to two Al anionic sites in close proximity. The thermodynamics of CH_4 activation on $[\text{Cu-O-Cu}]^{2+}$ is the most favorable of all active sites explored in our study, with ΔE_{rxn} ranging from -0.66 to -1.22 eV, and E_a ranging from 0.7 to 0.85 eV. We note that the final state of this mechanism is the formation of a $[\text{Cu-OH-Cu-CH}_3]^{2+}$ complex coordinated to both Al sites, and is visualized in Table S4. This geometry is also favored by $[\text{Fe-O-Fe}]^{2+}$, while $[\text{Zn-O-Zn}]^{2+}$ splits upon CH_4 dissociation to form a fully separated $[\text{ZnCH}_3]^+$ and a $[\text{ZnOH}]^+$ species bound to one Al anionic site each. Barriers and reaction pathways computed in this work agree well with those reported in literature.^{120–122}

Mahyuddin and coworkers studied the effects of confinement on the stability and activity of the $[\text{Cu-O-Cu}]^{2+}$ motifs in the conversion of CH_4 to CH_3OH over various zeolites, including ZSM-5 and SSZ-13.^{99,123} They suggested that an interplay between the zeolite pore structure and the angle of $[\text{Cu-O-Cu}]^{2+}$ bridge leads to a stabilization of the transition state, with lower energy transition states favored with smaller angles, and by extension, more confinement. These conclusions agree with the $[\text{Cu-O-Cu}]^{2+}$ structures and the corresponding energies obtained in this work. This motif exhibits the smallest angle of 110.5° in ZSM-5, with an $E_a \sim 0.4$ eV less endothermic than corresponding values on the $2 \times 5\text{T}$ cluster (116.2°) and ZSM-22 (120.9°). Similarly, Göltl showed that confinement in iron-oxo centers in zeolites reduced the barriers to CH_4 dissociation by more than 50% , with a large stabilization attributed to van der Waals interactions.¹²⁴

Overall, a qualitative analysis of CH_4 activation over Lewis acids bonded to isolated and paired Al sites over zeolite models of various complexity suggests that the activity of a metal-exchanged zeolite towards CH_4 activation is primarily attributed to the nature of the Lewis acid site, and by extension, the identity of its metal center. In this preliminary analysis, we have neglected the influence of

the framework geometry and position of Al sites on the stability and likelihood of formation of cationic complexes. The stability of these complexes is intimately linked to the location and proximity of framework anions, and accurate treatment of these effects require careful investigation.¹⁴ However, if we compare identical Lewis acid sites in dissimilar frameworks, the energetics of CH₄ activation depend to a lesser extent on geometric factors such as confinement and pore structure, or electronic factors such as charge localization and vdW interactions.

3.3.4. Factors Affecting the Reactivity of Lewis Acids towards CH₄ Activation

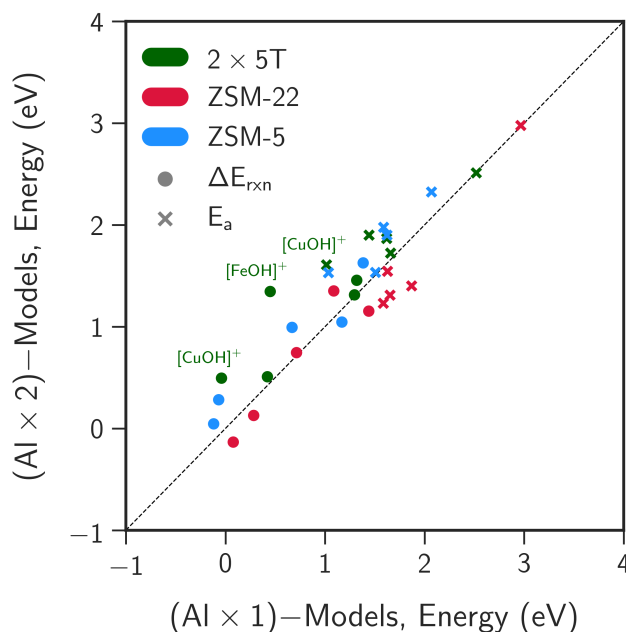


Figure 3.7. Parity plot comparing the energies of reaction (solid dots) and activation (crosses) of isolated Lewis acids in (Al × 1) models and in the presence of a proximal Brønsted acid in (Al × 2) models.

To investigate the effect of a charge localization on the Lewis acid's activity towards CH₄ activation due to the presence of a proximal Brønsted acid site, the activity of Lewis acids in both (Al × 1) and (Al × 2) models were compared by

means of a parity plot in Figure 3.7. Paired acid sites are commonly encountered as a result of partial or incomplete ion-exchange in metal-exchanged zeolites, resulting in paired Brønsted-Lewis acid sites. Additional motivation for such a comparison is to highlight any potential interplay between the Brønsted and the Lewis acid. The parity for ΔE_{rxn} and E_a between most data-points corresponding to $(Al \times 1)$ and $(Al \times 2)$ models suggests that the dominant role of the Lewis acid is retained even in the presence of a proximal Brønsted acid site. Data points that deviate >0.4 eV correspond to $[CuOH]^+$ and $[FeOH]^+$ on the $(2 \times 5T)$ cluster models. The dissociation energy of CH_4 on these active sites anchored in a $(2 \times 5T)-(Al \times 2)$ is more endothermic in the presence of a proximal Brønsted acid site. The local environment in cluster models can also be altered by changing the cluster termination and a detailed discussion on its effect is given in section A.

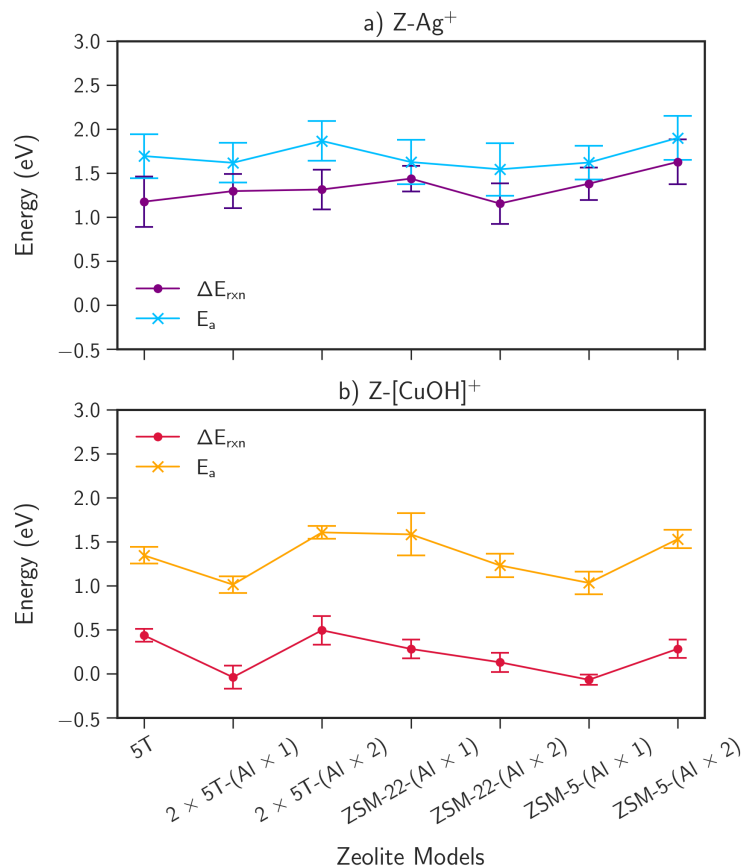


Figure 3.8. Parity plot comparing the energies of reaction (solid dots) and activation (crosses) of isolated Lewis acids in (Al \times 1) models and in the presence of a proximal Brønsted acid in (Al \times 2) models.

The variation of CH₄ dissociation energy and activation energy for the monovalent Lewis acid Ag⁺ and divalent [CuOH]⁺ species in different zeolite representations are depicted in Figure 3.8. Also included is the BEEF-vdW standard error associated with each energetic quantity. Analysis of Figure 3.8 suggests that ΔE_{rxn} and E_a for these Lewis acids are subject to a coupled relationship, akin to the well-established Brønsted-Evans-Polanyi relationships. The error bars for each data point indicate the inherent DFT errors associated with each calculation and quantify an error of one standard deviation (σ) from the ensemble average energy (μ). There are larger error bars associated with the Ag⁺ exchanged zeolite models, with a significant overlap of these error bars from the smallest 5T cluster

to the largest and most complex ZSM-5 periodic cell. The magnitude of the errors could be associated with the weakly bound nature of $\text{Ag}^+\text{-CH}_3^-$ species, such that the methane activation characteristics of Ag^+ appear to be indifferent to the choice of zeolite model.

The error bars for $[\text{CuOH}]^+$ across the zeolite models are of lower magnitude, clearly separated, and do not overlap significantly. These observations also hold true for the analogous $[\text{FeOH}]^+$ and $[\text{ZnOH}]^+$ motifs in Figure A.1. The coupled changes of ΔE_{rxn} and E_a imply that the thermodynamics and kinetics of CH_4 activation are similar on $[\text{MOH}]^+$ across different models, and minor variations in the energies are attributed to the characteristics of the model.¹²⁵ The small magnitude of DFT errors suggests that CH_4 activation is well described by the BEEF-vdW exchange correlation functional, with subtle variations in description of the physics of these models. While the separated error bars suggest that the $[\text{MOH}]^+$ motifs do indeed show some zeolite model dependence, Figure 3.8 suggests that the nature of the Lewis acid still retains its primary importance in determining the efficacy of the active site towards CH_4 activation. With reference to the coupled relationship between the thermodynamics and kinetics of CH_4 activation over these Lewis acids across different zeolite models, we limit all following analyses in this work to the activation energy barrier E_a for CH_4 dissociation.

Our results suggest that the nature of the Lewis acid site is paramount in determining the catalytic activity of the metal-exchanged zeolite. The mean average error (MAE) in activation energy (E_a) for the same $[\text{CuOH}]^+$ motif across all zeolite models was found to be 0.21 eV, while that for all different Cu motifs in ZSM-5 was found to be 0.31 eV. To substantiate this hand-waving argument that the complexity of the zeolite model is of secondary significance, we have performed a statistical analysis of our computed activation energies and associated

error ensembles in the sections that follow.

3.3.5. Statistical Analysis of Error Ensembles

The zeolite models used as training sets span a small cluster (5T), an extended cluster ($2 \times 5T$), a small pore straight channel zeolite (ZSM-22), and a zeolite with intersecting channels (ZSM-5). A combined ensemble for each Lewis acid was constructed by combining the BEEF-vdW ensembles for E_a of CH_4 activation for all Lewis acid motif–zeolite model configurations. With this range of model complexity, we expect that the energy for the activation of CH_4 in any other similar zeolite framework falls into the range of energies defined by the combined ensemble. This hypothesis should hold true for most zeolites provided their activity towards the activation of CH_4 is primarily dependent on the exchanged metal species and not prohibited by extremely narrow pores or cages. A quick evaluation of this hypothesis was done by comparing the range of energies predicted by the combined ensemble for the $[\text{Cu-O-Cu}]^{2+}$ motif with those reported in literature. As seen in Figure A.2 energies computed for this motif on frameworks such as other cluster models, MOR, FAU and SSZ-13 fall within one standard deviation of the mean of the combined ensemble. To qualitatively test our assertion, we validate the predictive ability of our ensemble energies for each Lewis acid site with the values obtained for a periodic representation of the medium pore zeolite SSZ-13, which was not included in the generation of the combined ensemble.

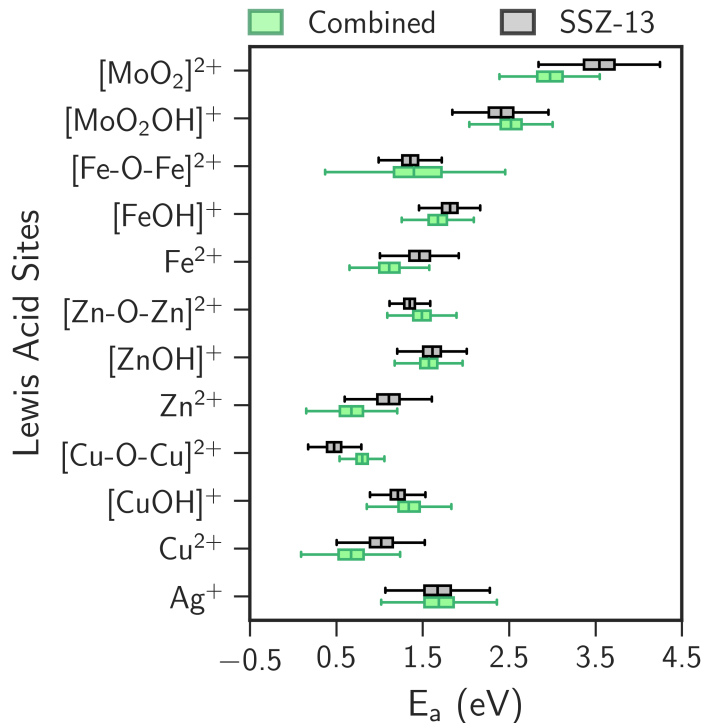


Figure 3.9. Boxplots comparing the E_a ensembles for CH_4 activation over Lewis acids in periodic SSZ-13 and combined ensembles using descriptive statistics.

The energies of reaction (ΔE_{rxn}) and activation barriers (E_a) of CH_4 activation over different Lewis acid exchanged SSZ-13 models are provided in Table A.5 and Table A.5. If the nature of the Lewis acid site dominates the intrinsic catalytic activity, quantities such as the mean and the standard deviation of SSZ-13 ensembles should overlap with those of the combined ensemble for the same Lewis acid. However, the combination of distributions of different (μ, σ) forming an ensemble may be multimodal or have irregularly tailed distributions, and typically do not follow a normal distribution. Hence, commonly used statistical measures such as mean and standard deviation are prone to fail in appropriately describing the combined ensemble and in providing a meaningful comparative basis. The combination of ensembles from the Lewis acid sites sampled in this investigation gives rise to such non-normal distributions. To account for the non-normal

nature of the combined ensembles, we used descriptive statistics to analyze and compare the ensembles. Boxplots comparing the combined ensemble of a Lewis acid with the corresponding ensemble for an SSZ-13 periodic unit cell are shown in Figure 3.9.

The boxplots describing the energy of activation of CH_4 (E_a) in Figure 3.9 on the Lewis acids anchored on SSZ-13 models are depicted in grey and the combined ensembles in green. A visual inspection of the figure confirms our previously made assertion that the combined ensemble is effectively able to describe the activation of CH_4 on a new zeolite model. We base our conclusion on the large extents of overlap and similarity in the boxplot range (whiskers) corresponding to the SSZ-13 model and the combined dataset. An appropriate indicator of similarity between the datasets is the overlap of the interquartile (IQR) range. The IQR consists of the middle 50% or the midspread of that data; therefore, complete overlap of the IQR would mean that over 50% of the data are common in both datasets. A large extent of overlap of the IQR boxes is observed for Lewis acid motifs at isolated acid sites. Conversely, the larger motifs that bond to paired Al anionic sites show more variability. A range of 0.25–0.5 eV for the IQRs suggest that one can increase motif reactivity within this range by tuning factors such as strain or confinement. However, larger changes in energy can only be achieved by changing the active site or the metal type. These observations again highlight the primary importance of the Lewis acid type but show that its geometry and reactivity are influenced by the framework structure, particularly when multiple Al atoms are involved in forming the active site.

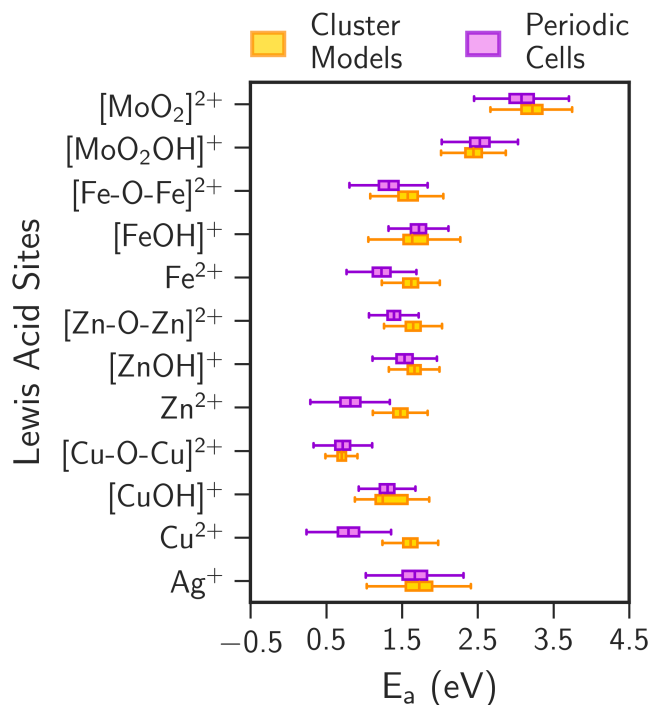


Figure 3.10. Boxplots comparing the E_a ensembles for cluster models and periodic cells.

Combined ensembles for cluster models (5T and $2 \times 5T$) and periodic cell models (ZSM-22, ZSM-5 and SSZ-13) were constructed to further investigate the influence of the framework periodicity on the activity of the Lewis acid towards CH_4 activation. The boxplots comparing both datasets are given in Figure 3.10. The cluster models perform well in describing the activation of CH_4 at isolated Al sites, i.e. $[\text{M}_x\text{O}_y\text{H}_z]^+$, with a large overlap of respective IQRs. The boxplots describing the Lewis acids bonded to paired zeolite acid sites ($[\text{M}_x\text{O}_y\text{H}_z]^{2+}$) show larger variation between the cluster models and periodic cell models particularly, the M^{2+} Lewis acids. Overall, cluster models are efficiently able to capture the intrinsic reactivity of isolated acid sites and would serve as excellent proxy models for studying hydrocarbon conversion on larger periodic cell models that consist of these active sites. Conversely, reliable investigations of the catalytic activity of M^{2+} Lewis acids would require a careful selection of zeolite periodic cell model

Table 3.4. Probabilities $P(M1 > M2)$ for metal M1 showing a lower activation energy barrier for CH_4 dissociation than metal M2.

	Cu	Zn	Fe	Ag	Mo
Cu	-	80.4	85.6	94.6	100
Zn	19.6	-	62.3	75	100
Fe	14.4	37.7	-	60.3	97.5
Ag	5.4	25	39.7	-	99.7
Mo	0	0	2.5	0.3	-

and geometric characteristics of the active site.

The error ensembles can also be combined such that the distribution includes all possible active site motifs of a particular metal, e.g. $[MOH]^+$, M^{2+} , $[M-O-M]^{2+}$, etc. The resulting combined distribution would in theory, describe the reactivity of a metal-exchanged zeolite, inclusive of the reactivity of all active site motifs within. The need for such a distribution can be motivated by synthesis dependent non-uniform distribution of framework aluminums,⁷¹ and subsequent non-uniform concentration and distribution of Lewis acid sites within a zeolite, each of which would contribute non-trivially to the overall activity of the zeolite. A dataset (metal distribution) that can estimate the activity of a metal-exchanged zeolite without requiring an in-depth analysis into the various possible active sites and associated mechanisms possesses an immense value as a screening tool. Accordingly, a measure of probability such that metal-exchange candidate M1 activates CH_4 in comparison to candidate M2 was computed using the expression given in Equation 3.7. This probability was calculated for all (M1, M2) combinations of Cu, Zn, Fe, Ag and Mo.

The probabilities computed independently for the distributions corresponding to the energy of activation E_a are given for each (M1, M2) combination in Table 3.4. Cu-exchanged zeolites show the highest probability of activating CH_4 favorably in comparison to the other metal-exchange candidates included in this

study, i.e. Zn, Fe, Ag and Mo. In other words, metal-exchanged zeolite models comprised of Cu Lewis acids will activate methane more favorably than Zn-exchanged zeolites with a probability of $\sim 80\%$. The order of activity towards CH_4 activation among the metals was found to be $\text{Cu} > \text{Zn} > \text{Fe} > \text{Ag} > \text{Mo}$. Under the assumption that CH_4 activation is the rate determining step in a typical CH_4 upgrade process in a metal-exchanged zeolite, Cu-exchanged zeolites are expected to be the most reactive and show the largest intrinsic rates of reaction. We note that we limited the active site representation in Mo-exchanged zeolites to $[\text{MoO}_2\text{OH}]^+$ and $[\text{MoO}_2]^{2+}$, while there is evidence for Mo_xC_y or $\text{Mo}_x\text{O}_y\text{C}_z$ species as active centers for the cleavage of the C-H bond in CH_4 . This discrepancy explains why we predict poor methane activation ability for Mo-exchanged zeolites, whereas they have known activity towards methane aromatization once the $\text{Mo}_x\text{O}_y\text{C}_z$ phase is formed.²⁴

The implications of being able to sort a list of metal-exchanged zeolites in their order of intrinsic activity possesses value in screening studies to determine active catalysts towards CH_4 activation. Such a study would entail modeling the reaction on all possible Lewis acid motifs that are known to be present as active sites, obtaining relevant distributions from the Bayesian error ensembles, combining them and computing probabilities of catalytic performance improvements of one metal over the other. Given the similar trends between periodic zeolite models of different complexity, we propose that using smaller zeolite models such as SSZ-13 can provide good qualitative comparisons for preliminary studies and screening. For instance, we modeled the activation of CH_4 on divalent Pd Lewis acid motifs that are structurally similar to Cu, Zn and Fe motifs, bound to SSZ-13. SSZ-13 is a computationally inexpensive zeolite model and we have demonstrated in Figure 3.9 that it shows in general a sufficient overlap with the combined ensemble energies representing a range of disparate zeolite models.

Hence, the ensembles corresponding to E_a for $[\text{MOH}]^+$, M^{2+} and $[\text{M-O-M}]^{2+}$ anchored to SSZ-13-(Al \times 1) and (Al \times 2) models were combined to form energy distributions allowing a comparison of methane activation performance between Pd-SSZ-13 and Cu-SSZ-13.

Inexpensive DFT calculations of CH_4 activation on four Lewis acid motifs on SSZ-13 were performed and an initial measure of a reactivity of a Pd-zeolite can be computed. Except for simply changing the identity of the Lewis acid, no prior information about Pd species was considered in our calculations. The probability of Pd-SSZ-13 being a more reactive catalyst than Cu-zeolite was found to be $\sim 80\%$. Pd zeolites are commonly used as catalysts for the combustion of CH_4 , and our estimation of the high likelihood of CH_4 activation over these zeolites is in good agreement with results reported in literature.^{126,127} The limitation of the low energy barriers to C-H bond activation over Pd zeolites is the implied preference to total oxidation or coke formation, as opposed to the formation of value-added products.

3.4. Conclusions

This work computationally assesses the reactivity of metal-exchanged zeolite models towards CH_4 activation by leveraging uncertainty quantification of intrinsic DFT errors and active site approximations. Various Lewis acid motifs and associated mechanisms of CH_4 activation were examined and the dominant pathway for each motif was determined. The smaller cluster models, 5T and $2 \times 5\text{T}$ showed the same general trends in reaction and activation energies as those obtained on larger periodic systems, such as ZSM-22 and ZSM-5. Inclusion of the BEEF-vdW error estimates into our analysis showed that the dissociation of CH_4 on the monovalent Ag^+ Lewis acid site exhibits a significant extent of error

bar overlap and is equivalently described by all zeolite models. Lewis acid sites formed from multivalent metal cations show some sensitivity to the choice of zeolite model, but qualitative activity trends were mostly impervious to electronic and steric factors. An exception to the robust activity trends is constituted by M^{2+} sites, which show a strong dependence on the geometry of the pair of anionic anchor points in the zeolite framework.

An approach to combine the BEEF-vdW error ensembles from different active site representations was developed to compute distributions that describe CH_4 dissociation kinetics across different metal-exchanged zeolite models. We tested this approach by comparing the model averaged energies with a dataset obtained by modeling CH_4 activation on SSZ-13, which was not included in the training data. A reasonably large overlap of the boxplot inter quartile ranges between the combined ensemble and that of SSZ-13 reinforces the observation of the Lewis acid being central to CH_4 activation chemistry in a metal-exchanged zeolite. Exceptions to this centrality are seen with M^{2+} Lewis acids and care must be taken to represent these active sites in an appropriate zeolite model correctly. The existence of competing Lewis acid motifs is also model and configuration dependent and investigations into elementary steps and associated reaction mechanisms must proceed with caution.

Probability distribution functions describing combined ensembles for a generic zeolite, inclusive of all Lewis acid motifs of a particular metal in the presence of isolated and paired acid sites were computed and used to screen metal exchange candidates based on their activity towards CH_4 activation based on probabilistic measures. It is reasonable to speculate that these conclusions extend to Lewis acid catalyzed reactions of other small molecules that are not severely constrained within the zeolite pore. Overall, the use of the combined ensemble as a descriptor of a metal exchanged zeolite’s reactivity towards probe hydro-

carbon conversion reactions will help build rigorous screening frameworks that can be used to arrive at suitable candidates for a desired hydrocarbon conversion reaction.

4. Bifunctional Lewis and Brønsted Acid sites In Ag-H-ZSM-5 Catalysts for Ethylene Dimerization and Aromatization

The research presented in this chapter investigates the atomistic origins of the enhanced selectivity to aromatics exhibited by silver-exchanged ZSM-5 catalysts. A majority of this project is in collaboration with Yunwen Zhou and Prof. Jeffrey D. Rimer of the department of Chemical and Biomolecular Engineering, University of Houston. The manuscript detailing the research is in preparation and is due for submission in Spring 2020.

4.1. Introduction

Benzene, toluene and xylenes (BTX) are an important class of hydrocarbons of immense economic value in the petrochemical industry. They are used as solvents and in the production of plastics, paints etc. Global consumption of benzene, estimated at more than 50 million tons, showed an unprecedented growth of more than 3 million tons from the level seen in the last decade. With the demand steadily growing, prices have gone up from 800-900 \$/ton in 2010 to around 1200-1500 \$/ton. BTX are traditionally obtained from naphtha through catalytic reforming or steam cracking with a global production pushing 100 million metric

tons per year that is projected to grow at a rate of 3.5–4% in the next five years.¹²⁸ The push towards moving away from crude-oil based feedstocks required for the production of BTX has resulted in a renewed focus in converting easily available methane feedstocks to liquids, commonly referred to as gas-to-liquids (GtL). The surge in natural gas production across the world has incentivized the search for processes that can utilize methane and light olefin derivatives in the manufacture of aromatic products. The conversion of methane to aromatics or the dehydroaromatization (DHA) over zeolite catalysts has evolved into a mature field of research occupying the minds of many researchers across the world.^{105,129–131}

To date, the most active catalyst reported for such a transformation are Lewis and Brønsted acidic molybdenum-exchanged/modified ZSM-5 zeolites.¹³² There is plenty of research devoted to understanding the fundamental mechanisms that enable the activation and transformation of methane and the active sites and pathways reported are numerous. Despite the complexity of the catalysis there appears to be a consensus that the first carbon–carbon bond formed in DHA chemistry is than in ethylene ($\text{H}_2\text{C}=\text{CH}_2$) at the Mo-active sites, which then undergoes oligomerization, hydrogen-transfer and cyclization reactions at the Brønsted acid sites of the zeolite.^{3,109,133,134} The activation of methane and the subsequent formation of ethylene appear deceptively simple but is postulated to occur at a range of Mo_xC_y active sites.^{24,25}

While popular with methane DHA, the use of Lewis acids expands the applicability of H-ZSM-5 catalysts into other applications such as hydroisomerization reactions,¹³⁵ selective catalytic reduction (SCR) in catalytic converters,^{50,136} and the production of fine chemicals,¹³⁷ amongst other uses. Other metal-exchanged zeolites have also been extensively tested as catalysts for methane DHA such as Pd, Ir, Ru, Ni, Cu in the work of Conte and coworkers.¹³⁸ In our work, the catalyst of choice is Ag-exchanged ZSM-5 (Ag-H-ZSM-5), which has proven to be an

active catalyst for methane DHA,^{52,53} SCR, and alkane aromatization reactions.¹³⁹ Silver-exchanged ZSM-5 offers the possibility of less-complex active sites under reaction conditions due to the stability and preference of a monovalent character in its cationic form. Previously, we have tested the performance of Ag-H-ZSM-5 zeolites of various Ag loading and reported a four-fold enhancement in selectivity to BTX at high conversions when using ethylene as feedstock, while methane showed negligible activity towards DHA.²⁹

Despite the ubiquity of research concerning hydrocarbon conversion using metal-exchanged zeolites, a full picture of the interplay between Brønsted acid sites and metal-based Lewis acid sites is still missing. However, it is a known fact that the presence of these metal-sites has a significant effect on the catalytic activity of the zeolite. Accordingly, in this work, we systematically attempt to deconvolute the roles of the Brønsted and Lewis acid sites in the secondary aspect of accepted DHA chemistry, i.e. the conversion of ethylene to aromatics using a combination of transient pulsing experiments with a temporal analysis of products reactor and density functional theory (DFT) calculations. First, detailed characterization of the synthesized Ag-H-ZSM-5 samples was performed using experimental and computational UV-Vis spectroscopy, followed by X-ray absorption spectroscopy and temperature programmed desorption. Transient experiments enable the investigation of the intrinsic activities of Lewis and Brønsted acid sites in reactant-limited regimes of reaction and information gleaned from these experiments help drive a feasible exploration of activation and reaction mechanisms using DFT calculations. The minute quantity of reactants pulsed in does not change the state of the catalyst and provides crucial information on how the reactants interact with the active sites. Overall, we show that a mix of Brønsted and Lewis acid sites appear to drastically increase the residence time and interaction of ethylene molecules with the catalyst at the Ag⁺ sites with in-

creased selectivities to hydrogen transfer and cracking pathways.

4.2. Experimental Methods

4.2.1. Temporal Analysis of Products Experiments

All transient experiments were performed on a TAP-1 setup described in detail elsewhere.^{5,41,140} Ethylene (Matheson 99.999%) and helium (Matheson 99.999%) mixtures of ratio 4:1 were prepared in a mixing tank and a precise quantity of gas was admitted into a quartz microreactor by means of pulse valves (Parker Hannifin), two of which are housed in a manifold assembly heated to a temperature of 95 °C. The quartz microreactor was heated by nichrome resistance wire and the temperature of the bed was monitored a K-type thermocouple positioned at the catalyst bed and controlled by PID temperature controller (Eurotherm). The reactor and mass spectrometer chambers were then pumped down to vacuums of 10^{-6} and 10^{-8} torr, respectively. Time-resolved flow of unreacted ethylene, helium and products for each input pulse of C₂H₄/He was measured by an online UTI 100C quadrupole mass spectrometer (MS). The intensity in signal measured as the zeroth moment or area,

$$a_{\text{AMU}} = \int_0^t V(t) dt, \quad (4.1)$$

where $V(t)$ is the temporal signal and t is the collection time for each response. Areas were related to molar quantities by means of calibration factors. Further information is provided in chapter 2.

Multi-pulse experiments were performed over ~10 mg of catalyst housed in a thin zone configuration sandwiched between inert silica (Sigma Aldrich) beds.^{140,141} The catalyst was pretreated in-situ under continuous pulsing of he-

lium with pulse spacing of 0.5 s. The bed was heated at a rate of 5 °C per min to 550 °C, held at that temperature for 90 min, and then cooled to the desired reaction temperature. Regeneration of the catalyst bed followed the same protocol. The catalysts were pelleted, crushed, and sieved to obtain agglomerates of size 250-400 μm . Silica gel of identical particle size distribution were used to ensure uniformity in porosity along the reactor bed.

Typically, TAP multi-pulse experiments are set up such that for every pulse of reactant gas mixture admitted, the MS quantified and cycled through a series of pre-determined mass-to-charge (m/z) ratios based on expected primary and secondary products of the chemistry under investigation. However, these multi-pulse experiments consist of MS recordings that are staggered in time and therefore, fail to provide information about reactants consumed and products formed at the same instant in time. To overcome this gap in information, replicate/duplicate experiments were performed in which only He and a reactant or product are monitored. Upon collection of 100 pulses for one m/z ratio, the catalyst was regenerated, and the experiment was repeated for the next product. The measurements for all products were compiled to obtain a detailed time-resolved development of product yields and selectivities as a function of pulses. Accordingly, replicate experiments were performed in which 100 ethylene/helium pulses were admitted into the microreactor and pulse responses for a set of m/z ratios configured beforehand. It was ensured that data collection persisted till the signal for the reactant or the product attained baseline, and no temporal information was lost or truncated.

The analysis of hydrocarbons with mass spectrometry is complicated due to the presence of overlapping fragments at lower ratios. For example, the signal measured at an m/z ratio of 28 consists of contributions from ethylene, propene, propane, butene and butadiene, and nearly every higher olefin. A matrix of over-

Table 4.1. The coefficient matrix of relative signals at overlapping m/z ratios.

m/z	C_2H_4	C_3H_8	C_4H_6	C_4H_8	CH_4	H_2
28	1	0.7784	0.585	0.309	0	0.0905
29	0.0223	1	0.0100	0.141	0	0
39	0.0010	0.2451	1	0.512	0	0
41	0.0003	0.1986	0.0039	1	0	0
16	0.0039	0	0.0092	0	1	0
2	0.0073	0.0027	0.0085	0.004	0.0067	1

lapping coefficients was constructed by performing calibration experiments for pure gases over silica for ethylene, methane (Matheson 99.999%), propane (Matheson 99.999%), propene (Matheson 99.999%), 1-butene (Matheson 99%) and 1,3-butadiene (Sigma Aldrich $\geq 99\%$) and are given in Table 4.1. Assuming that the measured signal at a particular m/z ratio is a linear combination of contributions from all pure hydrocarbons with fragments at that ratio, the signals of pure components were calculated from a constrained optimization of the solution to a system of linear equations and given as

$$\underbrace{\begin{bmatrix} 1.00 & \cdots & 0.0905 \\ \vdots & \cdots & \vdots \\ 0.0073 & \cdots & 1.000 \end{bmatrix}}_{\bar{A}} \underbrace{\begin{bmatrix} C_2H_4 \\ \vdots \\ H_2 \end{bmatrix}}_{\bar{x}} = \underbrace{\begin{bmatrix} a_{28} \\ \vdots \\ a_2 \end{bmatrix}}_{\bar{b}} \quad (4.2)$$

and

$$\min U(y) = (\bar{A} \bar{x} - \bar{b})^2 \quad \text{such that} \quad x_i \geq 0; x_i \in x. \quad (4.3)$$

The moles of reactant pulsed in can be calculated from the pulse responses pertaining to the inert gas, helium. The evolution in defragmented products was then obtained as a function of 100 pulses. The product yield for all measured products was calculated as the percentage of product formed per mole of reactant

consumed as

$$\% \text{ yield}_{\text{product}} = \sum_{N=100} \frac{\text{moles}_{\text{product}}}{\text{moles}_{\text{reactant consumed}}} \times 100. \quad (4.4)$$

4.2.2. UV-Vis Spectroscopy

Experimental Measurements

Diffuse reflectance UV-Vis spectroscopy spectra of Ag-H-ZSM-5 samples were recorded using an Agilent Cary 5000 UV-Vis-NIR spectrometer. Measurements with a step size of 1 nm were collected in the 200-800 nm range with polytetrafluoroethylene fine powder used as the 100% reflectance standard.

Simulated UV-Vis Spectroscopy

Computational Parameters and Setup

Ab initio molecular dynamics (AIMD) of Ag species in zeolite models were performed to account for finite-temperature dynamics of the structure and interactions of the Ag species with the zeolite pores at ambient temperature. A CHA periodic unit cell was chosen as it represented the best compromise between computational expense and similarity to the much larger MFI periodic unit cell of ZSM-5. Moreover, it has been shown previously that Ag-SSZ-13 is an excellent approximation of Ag-ZSM-5 in terms of Lewis acid reactivity.¹⁴² The CHA unit cell consists of 12 crystallographically identical T-sites and substitution of one of the framework Si atoms with Al results in a model with a silicon to aluminum ratio (SAR) of 11. The SAR of these models compare well with the ZSM-5 samples characterized experimentally (SAR \sim 12). Structures of various Ag-exchanged SSZ-13 models were first relaxed to their ground states using the BEEF-vdW exchange correlation functional. Independent AIMD simulations of various Ag-SSZ-13 pe-

periodic unit cells were performed at 300 K for 80 ps with a 1 fs time step. We used the Vienna ab initio simulation package (VASP) to set up the simulations within the canonical (NVT) ensemble with the Nosé -Hoover Thermostat used to attain the target temperature of 300 K.^{79,79,82,143} The BEEF-vdW exchange-correlation functional and the projector augmented wave (PAW) method was used to solve the Kohn-Sham equations with a cutoff energy of 540 eV.^{40,84,144} The Brillouin zone was sampled at the gamma point and electronic convergence set to require at least three self-consistent field (SCF) steps.

Calculation of Absorption Coefficients

Upon completion of the AIMD simulations, 10 random images were chosen from the trajectories sampled by the simulation after a time of 40 ps. This was done to ensure that the dynamics of the system were sufficiently equilibrated and that the structures chosen were representative of an actual Ag-SSZ-13 sample at ambient conditions. The excitonic effects within the frequency-dependent dielectric function was calculated for these structures by solving the Bethe-Salpeter equation (BSE), preceded by a sequential upgrade of wavefunctions through a multi-step procedure. An initial wavefunction was generated from single-point GGA calculations using the BEEF-vdW functional, with the number of bands (NBANDS) set to 1000. To accommodate core-hole transitions, the number of bands chosen was significantly higher than those occupied in the ground state. The HSE06 functional (LHFCALC = .TRUE., HFSCREEN = 0.2) was used to generate electronically accurate wavefunctions.¹⁴⁵ The derivatives of orbitals with respect to the Bloch wave vector were then calculated using the PEAD formalism within the TD-DFT framework (IBRION = 7). The next step involved the calculation of quasiparticle energies for 600 bands by performing partially self-consistent GW0 calculations with an GW energy cutoff of 150 eV.^{146,147} The optical response func-

tion for each structure was computed by solving the BSE equation on top of the previously generated GW0 wavefunctions.^{148,149} The optical response was computed for 472 occupied and 178 unoccupied bands and electronic convergence for all steps was set to 10^{-6} eV. The frequency-dependent dielectric function $D(\omega)$ for each structure can be extracted and the imaginary components in the x , y and y directions were used to obtain a quantity analogous to the experimentally measured Kubelka-Munk absorption coefficient.

4.2.3. X-Ray Absorption Spectroscopy

Ag K-edge X-ray absorption spectroscopy (XAS) data was collected at the QAS, NSLS-II beamline at Brookhaven National Laboratory. Measurements were conducted in transmission and fluorescence modes, with the monochromator calibrated using Ag-foil as reference. Edge energies were calibrated to that of Ag-foil which was set to 25514.0 eV. Powdered catalyst samples were brushed onto Kapton tape and ex-situ measurements were acquired for samples in their hydrated states at ambient conditions. Higher quality fluorescence signals were obtained for the Ag-ZSM-5 samples compared to transmission signals. This data was subsequently subjected to normalization and background correction in the Athena software. Data was converted into the kinetic energy (k -space) by assigning the K-edge as the first point of inflection of the absorption edge. Extended X-ray absorption fine structure (EXAFS) spectra or radial distribution functions were obtained by Fourier transforming k^2 -weighted $\chi(k)$ functions between 1.5 \AA^{-1} and 8 \AA^{-1} for the Ag-ZSM-5 samples using the Artemis software. These spectra were fitted to the first coordination shell of Ag in a periodic Ag-ZSM-5 unit cell obtained from density functional theory calculations. This unit cell was used by the FEFF6 module in Artemis to generate *ab initio* multiple-scattering paths for Ag and its neighbors up to distances of 6 \AA . The amplitude reduction factors

S_0^2 were first obtained by fitting 2 coordination shells of the FT-EXAFS spectra of Ag-foil and were set at 0.905. These factors were used in the fitting procedure to obtain estimates of the first-shell coordination numbers (N), Debye-Waller factors (σ^2), energy shifts (E_0) and interatomic distances (R) for the Ag-ZSM-5 samples.

4.3. Density Functional Theory Calculations

Density functional theory (DFT) simulations of ethylene upgrade and conversion were carried out using the Vienna Ab-initio Simulation Package (VASP) in combination with the Atomic Simulation Environment (ASE).^{79–81} The Kohn–Sham equations for all calculations were solved using the projector augmented wave (PAW) method and the exchange and correlation energy provided for by the Bayesian error estimation functional with van der Waals correlation (BEEF-vdW).^{40,84} This functional appropriately describes the interaction of molecules with the zeolite pores with the inclusion of long range van der Waals forces. An energy cutoff of 540 eV, Gaussian smearing of $kBT = 0.1$ eV were used to ensure electronic convergence and the Brillouin-zone was sampled at the Γ -point. All calculations were run such that the residual force on each atom did not exceed 0.02 eV/Å. Transition state structures and energies were computed using the climbing image nudged-elastic-band method (NEB) and refined using the Dimer method to a force convergence criterion of 0.05 eV/Å.^{85,86}

The lattice parameters of the ZSM-5 periodic unit cell were optimized with the BEEF-vdW functional and lattice constants were found to be $a = 20.41$ Å, $b = 20.05$ Å and $c = 13.35$ Å. These lattice parameters correspond to an error of less than 1% from those obtained experimentally.⁹² All reactions were modeled at the T-12 site of the ZSM-5 periodic cell, allowing for sufficient void space to sample larger transition states that were encountered while exploring reaction

mechanisms. The T-12 Si atom was replaced by an Al, requiring extraframework species such as an Ag atom (Ag-ZSM-5) or a proton (H-ZSM-5) to balance the excess negative charge of the framework. Additional Ag motifs with a net unipositive charge were also considered as active sites for ethylene activation and oligomerization.

Enthalpies and entropies of the adsorbates and periodic cell models at reaction temperatures were calculated using the quasi-rigid rotor harmonic oscillator approximation (qRRHO) developed first by Grimme¹⁵⁰ and improved by Head-Gordon.¹⁵¹ This approximation systematically replaces low-magnitude vibrational modes with rotational modes based on a frequency dependent weighting function, thus overcoming the problems of overestimating entropy and enthalpy within the harmonic approximation.^{151,152} Additional imaginary frequencies for adsorbed species were considered as floppy modes and were replaced by 12 cm^{-1} .^{114,153} The vibrational frequencies and zero point energies required for the calculation of enthalpy and entropy were obtained from the finite difference approximation of the Hessian matrix calculated by displacing “participating” atoms by 0.01 \AA . In addition to all extraframework atoms, framework atoms located within a separation of 5 \AA from the T-12 site were allowed to vibrate. An electronic convergence criterion of 10^{-8} eV was employed to ensure accuracy of the Hessian matrix and ensuing entropy calculations.

4.4. Results and Discussion

4.4.1. Characterization of Active Sites

UV-Vis Spectroscopy

The UV-Vis spectra of as-synthesized $\text{Ag}_x\text{-H-ZSM-5}$ samples (SAR ~ 12) were collected at ambient conditions for four Ag loadings ($\text{Ag}/\text{Al} = 0.08, 0.25, 0.38$ and 0.46) and are shown in Figure 4.1 a. All four spectra show bands in the 200-220 and 260-280 nm ranges that are characteristic features of exchanged cationic Ag^+ in zeolite channels.^{94,154,155} The absence of features at higher wavelengths suggests that larger clusters or metallic Ag species are not formed during synthesis. To confirm the absence of metallic Ag, the UV-Vis spectra of $\text{Ag}_{0.25}\text{-ZSM-5}$ synthesized by incipient wetness impregnation was recorded and is shown in comparison with $\text{Ag}_{0.25}\text{-ZSM-5}$ synthesized by ion-exchange in Figure 4.1 b. This mode of synthesis is more susceptible to the formation of zoned-metal on the external surface of the zeolite, metal-clusters or oxides.²⁹ While a majority of features in the spectra are characteristic of cationic Ag^+ , there exists a broad feature at 405 nm, as seen in the inset of Figure 4.1 b. Therefore, UV-Vis characterization of various Ag-ZSM-5 samples is consistent with the formation of Ag^+ Lewis acid sites inside the zeolite pores upon complete ion-exchange. In contrast, incipient wetness impregnation leads to the formation of Ag clusters or metallic Ag that are most-likely deposited on the exterior of the zeolite surface.

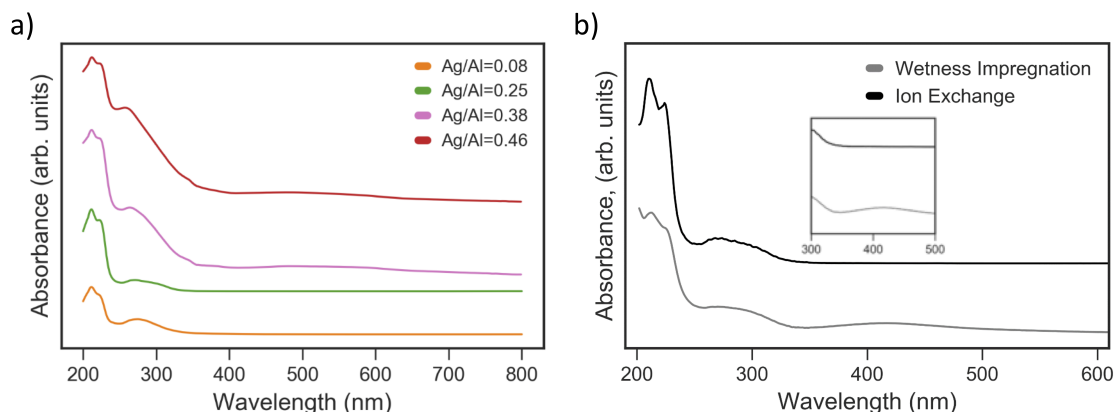


Figure 4.1. UV-Visible spectra collected at 27 °C for various Ag-ZSM-5 samples (SAR \sim 12) for various Ag loadings (Ag/Al) in a) and for different methods of synthesis (indicated in the legend) of Ag_{0.25}-ZSM-5 in b).

Experimentally measured UV-Vis spectra are cumulative function of all photo-active species in the sample. The origin of photo-activity in the UV-Visible spectrum is due to the electronic transitions that occur upon absorption of light. These transitions are largely affected by the oxidation state, local environment and coordination of ligands to the metal species. Therefore, identifying the origin of features in the ligand to metal charge transfer (LMCT) region and their assignment to known electronic transitions is a non-trivial exercise.¹⁵⁶ To help assign experimentally observed UV-Vis transitions in Figure 4.1 to identifiable Lewis acid motifs, we simulated the frequency-dependent dielectric matrix of various Ag-exchanged SSZ-13 species. The absorption coefficient for various Ag motifs in SSZ-13 was extracted from the computed dielectric matrix and compared with the experimental spectra in Figure 4.2.

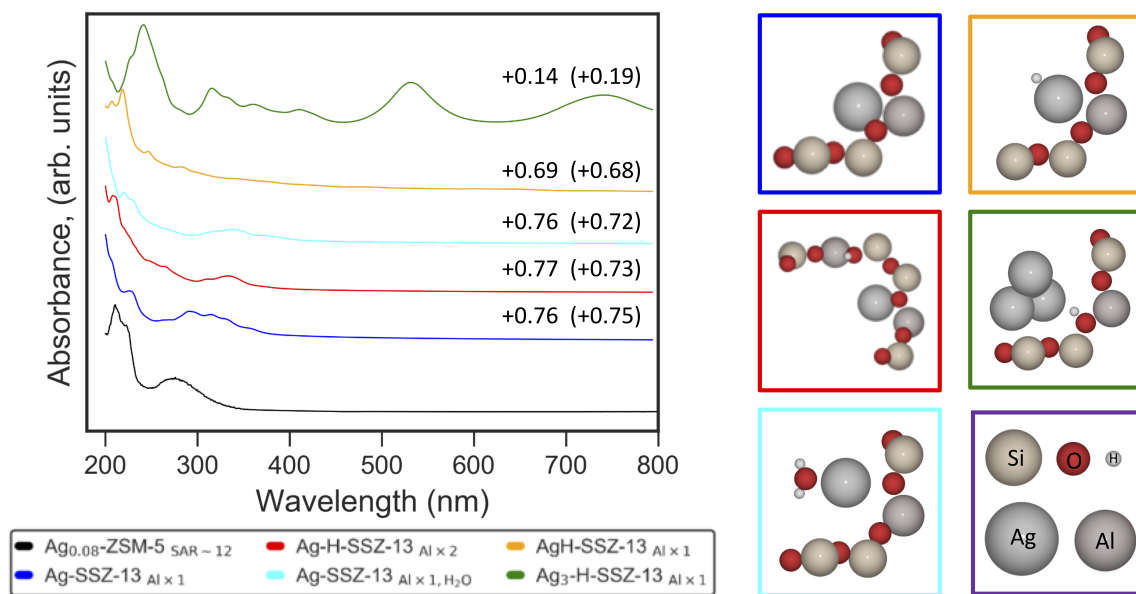


Figure 4.2. Computed UV-Vis spectra of five Ag-SSZ-13 zeolite models, i.e. Ag-SSZ-13 (blue), Ag-H-SSZ-13_{Al × 2} (red), Hydrated Ag-SSZ-13+H₂O (cyan), AgH-SSZ-13 (gold) and clustered Ag₃-H-SSZ-13 (green).

The absorption spectra of a series of Ag-SSZ-13 models was simulated based on typical structures reported in literature. Silver can satisfy the negative charge of an $[\text{AlO}_4]^-$ tetrahedral site in a zeolite as an Ag^+ ion. Under ambient conditions, it is reasonable to assume the Ag^+ to be hydrated by atmospheric moisture, as is commonly observed for Cu-SSZ-13.¹⁴ The spectra for an Ag-SSZ-13 zeolite model as an isolated Lewis acid site (blue), a paired Lewis-Brønsted acid site (red) and for an hydrated Ag^+ in Ag-SSZ-13 (cyan) are shown in Figure 4.2. The cationic nature of Ag in the vicinity of the Al anionic site is verified by Bader charges of +0.75, consistent with those reported in literature.^{157,158} The spectra have LMCT features at 210-220 nm and broader features in the 250-350 nm range. These features are attributed to $4d^{10} \rightarrow 4d^9 5s^1$ transition of a trigonally coordinated Ag^+ ion.¹⁵⁴ Texer and coworkers suggested that the broader features at 250 nm could also be attributed to the ligand field effects of the primary hydration sphere around Ag^+ .¹⁵⁶ This interpretation is congruent with coordination of water

molecules around the isolated and highly reactive Ag^+ sites in ZSM-5. The secondary features for the simulated spectra do not align at the same wavelength as that for the experimentally measured spectra. This divergence is not unexpected and could be attributed to the ideal treatment of the core-hole excitonic effects in the simulations and temperature dependent variations in local structure around the Ag^+ Lewis acid. It must also be pointed out here that the simulations have been performed for Ag-SSZ-13 periodic unit cells, and some differences in the binding of Ag to SSZ-13 and to ZSM-5 are expected. These differences are subtle and evident in the lack of complete agreement in Bader charges of Ag in SSZ-13 and ZSM-5 in Figure 4.2. Considering all approximations, the simulations of the UV-Vis spectra for isolated Ag^+ ions agree well with that of the experimentally measured samples.

The active site of Ni in Ni-zeolites for C_2H_4 dimerization has been identified as a $[\text{Ni-C}_2\text{H}_4\text{-H}]^+$ motif, with an agostic H atom binding to the Ni^{2+} species during the pretreatment of the catalyst. This motif is responsible for the initial activation of ethylene and its subsequent dimerization via the Cossee-Arlman mechanism.^{153,159} An analogous $[\text{Ag-H}]^+$ -SSZ-13 motif was also modeled and its absorption spectra was calculated. The features exhibited by the UV-Vis spectra for AgH-SSZ-13 are similar to that of the Ag-SSZ-13 motifs and the Bader charge of +0.69 suggests that the feature at 220 nm is a fingerprint of Ag^+ in the zeolite with a small charge transfer to the agostic H atom. However, the absence of secondary features at 250-350 nm suggests that the LMCT transitions differ for a tetrahedrally coordinated Ag^+ ion, as seen in AgH-SSZ-13. Finally, the spectra for a 3 atom Ag-cluster in the vicinity of a Brønsted acid was calculated to identify features that identify metal/metal-cluster formation. The metallic nature of the cluster is confirmed by an average Bader charge of 0.14. The spectra corresponding to the Ag clusters consist of multiple features, particularly at higher

wavelengths. The broad feature at ~ 405 nm for Ag-ZSM-5 synthesized by incipient wetness impregnation in Figure 4.1 b can now be confirmed as a feature originating from metallic Ag in the zeolite.

The measured UV-Vis spectra correspond to the net absorbance of an ensemble of photo-active Ag species, and our UV-Vis simulations provide reasonable evidence for the presence of Ag^+ ions in the zeolite as the dominant Lewis acid sites. While these sites are likely coordinated with H_2O molecules in ambient conditions, water is not expected to exist after pretreatment or during ethylene dehydroaromatization experiments.

X-Ray Absorption Spectroscopy

The presence of isolated cationic Ag^+ species as Lewis acids in Ag-ZSM-5 were supported by Ag K-edge X-ray absorption spectroscopy (XAS). The Ag K-edge energies for $\text{Ag}_{0.08}$ -ZSM-5, $\text{Ag}_{0.48}$ -ZSM-5, Ag_2O are given in Table 4.2, and the corresponding XANES spectra including that of Ag-foil are shown in Figure 4.3. The edge energies for the Ag-ZSM-5 samples with Ag loadings (Ag/Al) of 0.08 and 0.46 agree with that of Ag_2O confirming that all Ag in the zeolite are in the form of exchanged univalent cations coordinated to O atoms. The divergence in peak features and maxima in the Ag-foil, Ag_2O and Ag_x -ZSM-5 samples ($x=0.08, 0.46$) in the range of 25510-25540 eV suggest that the binding geometry of Ag to its neighboring O atoms in ZSM-5 is indeed different from that in Ag-foil and Ag_2O . The first coordination shell in Ag_2O consists of Ag–O bonds, followed by a second coordination shell of Ag–Ag bonds. Shibata and coworkers investigated the active structure of Ag species in ZSM-5 catalysts. The XANES obtained for the Ag_x -ZSM-5 samples characterized in this work agree well with those obtained for Ag-ZSM-5, Ag-MOR and Ag_2SO_4 in the work of Shibata and Abney.^{154,160} Ag in Ag_2SO_4 is coordinated to 6 O atoms in its first coordination

Table 4.2. Ag K-edge ex-situ XANES edge energies of Ag_2O and $\text{Ag}_x\text{-ZSM-5}$ samples ($x=0.08, 0.46$) measured at ambient conditions.

Sample	Edge Energies (eV)
Ag_2O	25514.7
$\text{Ag}_{0.08}\text{-ZSM-5}$	25514.7
$\text{Ag}_{0.46}\text{-ZSM-5}$	25514.7

shell and is a representative standard for an Ag^+ ion surrounded by O atoms and its XANES spectra agrees well with that of the $\text{Ag}_x\text{-ZSM-5}$ samples. Overall, the XANES spectra of the $\text{Ag}_x\text{-ZSM-5}$ samples indicate the absence of Ag-Ag bonds and the presence of Ag^+ as isolated Lewis acids coordinated to O atoms.

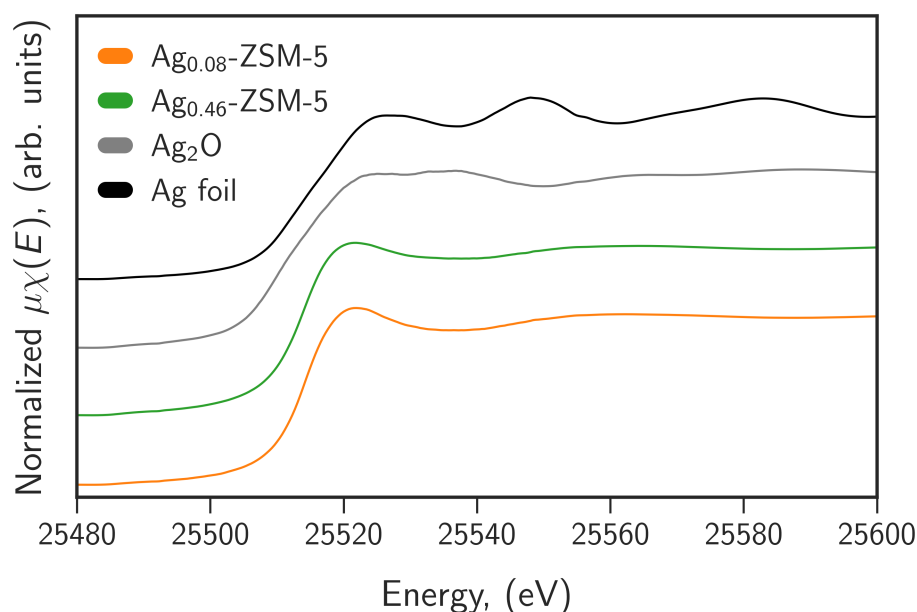


Figure 4.3. Normalized Ag K-edge X-ray absorption near edge spectra (XANES) for Ag-ZSM-5 samples collected ex-situ at ambient conditions.

Further evidence of the isolated nature of Ag^+ in ZSM-5 was obtained from the Fourier transform of the k^2 -weighted EXAFS spectra of the $\text{Ag}_x\text{-ZSM-5}$ and Ag-foil and Ag_2O samples collected under ambient conditions. The FT-EXAFS for these samples are given in Figure 4.4. The samples containing Ag^+ show

dominant features at ~ 2 Å in the R -space due to the backscattering of the ejected photoelectron from the O atoms coordinated to the central Ag atom. The FT-EXAFS of Ag_2O consists of an intense peak at ~ 1.9 Å that corresponds to the same Ag–O coordination shell as in Ag-ZSM-5. Less-intense peaks at ~ 2.2 Å are due to scattering within second coordination shell (Ag-O-Ag linkages) and at ~ 2.7 Å due to the third Ag-Ag coordination shell. A prominent feature at the same distance is also observed for the Ag-foil FT-EXAFS, and the absence of these features in the spectra of the Ag_x -ZSM-5 samples confirms the isolated nature of the Ag^+ exchanged into the zeolite.

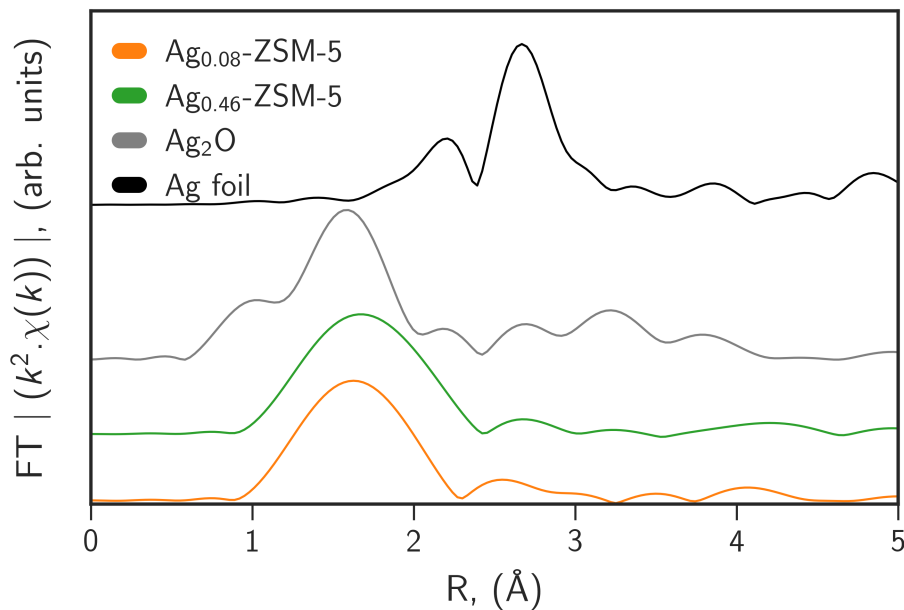


Figure 4.4. Fourier transforms of k^2 -weighted EXAFS spectra of $\text{Ag}_{0.08}$ -ZSM-5, $\text{Ag}_{0.46}$ -ZSM-5, Ag_2O and Ag foil collected at ambient conditions.

First-coordination shell fits to the phase-corrected spectra were obtained for Ag_x -H-ZSM-5 and Ag_2O samples and the corresponding fitting parameters are given in Table 4.3. The Ag^+ cation is coordinated to approximately 4 O atoms in both the $\text{Ag}_{0.08}$ - and $\text{Ag}_{0.46}$ -H-ZSM-5 samples at a separation of 2.34 Å, in excellent agreement with the Ag-O bond length of 2.36 Å in the theory generated

Table 4.3. Parameters obtained from EXAFS-fits to FT-EXAFS of $\text{Ag}_x\text{-ZSM-5}$ ($x=0.08, 0.46$) and Ag_2O samples at ambient conditions.

Sample	$\text{Ag}_{0.08}\text{-ZSM-5}$	$\text{Ag}_{0.46}\text{-ZSM-5}$
N	4.2 ± 0.71	3.8 ± 1.29
ΔE_0	1.38 ± 1.14	1.12 ± 2.51
R	2.32 ± 0.01	2.34 ± 0.003
σ^2	0.019 ± 0.003	0.022 ± 0.007

Ag-ZSM-5 periodic unit cell. This local structure can be rationalized by taking into account the presence of moisture at ambient conditions with H_2O molecules coordinating to the Ag^+ cation in the ZSM-5 sample. The presence of an H_2O -coordinated Ag^+ Lewis acid can be confirmed through the work of Yamaguchi and coworkers, who investigated the structure of 1.5 M AgNO_3 confined in the pores of MCM-41 zeolite using EXAFS and found that a Ag^+ ion is stabilized in a four-fold coordination of O atoms in the system at a bond distance of 2.3 Å.¹⁶¹

Water molecules bind strongly to the Ag^+ Lewis acid site with a high coverage structure of 4 molecules adsorbed with a $\Delta G = -0.28$ eV per atom of H_2O . The bond lengths of $\text{Ag-O}_{\text{H}_2\text{O}}$ however, increase with H_2O coverage to 2.5 Å and deviate from the bond lengths predicted by the EXAFS fit. Inexact agreement in interatomic distances between DFT and EXAFS fits are expected and well-documented. They are attributed to the high degree of thermal and structural disorder in highly dispersed metal species and result in underestimated interatomic distances from EXAFS.¹⁶² Overall, the XANES, FT-EXAFS and EXAFS-fitting Ag^+ cation binds to a framework oxygen, thus charge-balancing the anionic site of the zeolite with the rest of the coordination shell satisfied by adsorbed H_2O molecules.

Temperature-programmed Desorption

The presence of hydrated Lewis acid sites in Ag-H-ZSM-5 were confirmed by temperature programmed desorption (TPD) experiments. The temperature

program was set up to obtain a measure of the initial baseline corresponding to the ratio for H₂O at 35 °C (308 K). These measurements were used to baseline correct the pulse responses recorded during the temperature ramp of 5 °C/min. This protocol accounts for the increase in background for $m/z = 18$ during the desorption of H₂O. The zeroth moments of the pulse responses were then converted to equivalent molar quantities, and the resulting TPD spectra for all samples analyzed are given in Figure 4.5.

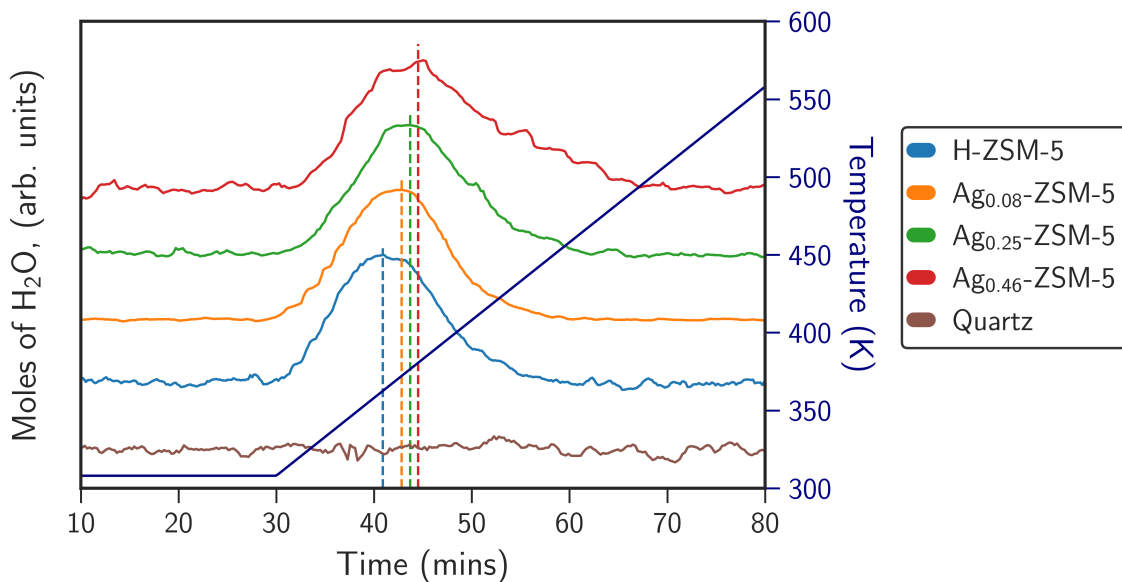


Figure 4.5. TPD spectra for quartz (brown), H-ZSM-5 (blue), Ag_{0.08}-ZSM-5 (orange), Ag_{0.25}-ZSM-5 (green) and Ag_{0.48}-ZSM-5 (red) for temperature ramps of 5 °C/min.

The TPD spectra for all catalyst samples except that of quartz show one prominent H₂O desorption feature that develops as the temperature ramp is initiated. Upon further heating, desorption of H₂O continues for all ZSM-5 samples and encounters a maximum, as indicated by the dashed lines in Figure 4.5. The pulse responses for $m/z = 18$ in Figure 4.5 show that in addition to an enhanced baseline due to continuous desorption of H₂O, molecules also desorb as pulses suggesting that the pulsing of He aids in dislodging H₂O molecules from within

the pores of the zeolite. The peak temperature is lowest for H-ZSM-5 and shows a moderate increase with Ag loading. The H₂O signal for H-ZSM-5 tails off at ~450 K while the Ag-ZSM-5 samples continue to desorb water at even higher temperatures.

The TPD profile for Ag_{0.08}-H-ZSM-5 is similar to that of H-ZSM-5 in its onset temperature, but differs in the temperature at which the peak rate of H₂O desorption occurs. This is consistent with the stronger binding of H₂O to the previously identified isolated Ag⁺ Lewis acid sites in Ag-H-ZSM-5 as compared to the H⁺ Brønsted acid sites. The cleavage of stronger Ag–H₂O bonds requires higher temperatures, and the apparent increase in peak temperature from 362 K for H-ZSM-5 to 372 K is consistent with this hypothesis. The TPD spectra for Ag-H-ZSM-5 with higher silver loadings (Ag/Al) of 0.25 and 0.46 also show a monotonic increase in peak temperatures, with the highest rate of desorption occurring at 375 K for Ag_{0.25}-ZSM-5 and 383 K for Ag_{0.46}-ZSM-5. Analogous DFT-calculated free energies of adsorption of H₂O at the H⁺ Brønsted acid and Ag⁺ Lewis acid sites as a function of active site coverage are given in Figure 4.6. Both acids sites show stronger stabilization of a single H₂O in the vicinity of the acid sites and increasing the number of H₂O molecules reduces the overall stability of the system with the overall energy converging to that of a H₂O molecule in a zeolite pore (dashed line).

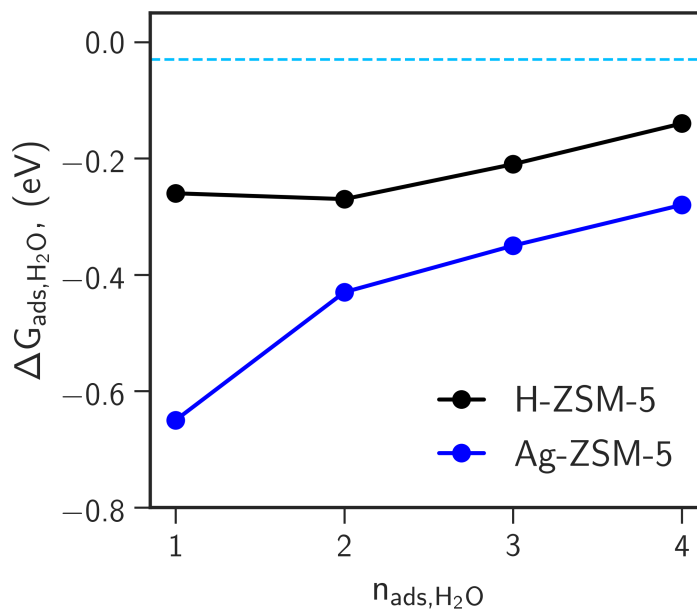


Figure 4.6. Free energies of adsorption of H_2O ($\Delta G_{\text{ads,H}_2\text{O}}$) in the vicinity of the Brønsted and Lewis acid sites in H-ZSM-5 (black) and Ag-ZSM-5 (blue) periodic cell models as a function of the number of molecules adsorbed.

Additional evidence for H_2O strongly bound to Ag^+ is seen in the elongated tails in the spectra for $\text{Ag}_{0.25}\text{-ZSM-5}$ and $\text{Ag}_{0.46}\text{-ZSM-5}$, which show H_2O desorbing at temperatures of 500 K. The elongated feature also appears to be a function of the Ag loading of the zeolite, which could be rationalized by the proportional increase in strong binding sites in the zeolite. Overall, the detection of H_2O during the temperature ramp supports the local geometry predicted by the EXAFS-fitting and UV-Vis spectroscopy, with H_2O molecules coordinating to the highly active Ag^+ species at ambient conditions. Upon pretreatment in inert conditions at elevated temperatures of (823 K) 550 °C, these H_2O molecules desorb and activate the catalyst for ethylene activation and upgrade.

4.4.2. Evaluation of Catalytic Activity

Transient kinetics experiments of H-ZSM-5, Ag_x-H-ZSM-5 (Ag/Al = x = 0.08, 0.25, 0.46) and Ag_{0.08}-Na-ZSM-5 with zeolite silicon-to-aluminum ratio (SAR) \sim 12 were performed on the TAP reactor at a reaction temperature of 400 °C. This temperature was chosen because of the excellent activity exhibited by similar Ag-ZSM-5 catalysts in previously published flow catalytic results.²⁹ The pulse valve was tuned such that $\sim 3 \times 10^{-7}$ moles of ethylene entered the microreactor per reactant pulse. Janda and coworkers characterized the commercially available H-ZSM-5 catalyst (Zeolyst International, CBV 2314) to contain 7.34 Al per unit cell and 7.24 H⁺ per unit cell.¹⁵² Using this metric, 10 mg of H-ZSM-5 would contain 1.26×10^{-5} moles of H⁺ and Ag_x-H-ZSM-5 catalysts would consist of proportional concentration of Brønsted and Lewis acid sites defined by the silver loading (Ag/Al). The approximate measure of overall acid site concentration while accounting for factors such as sites inaccessible for reaction indicate that moles of active sites outnumber the moles of ethylene available for reaction by a factor of \sim 40. Considering the bimolecularity of ethylene dimerization, the primary reaction, the hydrocarbon chemistry within the zeolite pores is severely reactant-limited under these reaction conditions. Any products formed are likely due to intrinsic catalytic activity or zeolite-controlled confinement effects.

The height-normalized pulse responses for unreacted ethylene ($m/z = 28$) collected over 100 pulses are given in Figure 4.7. Signals measured at this ratio also contain contributions from fragments of higher hydrocarbons that are formed during the reaction, diffuse out of the microreactor and ionize at the MS filaments. However, the yield of products with fragments at $m/z = 28$ are relatively insignificant compared to the moles of unreacted ethylene and therefore, do not affect any qualitative analysis performed on the pulse responses. Height-normalization enables the visual inspection of pulse response features such as the rise, peak time

and tail. Figure 4.7 depicts the differences in the ethylene pulse responses for five catalyst beds at 400 °C. The signal attains baseline within 0.8 s of data collection for inert silica and H-ZSM-5. However, exchange of Ag⁺ into H-ZSM-5 drastically increases the tail of the ethylene pulse which takes up to ~6 s to attain baseline signals.

On the other hand, ethylene pulses are only modestly delayed when Ag⁺ is exchanged into Na-ZSM-5, with the signals attaining the baseline within ~1.2 s. Overall, it appears that isolated Ag⁺ atoms in Ag_{0.08}-H-ZSM-5 and Ag_{0.08}-Na-ZSM-5 bind ethylene strongly due to the delayed desorption characteristics, but the effect is much more pronounced for Ag_{0.08}-H-ZSM-5. The drastic difference in pulse response tails between Ag_{0.08}-H-ZSM-5 and Ag_{0.08}-Na-ZSM-5 points to proximity-effects or synergistic interactions of the Brønsted and Lewis acid sites (H⁺–Ag⁺) with ethylene.

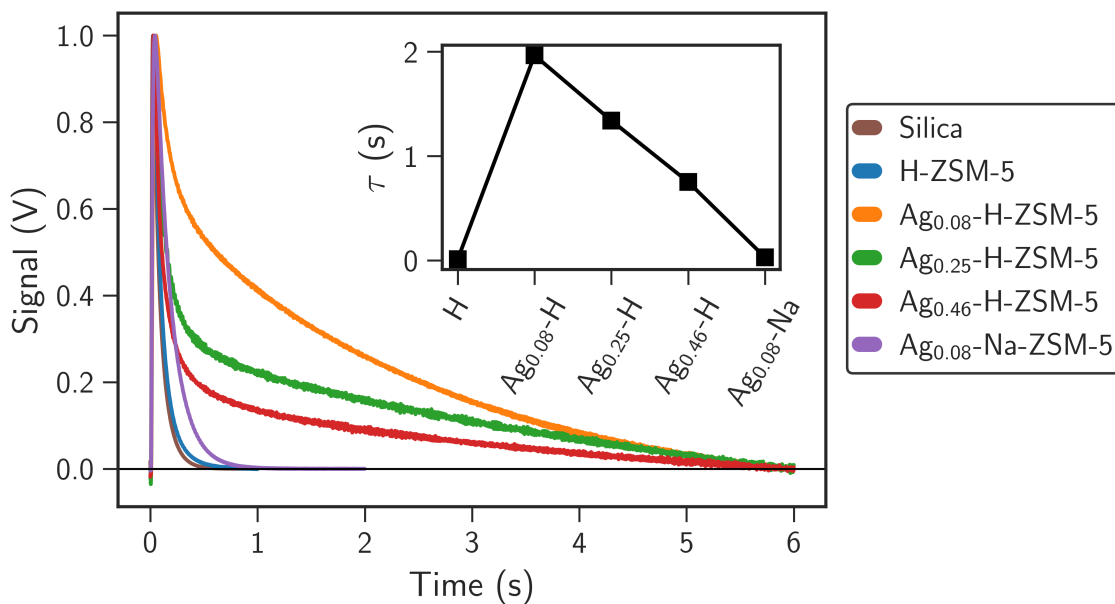


Figure 4.7. Height-normalized pulse responses for ethylene ($m/z = 28$) exiting the microreactor for various catalyst samples (color indicated in the legend). Inset depicts the mean residence time (τ) for ethylene pulses.

A quantitative measure of the interaction of ethylene with the catalyst beds

is the mean residence time or the first moment of the pulse response calculated as . The mean residence time was calculated for height-normalized pulse responses and therefore, represents the contact time of ethylene with the zeolite sample. The inset of Figure 4.7 charts the mean residence times (τ) for H-ZSM-5, $\text{Ag}_x\text{-H-ZSM-5}$ ($x = 0.08, 0.25$ and 0.46) and $\text{Ag}_{0.08}\text{-Na-ZSM-5}$. Incorporation of Ag^+ into 8% of the available Al anionic sites results in a 166-fold increase in τ from 8 ms in H-ZSM-5 to 1.96 s in $\text{Ag}_{0.08}\text{-H-ZSM-5}$, respectively. Increasing Ag-loading (Ag/Al) to 0.25 and 0.46 decreases τ to 1.34 s and 0.76 s. In contrast, a pulse of ethylene spends only ~ 31 ms in $\text{Ag}_{0.08}\text{-Na-ZSM-5}$ and the huge disparity between Ag-Na and Ag-H for Ag/Al = 0.08 suggests that while Ag^+ does indeed bind ethylene strongly, the origin of the delayed tail in the Ag-H-ZSM-5 catalysts is cumulative of interactions of ethylene with a synergistic Brønsted acid chemistry. Notably, the concentration of Ag^+ (Ag/Al = 0.08) shows the highest residence time indicating the existence of a residence time maximum. Previously, we had reported that the same loading of Ag/Al = 0.08 results in the highest selectivities to aromatic hydrocarbons (benzene, toluene and xylene) from ethylene.²⁹ Similar aromatic-selectivity – metal-loading relationships have also been reported for the methanol to olefins reaction over Zn-ZSM-5.¹³⁴ Overall, these studies strongly indicate that the extent of metal-exchange can be used to optimize catalytic performance.

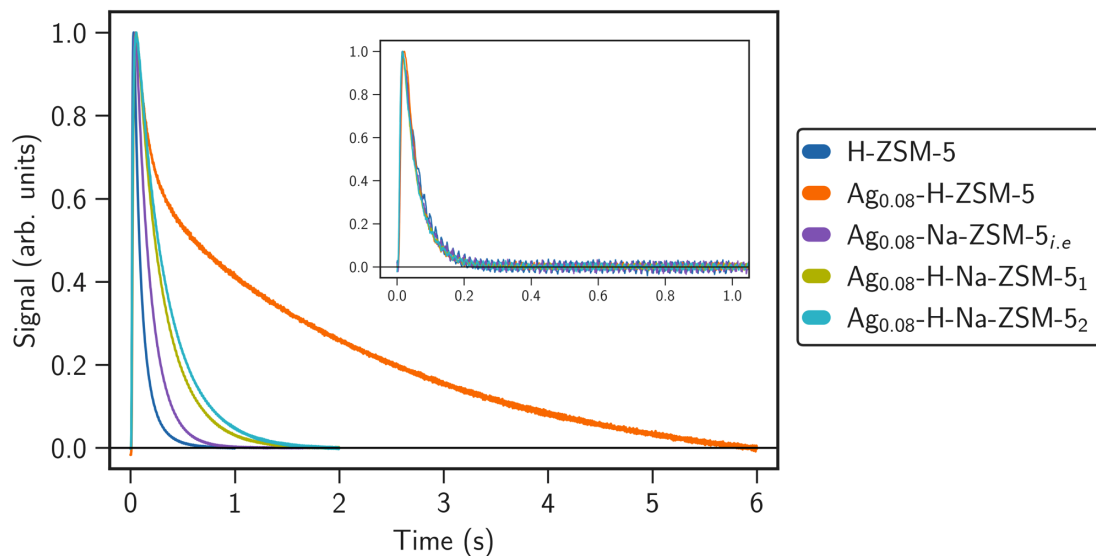


Figure 4.8. Height normalized ethylene (helium in inset) pulse responses exiting the microreactor for H-ZSM-5, Ag_{0.08}-Na-ZSM-5 and the Ag-H-Na-ZSM-5 physical mixtures (colors indicated in the figure legend).

To understand the origin of delay of ethylene pulses over the Ag_{0.08}-H-ZSM-5, additional experiments were performed over two Ag-H-Na-ZSM-5 catalyst beds prepared as physical mixtures of H-ZSM-5 and Ag_{0.08}-Na-ZSM-5 such that the ratio of H⁺/Ag⁺ remained the same as in Ag_{0.08}-H-ZSM-5. The first bed (Ag_{0.08}-H-Na-ZSM-5₁) consisted of a 10 mg mixture of H-ZSM-5 and Ag_{0.08}-Na-ZSM-5 (250-400 μ m) particles while the second bed (Ag_{0.08}-H-Na-ZSM-5₂) consisted of 10 mg of pelleted, crushed and sieved particles formed by mixing as-synthesized and fine H-ZSM-5 and Ag_{0.08}-Na-ZSM-5 powders. These mixtures are essentially catalysts that contain both Brønsted and Lewis acid sites that are in macroscopic proximity of each other. The physical characteristics such as the porosity, tortuosity, pore volume and surface areas remain unchanged, as seen in the height-normalized pulse responses for helium in the inset of Figure 4.8, and the changes in ethylene pulse responses seen in Figure 4.8 are solely due to reactivity. This confirms our initial observation that the delayed desorption

and stronger interaction of ethylene arise from the simultaneous presence of Ag^+ cations and active Brønsted acid chemistry. The peak tailing decreases as the average separation between H^+ and Ag^+ ($d_{\text{Ag}^+ - \text{H}^+}$) increases in samples containing both types of acid sites i.e. $\text{Ag}_{0.08}\text{-H-ZSM-5} > \text{Ag}_{0.08}\text{-H-Na-ZSM-5}_1 > \text{Ag}_{0.08}\text{-H-Na-ZSM-5}_2$. These trends do not explicitly rule out an $\text{H}^+ - \text{Ag}^+$ acid site synergy within the same pore or ring within the zeolite, but in general suggests that ethylene interacts strongly at the Ag^+ sites with reaction intermediates formed at the Brønsted acid sites.¹⁶³ Furthermore, the trends in pulse response tails suggest that these intermediates, commonly known as carbenium ions, are mobile, reactive and interact with diffusing ethylene at finite length and time scales.

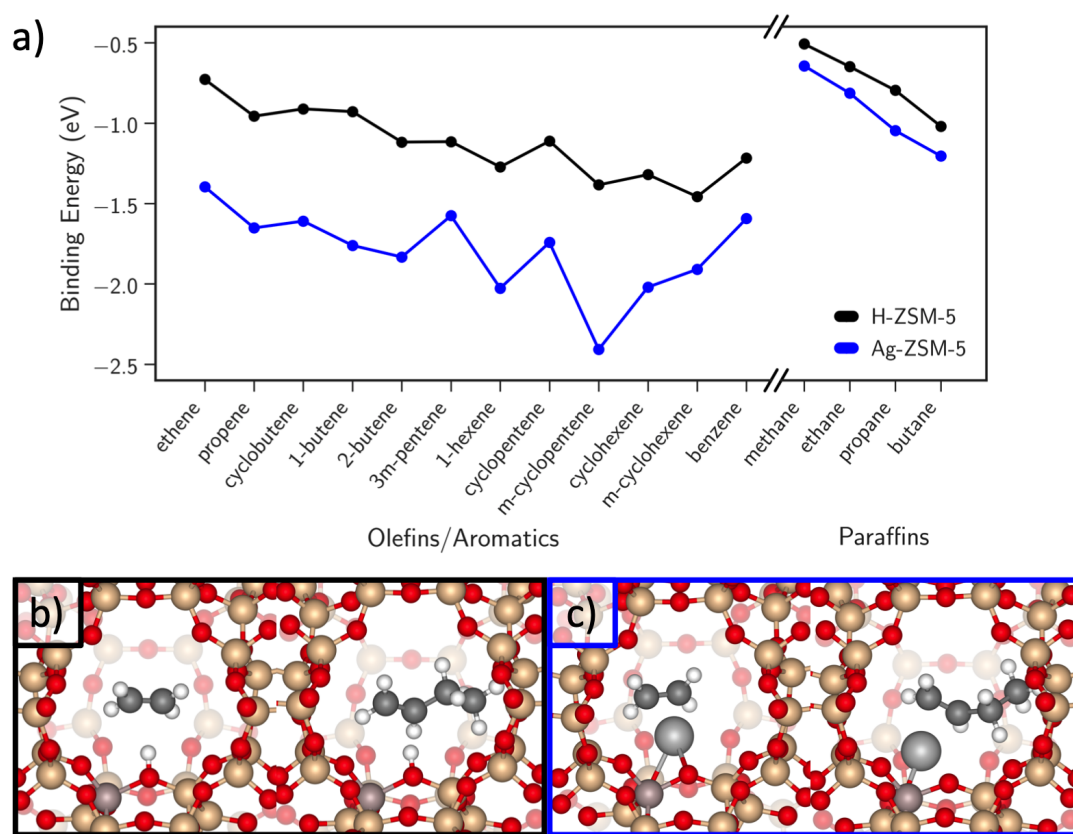


Figure 4.9. a) Binding energies in eV of olefins and paraffins to Ag^+ (blue) and H^+ (black). Visualizations of the π -bonded geometries through which ethylene and 1-butene bind to b) Ag^+ and c) H^+ acid sites in a ZSM-5 periodic cell.

Typically observed intermediates in hydrocarbon chemistries in zeolites include higher olefins, paraffins and aromatics. Figure 4.9 a shows the DFT-calculated binding energies for olefins, benzene and light paraffins that are known to form in typical zeolite hydrocarbon chemistries.^{18,23} The binding strength of all olefins and paraffins to both Brønsted and Lewis acid sites become stronger with increasing carbon number, with olefins binding more strongly than paraffins. This behavior is consistent with metal–alkene complexes commonly found in organotransition metal chemistry and are well described by the Dewar-Chatt-Duncanson model of binding.¹⁶⁴ The olefin donates electron density from its π -orbital and concomitantly receives π^* -backbonding electron density from the filled d -orbitals of the Ag^+ atom. This redistribution of the olefin electron density into its antibonding orbitals weakens the C=C bond and reduces the bond order. Therefore, the presence of isolated Ag^+ atoms help electronically stabilize and partially activate the C=C bond of ethylene and other higher olefins. Binding of olefins to the Brønsted acid site also proceed through π -complexes that are weakly bound to the acid site.¹¹³ Example visualizations of the binding of ethylene and 1-butene to the H^+ and Ag^+ site are given in figure Figure 4.9 b. Finally, paraffins appear to be stabilized by only zeolitic confinement effects and van der Waals interactions and in general, show weaker binding than the π -bonded olefins.

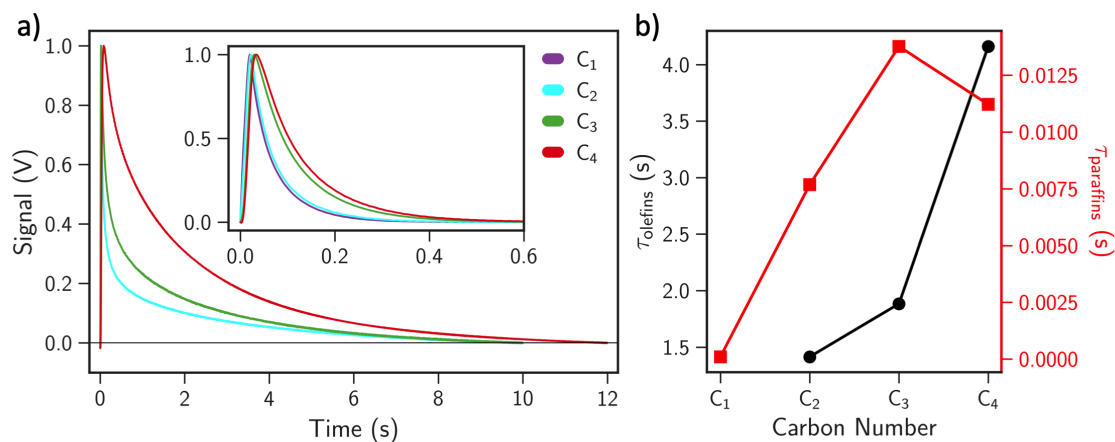


Figure 4.10. a) Height-normalized pulse responses for α -olefins and paraffins (inset). b) depicts the mean residence times of the pulses in a) as a function of carbon number for α -olefins in black and for alkanes in red.

TAP pulse responses collected over Ag_{0.08}-H-ZSM-5 for higher olefins (ethene, propene and 1-butene) and paraffins (methane, ethane, propane and butane) confirm the strongly interacting nature of olefins in comparison to paraffins. The height-normalized average pulse responses and their corresponding mean residence times (τ) are shown in Figure 4.10 a and b. The delayed desorption characteristics of ethylene are shown by higher olefins (propene and butene) and can take up to 12 s to completely exit the microreactor. The observations of strong olefinic interaction with a catalyst consisting of both Brønsted and Lewis acid sites also remain. The mean residence times increase with carbon number and the increasing trends are consistent with the slower diffusion and higher reactivity of higher olefins. On the other hand, the signal for paraffins attain their baselines within 0.7 s of data collection, indicating a weak interaction with the active sites in Ag_{0.08}-H-ZSM-5. Mean residence times for paraffins are two orders of magnitude shorter and negligibly interact with the catalyst bed and diffuse rapidly out of the pores of the zeolite.

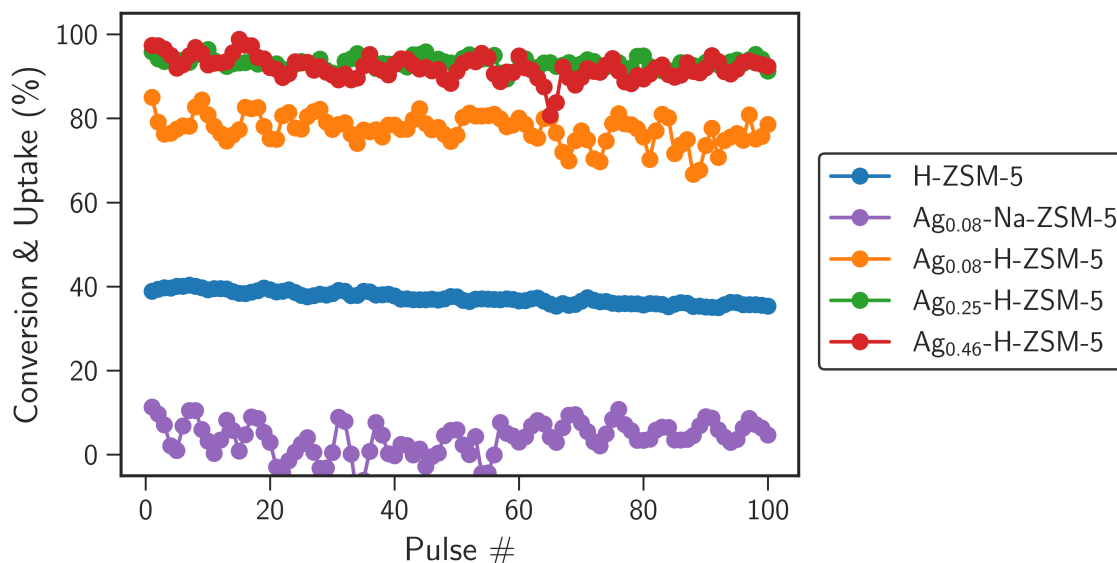


Figure 4.11. Conversion and uptake (X) as a function of pulses. Colors refer to catalysts indicated in the figure legend.

The catalytic consequences of enhanced interactions and longer residence time of ethylene in the selected catalysts were evaluated under the transient reaction conditions. Figure 4.11 charts ethylene conversion and uptake (X) as a function of pulses admitted for replicate experiments performed over 10 mg of catalyst at 400 °C. The unique reaction conditions necessitate the need to include ethylene uptake along with the traditional definition of conversion due to incomplete carbon balances observed for all experiments. All catalysts exhibit conversions that are mostly impervious to pulses admitted with an $\sim 3\%$ drop over 100 total pulses. Amongst the catalysts containing Brønsted acid sites, X increases with Ag loading while the Ag_{0.08}-Na-ZSM-5 sample is the least active catalyst with an average conversion of $\sim 5\%$. There are no obvious non-uniformities in conversion profiles for any sample, indicating that ethylene consumption from the first pulse onwards is steady. These trends coupled with the reactant-limited nature of experiments suggest that non-selective deactivation of the catalyst takes place and any uptake or build-up of hydrocarbons appears to minimally affect

the reactivity of the acid sites in the zeolites over 100 total pulses.¹⁰⁵

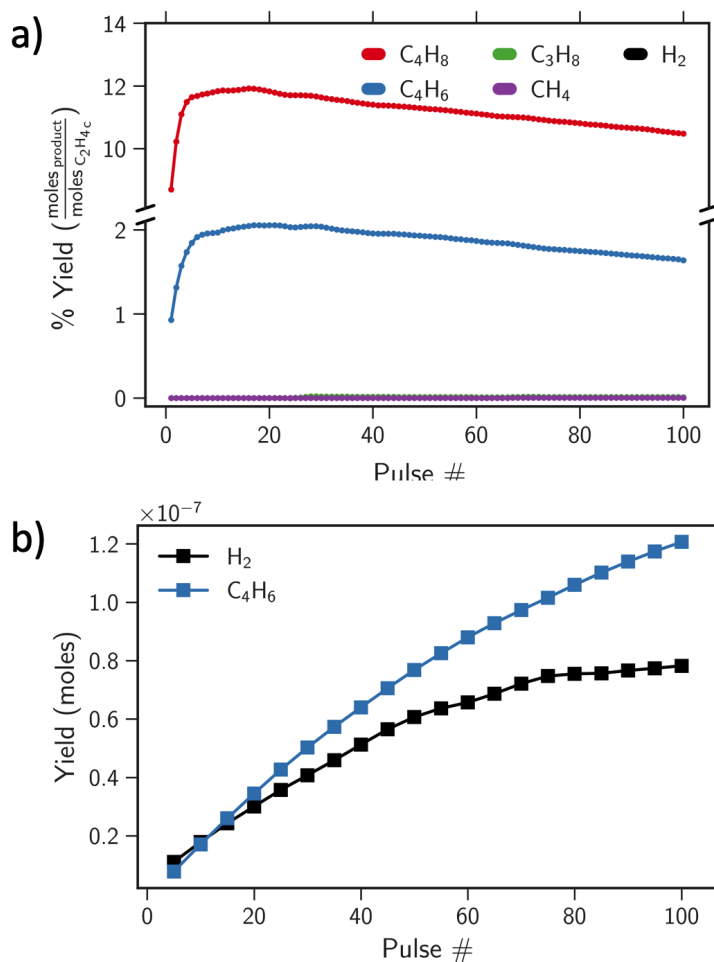


Figure 4.12. a) Percentage yields for 100 ethylene/helium pulsed over 10 mg of H-ZSM-5 at 400 °C. b) charts the yields of 1,3-butadiene and hydrogen as a function of pulse admitted.

To elucidate the roles of the H⁺ Brønsted acid and the Ag⁺ Lewis acid sites in all samples, the percentage yields of products per mole of ethylene consumed were obtained by defragmenting the zeroth moments of pulse responses collected from TAP experiments performed for all catalyst samples under consideration. Based on the products detected in preliminary experiments only five m/z ratios for butene (41), 1,3-butadiene (39), propane (29), methane (16) and hydrogen (2) were monitored. The corresponding percentage yields obtained over H-ZSM-5 are

given in Figure 4.12 a. The defragmentation quantifies only the primary product of ethylene oligomerization i.e. butene, and its dehydrogenation products 1,3-butadiene (C_4H_6) and hydrogen. The absence of other hydrocarbons confirms the transient nature of reaction with a negligible extent of secondary reaction attained over 100 pulses. Interestingly, the cumulative yield of 1,3-butadiene for the first 20 pulses follows that of hydrogen (Figure 4.12 b) suggesting that a fraction of butene formed undergoes dehydrogenation to form 1,3-butadiene and hydrogen. The formation of butene and 1,3-butadiene as primary reaction products is inconsistent with a similar investigation into the conversion of ethylene to aromatics over H-ZSM-5 published by Batchu and coworkers, who reported the detection of higher olefins (pentene, hexene) and aromatics (benzene and ethylbenzene).¹⁶⁵ An important difference, however, is that in our experiments each pulse admits $\sim 3 \times 10^{-7}$ moles of ethylene compared to 1.3×10^{-6} moles admitted in their work. Pulses of higher intensity could potentially alter the regime of reaction and in theory, facilitate an ~ 1600 -fold increase in rate of oligomerization which is a bimolecular reaction. Therefore, the results obtained in our work are not directly comparable with those published by Batchu and coworkers.

To assist the interpretation of TAP data, ethylene dimerization mechanisms were investigated by modeling the activation and subsequent oligomerization of ethylene at the H^+ Brønsted acid sites using DFT. All reaction intermediates were modeled at the T-12 site allowing for sufficient void space to accommodate the larger cationic complexes formed during oligomerization.¹⁶⁶ As seen in Figure 4.9 b, ethylene prefers to bind to the Brønsted acid site through a weakly bound π -complex with a binding free energy of -0.74 eV in reference to an isolated ethylene molecule in the gas phase. The free energy of stabilization includes the effect of van der Waals interactions, entropy loss and changes in zero-point energy. To investigate pathways for the formation of 1-butene and 2-butene we

considered two ethylene molecules co-adsorbed in the vicinity of H^+ as the initial state. Of the pair, one ethylene molecule accepts the Brønsted acid proton with a free energy barrier (ΔG^\ddagger) of 1.54 eV forming an ethoxide. This value compares well with a of 1.60 eV reported in literature.¹¹³ The complete free energy diagrams for the dimerization of ethylene to 1-butene and 2-butene, and dehydrogenation of 1-butene to 1,3-butadiene are given in Figure 4.13. We also considered an alternate pathway for ethylene activation through the cleavage of a C–H bond of ethylene, followed by proton addition and elimination of a dihydrogen molecule. This concerted mechanism has a prohibitive activation barrier of 3.14 eV forming a highly unsaturated vinyl species $[\text{CH}_2=\text{CH}]^+$. Therefore, the alkoxide pathway is expected to be favored for ethylene activation forming an active framework-bound ethoxide species. Visualizations of initial, transition and final states are provided in the Figure 4.14.

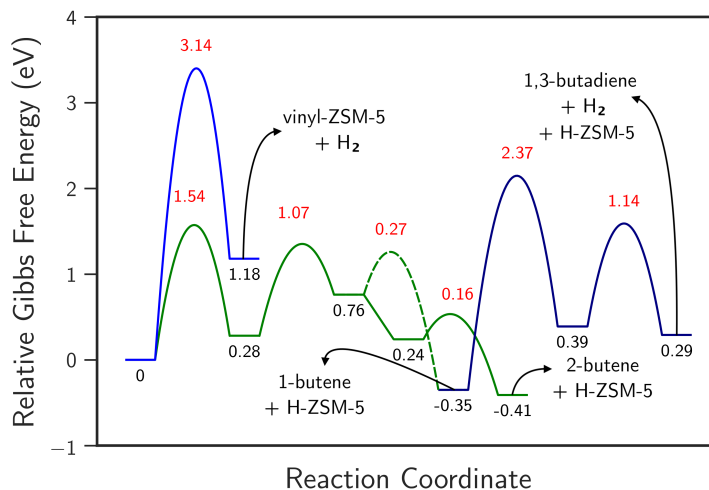


Figure 4.13. Gibbs free energy diagram for the activation and oligomerization of ethylene for H-ZSM-5 with the Brønsted acid site located at the T-12 site in a ZSM-5 periodic unit cell. Annotations in black indicate the absolute energy of stable intermediate states while those in red indicate the activation energy barriers relative to the previous stable state.

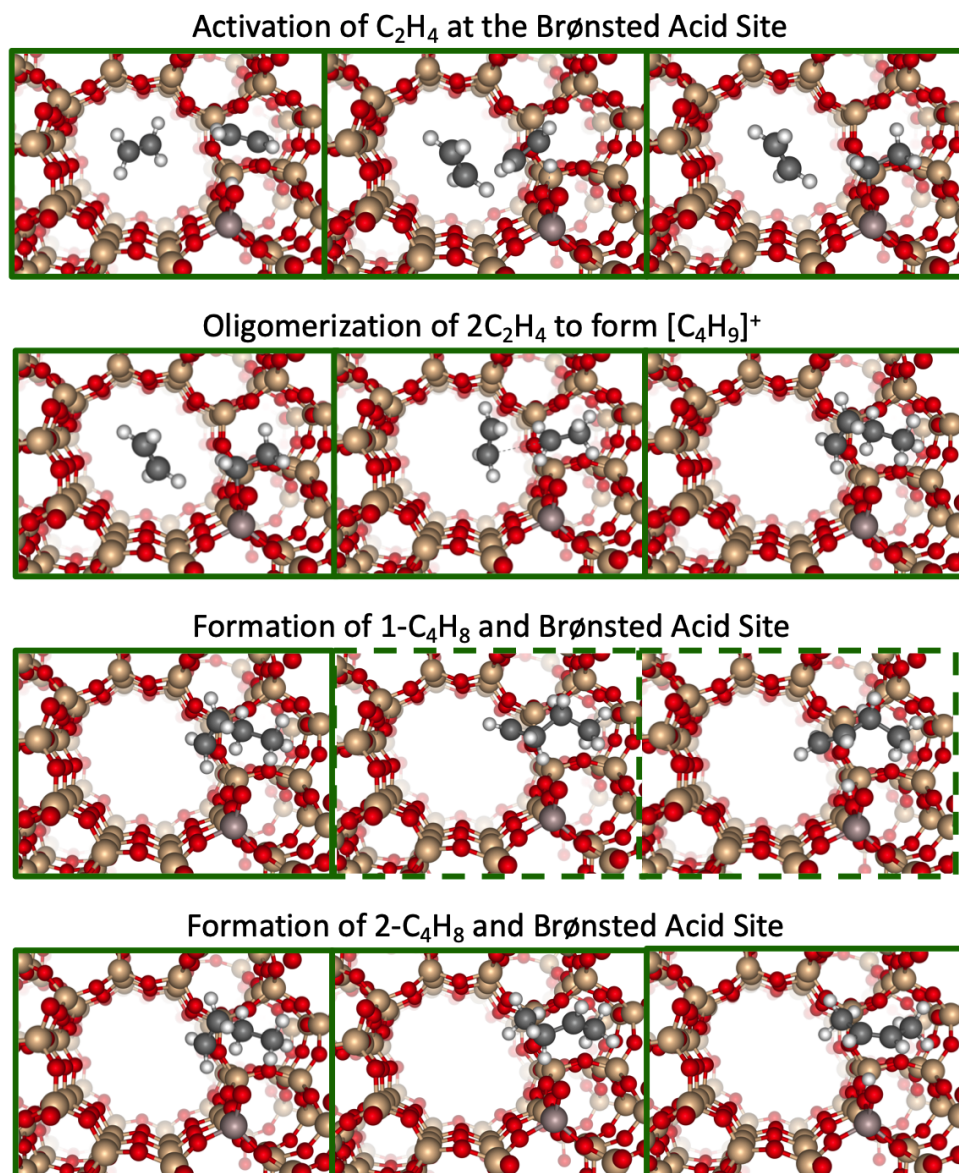


Figure 4.14. Visualizations of the initial (IS), transition (TS) and final states (FS) for intermediate steps in the activation and oligomerization of ethylene on H-ZSM-5.

Additionally, reaction mechanisms for the dehydrogenation of 1-butene forming 1,3-butadiene and hydrogen were explored. While other mechanisms cannot be excluded, we consider 1-butene dehydrogenation to 1,3-butadiene as a representative mechanism due to the desired location of a $C=C$ double bond and the potential ease of dehydrogenation of neighboring H atoms bound to the γ -

and δ -C atoms of 1-butene ($^{\alpha}\text{CH}_2=^{\beta}\text{CH}-^{\gamma}\text{CH}_2-^{\delta}\text{CH}_3$). The free energy diagram for the formation of 1,3-butadiene from 1-butene is given by the dark blue lines in Figure 4.13. Visualizations of intermediates that precede the formation of 1,3-butadiene are provided in Figure 4.15. The H atom bound to the γ -C reacts with the Brønsted acid H^+ atom with a large barrier of 2.37 eV releasing a hydrogen molecule. This is simultaneously followed by the coordination of the $[^{\alpha}\text{CH}_2=^{\beta}\text{CH}-^{\gamma}\text{CH}_2-^{\delta}\text{CH}_3]^+$ species to the framework oxygen. A H-transfer from the γ -C to the δ -C occurs forming a $[^{\alpha}\text{CH}_2=^{\beta}\text{CH}-^{\gamma}\text{CH}-^{\delta}\text{CH}_3]^+$ species with a partial double bond character and uphill in energy by 1.05 eV. The system is finally stabilized by regeneration of the Brønsted acid site from the H bound to the γ -C ($\Delta G^\ddagger = 1.14$ eV) and the formation of 1,3-butadiene ($\text{CH}_2=\text{CH}-\text{CH}=\text{CH}_2$). The barriers that precede its formation are large and reduce the likelihood that this reaction occurs. However, the detection of 1,3-butadiene in our TAP experiments indicates that either higher activation barriers are indeed surmountable at reaction conditions, or that DFT overestimates reaction barriers or an alternate mode of formation exists that requires an in-depth exploration of reaction mechanisms.

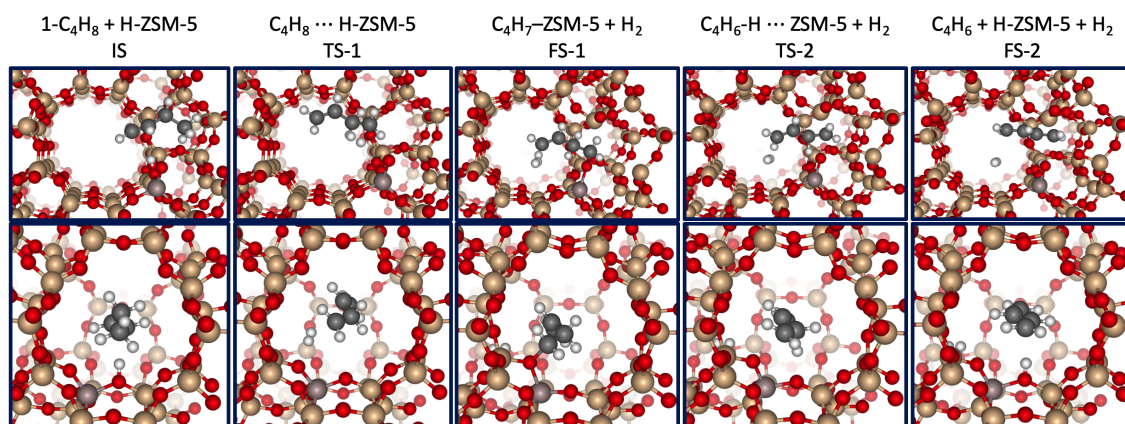


Figure 4.15. Initial, transition and final state geometries sampled in the dehydrogenation of 1-butene to 1,3-butadiene. Reaction steps are given in the annotations above each structure.

TAP and DFT results have identified Brønsted acid sites as sites that cat-

alyze ethylene oligomerization and formation of butenes and possibly 1,3-butadienes. To probe the catalytic activity of the extra-framework Ag^+ Lewis acid sites, we turn our attention to results from TAP experiments performed on $\text{Ag}_{0.08}\text{-Na-ZSM-5}$ under the same conditions, i.e. 10 mg catalyst, $n_{\text{C}_2\text{H}_4}/\text{pulse} = \sim 3 \times 10^{-7}$ moles and $T = 400^\circ\text{C}$. This catalyst is purely Lewis acidic and most of the framework Al atoms are blocked off by the post-synthetic exchange of Na^+ . Ethylene conversion and uptake profiles for this catalyst in Figure 4.11 are noisy but average around $\sim 5\text{-}6\%$ over 100 pulses. This is in stark contrast to the much higher average conversion and uptake of around $\sim 40\%$ obtained for H-ZSM-5. The averaged ethylene pulse responses in Figure 4.7 for $\text{Ag}_{0.08}\text{-Na-ZSM-5}$ are more delayed than for H-ZSM-5 and spends approximately four times longer in the catalyst. Therefore, initial observations indicate that despite the stronger interaction with ethylene, Ag^+ does not effectively activate or oligomerize ethylene to higher olefins or other hydrocarbons.

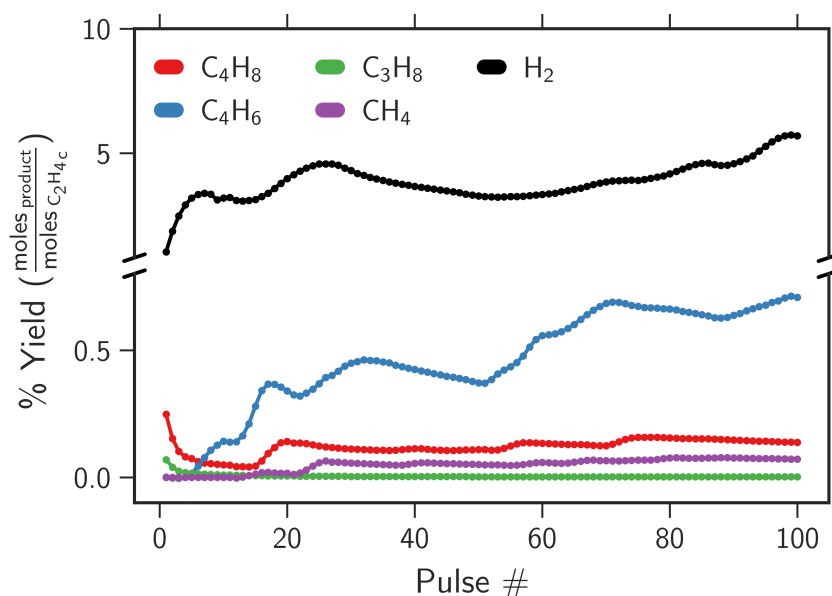


Figure 4.16. Percentage product yields obtained for 100 pulses of ethylene/helium admitted to 10 mg of $\text{Ag}_{0.08}\text{-Na-ZSM-5}$ at 400°C .

The only products detected at the MS were 1(2)-butene, 1,3-butadiene,

propane, methane and hydrogen and yields are provided in Figure 4.16. The net production of 1,3-butadiene surpasses that of 1-butene after the 5th pulse and the trends remain the same henceforth. The presence of C₄ hydrocarbons as the primary product confirms that the Ag⁺ sites do indeed activate and oligomerize ethylene to form butenes. The higher selectivity towards the dehydrogenated product, 1,3-butadiene in comparison to C₄ selectivities over H-ZSM-5 suggests that the Lewis acids also enhance rates of dehydrogenation. Hydrogen was quantified during the experiment, but unlike the results obtained for H-ZSM-5, yields of 1,3-butadiene and hydrogen are not stoichiometrically consistent. The total moles of hydrogen produced exceeds that of other products by a factor of at least ten, suggesting that unsaturated hydrocarbons accumulate in the zeolite bed. Paraffins such as propane and methane are also detected, and selectivity shifts from propane to methane after about 20 pulses. Overall, the eluting species and their respective yields indicate that in addition to ethylene dimerization, cracking and dehydrogenation pathways are promoted by Ag⁺ Lewis acid sites, rapidly accumulating hydrogen-deficient aromatics-forming precursors within the zeolite.

The increased stabilization and strong binding of ethylene at the Ag⁺ Lewis acid sites observed in TAP responses and DFT calculations do not appear to translate to enhanced catalytic activity. TAP experiments over Ag-Na-ZSM-5 show low ethylene conversions and correspondingly low yields to C₄ olefins and other products. These observations predict that in comparison to the H⁺ sites, Ag⁺ sites offer few, if any kinetically accessible pathways to dimerization. To test for these predictions, various mechanisms of ethylene activation and dimerization over an isolated Ag⁺ acid site were modeled. Reaction intermediates and pathways were modeled in a manner similar those in the work of Brogaard and coworkers, who investigated mechanisms of ethylene dimerization over Ni-AFI periodic unit cells.¹⁵³ The authors of that work concluded that the most likely

mechanism of ethylene oligomerization to butene proceeds through the Cossee-Arlman mechanism. However, this mechanism requires a Ni-H active site, and considering the pretreatment protocol followed in our work, the corresponding Ag-H active sites are not likely to form as initial active sites. Therefore, DFT calculations were limited to the “Deprotonation” and “Metallacycle” mechanisms for ethylene dimerization to butene. The free energy diagrams for the deprotonation and metallacycle mechanisms are given in Figure 4.17 a and b. Visualizations of all intermediates sampled in the deprotonation pathway are given in Figure 4.18.

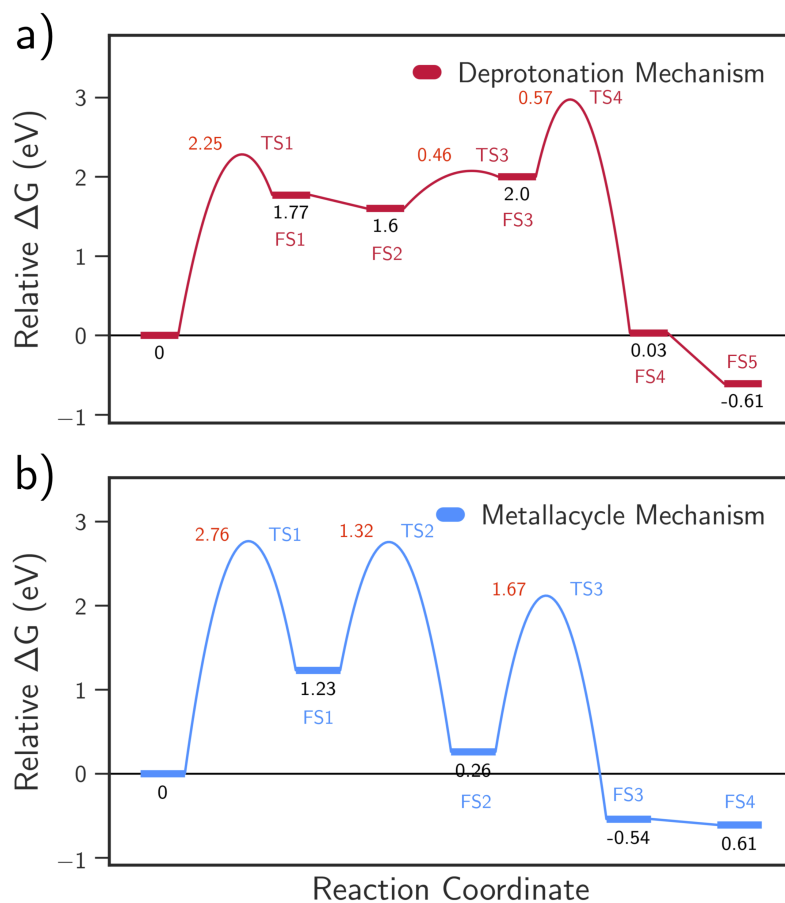


Figure 4.17. Free energy diagrams ($T = 400\text{ }^{\circ}\text{C}$ and $P = 101325\text{ Pa}$) for a) the deprotonation mechanism and b) the metallacycle mechanism for the dimerization of ethylene.

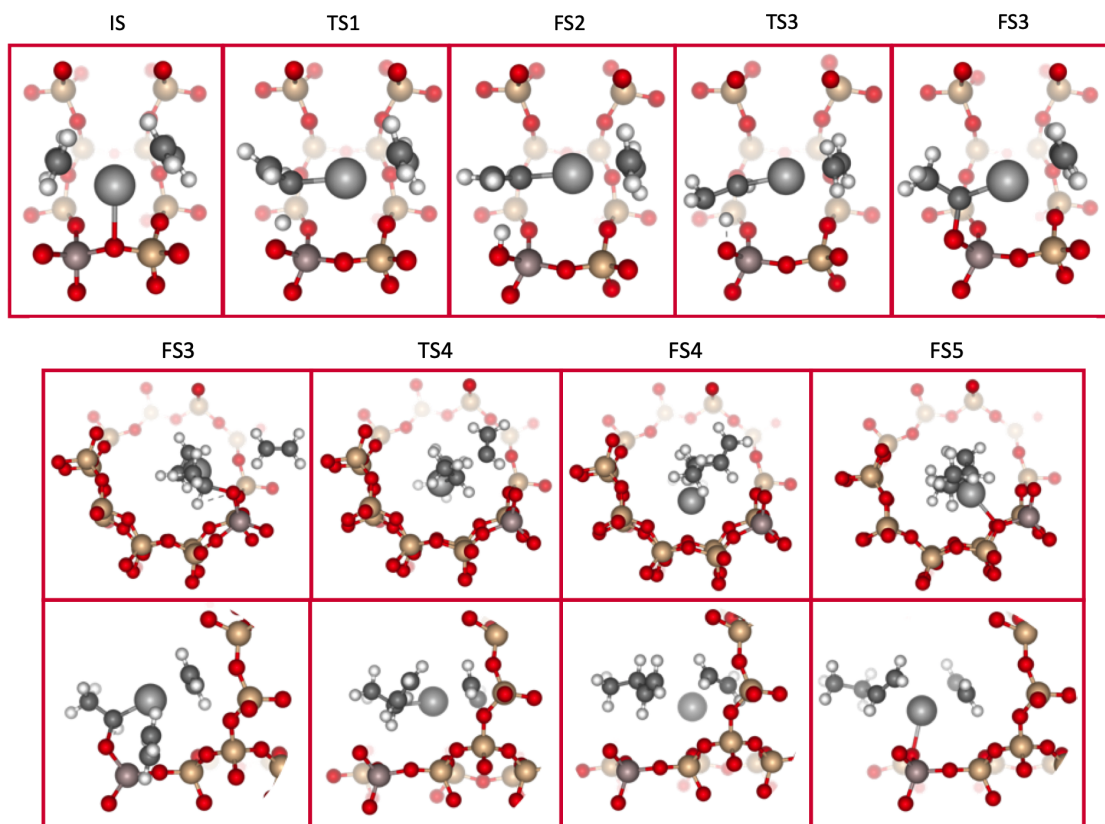


Figure 4.18. Depictions of the intermediate states sampled as part of the deprotonation pathway. The figures for IS through FS3 in the first row visualize geometries along the sinusoidal channel of ZSM-5. Figures for FS3 through FS6 visualize geometries along the straight channel (second row) and the sinusoidal channel (third row) of ZSM-5.

Ethylene binds strongly to the isolated Ag^+ site through a π -bonded complex, with two molecules adsorbing at reaction conditions (400 °C) with a free energy release of -0.05 eV per molecule of ethylene (Figure 4.9 c). Therefore, this structure was considered as the initial state for all mechanisms explored in this study. The deprotonation or proton-transfer mechanism was adapted from research investigating ethylene polymerization mechanisms over various manifestations of the Phillips catalyst by Fong and coworkers.^{167,168} In the proposed mechanism, the chromium oxide-stabilized ethylene molecules are deprotonated by the silica support at the metal-support interface for the initiation step of the polymerization process. For Ag-ZSM-5, the proton of the π -bonded ethylene is

abstracted by the framework oxygen (forming a Brønsted acid site) with an ΔG^\ddagger of 2.25 eV through a transition state TS1 shown in Figure 4.17 a. This results in the formation of a vinyl complex $[\text{CH}_2\text{CH-Ag-C}_2\text{H}_4]$ that remains bound in the vicinity of the Al anionic site, but not directly to the framework oxygen. The initial activation of ethylene and the subsequent formation of FS1 is uphill in free energy and requires 1.77 eV. Reorientation of FS1 such that the axis of the vinyl radical is perpendicular to the axis of the Brønsted acid O-H forming a π -bonded geometry, FS2, stabilizes the system by -0.17 eV. Next, The framework-bound H^+ (Z-O-H) undergoes an addition reaction to the unsaturated vinyl with the concomitant formation of $[\text{CH}_3\text{CH-Ag-C}_2\text{H}_4]^+$ complex (FS3) including the Lewis acid site. The addition of the Brønsted acid is both kinetically and thermodynamically exergonic in energy with an $\Delta G^\ddagger = 0.46$ eV and a ΔG_{rxn} of 0.4 eV. The final oligomerization step follows in which the co-adsorbed ethylene molecule undergoes a migratory addition to the unsaturated C atom in FS3 to form a C-C bond and transfer a H atom in a concerted fashion resulting in the intermediate FS4. This step is highly exergonic in free energy, releasing -1.97 eV and has a moderate barrier ΔG^\ddagger of 0.57 eV. The final state obtained (FS4) is a 1-butene molecule bound to the Ag^{arg} Lewis acid site. The initial state is regenerated by the desorption of 1-butene and the re-adsorption of two ethylene molecules with a net energy release of -0.64 eV.

The reverse deprotonation or proton-transfer mechanism was also considered in which an $[\text{H-Ag-C}_2\text{H}_4]$ complex and a framework bound vinyl group $[\text{Z-O-CHCH}_2]^-$ were formed. However, the barriers to the cleavage of the C-H bond and associated reaction energies are even higher ($\Delta G^\ddagger = 3.73$ eV and $\Delta G_{rxn} = 2.41$ eV), resulting in highly unfavorable energetics for the reaction to occur. The transition and final state for this mechanism is depicted in Figure 4.19 a. Both mechanisms of activation considered thus far proceed with the cleavage of

the Lewis acid site and the regeneration of the Brønsted acid site and are not reflective of the distinctly different catalytic behavior exhibited by the Ag-ZSM-5 catalysts in both flow and TAP experiments.

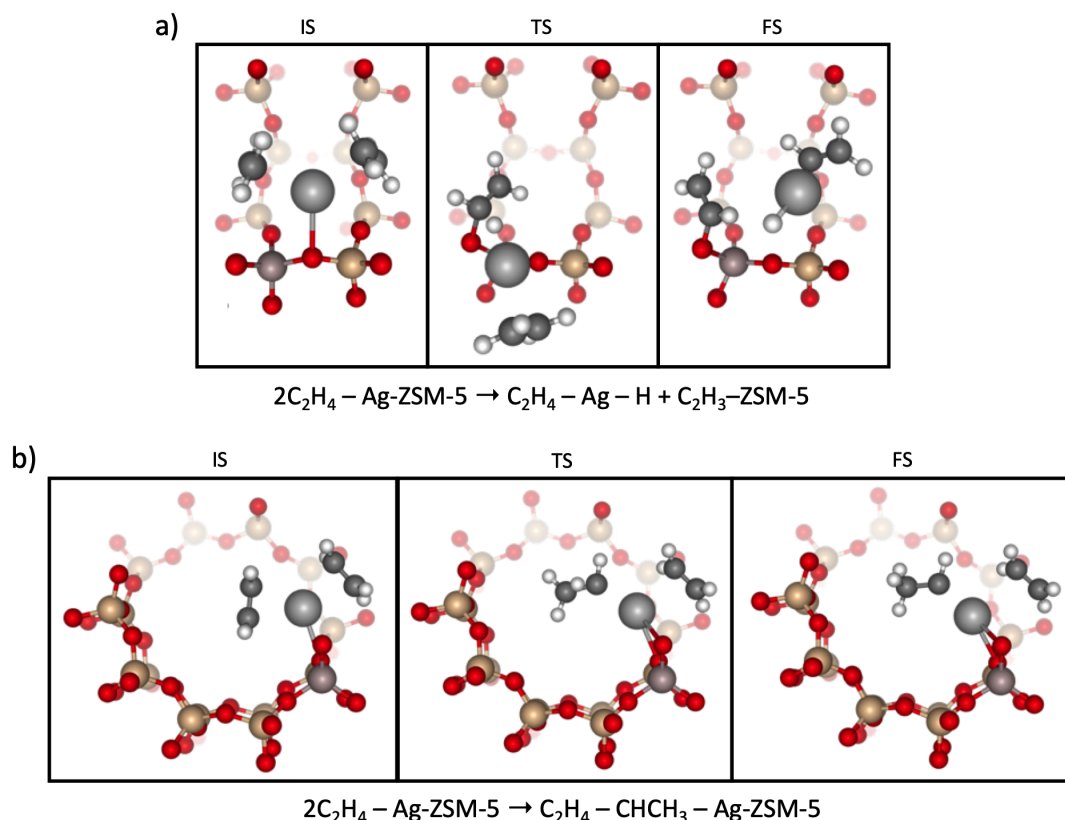


Figure 4.19. Visualizations of the initial, transition and final states for the a) reverse deprotonation mechanism as seen through the sinusoidal channel and b) the internal hydrogen transfer mechanism seen through the straight channel.

The deprotonation pathway studied in this work essentially models the formation of an activated $[\text{C}_2\text{H}_4 - \text{CH}_3\text{CH} - \text{Ag}]^+$ by the transfer of a H atom to the framework and back to the terminal C atom of the ethylene molecule. This mechanism also involves the shuttling of the acid site from a Lewis character to Brønsted and back to Lewis acid character. The same activated ethylene complex can also be formed via an internal hydrogen transfer starting from a strongly bound initial state depicted in Figure 4.9 c. The hydrogen transfer passes through

a transition state with a ΔG^\ddagger of 2.03 eV, with the reaction step requiring 1.97 eV of energy. The initial, transition and final states are shown in Figure 4.19 b. The initial steps of the deprotonation mechanism and the hydrogen transfer mechanism discussed here both arrive at the same activated state of ethylene in the $[\text{C}_2\text{H}_4 - \text{CH}_3\text{CH} - \text{Ag}]^+$ complex. The free energies of reaction required for the formation of this complex through both mechanisms are 2.0 and 1.97 eV, respectively. This negligible difference in energy is due to subtle variations in initial state required to model both mechanisms and are well within errors typically associated with DFT calculated free energies. However, the largest free energy barriers to the formation of the activated complex are 2.25 and 2.03 eV and therefore, would suggest that a hydrogen-transfer step is more likely to occur over a deprotonation by the framework.

The next mechanism considered for the dimerization of ethylene to butene was the metallacycle mechanism. These mechanisms are commonly proposed for various ethylene dimerization and trimerization processes over transition metals and are subject to an extensive body of work.¹⁶⁹ The free energy diagram and visualizations of all intermediate states sampled for this mechanism are given in Figure 4.17 b and Figure 4.20, respectively. Two adsorbed molecules of ethylene combine to form a metallacyclopentene with a ΔG^\ddagger of 2.76 eV through a transition state TS1. The formation of the C–C bond requires the partial desorption of the second ethylene molecule which then attacks the adsorbed ethylene through an Eley-Rideal type mechanism. The next step consists of a hydrogen transfer step forming a terminal methyl group. The intermediate that follows is a methylcyclopropene bound to the Ag^+ which then undergoes another hydrogen transfer step in TS3, finally forming a 1-butene molecule. Both hydrogen transfer steps are kinetically prohibitive, with barriers of 1.32 and 1.67 eV. The initial state is restored through the desorption of 1-butene and the re-adsorption of two ethylene

molecules. This mechanism also allows for the desorption of cyclobutene through the decomposition of the metallacyclopentane ($\Delta G_{rxn} = -0.57$ eV and $\Delta G^\ddagger = 0.41$ eV) in FS1. However, the large barrier of 2.76 eV that has to be overcome to form metallacyclopentane renders further investigations of this pathway irrelevant.

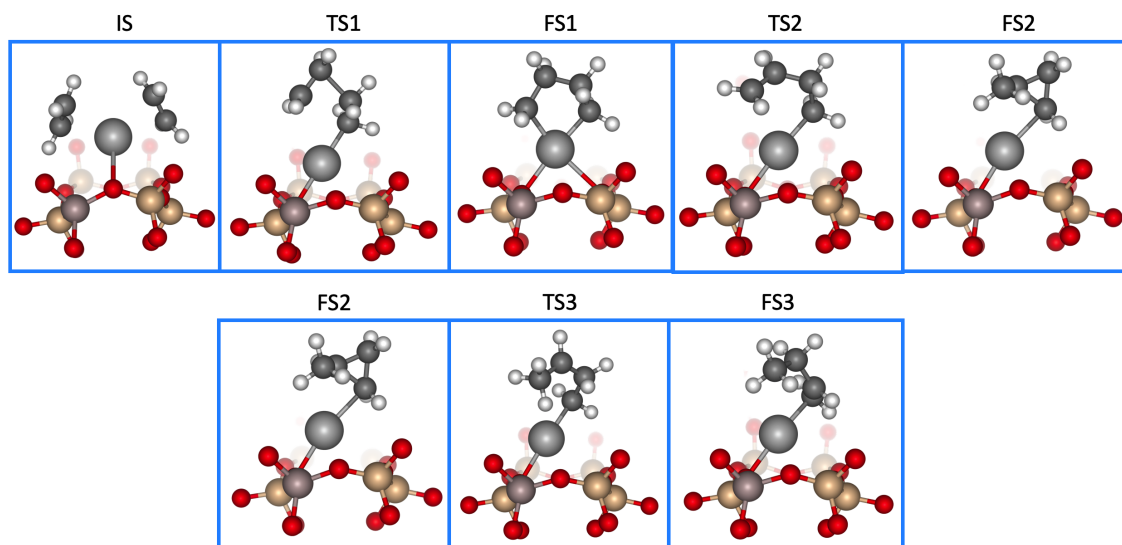


Figure 4.20. The initial, transition and final states sampled while modeling the metallacycle mechanism for the dimerization of ethylene to 1-butene. The figures are annotated according to those introduced in Figure 4.17 b

All mechanisms of ethylene activation studied thus far show prohibitively large barriers to activation and adequately rationalize the negligible catalytic activity seen from TAP experiments performed over the purely Lewis acidic $\text{Ag}_{0.08}\text{-Na-ZSM-5}$. Therefore, all evidence points to Ag^+ performing the role of a secondary catalyst as a site for the interaction/reaction of ethylene and intermediates formed through reactions catalyzed at the Brønsted acid sites. Ethylene conversion yields for catalysts containing both H^+ Brønsted acid sites and Ag^+ Lewis acid sites are given in Figure 4.11, with average conversions in the order of $\text{Ag}_{0.46}\text{-H-ZSM-5} > \text{Ag}_{0.25}\text{-H-ZSM-5} > \text{Ag}_{0.08}\text{-H-ZSM-5} > \text{H-ZSM-5}$. The percentage product yields for gases detected at the exit of the reactor for H-ZSM-5, $\text{Ag}_{0.08}\text{-}$,

Ag_{0.25}- and Ag_{0.46}-H-ZSM-5 over the duration of the respective experiments are given in Figure 4.21.

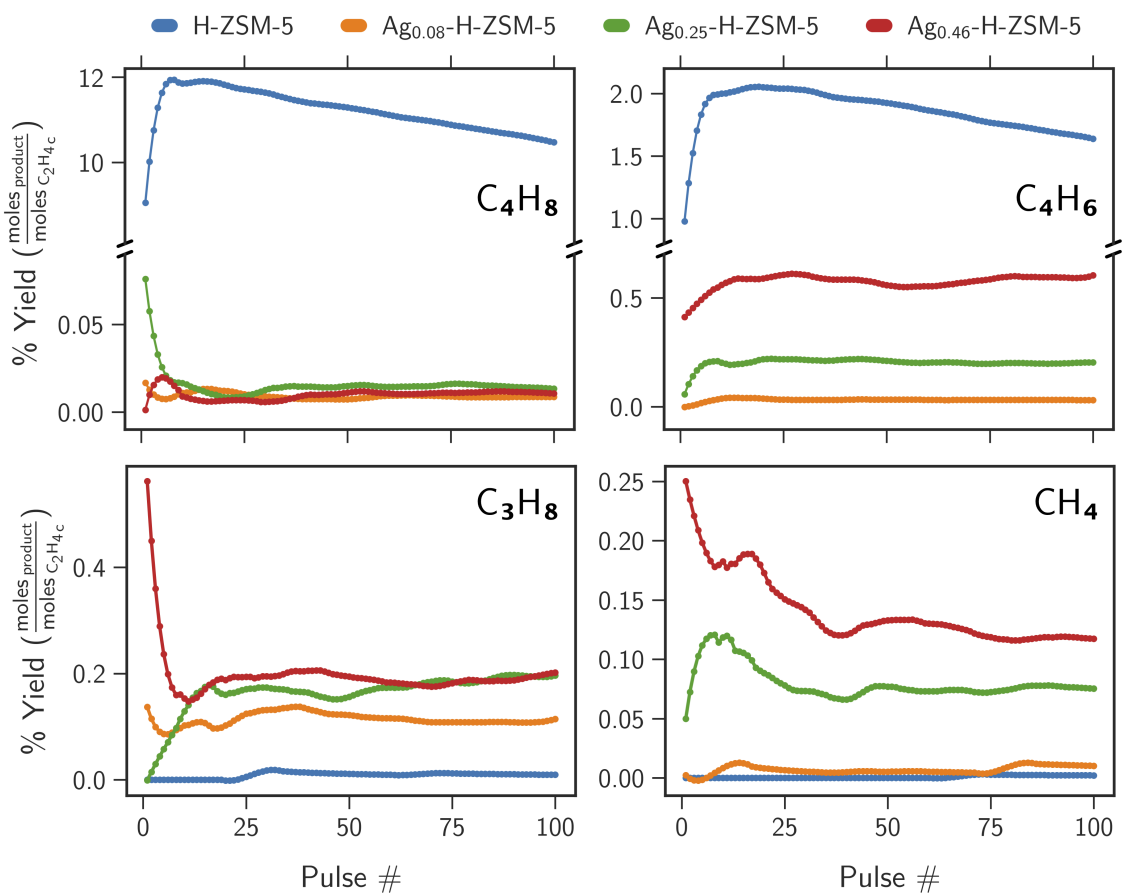


Figure 4.21. Yields for butenes (1-C₄H₈, 2-C₄H₈), 1,3-butadiene (C₄H₆), propene (C₃H₈) and methane (CH₄) obtained over for 100 ethylene/helium pulses admitted into microreactor.

With the exception of H-ZSM-5, the percentage yield profiles for products plotted in figure x show strong variations for the first 25–30 pulses, but thereafter show distinct differences in yields and product selectivities. The inconsistent trends for methane and propene during the first 30 pulses as the Ag loading is increased from 0.08 to 0.46 is likely due to noise in MS data collection and noise propagation through the defragmentation procedure given the low overall product yields.

The height-normalized pulses for butene collected over all catalyst samples under consideration are shown in Figure 4.21 a. The elongated tail in the response belonging to H-ZSM-5 indicates that the kinetics of butene formation is activated. This origin of this delay is attributed to the reactant limited nature of experiments and the bimolecularity of ethylene dimerization to butene. The averaged pulse response also shows a prominent shoulder. A closer inspection of the first 20 pulse responses for butene in figure sx reveals that the broad shape represents the formation of butene, and the sharper feature develops from the second pulse onwards. The sharper feature is attributed to residual butene being displaced and pushed out by the significantly larger quantity of ethylene pulsed in to the microreactor.

The absence of butene measured at the microreactor exit for catalysts containing both Ag^+ and H^+ active sites confirms that all butene molecules turned over at the Brønsted acid sites are retained within the zeolite at the Lewis acid sites or converted to secondary products. Most significantly, the exchange of only 8% of Brønsted acid sites with Ag^+ cations completely prevent any butene release by the catalyst. The drastic differences in butene yield between H-ZSM-5 and $\text{Ag}_{0.08}$ -H-ZSM-5, in spite of a theoretical 92% expected yield from $\text{Ag}_{0.08}$ -H-ZSM-5 suggests that Ag^+ aggregates or converts olefins produced at the Brønsted acid sites under reactions conditions. Increasing silver loading (Ag/Al) proportionately decreases the concentration of Brønsted acid sites and the retention of any olefins formed at the Brønsted acid site persists. Simultaneously, the increase of silver loading corresponds to increased selectivity to the formation of 1,3-butadiene.

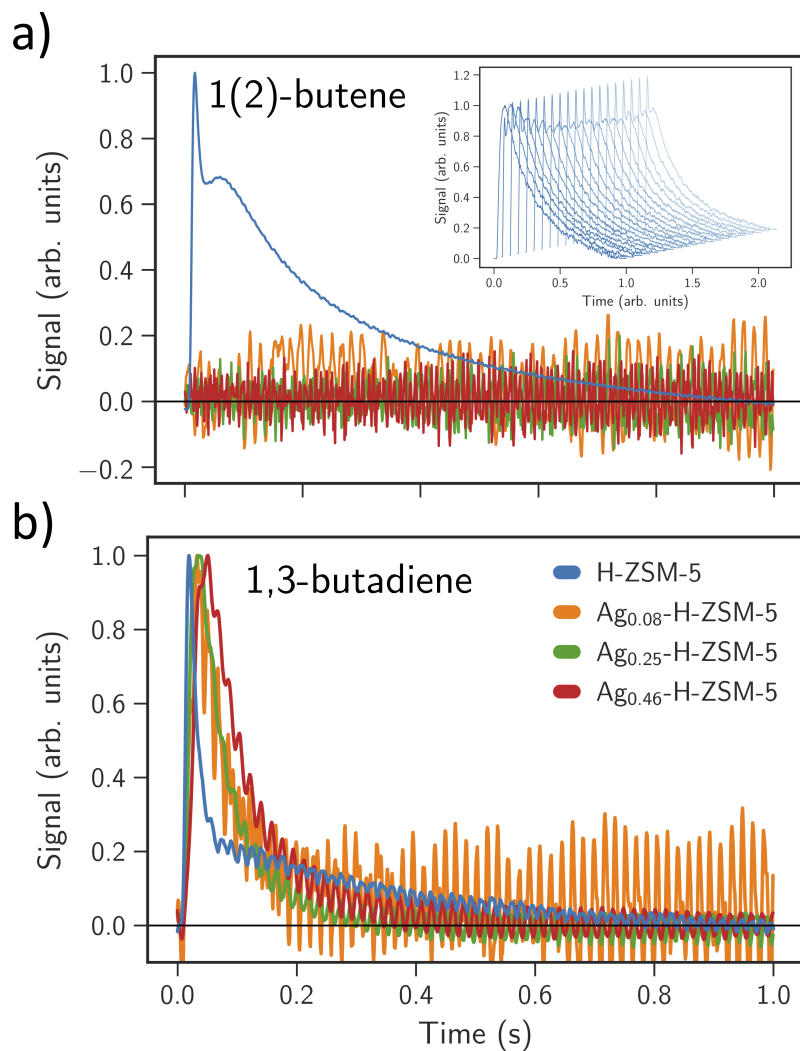


Figure 4.22. Height normalized averaged pulses for 1(2)-butene in a and 1,3-butadiene in b. The inset in a) shows the development of the peak-shoulder feature over the first 20 butene pulses recorded over H-ZSM-5

The features of the height-normalized averaged pulse responses for 1,3-butadiene in Figure 4.22 b suggest distinct modes of formation. The response collected for H-ZSM-5 again has the same initial maxima as that obtained for butene in Figure 4.22 a and is attributed to the succeeding ethylene pulse expelling residual 1,3-butadiene from the microreactor. The delay in pulse response tail (almost 1 s) indicates a slow rate of formation and is consistent with observations made

earlier in this section. On the other hand, the pulse responses obtained for Ag_{0.08}-, Ag_{0.25}- and Ag_{0.46}-H-ZSM-5 show less pronounced tails that attain the baseline within ~ 0.6 s. The lack of tail is surprising, given the previously observed strong binding nature of olefins at the Ag⁺ sites seen in DFT binding energies and TAP experiments. The distinct features, including delayed peak times, point to distinct mechanisms of formation for 1,3-butadiene in H-ZSM-5 and Ag-H-ZSM-5. Therefore, initial observations from the pulse responses combined with the Ag loading dependent 1,3-butadiene yields in Figure 4.21 are congruent with observation of Lewis acid sites catalyzing dehydrogenation reactions from the first pulse onwards. These secondary reactions appear to be the result of instantaneous olefinic saturation of the Lewis acid sites with 1,3-butadiene forming but not suffering from strong product binding at Ag⁺ cations, resulting in its rapid expulsion from the microreactor without further interaction with other hydrocarbons.

The negligible percent yields of 1,3-butadiene obtained from Ag_{0.08}-H-ZSM-5 as compared to H-ZSM-5 in Figure 4.21, however, do not agree with the notion that the Ag⁺ Lewis acid sites alter selectivity to dehydrogenation products. The significant decrease in percent yield of all products except propane and to some extent methane upon exchanging 8% of Brønsted acids with Lewis acids coupled with a higher conversion and uptake ($\sim 75\%$) than H-ZSM-5 ($\sim 40\%$) suggests an incompletely understood synergism between the Brønsted and Lewis acid sites. The increased yields to propane and methane for Ag_{0.08}-H-ZSM-5 compared to H-ZSM-5 indicate an increased selectivity to cracking pathways over the Lewis acid sites. Increasing the Ag loading to 0.25 and 0.46 further increases the yields of cracking products as well as that of 1,3-butadiene. Overall, the trends in product yields associated to dehydrogenation and cracking pathways are ample evidence for the conclusion that Lewis acid sites catalyze these mechanisms post the formation of higher olefins at the Brønsted acid sites.

4.5. Conclusions

The chemistry that drives the selective production of aromatic hydrocarbons from ethylene using a silver exchanged ZSM-5 catalyst was systematically dissected using an integrated experimentation and computational simulation approach. The active sites in Ag-H-ZSM-5 were subjected to *ex situ* characterization and identified as predominantly isolated Ag^+ cations through a combination of experimental and simulated UV-vis spectroscopy, X-ray absorption spectroscopy and temperature-programmed desorption, adeptly aided by density functional theory calculations throughout. Transient pulsing experiments using the temporal analysis of products technique showed that ethylene molecules exhibit an unusually long intrinsic residence time inside a catalyst that contains both Ag^+ Brønsted and H^+ Lewis acid sites, but not inside purely Brønsted and Lewis acidic catalysts. Congruent density functional theory calculations confirm the strong-binding nature of olefins to isolated Ag^+ sites, and were used to explore mechanisms of ethylene activation and oligomerization as the initiation towards the formation of aromatic hydrocarbons.

The initial evidence of bifunctional catalysis between the two types of acid sites was confirmed by the trends in product formation. The Ag^+ Lewis acid site retains all of the olefins formed at the Brønsted acid site and catalyzes the interaction of ethylene and products formed at H^+ site, and ultimately enables dehydrogenation and hydrogen-transfer pathways. Overall, the role of Ag^+ appears to be that of a secondary catalyst that accelerates the retention of highly unsaturated aromatic hydrocarbon precursors inside the pores of the zeolite and thus, increase the selectivity towards these valuable products. The results from this work outline the potential of optimizing the concentration of Brønsted and Lewis acid sites in the zeolite, providing basis for the rational design of metal-exchanged zeolites for tailored hydrocarbon conversion processes.

5. Toluene Alkylation with Methanol over H-ZSM-5 Catalysts: Insights from Transient Pulsing Experiments

This section describes the main results obtained from the investigation into the fundamental mechanisms of toluene alkylation with methanol. All experiments were performed on a TAP-3E reactor at the Laboratory of Chemical Technology in Ghent University, Belgium during my stay there as a visiting student researcher in the summer of 2019. The work was in collaboration with Juan Mirena Seguias and Dr. Vladmir V. Galvita. The results of this work are being compiled as a manuscript due for submission in spring 2020.

5.1. Introduction

Benzene, toluene and xylene (BTX) are important commodity chemicals that serve as raw materials for several aromatic derivatives such as cumene, linear alkylbenzene and ethylbenzene which are extremely important feedstocks for the synthesis of high-value chemicals.^{170,171} The requirement for BTX by the industry depends on various economic variables such their consumption rate, availability of feedstock, as well as environmental regulations and consequently, the demand for BTX has been continuously increasing over the past decade. His-

torically, BTX has been produced by catalytic reforming and pyrolysis of naphtha derived from petroleum feedstocks. Of the BTX hydrocarbons, toluene is mostly used as a solvent and in the production of benzene and xylene. A surplus of toluene production over time has reduced its market value and increased its suitability as feedstock material. Xylenes on the other hand, particularly p-xylene, have shown a steady 7% increase in demand annually and has the highest gain in market value. Benzene is mainly used to produce styrene, cumene and nylon.¹⁷²

Existing avenues of production of BTX are not flexible to selectively produce either one of benzene or xylene based on market demand and is limited to equilibrium mixtures of 32:36:32 for benzene:toluene:xylene.¹⁷³ A complicating factor here is the existence of xylene isomers; para-xylene (1,4 dimethylbenzene), meta-xylene (1,3 dimethylbenzene) and ortho-xylene (1,2 dimethylbenzene). The market demand for each isomer is different with p-xylene the most sought-after isomer of xylene. It is the major raw material for the production of terephthalic acid (PTA) and dimethyl terephthalate (DMT) which are feedstock materials in the production of polyesters and polyethylene terephthalate (PET), mainstays of the textile and packaging industries. Therefore, production routes that enable the conversion of o-xylene and m-xylene to the highly valuable p-xylene have been established.¹⁷²

Novel technologies for the selective production of p-xylene from toluene holds great economic potential in being able to convert low-value feedstock to high-value chemicals. Multiple avenues are being explored to capitalize this gap in technology such as toluene disproportionation,⁴⁸ transalkylation of trimethylbenzenes with toluene¹⁷⁴ and toluene alkylation with methanol.^{48,175} Many such processes have been commercialized using modified zeolite catalysts by UOP and ExxonMobil, but are not entirely optimized for p-xylene yields and overall costs of production. A commercially relevant production route is the alkylation of toluene

with methanol to form p-xylene. The route is particularly attractive because of the use of cheap methanol feedstocks and the absence of benzene as a by-product. The conversion of toluene to xylene with methanol is an acid catalyzed pathway and many zeolites such as ZSM-5, MOR, SAPO-34 and MCM-22 have been tested as catalysts for this reaction.¹⁷⁶ However, low p-xylene yields remain elusive and this is a major driving force in the search for catalysts that can achieve industry standards.

ZSM-5 catalysts are the most commonly used industrial catalysts for the methylation of toluene. The performance and selectivity achieved by using Brønsted acid H-ZSM-5 suffers from the prevalence of side reactions such as toluene disproportionation and isomerization.⁴⁸ ZSM-5 can be modified by tuning the acidity of active sites and partial blocking of pores by using metal oxides. Upon modification, up to 89% p-xylene selectivity among xylenes were achieved.¹⁷⁷ Deactivation of unselective external sites on the zeolite surface and increased diffusion limitations by blocking the entrances to pores helps in improving p-xylene selectivity.¹⁷⁸ While these strategies succeed in driving up selectivities to p-xylene, there is considerable uncertainty on the mechanisms that take place at the acid sites in the zeolite. For instance, the ways in which the differing chemistries of methanol dehydration, toluene disproportionation and toluene methylation interact with the acid site, and the effect of one over the other is unknown.

In this work, a systematic investigation of the interaction of reactants with the acid site in H-ZSM-5, along with the eventual methylation of toluene by methanol are studied by means of low-pressure transient pulsing experiments using the temporal analysis of products technique. Saturation and pulsing experiments were designed to understand the type and concentration of surface species that interact with each other in formation of xylene. These experiments conclusively showed that methanol binds competitively over toluene and surface

methoxy species are important reaction intermediates. Pump-probe reveal that xylene yields increase when a toluene pulse is able to interact with the zeolite within 0.5 s of a methanol pulse. These results provide invaluable insights into the fundamental mechanisms that take place at the acid sites of H-ZSM-5 and enable the rational design of zeolite catalysts for efficient methylation of toluene to p-xylene.

5.2. Experimental Methods

5.2.1. Materials

Brønsted acid ZSM-5 catalyst was obtained by calcining commercially available NH_4 -ZSM-5 (Zeolyst International CBV 2314) in air at 550 °C. The catalyst powder was pelleted, crushed and sieved to obtain catalyst particles of size distribution 250-400 μm . Silica (Sigma Aldrich) of the same particle size distribution were used as the inert media in the packed bed of the microreactor. Evaporated methanol (Sigma Aldrich $\geq 99.9\%$) and toluene (Sigma Aldrich $\geq 99.8\%$) mixtures were prepared with helium (Praxair 99.999%) for pulsing experiments.

5.2.2. Experimental Setup and Procedures

All pulsing experiments were performed using the TAP-3E reactor at the Laboratory of Chemical Technology, Ghent University in Belgium. Detailed descriptions of the experimental setup are provided in the work of Batchu and coworkers.^{165,179} Preparation of gas mixtures consisting of liquid components require the mixing tanks, feed lines, pulse valves and the pulse valve manifold to be maintained at elevated temperatures. Accordingly, the tanks were heated to a steady temperature of 160 °C using flexible heaters and the feed lines were kept

at a temperature of 140 °C using Habia trace cables. The pulse valves and manifold were heated to 100 °C and this temperature was assumed to be the lower limit while preparing liquid/gas mixtures of specific concentration. This is an important consideration to prevent the condensation of liquid components in any component of the feed setup. A known quantity of liquids was injected into the blending tanks by piercing sealing septa with Hamilton gastight syringes and 15% liquid/helium mixtures were prepared. The pulse valves were tuned based on the signal for helium such that the moles of toluene pulsed in are a factor of at least three times more than the moles of methanol.

Pulse responses for mass-to-charge ratios (AMU) relevant to the reactants and products formed were monitored at the Extrel 150QC quadrupole mass spectrometer (MS) with its axis lined perpendicular to that of the reactor. AMU switching experiments were performed where the MS switches through a series of pre-set AMUs during the pulsing experiments. Calibration experiments were also performed to map the signal and sensitivity of the MS to molar quantities of gas through the calculation of calibration factors. A complicating factor in the analysis of hydrocarbons using mass spectrometry is the presence of overlapping fragments of higher hydrocarbons at lower AMUs. Therefore, it was assumed that the net signal measured at an AMU is the cumulative sum of the fragments of individual components and a system of linear equations was set up and solved as a constrained minimization problem for each set of measurements pertaining to a given set of AMUs. The coefficients relating overlapping fragments are given

in the matrix $\overline{\overline{A}}$ in Equation 5.1 and the minimization problem in Equation 5.2 as

$$\underbrace{\begin{bmatrix} 1.00 & 0 & 1.00 \\ 0 & 1.00 & 0.08 \\ 0 & 0 & 0.45 \end{bmatrix}}_{\overline{\overline{A}}} \underbrace{\begin{bmatrix} \text{Toluene} \\ \text{Benzene} \\ \text{Xylene} \end{bmatrix}}_{\overline{x}} = \underbrace{\begin{bmatrix} a_{91} \\ a_{78} \\ a_{106} \end{bmatrix}}_{\overline{b}} \text{ and} \quad (5.1)$$

$$\min U(y) = (\overline{\overline{A}} \overline{x} - \overline{b})^2 \quad \text{such that} \quad x_i \geq 0; x_i \in x. \quad (5.2)$$

Due to the transient nature and short contact times of reactants in TAP experiments, the yields of product obtained are quantified as a per mole of reactant consumed basis and is shown in Equation 5.3

$$\% \text{ yield}_{\text{product}} = \sum_N \frac{\text{moles}_{\text{product}}}{\text{moles}_{\text{reactant consumed}}} \times 100 \quad (5.3)$$

The methylation of toluene was investigated by two modes of TAP experiments. A visual depiction of saturation experiments and pump-probe experiments performed are given in Figure 5.1 a and b, respectively. Data is collected at the mass spectrometer signals for the time period indicated by $\Delta T_{\text{MS, collect}}$ and switches from one AMU to the next at times indicated by the grey lines. These experiments enable the systematic analysis of various chemistries that occur within the pores of the zeolites and help probe competitive binding effects and reaction intermediates.

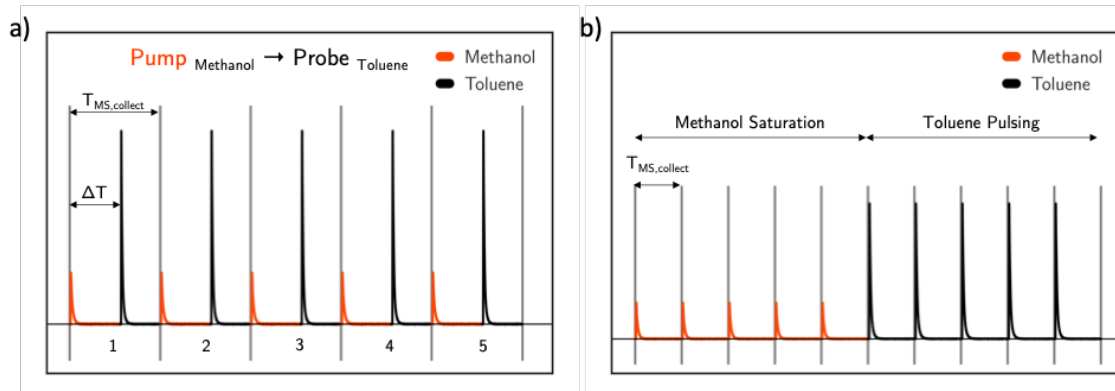


Figure 5.1. Representative descriptions of a) pump-probe experiments and b) saturation experiments performed in this work.

5.3. Results and Discussion

To understand the interaction of methanol and toluene with the acid sites in H-ZSM-5 (SAR ~ 12 and with itself, a series of TAP experiments were performed at a reaction temperature of 350 °C. Typically in toluene methylation, methanol (MeOH) reacts with a toluene to form any of o-, m-, or p-xylene. This reaction is hampered by several side reactions that form light hydrocarbons and products of successive methylation steps i.e trimethylbenzene and tetramethylbenzene.^{48,175} An approach to suppress these side reactions is to use a feed containing excess toluene relative to methanol. However, a consequence of this is reduced toluene conversions and relatively high selectivity to light hydrocarbons. In TAP experiments performed in this work, the pulse valves were tuned such that the molar quantity of toluene was 3–4 times that of methanol.

A starting point to understanding the methylation reaction is to identify the individual and possibly independent chemistries that if active, inhibit the desired formation of xylenes at higher selectivities. Therefore, saturation experiments were performed in which a pretreated and pristine zeolite is subjected to continuous pulsing of one reactant while at the same time monitoring the products

at the mass spectrometer that are representative of the reactions occurring at the catalyst. Then, the other reactant is pulsed while appropriate products are monitored. The outcome of these experiments is to correctly identify active surface species that are formed upon the interaction of a reactant with the zeolite. The subsequent pulsing of the second reactant probes its interaction with the surface species formed from the saturation step.

First, an experiment in which H-ZSM-5 was saturated by toluene and then probed by methanol was performed. Under these conditions, however, toluene is expected to disproportionate into an equilibrium mixture of benzene and xylene and subsequent transalkylation reactions form higher substituted methylbenzene isomers as well.^{48,175} A pulse train of 100 pulses containing approximately 1×10^{-6} moles of toluene per pulse was admitted into the zeolite. The m/z ratios (AMUs) monitored were those of the inert (He), toluene, xylene and benzene and the moles of toluene pulsed in and unreacted are shown in Figure 5.2 a and yields of products obtained are shown in Figure 5.2 b.

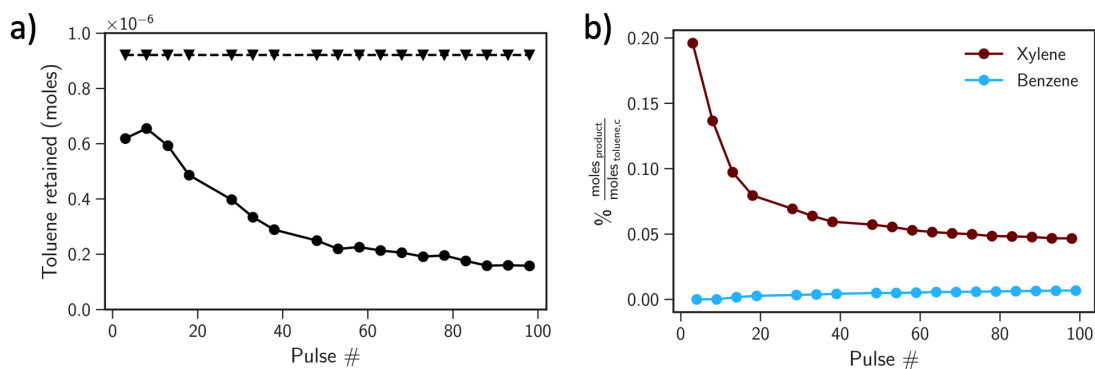


Figure 5.2. (a) Moles of toluene pulsed in (∇) and moles retained in the zeolite (\circ) and b) Percentage product yields for benzene and xylene obtained while saturating the ZSM-5 catalyst with toluene (1×10^{-6} moles/pulse).

The zeolite shows substantial uptake of toluene initially and the retention tails off to a steady 2×10^{-6} moles/pulse. However, this build-up of toluene does

not translate to significant disproportionation activity in the zeolite. Figure 5.2 b) shows that the highest yield of xylene obtained initially corresponds to the regime of highest toluene concentration within the zeolite with approximately 0.2% of the toluene in the zeolite undergoing disproportionation. This reaction should also result in a stoichiometric formation of benzene, which appears to be negligible in the products detected at the mass spectrometer. Meshram and coworkers identified acid sites inside the pores of the zeolites to be responsible for disproportionation of toluene.¹⁸⁰ The steep drop in xylene production indicates that the acid sites inside the zeolite pores are rapidly blocked off by the excess toluene. The absence of benzene suggests that it is either retained or undergoes further reactions within the pores of the zeolite.

The saturation of the zeolite with toluene is followed by pulsing of methanol, with 3×10^{-7} moles admitted into the reactor per pulse. In addition to the AMUs monitored for the previous step of this experiment, those corresponding to methanol, dimethyl ether (DME) and water are also included. The conversion of methanol and the methanol pulses measured are shown in Figure 5.3 a and in the inset of Figure 5.3 a, respectively. Methanol is almost completely consumed (> 95%) from the first pulse onwards, after which, a small amount of unreacted methanol is detected. It is either consumed by the accumulated toluene in the zeolite in a methylation reaction or undergoes dehydration at the acid sites of the zeolite. Both reactions proceed with the stoichiometric formation of water (H₂O). The percentage yield of products detected while pulsing methanol are given in Figure 5.3 b.

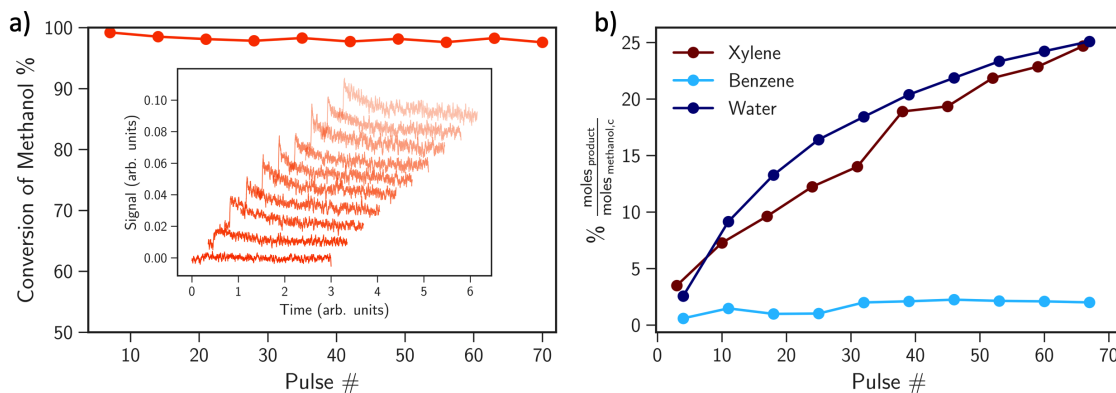


Figure 5.3. a) Methanol conversion profiles obtained as a function of methanol/helium pulse number for a H-ZSM-5 catalyst sample saturated *a priori* with toluene. b) percentage product yields obtained per mole of methanol consumed.

Upon pulsing of methanol, toluene was detected at the reactor confirming that it is simply accumulated within the zeolite and was not seemingly activated or converted into other hydrocarbons. A height-normalized comparison of averaged toluene and xylene pulses collected from the saturation step and during methanol pulsing is given in Figure 5.3 a and b, respectively. The toluene pulse response obtained during saturation consist of a peak and a shoulder, of which the peak appears to be a flux of accumulated toluene pushed out of the zeolite by the incoming toluene pulse. On the other hand, the shoulder is more representative of the interaction of toluene with H-ZSM-5 (see the first pulse Figure 5.5). The excess toluene diffusing out during methanol pulsing exhibits a more conventional pulse feature. The diffusion is faster due to the presence of methanol, which could displace toluene coordinated and stabilized by the acid sites due to competitive binding effects. The pulse responses for xylenes in Figure 5.3 b are very similar to each other, pointing to similar diffusional limitations encountered while exiting the zeolite. Both mechanisms of xylene formation are acid catalyzed, and the similar features seen in the xylene pulse responses confirm the involvement of zeolitic acid sites.

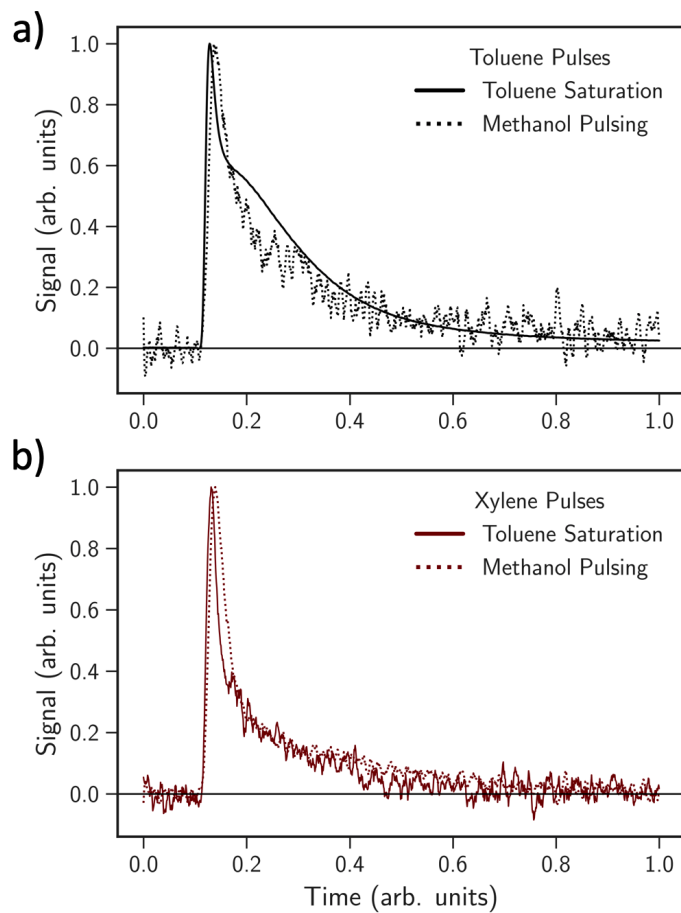


Figure 5.4. a) Height-normalized averaged pulse responses for toluene corrected for overlapping fragments of xylene and b) height-normalized pulse responses for xylene.

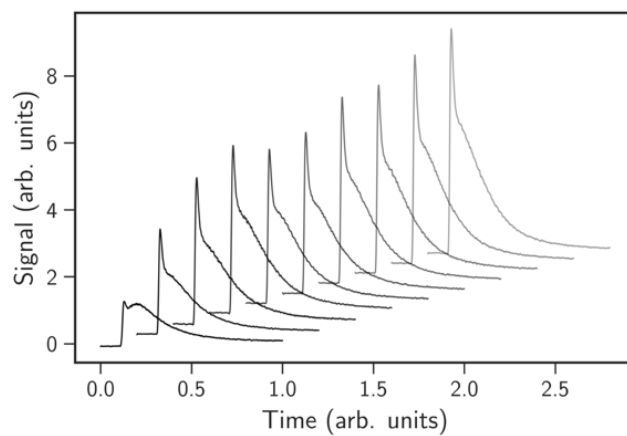


Figure 5.5. Signals of unreacted toluene collected while saturated H-ZSM-5.

Of the products monitored, the trends in yield for xylene and water overlap over the course of the experiment, indicating that the toluene contained in the zeolite is being converted into xylene with the methanol pulsed in through a direct methylation pathway. The utilization of methanol in the production of xylene is significantly higher than the corresponding utilization of toluene in the saturation stage of the experiment. The increasing percentage yield of xylene and methanol utilization appears to be the cumulative effect of unreacted toluene, xylene and small amounts of benzene leaving the zeolite, thus exposing more acid sites for the methylation reaction to take place. Taking this into account, the origin of water is from the dehydration of methanol at the acid site. These initial observations also support the competitive binding of methanol over toluene at the acid sites in H-ZSM-5, with most of the toluene remaining benign within the pores of the zeolite.

Having identified initial evidence of methanol competitively binding over toluene at the acid sites in H-ZSM-5, the effect of saturating the zeolite with methanol instead of toluene was investigated. All experimental settings were kept identical, and AMUs for methanol, water, DME and helium were monitored. The dehydration of methanol at the acid sites accompanied by the formation of water is the first reaction that is expected to occur and is subject to a large body of literature.^{114,181,182} The pulsing of methanol was kept to a minimum to minimize the extent of the methanol to olefins reaction that takes place within the pores of the zeolite. This was confirmed by monitoring the AMU corresponding to all olefins, i.e. 28. The salient results obtained from the saturation of the zeolite with methanol are shown in Figure 5.6 a and b.

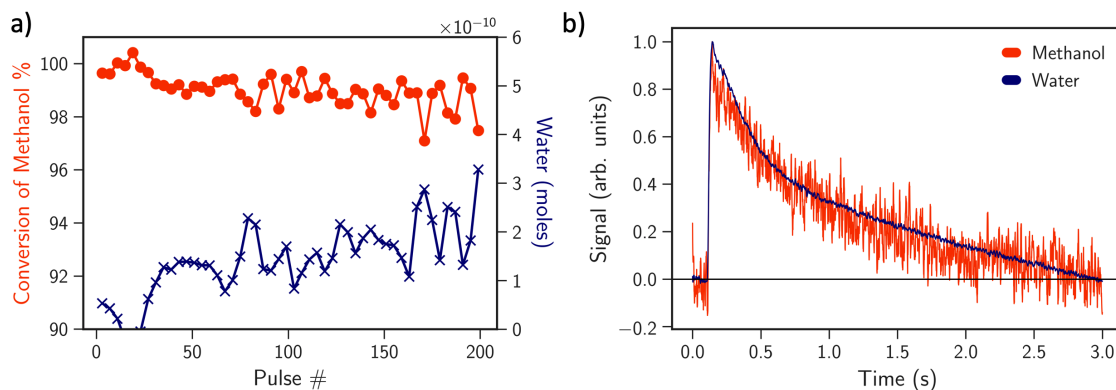


Figure 5.6. a) Methanol conversion and moles of water as a function of pulses and b) height normalized pulse responses for unreacted methanol and water detected at the MS.

The entirety of methanol pulsed into the zeolite was consumed with the overall conversion greater than 97% over 200 pulses. The trends in yield of water in Figure 5.6 a are noisy and the overall moles of water was found to be 3 orders of magnitude lesser than the moles of methanol pulsed in. This indicates that a majority of the water formed as a result of methanol dehydration is accumulated inside the pores of the zeolite and desorbs out slowly. Evidence of slow desorption is seen in the averaged pulse response for water in Figure 5.6 b. The similarity in features of unreacted methanol and water pulse responses are suggestive of an interdependency of the kinetics of formation of water on methanol. The consequence of continuous pulsing of methanol is that the acid sites in the zeolite consist of adsorbed methanol or methylated with CH_3^+ species and are primed for the acid catalyzed methylation when toluene is pulsed into the zeolite.

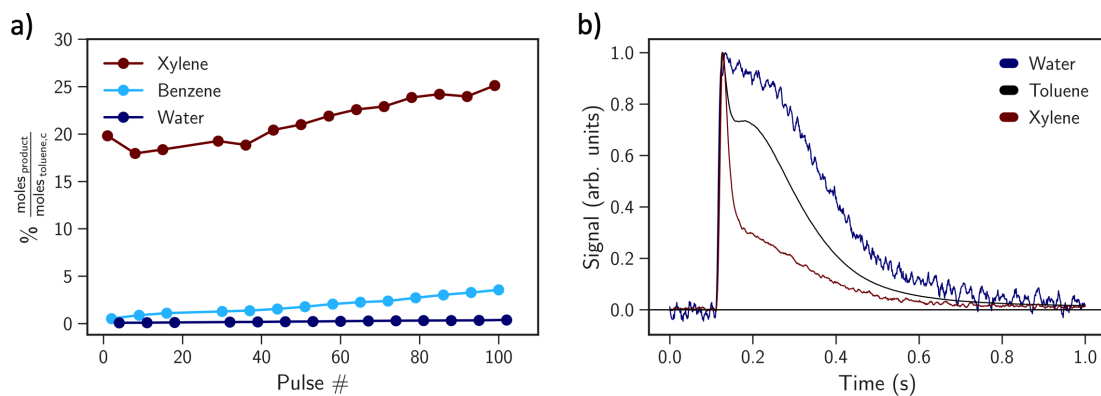
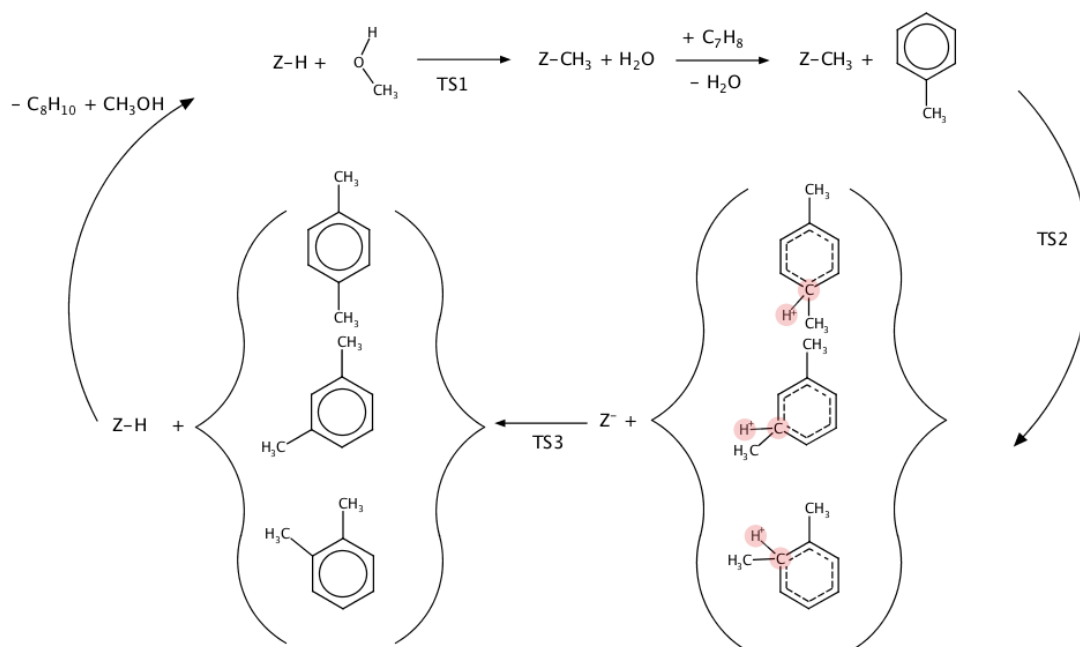


Figure 5.7. a) Percentage product yields per mole of toluene consumed when toluene is pulsed into H-ZSM-5 saturated with methanol *a priori* and b) Height-normalized averaged pulse responses for toluene, xylene and water.

The percentage yields of xylene, benzene and water per mole of toluene consumed is shown in Figure 5.7 a and the corresponding averaged pulse responses are given in Figure 5.7 b. Pretreating the ZSM-5 catalyst with methanol increases the yield such that one in five toluene molecules are converted to xylene from the first pulse onwards. The yield of xylene increases as a function of toluene pulses to 25% by the 110th pulse of toluene. The moles of benzene also increase over time due to the probable occurrence of disproportionation reactions of toluene and xylene to form dimethylbenzene and benzene. However, negligible moles of water are detected with the moles of water not within two orders of magnitude of xylene and toluene. Therefore, preliminary observations from the toluene saturation experiment suggesting that methanol competitively binds over toluene and undergoes dehydration reactions appear to be confirmed. Thus, toluene reacts with the surface methoxy (O-CH_3^+) species at the acid sites and forms xylene and regenerates the acid site. This reaction is visualized as follows:



The height-normalized pulse responses for toluene, xylene and water detected at the MS is visualized in Figure 5.7 b. The peak-shoulder-features exhibited by the toluene and xylene pulses are once again attributed to a combination of convective flux from accumulated product (peak) and the intrinsic diffusion of the products (shoulder). The similarity in pulse response tails of xylene and toluene are indications that they are mechanistically linked. However, the pulse response for water appears to be different from that obtained while saturating the zeolite with methanol in Figure 5.6 b. Assuming that water formed from the dehydration of methanol is accumulated inside the pores of the zeolite, the agreement between water pulse response and that of toluene and xylene suggests that the water molecules are transported out by the larger toluene pulse. Further confirmation of the predominance of methanol binding and dehydration over toluene disproportionation at the acid sites can be seen in Figure 5.8, which compares water pulse responses obtained across both saturation experiments per-

formed thus far. The unique pulse response for water produced from methanol dehydration persists regardless of the presence of toluene in the zeolite. This is seen in the elongated pulse responses for methanol saturation (solid line) and methanol pulsing (circles) which both attain baseline at 3 s as compared to the rapid pulse measured while pulsing toluene in the methanol saturation experiment. The mechanistically decoupled nature of methanol dehydration and the reaction of dehydration intermediates to higher hydrocarbons has also been observed for the dehydration of ethanol over H-ZSM-5 and the results obtained in this work are consistent with those reported.¹⁷⁹

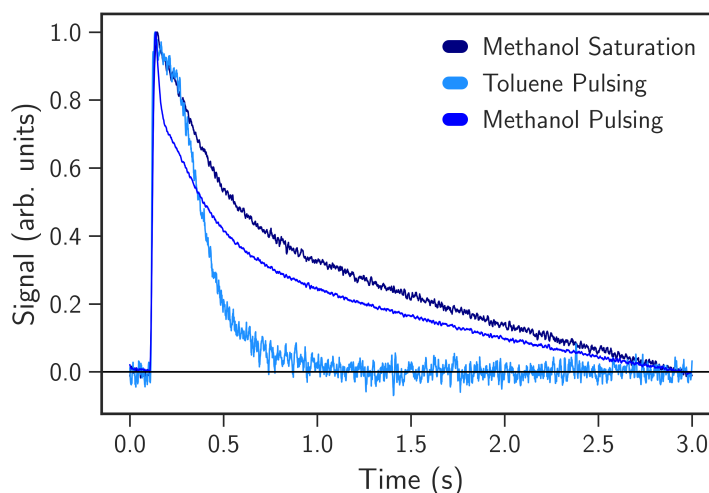


Figure 5.8. Height normalized averaged pulse responses for water collected from all saturation experiments performed in this work.

Having identified the importance of methanol dehydration and the presence of surface methoxy species for the efficient methylation of toluene, pump-probe experiments were performed to probe the nature of methanol dehydration intermediates and their effect on the yield of xylene. In these experiments, a “pump” pulse of methanol was followed by a “probe” pulse of toluene at a pre-set time delay. The time delay can be varied to sample methanol dehydration intermediates of finite lifetime. Experimental parameters were kept consistent with

those used in the saturation experiments, i.e. a toluene/helium pulse contains 1×10^{-6} moles of toluene and a methanol/helium pulse contains 3×10^{-7} moles of methanol. Four delay times were chosen; 0.1 s, 0.5 s and 5 s for experiments in which a toluene pulse probes a methanol pulse and 3 s for an experiment in which a methanol pulse probes a toluene pulse. The difference between the latter and former experiment is the first pulse of excess toluene. The time separation between two pulses of the same reactant were kept constant while varying the time delay between pulses of methanol and toluene.

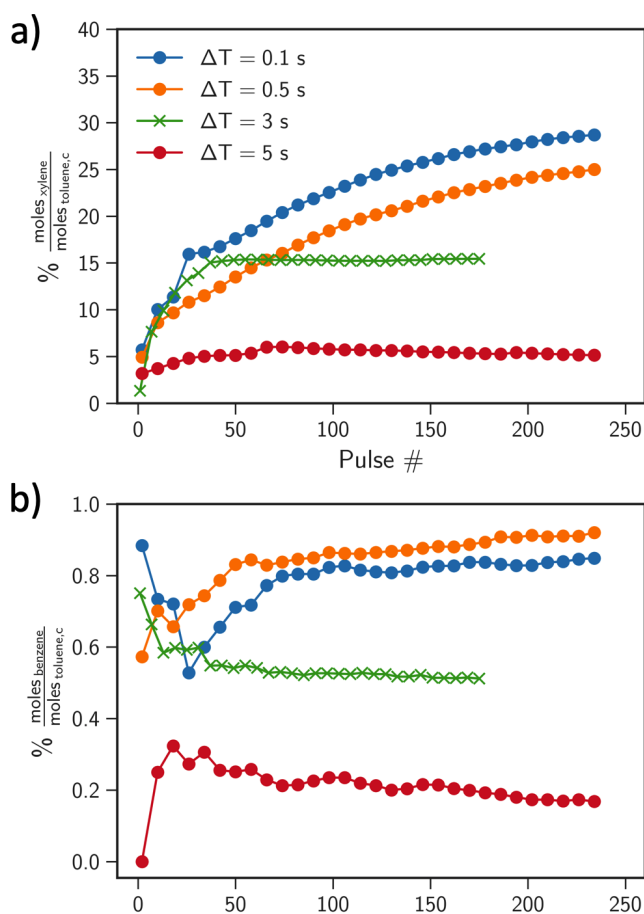
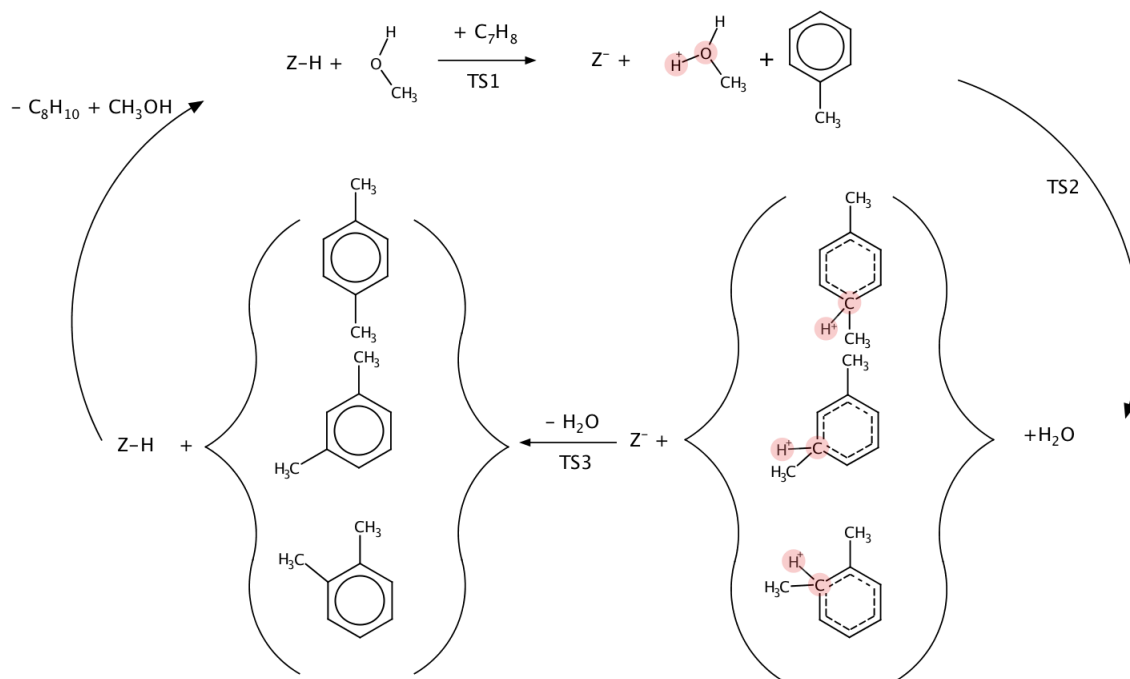


Figure 5.9. Percentage product yields of a) xylene and b) benzene per mole of toluene consumed. The trends indicated by the green cross marks (\times) are obtained from an experiment in which a methanol pulse probes a toluene pump pulse.

The percentage yields of xylene and benzene per mole of toluene consumed

is given in Figure 5.9 a and b, respectively. It is apparent that the methylation of toluene dominates over disproportionation after the third pulse due to the significantly higher utilization of toluene for the production of xylene. Figure 5.9 charts data obtained from two types of experiments previously introduced with the experiment in which methanol probes toluene plotted in green. Despite the swap in reactant pulse order, the overall xylene yields show a linear dependence on the delay time, with short delay times of 0.1 s between a methanol pump and a toluene probe showing the highest yield and 5 s showing the least. This indicates that the intermediates that form upon the dehydration of methanol must be attacked by toluene before they undergo further reaction. Benzene yields are inconclusive due to low calculated yields, but the matching trends with xylene are again indicative of toluene-xylene disproportionation reactions taking place with increasing toluene yield. Therefore, pump probe experiments suggest that toluene methylation could proceed via a mechanism that requires a toluene in close proximity to an activated methanol intermediate at the acid site of a zeolite and is depicted as follows:



5.4. Conclusions

Temporal analysis of products (TAP) pulsing experiments were performed to gain an understanding of atomic level phenomena occurring at the level of the Brønsted acid sites in H-ZSM-5 for the alkylation of toluene with methanol. A minute amount of reactants were pulsed in to the reactor held under high vacuum such that the pulse interacts with the catalyst for short time periods of < 2 s. Two variations of pulsing experiments were performed.

First, saturation experiments revealed the predominance of methanol dehydration in the pores of the zeolite both in the absence and presence of water. When pulsing methanol into a zeolite saturated with toluene, accumulated and unreacted toluene accompanied by low yields of xylene was observed. The displacement of toluene by the smaller methanol pulses also point to methanol competitively binding over toluene at the Brønsted acid sites. On the other hand,

prior saturation of the zeolite with methanol increases the xylene yield by a factor of twenty, confirming that methanol dehydration is necessary prior to the attack of the surface methoxy species by toluene.

Finally, pump-probe experiments in which methanol and toluene pulses were separated by pre-set delay times reveal an inverse linear dependence of the xylene yield on reactant pulse separations, with higher yields obtained from reactant pulses that follow each other closely in time. These experiments reveal that methanol dehydration under reaction conditions enabled by the TAP reactor proceeds through the formation of reaction intermediates that have a finite lifetime that are utilized by probe toluene pulses in efficiently forming xylene. Overall, results obtained from these experiments enable the understanding of the acid catalyzed mechanisms that underly the methylation of toluene and overall will aid in the design of zeolite catalysts that show excellent selectivity to p-xylenes.

6. Effects of Catalyst Phase on the Hydrogen Evolution Reaction of Water Splitting: Preparation of Phase-pure Films of FeP, Fe₂P, and Fe₃P and their Relative Catalytic Activities

This chapter details the work done in the identification, synthesis, and rationalization of the exceptional hydrogen evolution reaction kinetics exhibited by various iron-phosphide materials. Synthesis, structure characterization and electrocatalytic evaluation were done by our collaborators from Department of Chemistry, Rice University (Dr. Desmond E. Schipper and Dr. Kenton H. Whitmire) and from the Department of Electrical and Computer Engineering, University of Houston (Dr. Zhenhuan Zhao and Dr. Jiming Bao). Our contribution to this work is limited to providing a fundamental atomic understanding of catalyst surfaces, hydrogen dissociation and coverage effects for the iron-phosphorous systems through foundational concepts based on density functional theory simulations. The results from these collaborations were published as two papers in the journals *Nano Energy*¹⁸³ and *Chemistry of Materials*.¹⁸⁴

6.1. Introduction

The electrolysis of water into hydrogen fuel and oxygen offers a convenient route to store intermittent solar and wind energy chemically and an ideal solution for channeling off-peak power production and minimizing energy losses incurred in power transmission from often remote locations.¹⁸⁵ The utilization of active, stable electrocatalysts with lower overpotentials will increase efficiency and stability, and enable commercialization.^{186,187} Over the past several decades, tremendous progress has been made in the development of highly active catalysts composed of earth-abundant elements including transition metal phosphides (TMPs),^{188–190} carbides,^{191–193} nitrides,^{194–196} and chalcogenides^{197–199} as well as carbon-based nanomaterials^{200–202} for OER and HER. Catalysts active for both reactions in the same electrolyte are preferred for practical applications. However, the vast majority of existing catalysts are unsuitable for use in the same electrolyte due to the mismatch of pH ranges in which the electrocatalysts are both stable and sufficiently active.

Since the first report of the TMP Ni₂P as an electrocatalyst for water splitting in 2013,²⁰³ TMPs have emerged as premier electrocatalysts for OER,^{193,204} HER,^{188,203,205,206} and in some cases overall water splitting.^{207,208} For the TMPs that are capable of overall water splitting, their bifunctionality arises from the respective TMP's ability to catalyze the HER and serve as a precatalyst for the OER.²⁰⁹ The current preparation methods for TMPs can be grouped into four main routes: thermal phosphidation of films²¹⁰ or nanostructured/bulk alloys,^{193,208} electrochemical deposition,²¹¹ metallurgical synthesis,²¹² and solvothermal methods.^{205,206} However, these methods require harsh conditions with toxic gaseous chemicals, and offer little control over the metal-phosphorus stoichiometry, phase purity, and conductivity. For example, while (Co_{0.52}Fe_{0.48})₂P can be used as both anode and cathode to achieve a low cell voltage of 1.53 V, the material fabrication

process, which involves a combination of arc-melting Co_2P , Co and Fe followed by selective electrochemical etching,²⁰⁸ is not suitable for scaled-up production. As TMPs are known to oxidize rapidly to highly active metal oxyhydroxides at their surface upon OER operation, it is therefore important to retain a conductive TMP core for fast charge transport, a structural feature which is highly dependent on the fabrication method. With several examples of bifunctional TMPs, there is now an impetus for the development of new strategies to fabricate these high performance materials.

We have recently shown that metal-organic chemical vapor deposition using single-source molecular precursors (SS-MOCVD) has been a fruitful means to achieving thin films of binary and ternary TMPs. The method relies on the ability to control the stoichiometry of the produced materials by building the desired stoichiometry into the precursor.²¹²⁻²¹⁴ With this method, binary and ternary TMPs can be prepared by tailoring the metal elements in a single volatile precursor or by simply blending isolobal organometallic compound precursors. Recently, the SSP-MOCVD method was used to grow FeMnP on TiO_2 -nanorod arrays for photoelectrochemical OER, and it was found that the TiO_2 /FeMnP core/shell structure remained stable at the theoretical photocurrent density of TiO_2 .^{215,216} Fe_3P and FeMnP thin films on quartz have also been obtained using $\text{H}_2\text{Fe}_3(\text{CO})_9\text{P}^t\text{Bu}$ and $\text{FeMn}(\text{CO})_8(\mu\text{-PH}_2)$ as precursors. The method was extended to afford additional compositional variation by co-decomposing isostructural precursors with varying stoichiometry. This yielded $(\text{Fe}_{1-x}\text{Co}_x)_3\text{P}$ in the range $(0.09 < x < 0.22)$, which was synthesized by employing blends of $\text{H}_2\text{Fe}_3(\text{CO})_9\text{P}^t\text{Bu}$ and $\text{Co}_3(\text{CO})_9\text{P}^t\text{Bu}$ as the MOCVD feedstock. Among the key advantages of the SS-MOCVD method are the ability to grow complex, single-phase TMPs directly on active substrates non-destructively and without the use of binders. These materials were subjected to electrochemical characterization and enhanced electrocatalytic activity and hy-

drogen evolution observed for these metal-phosphide Fe_xP ($x = 1, 2, 3$) materials was rationalized by electrocatalytic testing and detailed density functional theory simulations.

6.2. Experimental and Computational Methods

6.2.1. Growth of FeP, Fe_2P and Fe_3P Crystals

The precursors $\text{Fe}(\text{CO})_4\text{PH}_3$ (**1**), $\text{Fe}(\text{CO})_4\text{P}^t\text{BuH}_2$ (**2**) and $\text{H}_2\text{Fe}_3(\text{CO})_9\text{P}^t\text{Bu}$ (**4**) were prepared according to literature methods and standard Schlenk technique. **3** is a new compound and its synthesis is reported below. Sodium hydroxide, tert-butyldichlorophosphine as a 1.0 M solution in diethyl ether, methanol, and iron pentacarbonyl were obtained from Sigma Aldrich and used without further purification. Sodium hydride as a 60% dispersion in mineral oil was rinsed with hexane (10 mL per 1 g NaH dispersion, three times) prior to use. Synthetic manipulations were performed exclusively under a dry nitrogen atmosphere, and solvents as well as iron pentacarbonyl were degassed prior to use. Compounds **1**, **2**, and **3** were stored at -10°C under nitrogen while **4** was stored at room temperature in a nitrogen-filled glovebox. FTO glass (TEC 7, with resistivity of $6\text{--}8\ \omega\text{cm}^{-2}$) was obtained from Hartford Glass Co. and cut into $1\text{ cm} \times 2\text{ cm}$ pieces. Quartz microscope slides (1 mm thick) were obtained from Ted Pella Inc. Films were stored under ambient conditions after deposition.

Synthesis of **3**: To a chilled (-10°C) suspension of sodium hydroxide (1.9 g, 46 mmol) in 10 mL of methanol was added 2 mL of iron pentacarbonyl (15 mmol) and the resulting solution stirred at 1 h at this temperature before warming to RT after which the solution was allowed to stir for 20 h. The solvent was then removed in vacuo and the solids thoroughly dried. To the resulting solids were then added 80 mL of tetrahydrofuran to extract $\text{Na}[\text{HFe}(\text{CO})_4]$, the solution of

which was filtered into a flask containing 0.1865 NaH (7.8 mmol). Strong bubbling signaling the release of hydrogen concomitant with the formation of $[\text{Fe}(\text{CO})_4]^{2-}$ was observed which subsided after 30 m at which point an infrared spectrum of the solution indicated the presence of both $[\text{Fe}(\text{CO})_4]^{2-}$ and $[\text{HFe}(\text{CO})_4]^-$. Then, 14 mL of a 1 M solution of P^tBuCl_2 (14.0 mmol) in diethyl ether was added in 2 mL aliquots spread over five minutes accompanied by a change in color from brown-orange to yellow-orange. After stirring overnight, the solvent was removed in vacuo and the solid treated with hexane (80 mL) and filtered. The filtered solution was then reduced to an oil in vacuo and left to crystallize at -10°C . After three days at this temperature, large masses of crystals were found in the oil which was filtered off. The crystals were washed with 10 mL of hexane to yield 0.41 g (9.4% yield) of crystalline 3. The filtered oil continued to produce crystals of 3 upon standing at room temperature and after two weeks of standing yielded another 0.47 g of product for a total yield of 23.6%.

6.2.2. Growth of Thin Films on Substrate

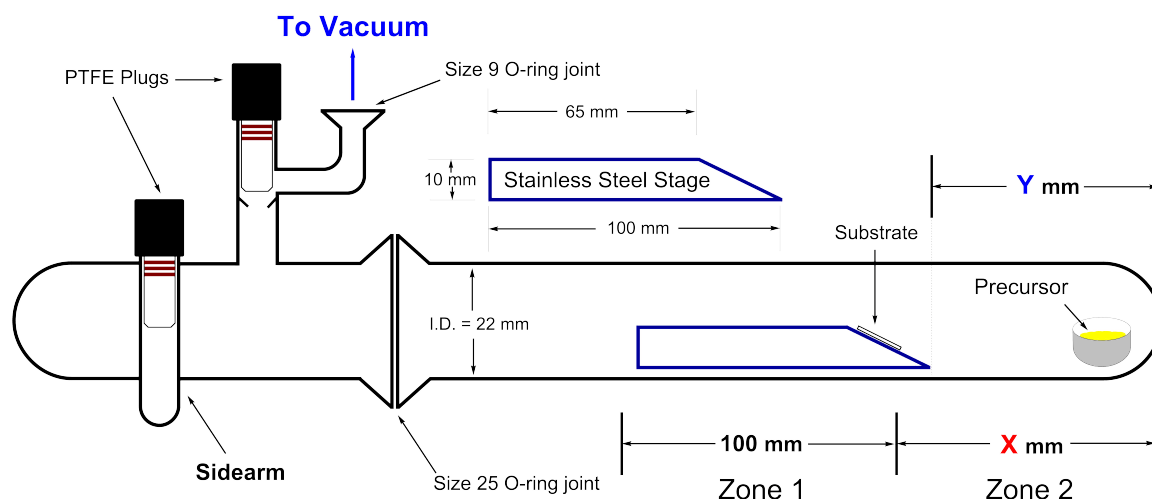


Figure 6.1. The deposition apparatus. X and Y parameters for each deposition can be found in Table B.1.

Film deposition was carried out in a similar manner as previously reported.²¹³ Key differences are that the distances of the tip of the metal stage to the end of the tube and the start of the heating zone were varied according to X and Y in Figure 6.1. Another key difference is that small boats/cups made out of aluminum foil (1 cm deep, 1 cm in diameter) were used to weigh and transfer the precursor to the bottom of the tube, which made it easier to get the precursor to the bottom of the tube without having any to stick to the walls. This was especially helpful when working with **2** as it is a liquid. Substrates were cut into $\sim 20.5\text{ mm} \times 11\text{ mm}$ sections and affixed to the stage with silver paste. The material production parameters are given in Table B.1. After deposition, the heating zone was shifted forward to envelop the stage and the material on the substrate allowed to anneal for two hours at the deposition temperature before slow cooling to room temperature. Note: Fe_3P was annealed for 24 h at 550°C to get a satisfactorily crystalline material, which was then used for HER testing. The unannealed PXRD for the Fe_3P on FTO is given in Figure B.13. An aluminum foil jacket was placed over the end of the tube for Fe_3P deposition to encourage volatilization of the precursor.

6.2.3. Characterization

The structure of all samples were characterized by SEM with an FEI Quanta 400 FEG microscope operated at 5 kV and a TEM (JEOL 2010H) operated at 200 kV. The element composition was analyzed by EDS mapping and wavelength dependent dispersive X-ray spectroscopy (WDS) with a JEOL JXA 8530F Hyperprobe. X-ray photoelectron spectroscopy (XPS) was carried out on a Physical Electronics PHI Quantera SXM instrument using a monochromatic Al $K\alpha$ source (1486.6 eV) operated at 40.7 W with a beam size of $200\text{ }\mu\text{m}$ and a take-off angle of 45° . Sputtering was performed with by 2 mm 3keV Ar^+ ion beam

with 0.5 mA current. The X-ray powder diffraction (XRD) was conducted on a SIEMENS Diffractometer D5000 equipped with a Cu target. The Raman spectra were recorded on a Horiba Triax550 spectrometer with an excitation wavelength of 532 nm. Powder-XRD scans were collected on a Rigaku Ultima II vertical θ - θ powder diffractometer using Cu K α radiation with Bragg-Brentano para-focusing optics. ^1H and ^{31}P NMR data were recorded on a 500 MHz Bruker spectrometer (202 MHz for ^{31}P). ESI-MS data were collected on a Bruker Daltonics microTOF ESI/MS coupled with an Agilent 1200 HPLC instrument. Elemental analyses were performed by Galbraith Laboratories Inc.

Diffraction data for the Fe_xP crystals were collected on a Rigaku SCX-Mini diffractometer (Mercury2 CCD) using graphite-monochromated Mo K α radiation ($\lambda = 0.71073 \text{ \AA}$). Integration was performed with CrysalisPro, and empirical absorption correction was applied using spherical harmonics implemented in the SCALE3 ABSPACK scaling algorithm. All structures were solved by direct methods and refined on F^2 by full matrix least squares using the SHELXTL software package. All thermal ellipsoid plots were generated using Olex2. The groups bound to the diphosphine unit were modeled in two parts, the occupancies were constrained to overall unit occupancy. The non-hydrogen atoms of part 1 were refined anisotropically and without restraints. However, the non-hydrogen atoms of part 2 were refined isotropically, and their bond lengths and angles set to refine to the corresponding atoms of part 1 with SADI commands.

6.2.4. Electrochemical measurements

Electrochemical measurements of the as-deposited FeP , Fe_2P and Fe_3P films were conducted on a 263A Princeton Applied Research (PAR) potential/galvanostat instrument in a three-electrode setup with $\text{Ag} \mid \text{AgCl}$ and Pt plate as the reference electrode, and counter electrode, respectively. The electrolyte solution was

0.5 M H₂SO₄ which was bubbled with N₂ gas for 30 min before use. Linear sweep voltammetry (LSV) was carried out at a scan rate of 5 mV/s for the polarization curves. Electrochemical impedance spectroscopy (EIS) was performed at an AC amplitude of 10 mV in a frequency range of 100000 Hz to 10 mHz at pre-set overpotentials. IR correction was made using the equivalent series resistance from the Nyquist plots in EIS measurements. Before use, the samples were wired using copper wire with silver paste. Epoxy was used to cover the silver paste and the sample leaving an exposed area of 0.5 cm². Cyclic voltammetry (CV) was performed at different scan rates in the non-Faradaic reaction potential range to derive the electrochemical double-layer capacitance for the calculation of electrocatalytically active surface area (ECSA). The potential versus that of reversible hydrogen electrode (RHE) was calculated with reference to Ag | AgCl according to the Nernst equation: $E_{\text{RHE}} = E_{\text{Ag} | \text{AgCl}} + 0.059 \times 0.3 + E^0$, where E_{RHE} is the potential vs RHE, $E_{\text{Ag} | \text{AgCl}}$ is the measured potential vs Ag | AgCl, and $E^0 = 0.2$ V at 25° C. The long-term stability was evaluated by chronoamperometry measurement at overpotential of 120 mV. The Faradaic efficiency was obtained by comparing the amount of produced H₂ at the electrode with the amount of calculated H₂ according to current. The produced H₂ was analyzed by a gas chromatography (GC) equipped with a thermal conduction detector (TCD) with Ar as the carrier gas, which was calibrated with H₂ in advance.

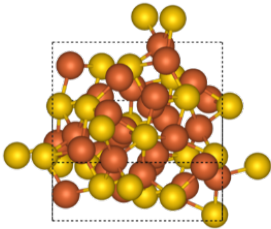
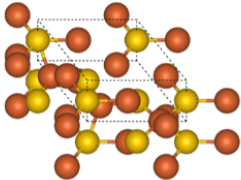
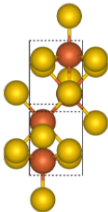
6.2.5. Density Functional Theory Calculations

Density functional theory (DFT) calculations were performed using the Vienna Ab-initio Simulation Package (VASP)^{79–81} and interfaced through the Atomic Simulation Environment (ASE).⁸³ The Bayesian error estimation functional^{40,144} was used in conjunction with the projector augmented wave (PAW) method⁸⁴ to iteratively solve the Kohn-Sham equations. A plane wave cutoff energy of 500

eV and a Gaussian smearing width $k_B T = 0.1$ eV was employed to ensure accurate extrapolation to obtain ground state energies. Bulk unit cells of Fe_xP were sampled with a $(12 \times 12 \times 12)$ Monkhorst-Pack k-point grid and surface facets created from these unit cells were sampled with a $(6 \times 6 \times 1)$ k-point grid.²¹⁷ The surface slabs were separated by a vacuum layer of 15 Å in the z-direction and were corrected for any spurious dipole moments arising from adsorbates present on only one side of the slab.²¹⁸ Convergence with respect to k-point grid and vacuum spacing was confirmed for all models and all unconstrained atoms in the models were relaxed using a force convergence criterion of 0.02 eV/Å.

The primitive unit cells of Fe_3P , Fe_2P and FeP were obtained from the Materials Project database²¹⁹ and were optimized for use with the BEEF-vdW functional and other calculation parameters chosen for the iron-phosphide surfaces. The optimized lattice parameters and bulk unit cell visualizations for all three materials are given in Table 6.1 and are in good agreement with those obtained from the characterization done in this work.

Table 6.1. Bulk unit cells and optimized lattice parameters of Fe₃P, Fe₂P and FeP

Iron Phosphide	Unit Cell	Lattice Parameters
Fe ₃ P		Crystal System: Tetragonal $a = b = 9.07 \text{ \AA}$ $c = 4.39 \text{ \AA}$
Fe ₂ P		Crystal System: Hexagonal $a = 5.82 \text{ \AA}$ $b = 5.04 \text{ \AA}$ $c = 3.42 \text{ \AA}$
FeP		Crystal System: Orthorhombic $a = 3.04 \text{ \AA}$ $b = 5.16 \text{ \AA}$ $c = 5.77 \text{ \AA}$

The existence of a diverse range of surface terminations under electrocatalytic conditions renders an exhaustive search of active surface facet intractable. Therefore, we employed the Bravais-Friedel-Donnay-Harker (BFDH) crystal morphology algorithm²²⁰ to obtain predictions of exposed surface facets based only on the lattice parameters of the primitive unit cells. Based on these predictions, the (100) facet for Fe₃P, the (100) and (001) facets of Fe₂P and the (100) and (011) facets of FeP were further investigated. Kibsgaard and coworkers¹⁸⁸ concluded that the P-terminated FeP(011) surface facet was an HER active surface termination. The same surface was used in the work of Chung et al.²²¹ and we considered it as additional surface to keep a common reference point to prior work. All surfaces were modeled as (2×2) or (3×2) surface unit cells with similar total surface area per unit cell and 4-layer equivalents along the z-direction. The adsorbates and the top half of the surfaces were unconstrained and allowed to relax to

their ground state geometries. Cleavage of Fe_2P along the (001) direction results in the formation of bilayered and asymmetrically terminated slabs. Therefore, the surface formation energy was calculated as per the procedure outlined in the work of Santos-Carballal and coworkers.²²² Similarly, a (011) FeP surface facet is also bilayered in nature can be exposed as either Fe-terminated or P-terminated surfaces.

All binding energies were referenced to a clean relaxed slab and a fully relaxed gas-phase hydrogen molecule, which was centered in a box of dimensions $12 \times 12 \times 12 \text{ \AA}$, sampled at the Γ -point. All other input parameters were set identical to those in surface calculations, except for the Gaussian smearing width, which was reduced to 0.01 eV.

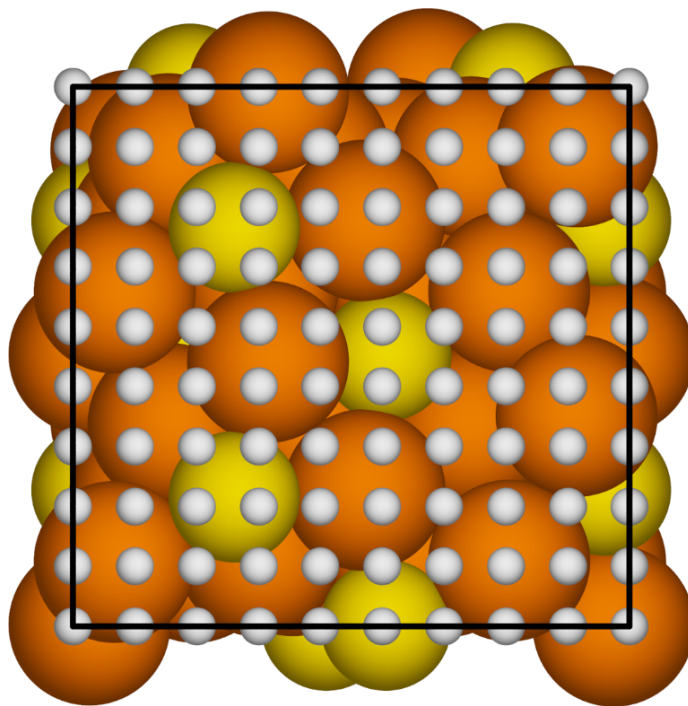


Figure 6.2. Regular grid of 100 H atoms fixed in their (x, y) cartesian coordinates on the $\text{Fe}_3\text{P}(100)$ surface.

The surface formation energies for all surface facets of Fe_xP models were calculated as per the procedure outlined in the work of Santos-Carballal and

coworkers.²²² The surfaces of Fe₃P, Fe₂P and FeP were populated with hydrogen atoms to determine preferred binding sites. This was done by adsorbing hydrogen atoms based on a grid on select surface facets. Hydrogen atoms were adsorbed onto the surface of the catalyst at pre-determined, regularly spaced and coordinates, as seen in Figure 6.2. While this image visualizes all hydrogen atoms in their respective grid positions, the actual relaxation was performed with only one atom at a time. The laterally constrained hydrogen adsorbate was allowed to move in the direction normal to the surface. In addition, the top half of the surface is allowed to relax as in all other calculations performed in this work. A force convergence criterion of 0.02 eV/Å² was used to ensure strict geometric convergence. Contour plots depicting areas of the surface that bind hydrogen strongly were generated.

All relaxed surfaces for Fe_xP show minor rearrangement to form distinct Fe-Fe bridge sites and hydrogen binds preferentially to these sites. Based on these observations, we define the surface coverage $\theta = \frac{n}{M}$, where n is the number of adsorbed hydrogen atoms, and M is the number of preferred adsorption sites. The average dissociative binding energy of hydrogen was calculated using

$$\Delta E_H^{avg}(n) = \frac{(E_{n_{ads}+slab} - n \cdot \frac{E_{H_2}}{2} - E_{slab})}{n}, \quad (6.1)$$

where n is the number of hydrogen atoms, $E_{n_{ads}}$ is the energy of the slab with n hydrogen atoms, E_{H_2} the gas phase reference energy, and E_{slab} the energy of a clean slab. The differential free energy of hydrogen adsorption is shown to be an excellent descriptor of intrinsic HER activity of transition metal phosphide surfaces.¹⁸⁸ To calculate the average free energy of formation of adsorbed hydrogen

atoms we use

$$\Delta G^{0,avg}(n) = \Delta E_H^{avg}(n) + \Delta ZPE - T\Delta S_H, \quad (6.2)$$

where ΔZPE is the zero-point energy difference and ΔS_H is the entropic correction at $T = 300$ K and $P = 1$ bar. Entropic contributions were estimated from vibrational frequencies obtained in the harmonic oscillator approximation. The differential free energy of adsorption ($\frac{\partial \Delta G_H}{\partial n_H}$) as a function of coverage was calculated as per the procedure outlined in ref²²³ according to

$$\frac{\partial \Delta G_H}{\partial n_H}(n) = n.\Delta G^{0,avg}(n) - (n-1).\Delta G^{0,avg}(n-1). \quad (6.3)$$

Water molecules and an additional electrostatic field have been found to negligibly affect the adsorption of hydrogen on the surface,²²⁴ and were not considered in our calculations.

6.3. Results and Discussion

6.3.1. MOCVD Growth of Phase Pure Thin Films of FeP and Fe₂P

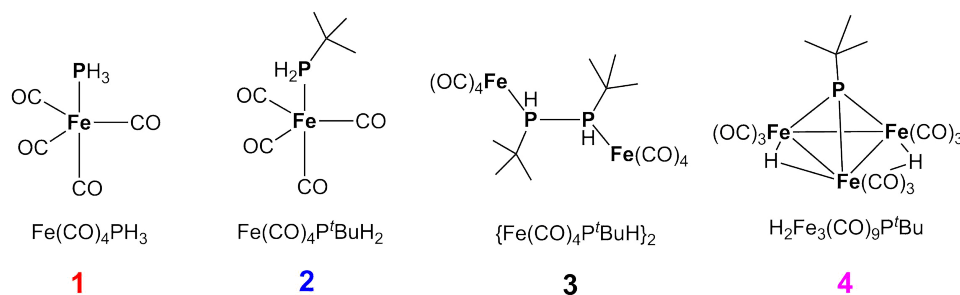
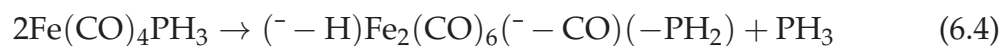


Figure 6.3. Structures of the molecular precursors 1-4 used for the synthesis of FeP, Fe₂P and Fe₃P in this work.

Compound **1** has been previously demonstrated to yield nanoparticles of FeP by solution-based decomposition²²⁵ and was explored as a CVD precursor; however, it was found that Fe₂P was the only material that deposited on a quartz substrate in our apparatus at 350~ C (Table B.1) . The ³¹P and ¹H NMR spectra of the off-gases from the decomposition of **1** under CVD conditions confirmed the elimination of PH₃ (Figure B.1, Figure B.2, Figure B.3 and Figure B.4). At temperatures $\geq 400^{\circ}$ C, a mixture of FeP and Fe₂P was obtained. The ability to form phase pure Fe₂P suggests that there is a very clean rearrangement process occurring at the lower temperatures to give a precise Fe₂P precursor with stoichiometric loss of P. A possible intermediate step is provided in Equation 6.4.



It was reasoned that with compound **2**, a ^tBu group in place of a hydrogen could slow, and potentially stop, the release of phosphorus as PH₃ during decomposition since PH₂^tBu is a stronger donor and should be bound more tightly.²²⁶ At 350~ C, Fe₂P was again the product but decomposition of **2** at 450~ C gave phase-pure FeP. Although both **1** and **2** lost phosphorus at 350~ C, the loss of phosphorus from **1** was slowed by increasing the decomposition temperature to 450~ C and eliminated completely using **2** at 450~ C, suggesting that decomposition occurs at that temperature before rearrangement with the loss of phosphorus can take place.

While both precursors gave Fe₂P as the sole product at lower decomposition temperatures (350 ~ C), more crystalline Fe₂P was obtained from **1**. In contrast, the new derivative **3** that contains a P–P bond was found to give pure FeP at 350 ~ C, although the deposition time required (8 h vs. 15 m) was longer due to the lower volatility of **3** compared to that of **2**. The films of FeP derived

from **2** or **3**, however, were indistinguishable.

Compound **3**, which is a rare example of metallated organodiphosphane, is prepared by treating an equal molar mixture of Na[HFe(CO)₄] and Na₂[Fe(CO)₄] with ^tBuPCl₂ in tetrahydrofuran. The molecule crystallizes in the chiral space group *P*₄₃*2*₁*2* as a racemic twin (Figure 6.3) possessing two crystallographically distinct, dimeric "Fe(CO)₄(H)P^tBu" units joined by a P–P bond. The diphosphine (P^tBuH)₂ has never before been observed as a ligand, and only six examples of a diphosphine with formula = PR(H) have been previously structurally characterized.^{227–231} Notably, the diphosphane coordinates at the equatorial rather than axial positions on Fe, an uncommon configuration usually associated with π– acceptor ligands.^{232,233} The molecule is C₂ symmetric and both enantiomers are observed in an 85:15 ratio in the structure, although the crystals themselves are chiral and refined as a racemic twin. Interestingly the two forms in the crystal structure show dramatically different rotational conformations (Figure 6.3). The ³¹P and ¹H NMR spectra show complex second order behavior with the overall pattern consistent with those observed for the few existing related compounds.^{228,229} Crystallographic refinement parameters and selected bond lengths and angles are available in Table B.2 and Table B.3.

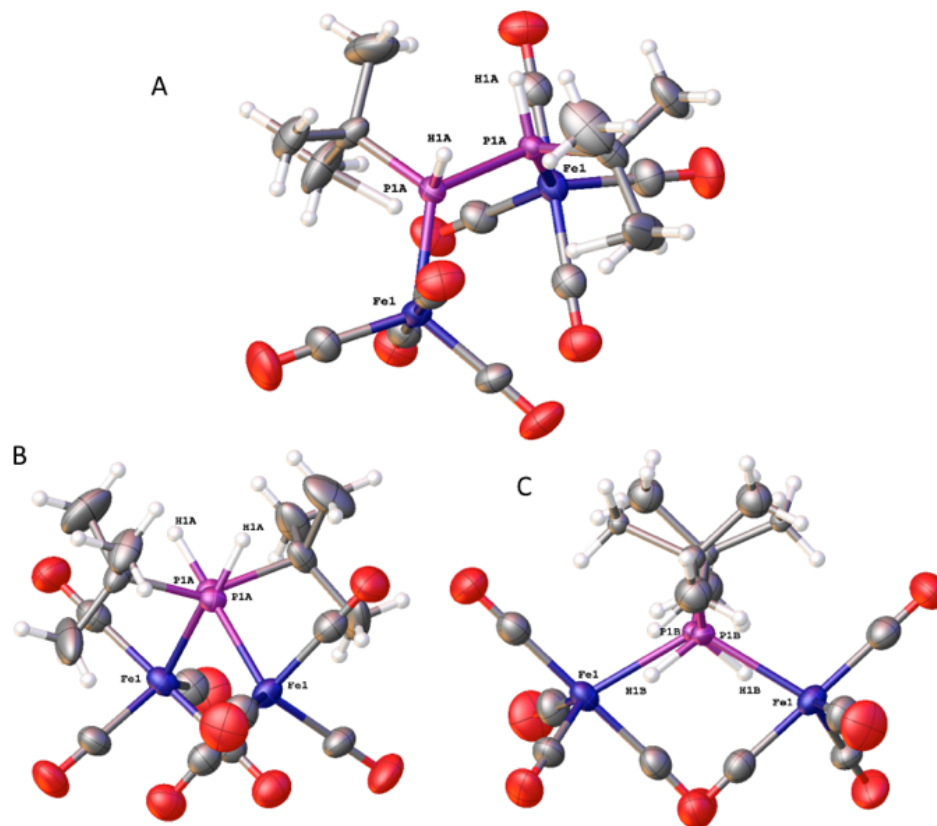


Figure 6.4. (A) Crystal Structure of the major component of 3 (R,R isomer). (B) Major component of 3 viewed down the P–P bond (C) Minor Component of 3 viewed down the P–bond. Thermal ellipsoids are given at 50% probability.

6.3.2. Film Characterization

The films on quartz were characterized by (1) Powder-X-Ray Diffraction (PXRD) to establish phase, (2) X-ray Photoelectron Spectroscopy (XPS) depth-profiling to ascertain homogeneity, and (3) Scanning Electron Microscopy (SEM) for morphology (Figure B.5, Figure B.6, Figure B.7, Figure B.8). The powder pattern of FeP was indexed to its known orthorhombic *Pnma* setting (Figure 6.5 A). XPS depth profiling confirmed a 1:1 Fe:P ratio with only trace oxygen and carbon (Figure 6.5 D). The surface was partially oxidized, but the interior was composed solely of Fe and P whose binding energies of 706.9 eV and 129.65 eV

closely match the literature values of 706.9 eV and 129.34 eV, respectively.²³⁴ The SEM images show that the film consists of rectangular crystallites approximately 500 nm in length (Figure B.6). Films of FeP on quartz from precursor **3** were morphologically similar (Figure B.7), although preferred orientation is apparent in the powder spectrum (Figure B.9).

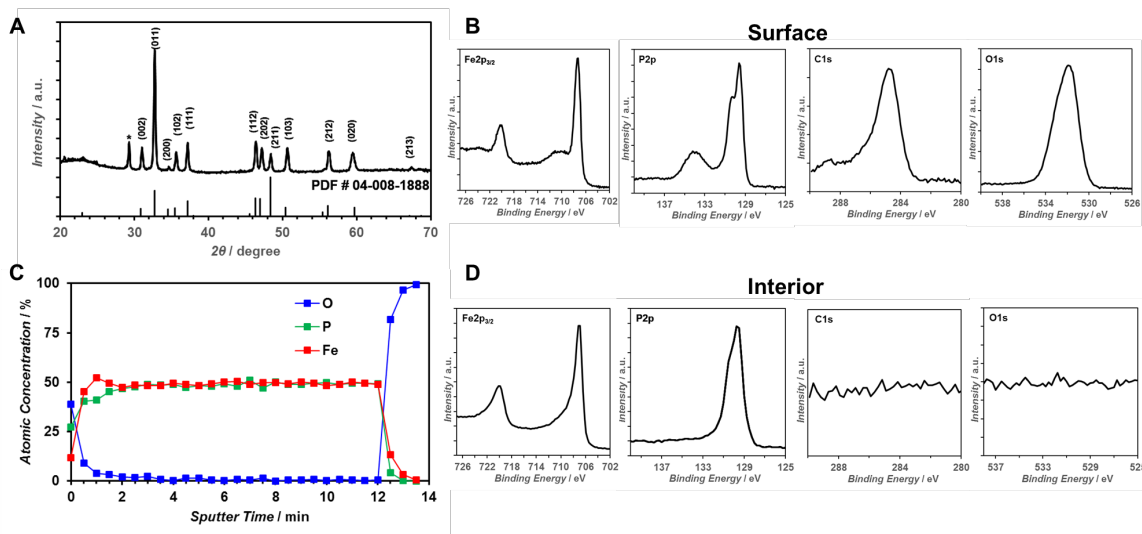


Figure 6.5. XRD, XPS, and XPS-Depth Profile of FeP on Quartz; A) XRD, B) Surface XPS Spectra, C) XPS Depth Profile, D) Interior XPS Spectra. Peaks denoted by * in the XRD pattern arise from the substrate.

Similarly, Fe₂P was characterized by SEM (Figure B.8), PXRD (Figure 6.6 A), and XPS analysis with depth profiling (Figure 6.6 B-D). The XRD pattern was indexed to the known hexagonal $P\bar{6}2m$ setting for Fe₂P. XPS depth profiling demonstrated the film is homogeneous with only trace oxygen and carbon. Like the FeP, the surface was partially oxidized, but the interior was pristine. The binding energies for Fe and P were 706.8 eV and 129.55 eV, close to the reported values of 706.8 eV and 129.31 eV.²³⁴ SEM shows the film to consist of contiguous hexagonal towers, reflecting the hexagonal symmetry of the Fe₂P crystal system.

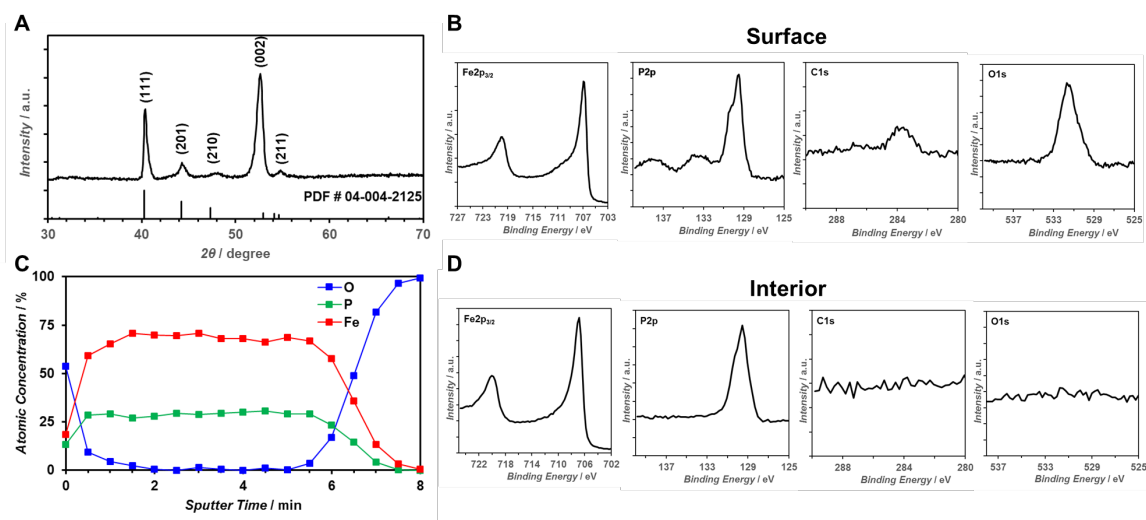


Figure 6.6. XRD, XPS, and XPS-Depth Profile of Fe₂P on Quartz; A) XRD, B) Surface XPS Spectra, C) XPS Depth Profile, D) Interior XPS Spectra.

FeP, Fe₂P, and Fe₃P were grown on FTO analogously to the depositions on quartz. Fe₃P was grown as previously reported.²¹² The films were characterized by XRD, SEM, and XPS. The XRD patterns of the respective materials confirm the phase identity and purity of the respective iron phosphides (Figure B.10, Figure B.11, Figure B.12, Figure B.13). SEM images reveal clear morphological differences among the iron phosphides (Figure 6.7).

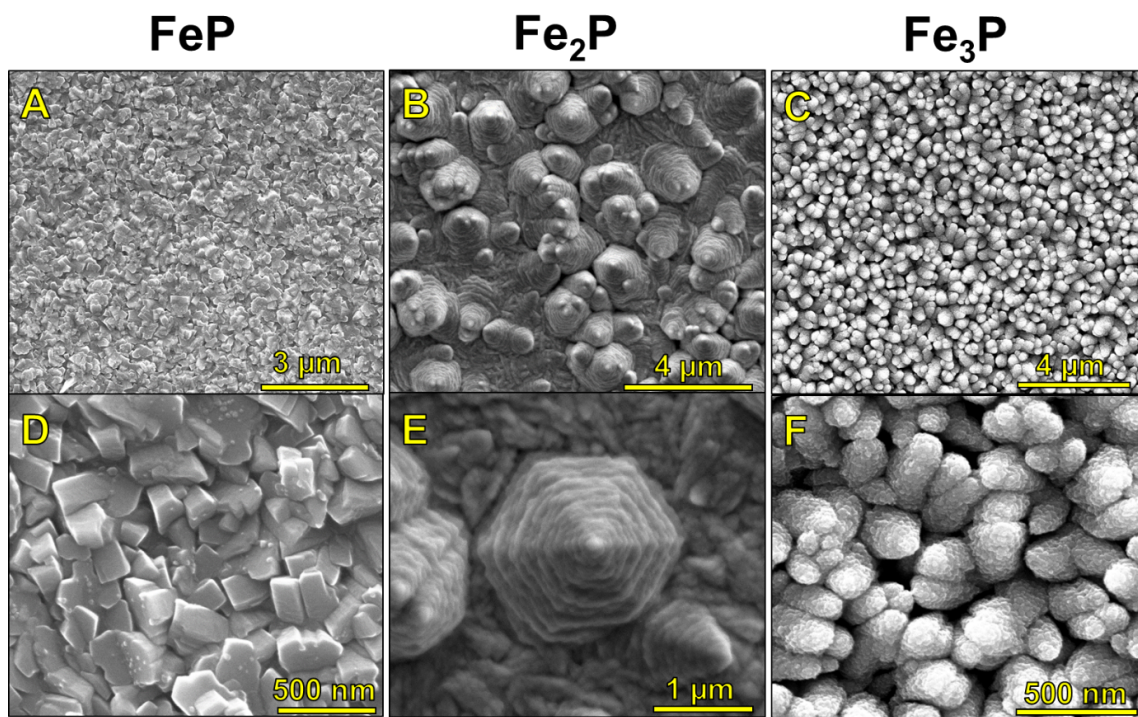


Figure 6.7. SEM images of FeP (A) and (D), Fe₂P (B) and (E), and Fe₃P (C) and (F) on FTO.

FeP consists of rectangular prisms, Fe₂P stacked hexagonal sheets, and Fe₃P cauliflower-like growths. These shapes can be attributed to the crystal structures of the respective iron phosphides. The rectangular blocks observed for FeP are consistent with an orthorhombic space group, the hexagonal sheets observed for Fe₂P are consistent with a hexagonal space group, and the cauliflower-like shape for the Fe₃P can be attributed to its tetragonal crystal system which has a tendency to twin along the {011} faces.

6.3.3. Catalytic Activity of the Iron Phosphide Films

For HER characterization, films of FeP, Fe₂P and Fe₃P, whose synthesis on quartz has been detailed previously starting from H₂Fe₃(CO)₉P^{*t*}Bu (4), were grown on FTO. Importantly, the ability to use a single-method to grow films of phase-pure, high quality (trace oxygen and carbon) materials cleanly on a con-

ductive substrate facilitates direct comparison of FeP, Fe₂P, and Fe₃P. It is shown that the sequence of HER activity follows the series Fe₃P > Fe₂P > FeP with stability following the same trend. These results point to metal-rich phosphides, particularly the Fe₃P phase, as being superior to metal-poor phosphides for HER.

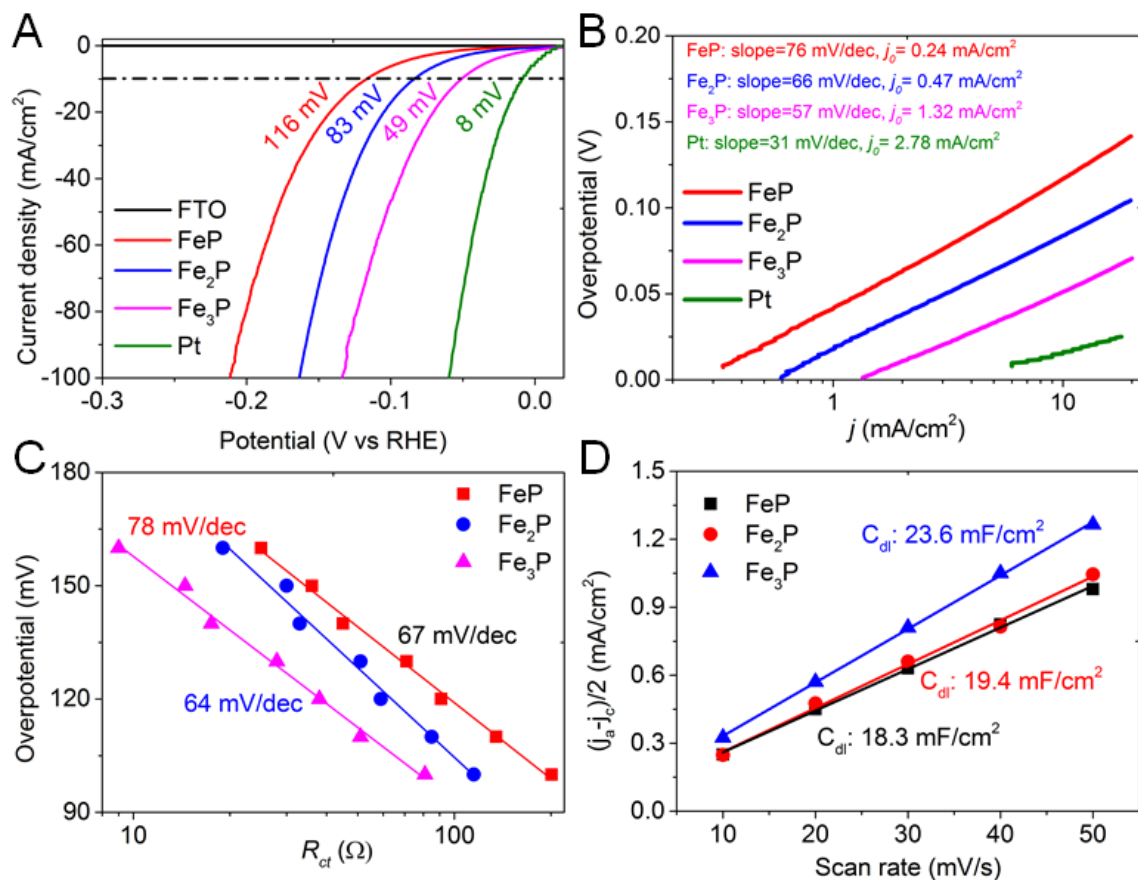


Figure 6.8. Electrochemical characterization. (A) Polarization curves. (B) Corresponding Tafel slopes. (C) Charge transfer Tafel slopes. (D) Half of the current density differences as a function of scan rate.

The HER activity was evaluated with a three-electrode configuration in 0.5 M H₂SO₄, and the respective as-deposited iron phosphide on FTO was directly used as the working electrode. Figure 6.8 A and B show the polarization curves after iR -correction and the corresponding Tafel slopes for the iron phosphides. The overpotential is defined as the potential to reach a current density of 10 mA/cm².^{2,235} The performance of Pt was used as a reference and is in good

agreement with reported values;²³⁶ the bare FTO shows negligible HER performance. The overpotentials for the FeP, Fe₂P and Fe₃P electrodes are 116 mV, 83 mV and 49 mV, respectively, as shown in Figure 6.8 A. The corresponding Tafel slopes for FeP, Fe₂P, and Fe₃P are 79 mV/dec, 66 mV/dec and 57 mV/dec. The HER performance increases in the order FeP, Fe₂P and Fe₃P, with the increase of iron content or with the decrease of P content. The exchange current density (j_0) was obtained by extrapolating the linear part of the Tafel plots to intersect with the x-axis.¹⁸⁹ Fe₃P has the highest intrinsic catalytic activity of the tested iron phosphides as assessed by having the highest exchange current density of 1.32 mA/cm² as shown in Figure 6.8 B.

Nyquist plots derived from electrochemical impedance spectroscopy (EIS) were employed to investigate the HER kinetics, as shown in Figure B.14. All electrodes show a similar semicircular profile without Warburg impedance in the low frequency range, indicating the mass transport is rapid and is kinetically controlled.²³⁷ The active sites at the surface can be easily accessed by the electrolyte ions. The Nyquist plots can be fitted with the equivalent circuit consisting of the equivalent series resistance (R_s) and the charge transfer resistance (R_{ct}) with the constant element referring to the double layer capacitance. All the electrodes have similar R_s values of about 5 Ω . Fe₃P exhibits the lowest charge transfer resistance of 25 Ω at the same overpotential of 160 mV, compared to FeP and Fe₂P, indicating that Fe₃P has the fastest charge transfer rate during the HER.²⁰⁰ The charge transfer Tafel slope was determined from the slope of the linear fitting of the plot of $\log R_{ct}$ versus overpotential (Figure 6.8 C and Figure S27). It is found that the values of the slopes fall between 39 mV/dec and 118 mV/dec, indicating the charge transfer is the rate determining step.²³⁸ The Fe₃P electrode displays the lowest charge transfer Tafel slope of 64 mV/dec, further confirming that its charge transfer kinetics in the HER process are faster than those of Fe₂P and FeP.

The electrocatalytically active surface area (ECSA) was obtained by measuring the electrochemical double layer capacitance using cyclic voltammetry in a non-Faradaic reaction potential range, as shown in Figure 6.8 D. The ECSA for FeP, Fe₂P and Fe₃P were 18.3 mF/cm², 19.4 mF/cm² and 23.6 mF/cm², respectively. The Fe₃P possesses the largest ECSA, in good agreement with it exhibiting the highest HER performance. We also investigated the long-term stability of the as-deposited catalysts by chronoamperometry measurements at an overpotential of 120 mV in 0.5 M H₂SO₄ solution (Figure Sx) . The current density of Fe₃P is almost 2.7 times higher and six times higher than that of Fe₂P and FeP, respectively, further confirming the superior HER performance of Fe₃P compared to Fe₂P and FeP. All the electrodes show stable current density over 20 hours operation. The Faradaic efficiencies of FeP, Fe₂P and Fe₃P were evaluated by comparing the measured amount of hydrogen by gas chromatography to the calculated amount of hydrogen according to the recorded current. The Faradaic efficiency was 96% , 98% and 97% for FeP, Fe₂P and Fe₃P (Figure B.15 B), respectively.

The oxidation states of the tested Fe₃P film were determined with XPS (Figure B.16). The surface XPS spectra indicates the existence of Fe and P consistent with an iron phosphide having peaks located at 707.6 eV for Fe and 129.4 eV for P. That both Fe and P were found at the surface following testing in their zero-valent state is consistent with catalysis of HER by the iron phosphide. Furthermore, we found that there was no detectable Pt at the surface of the tested Fe₃P sample. In order to eliminate this potential source of contamination,^{239,240} we conducted cyclic voltammetry at a scan rate of 100 mV/s for 600 cycles using Pt and a graphite rod as the counter electrode, respectively, as shown in Figure B.17. It was found that the profiles of the polarization curves are very close to each other. Compared to the 1st cycle, the curves at the 600th cycle shift to more negative potentials for the Pt and graphite rod counter electrodes. Therefore, we

can safely conclude that there is no Pt contamination of the working electrode.

In this study, we have precise control over the stoichiometry of the iron and phosphorus content, and the catalysts are deposited onto planar FTO substrates to form uniform thin films, meaning that the FTO substrate has less effect on the geometric current density than common 3D substrates like Cu foam and Ni foam. The normalized current density by ECSA in Figure B.18 indicates that the HER activity obeys the order of $\text{Fe}_3\text{P} > \text{Fe}_2\text{P} > \text{FeP}$. The as-deposited Fe_3P on FTO shows better than, or comparable, HER performance to Fe_2P and FeP in acidic media. Table B.4 summarizes the HER performance of recently developed transition metal phosphides for comparison.

6.3.4. Insights from density functional theory (DFT) calculations

The role of phosphorus in hydrogen evolution by TMPs has remained poorly understood but is of immediate importance given the number of M_xP_y phases available for any given metal (M). Furthermore, the question of how much phosphorus is optimal for the HER process is unresolved. Previous theoretical studies have suggested that transition metal atoms function as the catalytic reaction centers with the negatively charged and weakly basic P atoms assisting in trapping protons and promoting the desorption of H_2 .^{188,189,240} However, among literature reports, there is no clear trend in activities for the hitherto tested iron phosphides, namely FeP_2 , FeP , and Fe_2P . As summarized in **Table S4**, the overpotentials of reported FeP nanostructures range from 31 mV to 154 mV for 10 mA/cm^2 of current density (j),^{206,241–244} while the corresponding overpotentials of Fe_2P nanostructures range from 88 mV to 191 mV.^{210,245,246} The single report of FeP_2 as an HER electrocatalyst provides an overpotential value ($j = 10 \text{ mA}/\text{cm}^2$) of 61 mV, more in the range of FeP .²⁴⁴ The large variations, even for a given phase, likely stem from differences in electrode fabrication methods, the

types of nanostructures (e.g. nanoparticles vs. nanowires), the presence or lack of surface stabilizing agents, and the phase inhomogeneities which can be expected for the types of preparatory methods. Although previous reports of iron phosphide HER activities are unsupportive of a trend, more convincing trends can perhaps be accepted for Mo, Co, and Ni phosphides for which it was found that metal-poor phases outperformed metal-rich phases.¹⁸⁹ Conversely, Rappe and coworkers proposed that Ni_3P surfaces are better HER catalysts than Ni_2P surfaces although worse than Ni_5P_4 surfaces, based on a series of detailed DFT calculations and thermodynamic considerations of the active surface at typical reaction conditions.^{247,248} While this recent experimental and theoretical study adds some uncertainty to the generality of established activity trends among Ni phosphides, we provide experimental evidence for increasing HER activity with decreasing P content for Fe phosphides.

To further support our experimental observation and to gain additional understanding of the electrocatalytic activity among iron phosphides, we performed a series of DFT calculations to understand the hydrogen binding preferences on select surface facets predicted by the Bravais-Friedel-Donnay-Harker (BFDH) crystal morphology algorithm.²²⁰ The full simulation details are provided in the **SI** (see Density Functional Theory Methods and Hydrogen Binding Contours) and the resulting contour maps of the hydrogen binding preferences for the Fe_3P (100), Fe_2P (100) and the Fe-terminated FeP (011) surfaces are given in Figure 6.9. Additional contour maps for $\text{FeP}_{\text{P-t}}$ (011) and FeP (100) surfaces are given in **Figure S33**.

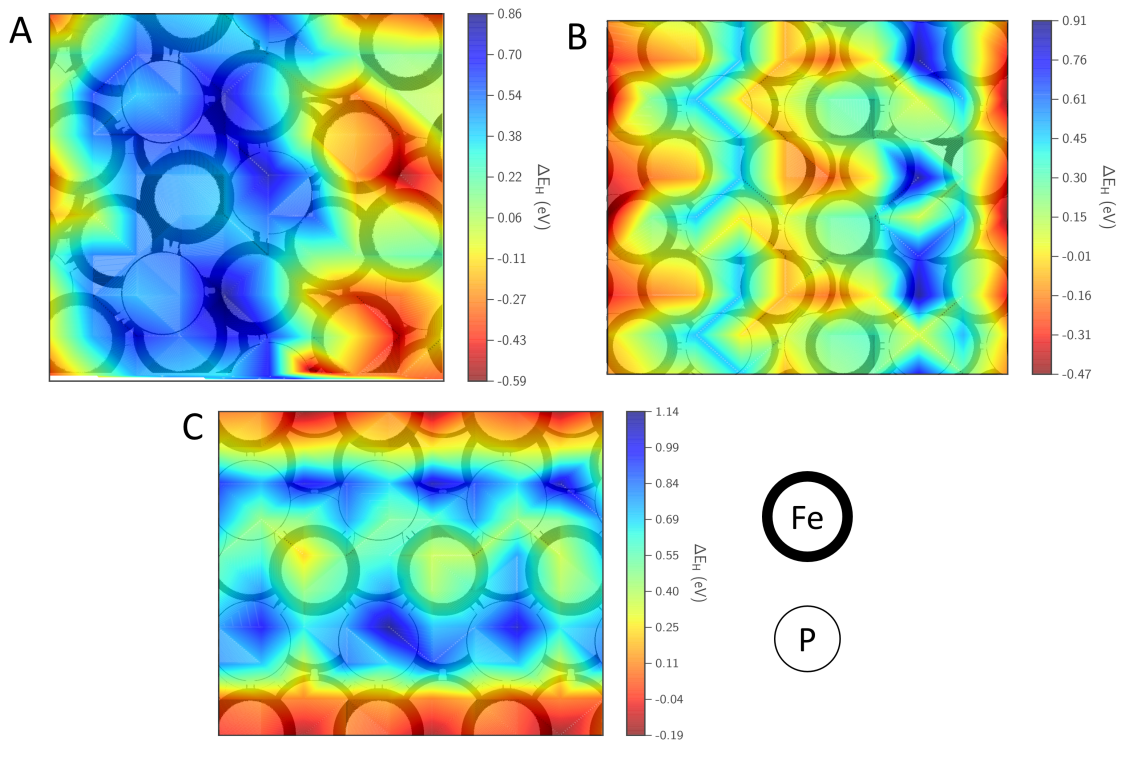


Figure 6.9. Contours of H binding strength on the surfaces of a) Fe_3P (100); b) Fe_2P (100); and c) $\text{FeP}_{\text{Fe-t}}$ (011). Fe atoms are depicted with thick boundaries, while P atoms are depicted with thin boundaries.

Analysis of binding preferences on representative Fe_3P (100) and Fe_2P (100) indicate that hydrogen generally prefers binding to Fe-rich areas. Cleavage of Fe_3P along the (100) direction exposes a stepped surface, where hydrogen preferentially occupies the exposed Fe threefold or Fe–Fe bridge sites at low coverages. The bilayered (001) surface of Fe_2P consists of threefold Fe sites, while the (100) surface forms Fe bridge sites, which are again amenable to strong hydrogen binding. The FeP (011) surfaces exhibit weak hydrogen binding at the Fe–Fe and Fe–P bridges on the Fe– and P–terminated surfaces, and overall, the weakest binding energies of all Fe_xP surfaces. Across all Fe_xP surfaces, the presence of a surface or sub-surface P atom weakens hydrogen binding and is evidenced by the blue colored regions in Figure 6.9 and Figure B.19. The low coverage adsorption geometries on $\text{FeP}_{\text{P-t}}$ (011) reported in our work are contrary to those

published by Kibsgaard and coworkers, who identified the active hydrogen atom to bind atop the $\text{FeP}_{\text{P-t}}$ (011) surface P atoms. This surface was shown to be HER active under low coverages of 0.25 ML, with $\Delta G_H = 0.13$ eV.¹⁸⁸ Assuming approximate entropic and zero-point energy contributions of 0.25 eV to ΔG_H in Equation 6.2, hydrogen binds to P with an adsorption energy of -0.12 eV. Our calculations show that hydrogen binds with a similar binding energy of -0.1 eV at the Fe–P bridge sites, but even more favorable binding of -0.22 eV is obtained for the Fe–Fe bridge site. We note that the computational setup used in this work is comparable to that used in the work of Kibsgaard and coworkers, but with a stricter force convergence criterion of 0.02 eV/Å. We speculate that the previously reported results might have been obtained by imposing artificial constraints on the hydrogen atom location for the purpose of consistency in comparing different catalysts and facets. The same $\text{FeP}_{\text{P-t}}$ (011) surface was used in the work of Chung et al. who also reported results only for hydrogen bound atop the surface P atoms.²²¹

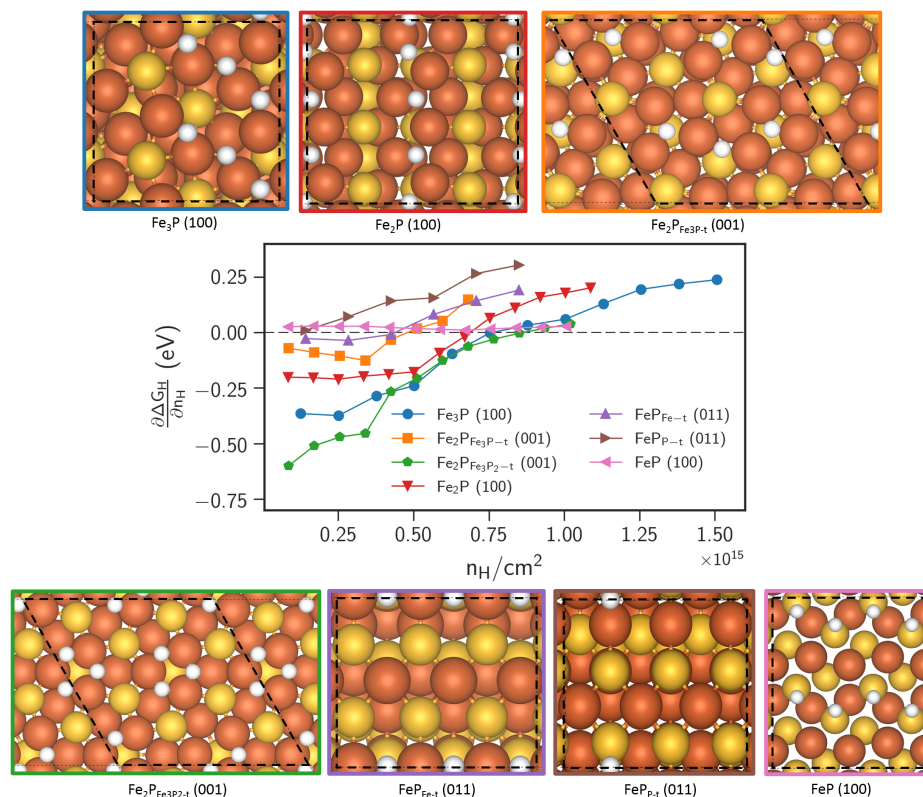


Figure 6.10. Coverage-dependent, differential Gibbs free binding energy for seven distinct Fe_xP models with different stoichiometry or termination.

The differential Gibbs free energy of adsorption of hydrogen, $\frac{\partial \Delta G_H}{\partial N_H}$, at steady state coverage is widely accepted as a descriptor of HER activity on transition metals and transition metal phosphides.^{188,223,249,250} This necessary, but not sufficient condition requires that the $\frac{\partial \Delta G_H}{\partial N_H}$ at the operating coverage be ~ 0 eV, ensuring facile proton adsorption through the Volmer step, and rapid recombination to evolve H_2 through the Tafel or Heyrovsky steps.²⁵⁰ Spontaneous adsorption and recombination of protons on the surface is conducive to high turnover rates, potentially resulting in excellent HER activity. Figure 6.10 charts the differential Gibbs free energy of hydrogen adsorption as a function of coverage in units of atoms n_H per unit area (cm^2) for all iron phosphide surfaces studied. Visualizations of all surface unit cells with steady state hydrogen coverage at the most thermoneutral differential ΔG_H are also provided in Figure 6.10. Normalizing the

number of hydrogens adsorbed per unit surface area provides for a meaningful metric that can be used to qualitatively and quantitatively compare models of different surface unit cell areas. All data used to generate Figure 6.10 are given in the supporting information document in the work of Schipper and coworkers.¹⁸⁴

All considered iron phosphide surfaces reach the thermoneutral condition $\frac{\partial \Delta G_H}{\partial N_H} \approx 0$ at some surface coverage, indicative of good HER performance. Moreover, most surfaces exhibit a reasonably flat dependence on hydrogen coverage near the thermoneutral value. The existence of a number of steps and kinks on most Fe_xP surfaces result in a largely accessible and flat potential energy surface for hydrogen adsorption. The exception to this trend is the Fe_2P (100) surface, which binds weakly through P-rich regions as hydrogen atoms are sequentially populated at HER active sites at higher coverages. Since all Fe_xP surfaces satisfy the necessary criterion of thermoneutral hydrogen adsorption, their activity differences may be attributed to different hydrogen surface coverages under reaction conditions. Invoking the law of mass action, the rate of HER depends quadratically on the surface concentration of hydrogen. The lowest predicted hydrogen coverage is obtained for $\text{FeP}_{\text{P-t}}$ (011), whereas the calculations show a ca. four times higher surface coverage on the Fe_2P and Fe_3P surfaces at the condition of thermoneutral hydrogen binding. Our consistently calculated hydrogen binding preferences across three distinct iron phosphide surfaces, Fe_3P (100), Fe_2P (100) and FeP (011) in Figure 6.9 is congruent with the interpretation that an increased P content on the FeP surface results in a lower hydrogen coverage and reduced HER activity can be expected. The lower active sites per unit surface area exhibited by FeP is again a direct consequence of the reduced availability of surface binding sites for H atoms, due to a higher stoichiometric concentration of P in FeP , compared to Fe_2P and Fe_3P .

Our simple analysis of various iron phosphide surfaces based on an ac-

cepted thermodynamic descriptor provides theoretical support for the observed HER activity of all three Fe_xP materials. Moreover, we propose that the higher hydrogen coverage for Fe_3P and Fe_2P under operating conditions is responsible for their better electrocatalytic performance compared to FeP , and we attribute the higher hydrogen coverage to the larger number of Fe rich sites on these surfaces. Our DFT calculations investigate the as-constructed Fe_xP surfaces for hydrogen binding and present HER activity trends for a particular surface relative to another. A more detailed analysis of these surfaces as HER catalysts would require determination of active surface terminations and surface reconstructions that may occur at reaction conditions similar to the work done by Rappe and coworkers.^{50,58} Additional discrimination between the HER activity of Fe_3P and Fe_2P would also require the investigation of other important factors that govern the HER activity of a catalyst, such as the recombination kinetics or the electrical conductivity.^{248,251–253}

6.4. Conclusions

The single-source precursor MOCVD method employed for the deposition of the iron phosphides has permitted the formation of phase pure thin films of FeP and Fe_2P for the first time. The synthesis of these films enabled a systematic experimental and theoretical study of electrocatalytic activities of the iron phosphides in the series Fe_xP ($x = 1-3$), which showed that their relative catalytic activity for the HER decreased with relative metal content in the order $\text{Fe}_3\text{P} > \text{Fe}_2\text{P} > \text{FeP}$. DFT investigations confirmed this trend with the primary conclusion that metal-rich phosphides Fe_3P and Fe_2P can support higher hydrogen coverages at thermoneutral hydrogen absorption conditions, congruent with significantly higher HER rates than FeP can display under the same conditions.

Investigation of the formation of the Fe_xP phases ($x=1,2$) showed that elimination of phosphine $\text{Fe}(\text{CO})_4\text{L}$ ($\text{L} = \text{PH}_3, \text{PH}_2^t\text{Bu}$) lead to films that are metal-rich rather than possessing the stoichiometry of the SSP; however, this was overcome by varying the temperature of decomposition or altering the structure of the SSP so that the phosphorus ligands are more strongly bound to iron. The use of a precursor that contains a diphosphane unit also circumvented phosphine elimination and allowed for production of the films with the desired stoichiometry at comparatively lower temperatures.

Together, these results provide not only a route to production of phase-pure thin films of additional members of the iron phosphide family but also further our understanding of the interplay between metal and phosphorus in TMP HER electrocatalysis. Additionally, that higher metal content is positively correlated with higher HER activity should influence future catalyst development, particularly of the M_3P phase, which will allow the practical realization of hydrogen production from water.

7. Perspectives and Scope for Future Work

This dissertation attempts to elucidate the fundamentals of hydrocarbon conversion chemistry at active sites in zeolite catalysts using a combination of detailed experimental and computational techniques. While many fundamental catalytic factors and functions of the active sites have been identified, much is still unknown. Overall, there is immense potential in employing the dual-pronged approach of temporal analysis of products (TAP) and computational modeling using density functional theory (DFT) to solve unanswered research problems in hydrocarbon – zeolite catalysis. The text that follows elaborates on a few avenues that remain if pursued, could lead to important fundamental insights.

Overall, these suggestions merely scratch the surface of possible experiments that will enable the comprehensive understanding of the exact roles of active sites in zeolite catalysts and in the grander scheme of things, accelerate the development of design principles for zeolites for hydrocarbon conversion.

7.1. Statistical Analysis of Model Errors in Metal-exchanged Zeolite Models for Hydrocarbon Activation

A bottom-up approach of combining BEEF-vdW error ensembles to construct a single distribution that contains statistical information of various com-

ponent ensembles was proposed. For example, a combined distribution for Cu-SSZ-13 consists of energy of activation distributions for methane at all possible Cu-motifs in the zeolite. Our work was limited using the activation of methane as a probe reaction. This methodology can be expanded to screen various metal-exchanged zeolites for a specific reaction of interest to obtain meaningful insights into structure-function relationships across zeolites in general, as well as across specific types of active sites, etc. Entire reaction networks can also be studied within this framework with minimal computational overhead. Second, the error ensembles are a list of 2000 numbers that describe DFT energies for the same configuration that can be obtained by using 200 flavors of typical DFT-GGA formulations. These energies can be used in high-level microkinetic modeling studies to study the effects of error propagation on overall rates of reactions for specific reactions of interest, such as the partial oxidation of methane to methanol over Cu-SSZ-13. Typically, DFT-predicted reaction rates differ from those calculated experimentally by orders of magnitude, and the use of these error ensembles to obtain an estimate of reaction rates may provide a more intuitive understanding of how one can model the intermediate reactions that precede the formation of the final product.

7.2. Computational Modeling and Transient Kinetics of Hydrocarbon Conversion over Zeolite Catalysts

A significant portion of this dissertation delves into the use of characterization techniques, TAP experiments and computation modeling using DFT to understand the roles and assign functions to the Brønsted and Lewis acid sites in zeolite catalysis for hydrocarbon conversion and upgrade. Detailed experimental and computational characterization of the active sites in Ag-ZSM-5 revealed

that the Lewis acid sites are Ag^+ cations bound in the vicinity of framework Al sites. However, characterization of spent catalyst samples reveals that the isolated cations cluster during the reaction, with UV-vis spectroscopy showing distinct broad features that identify Ag-clusters. However, it is not known whether the catalyst deactivates due to the build-up of coke and due to metal-clustering. Similarly, the methylation of toluene at the Brønsted acid sites was shown to be precluded by the dehydration of methanol. However, the type and abundance of surface intermediates in the pores of the zeolite are unknown. Therefore, operando experiments that simultaneously track the catalytic activity of the catalyst and characterize the active sites can be performed to provide a full picture of the catalytic chemistry in question.

Transient pulsing experiments with the TAP reactor were performed to sample the reactions and products formed under reactant-limited transient regimes of operation. Observations from these experiments provide a comparable basis to predictions from computational modeling due to reduced extents of reaction and kinetic conversion regimes. Analysis of TAP data collected under the Knudsen diffusion regime can be performed to obtain estimates of intrinsic reaction rates and effective diffusion coefficients. These can be used to drive the exploration of mechanisms using computational modeling using DFT. Other pump-probe experiments can also be performed to lend insight into the development of the hydrocarbon-pool inside pores of the zeolite by sampling the intermediates formed by a pump reactant with a probe molecule.

References

- [1] Weitkamp, J. Zeolites and catalysis. *Solid State Ionics* **2000**, *131*, 175–188.
- [2] Davis, M. E. Zeolites and Molecular Sieves: Not Just Ordinary Catalysts. *Industrial and Engineering Chemistry Research* **1991**, *30*, 1675–1683.
- [3] Spivey, J. J.; Hutchings, G. Catalytic aromatization of methane. *Chemical Society Reviews* **2014**, *43*, 792–803.
- [4] Pérez-Ramírez, J.; Kondratenko, E. V. Evolution, achievements, and perspectives of the TAP technique. *Catalysis Today* **2007**, *121*, 160–169.
- [5] Gleaves, J. T.; Yablonsky, G.; Zheng, X.; Fushimi, R.; Mills, P. L. Temporal analysis of products (TAP)—Recent advances in technology for kinetic analysis of multi-component catalysts. *Journal of Molecular Catalysis A: Chemical* **2010**, *315*, 108–134.
- [6] Shekhtman, S. O.; Yablonsky, G. S.; Gleaves, J. T.; Fushimi, R. “State defining” experiment in chemical kinetics—primary characterization of catalyst activity in a TAP experiment. *Chemical Engineering Science* **2003**, *58*, 4843–4859.
- [7] Appl, M. *A Century of Chemical Engineering*; Springer US, 1982; pp 29–53.
- [8] Lavoie, G. A.; Heywood, J. B.; Keck, J. C. Experimental and Theoretical Study of Nitric Oxide Formation in Internal Combustion Engines. *Combustion Science and Technology* **1970**, *1*, 313–326.

- [9] Park, G. B.; Kitsopoulos, T. N.; Borodin, D.; Golibrzuch, K.; Neugebahren, J.; Auerbach, D. J.; Campbell, C. T.; Wodtke, A. M. The kinetics of elementary thermal reactions in heterogeneous catalysis. *Nature Reviews Chemistry* **2019**,
- [10] Anenberg, S. C.; Miller, J.; Minjares, R.; Du, L.; Henze, D. K.; Lacey, F.; Malley, C. S.; Emberson, L.; Franco, V.; Klimont, Z.; Heyes, C. Impacts and mitigation of excess diesel-related NO_x emissions in 11 major vehicle markets. *Nature* **2017**, *545*, 467–471.
- [11] Schiermeier, Q. The science behind the Volkswagen emissions scandal. *Nature News* **2015**,
- [12] Milton, R. M. Molecular sieve adsorbents. 1959; US Patent 2,882,244.
- [13] Paolucci, C.; Khurana, I.; Parekh, A. A.; Li, S.; Shih, A. J.; Li, H.; Di Iorio, J. R.; Albarracin-Caballero, J. D.; Yezerets, A.; Miller, J. T.; Delgass, W. N.; Ribeiro, F. H.; Schneider, W. F.; Gounder, R. Dynamic multinuclear sites formed by mobilized copper ions in NO_x selective catalytic reduction. *Science* **2017**, *357*, 898–903.
- [14] Paolucci, C.; Di Iorio, J. R.; Ribeiro, F. H.; Gounder, R.; Schneider, W. F. *Advances in Catalysis*, 1st ed.; Elsevier Inc., 2016; Vol. 59; pp 1–4.
- [15] Paolucci, C.; Verma, A. A.; Bates, S. A.; Kispersky, V. F.; Miller, J. T.; Gounder, R.; Delgass, W. N.; Ribeiro, F. H.; Schneider, W. F. Isolation of the copper redox steps in the standard selective catalytic reduction on Cu-SSZ-13. *Angewandte Chemie - International Edition* **2014**, *53*, 11828–11833.
- [16] Smit, B.; Maesen, T. L. Molecular simulations of zeolites: Adsorption, diffusion, and shape selectivity. *Chemical Reviews* **2008**, *108*, 4125–4184.

- [17] Schwach, P.; Pan, X.; Bao, X. Direct Conversion of Methane to Value-Added Chemicals over Heterogeneous Catalysts: Challenges and Prospects. *Chemical Reviews* **2017**, *117*, 8497–8520.
- [18] Kosinov, N.; Hensen, E. J. M. Nonoxidative Dehydroaromatization of Methane. **2017**, 469–481.
- [19] Giannetto, G.; Monque, R.; Galiasso, R. Transformation of LPG into Aromatic Hydrocarbons and Hydrogen over Zeolite Catalysts. *Catalysis Reviews* **1994**, *36*, 271–304.
- [20] Wang, D.; Lunsford, J. H.; Rosynek, M. P. Characterization of a Mo/ZSM-5 Catalyst for the Conversion of Methane to Benzene. *Journal of Catalysis* **1997**, *169*, 347–358.
- [21] Kim, Y. H.; Borry, R. W.; Iglesia, E. Genesis of methane activation sites in Mo-exchanged H-ZSM-5 catalysts. *Microporous and Mesoporous Materials* **2000**, *35-36*, 495–509.
- [22] Johansson, R.; Hruby, S. L.; Rass-Hansen, J.; Christensen, C. H. The hydrocarbon pool in ethanol-to-gasoline over HZSM-5 catalysts. *Catalysis Letters* **2009**, *127*, 1–6.
- [23] Dahl, I. M.; Kolboe, S. On the reaction mechanism for hydrocarbon formation from methanol over SAPO-34. I. Isotopic labeling studies of the co-reaction of ethene and methanol. *Journal of Catalysis* **1994**, *149*, 458–464.
- [24] Gao, J.; Zheng, Y.; Jehng, J.-M.; Tang, Y.; Wachs, I. E.; Podkolzin, S. G. Identification of molybdenum oxide nanostructures on zeolites for natural gas conversion. *Science* **2015**, *348*, 686–690.

- [25] Gao, J.; Zheng, Y.; Fitzgerald, G. B.; De Joannis, J.; Tang, Y.; Wachs, I. E.; Podkolzin, S. G. Structure of Mo₂C_x and Mo₄C_x molybdenum carbide nanoparticles and their anchoring sites on zsm-5 zeolites. *Journal of Physical Chemistry C* **2014**, *118*, 4670–4679.
- [26] Baba, T.; Sawada, H. Conversion of methane into higher hydrocarbons in the presence of ethylene over H-ZSM-5 loaded with silver cations. *Physical Chemistry Chemical Physics* **2002**, *4*, 3919–3923.
- [27] Baba, T.; Abe, Y. Metal cation-acidic proton bifunctional catalyst for methane activation: Conversion of ¹³CH₄ in the presence of ethylene over metal cations-loaded H-ZSM-5. *Applied Catalysis A: General* **2003**, *250*, 265–270.
- [28] Ono, Y.; Osako, K.; Kim, G. J.; Inoue, Y. Ag-ZSM-5 as a Catalyst for Aromatization of Alkanes, Alkenes, and Methanol. *Studies in Surface Science and Catalysis* **1994**, *84*, 1773–1780.
- [29] Hsieh, M. F.; Zhou, Y.; Thirumalai, H.; Grabow, L. C.; Rimer, J. D. Silver-Promoted Dehydroaromatization of Ethylene over ZSM-5 Catalysts. *ChemCatChem* **2017**, *9*, 1675–1682.
- [30] Honkala, K.; Hellman, A.; Remediakis, I.; Logadottir, A.; Carlsson, A.; Dahl, S.; Christensen, C. H.; Nørskov, J. K. Ammonia synthesis from first-principles calculations. *Science* **2005**, *307*, 555–558.
- [31] Freeman, A. J.; Wimmer, E. Density functional theory as a major tool in computational materials science. *Annual Review of Materials Science* **1995**, *25*, 7–36.
- [32] Sholl, D.; Steckel, J. A. *Density functional theory: a practical introduction*; John Wiley & Sons, 2011.

- [33] Greeley, J.; Nørskov, J. K.; Mavrikakis, M. Electronic structure and catalysis on metal surfaces. *Annual review of physical chemistry* **2002**, *53*, 319–348.
- [34] Hammer, B.; Nørskov, J. K. *Advances in catalysis*; Elsevier, 2000; Vol. 45; pp 71–129.
- [35] Pauling, L.; Wilson, E. B. *Introduction to quantum mechanics with applications to chemistry*; Courier Corporation, 2012.
- [36] Dirac, P. A. M. Quantum mechanics of many-electron systems. *Proceedings of the Royal Society of London. Series A, Containing Papers of a Mathematical and Physical Character* **1929**, *123*, 714–733.
- [37] Hohenberg, P.; Kohn, W. Inhomogeneous Electron Gas. *Physical Review* **1964**, *136*, B864–B871.
- [38] Kohn, W.; Sham, L. J. Self-Consistent Equations Including Exchange and Correlation Effects. *Physical Review* **1965**, *140*, A1133–A1138.
- [39] Kohn, W. Nobel Lecture: Electronic structure of matter—wave functions and density functionals. *Reviews of Modern Physics* **1999**, *71*, 1253–1266.
- [40] Wellendorff, J.; Lundgaard, K. T.; Møgelhøj, A.; Petzold, V.; Landis, D. D.; Nørskov, J. K.; Bligaard, T.; Jacobsen, K. W. Density functionals for surface science: Exchange-correlation model development with Bayesian error estimation. *Physical Review B - Condensed Matter and Materials Physics* **2012**, *85*, 32–34.
- [41] Gleaves, J. T.; Ebner, J. R.; Kuechler, T. C. Temporal Analysis of Products (TAP)—A Unique Catalyst Evaluation System with Submillisecond Time Resolution. *Catalysis Reviews* **1988**, *30*, 49–116.
- [42] Cortright, R.; Dumesic, J. *Advances in Catalysis*; Elsevier, 2001; pp 161–264.

- [43] Somorjai, G. A.; Li, Y. *Introduction to surface chemistry and catalysis*; John Wiley & Sons, 2010.
- [44] Shannon, S. L.; Goodwin, J. G. Characterization of Catalytic Surfaces by Isotopic-Transient Kinetics during Steady-State Reaction. *Chemical Reviews* **1995**, *95*, 677–695.
- [45] Ross Kunz, M.; Borders, T.; Redekop, E.; Yablonsky, G. S.; Constales, D.; Wang, L.; Fushimi, R. Pulse response analysis using the Y-procedure: A data science approach. *Chemical Engineering Science* **2018**, *192*, 46–60.
- [46] Sauer, J. Molecular Models in ab Initio Studies of Solids and Surfaces: From Ionic Crystals and Semiconductors to Catalysts. *Chemical Reviews* **1989**, *89*, 199–255.
- [47] Vermeiren, W.; Gilson, J. P. Impact of zeolites on the petroleum and petrochemical industry. *Topics in Catalysis* **2009**, *52*, 1131–1161.
- [48] Kaeding, W.; Chu, C.; Young, L.; Butter, S. Shape-selective reactions with zeolite catalysts: II. Selective disproportionation of toluene to produce benzene and p-xylene. *Journal of Catalysis* **1981**, *69*, 392–398.
- [49] Young, I. T. Proof without prejudice: use of the Kolmogorov-Smirnov test for the analysis of histograms from flow systems and other sources. *Journal of Histochemistry & Cytochemistry* **1977**, *25*, 935–941.
- [50] Paolucci, C.; Parekh, A. A.; Khurana, I.; Di Iorio, J. R.; Li, H.; Albarracin Caballero, J. D.; Shih, A. J.; Anggara, T.; Delgass, W. N.; Miller, J. T.; Ribeiro, F. H.; Gounder, R.; Schneider, W. F. Catalysis in a Cage: Condition-dependent speciation and dynamics of exchanged Cu cations in SSZ-13 zeolites. *Journal of the American Chemical Society* **2016**, *138*, 6028–6048.

- [51] Narsimhan, K.; Iyoki, K.; Dinh, K.; Román-Leshkov, Y. Catalytic oxidation of methane into methanol over copper-exchanged zeolites with oxygen at low temperature. *ACS Central Science* **2016**, *2*, 424–429.
- [52] Baba, T.; Inazu, K. Heterolytic Dissociation of C–H Bond of Methane over Ag-exchanged Zeolites and Conversion of Methane into Higher Hydrocarbons in the Presence of Ethene or Benzene. *Chemistry Letters* **2006**, *35*, 142–147.
- [53] Baba, T.; Iwase, Y.; Inazu, K.; Masih, D.; Matsumoto, A. Catalytic properties of silver-exchanged zeolites for propene production by conversion of methane in the presence of ethene. *Microporous and Mesoporous Materials* **2007**, *101*, 142–147.
- [54] Vanelderen, P.; Hadt, R. G.; Smeets, P. J.; Solomon, E. I.; Schoonheydt, R. A.; Sels, B. F. Cu-ZSM-5: A biomimetic inorganic model for methane oxidation. *Journal of Catalysis* **2011**, *284*, 157–164.
- [55] Woertink, J. S.; Smeets, P. J.; Groothaert, M. H.; Vance, M. A.; Sels, B. F.; Schoonheydt, R. A.; Solomon, E. I. A $[\text{Cu}_2\text{O}]^{2+}$ core in Cu-ZSM-5, the active site in the oxidation of methane to methanol. *Proceedings of the National Academy of Sciences* **2009**, *106*, 18908–18913.
- [56] Mansoor, E.; Head-Gordon, M.; Bell, A. T. Computational Modeling of the Nature and Role of Ga Species for Light Alkane Dehydrogenation Catalyzed by Ga/H-MFI. *ACS Catalysis* **2018**, *8*, 6146–6162.
- [57] Phadke, N. M.; Van Der Mynsbrugge, J.; Mansoor, E.; Getsoian, A. B.; Head-Gordon, M.; Bell, A. T. Characterization of Isolated Ga^{3+} Cations in Ga/H-MFI Prepared by Vapor-Phase Exchange of H-MFI Zeolite with GaCl_3 . *ACS Catalysis* **2018**, *8*, 6106–6126.

- [58] Pidko, E. A.; Van Santen, R. A. Activation of light alkanes over zinc species stabilized in ZSM-5 zeolite: A comprehensive DFT study. *Journal of Physical Chemistry C* **2007**, *111*, 2643–2655.
- [59] El-Malki, E.-M.; van Santen, R.; Sachtler, W. Active Sites in Fe/MFI Catalysts for NO_x Reduction and Oscillating N₂O Decomposition. *Journal of Catalysis* **2000**, *196*, 212–223.
- [60] Heyden, A.; Peters, B.; Bell, A. T.; Keil, F. J. Comprehensive DFT study of nitrous oxide decomposition over Fe-ZSM-5. *Journal of Physical Chemistry B* **2005**, *109*, 1857–1873.
- [61] Wood, B. R.; Reimer, J. A.; Bell, A. T.; Janicke, M. T.; Ott, K. C. Nitrous oxide decomposition and surface oxygen formation on Fe-ZSM-5. *Journal of Catalysis* **2004**, *224*, 148–155.
- [62] Gaswirth, S. B. Assessment of Continuous Oil Resources in the Wolfcamp Shale of the Midland Basin, Permian Basin Province, Texas, 2016, Open File-Report 2017-1013. **2017**, 14 p.
- [63] Schwarz, H. Chemistry with methane: Concepts rather than recipes. *Angewandte Chemie - International Edition* **2011**, *50*, 10096–10115.
- [64] Aasberg-Petersen, K.; Dybkjær, I.; Ovesen, C. V.; Schjødt, N. C.; Sehested, J.; Thomsen, S. G. Natural gas to synthesis gas - Catalysts and catalytic processes. *Journal of Natural Gas Science and Engineering* **2011**, *3*, 423–459.
- [65] Ravi, M.; Ranocchiari, M.; van Bokhoven, J. A. The Direct Catalytic Oxidation of Methane to Methanol-A Critical Assessment. *Angewandte Chemie International Edition* **2017**, *56*, 16464–16483.

- [66] Nicholas, J. B. Density functional theory studies of zeolite structure, acidity, and reactivity. *Topics In Catalysis* **1997**, *4*, 157–171.
- [67] Van Speybroeck, V.; Hemelsoet, K.; Joos, L.; Waroquier, M.; Bell, R. G.; Catlow, C. R. A. Advances in theory and their application within the field of zeolite chemistry. *Chem. Soc. Rev.* **2015**, *44*, 7044–7111.
- [68] Hansen, N.; Kerber, T.; Sauer, J.; Bell, A. T.; Keil, F. J. Quantum chemical modeling of benzene ethylation over H-ZSM-5 approaching chemical accuracy: A hybrid MP2:DFT study. *Journal of the American Chemical Society* **2010**, *132*, 11525–11538.
- [69] Brogaard, R. Y.; Moses, P. G.; Nørskov, J. K. Modeling van der Waals interactions in zeolites with periodic DFT: Physisorption of n-Alkanes in ZSM-22. *Catalysis Letters* **2012**, *142*, 1057–1060.
- [70] Bukowski, B. C.; Greeley, J. Scaling Relationships for Molecular Adsorption and Dissociation in Lewis Acid Zeolites. *The Journal of Physical Chemistry C* **2016**, *120*, 6714–6722.
- [71] Ghorbanpour, A.; Rimer, J. D.; Grabow, L. C. Periodic, vdW-corrected density functional theory investigation of the effect of Al siting in H-ZSM-5 on chemisorption properties and site-specific acidity. *Catalysis Communications* **2014**, *52*, 98–102.
- [72] Jones, A. J.; Iglesia, E. The Strength of Brønsted Acid Sites in Microporous Aluminosilicates. *ACS Catalysis* **2015**, *5*, 5741–5755.
- [73] Mansoor, E.; Van der Mynsbrugge, J.; Head-Gordon, M.; Bell, A. T. Impact of long-range electrostatic and dispersive interactions on theoretical predictions of adsorption and catalysis in zeolites. *Catalysis Today* **2018**, *312*, 51–65.

- [74] McEwen, J. S.; Anggara, T.; Schneider, W. F.; Kispersky, V. F.; Miller, J. T.; Delgass, W. N.; Ribeiro, F. H. Integrated operando X-ray absorption and DFT characterization of Cu-SSZ-13 exchange sites during the selective catalytic reduction of NO_x with NH₃. *Catalysis Today* **2012**, *184*, 129–144.
- [75] Nystrom, S.; Hoffman, A.; Hibbitts, D. Tuning Brønsted Acid Strength by Altering Site Proximity in CHA Framework Zeolites. *ACS Catalysis* **2018**, *8*, 7842–7860.
- [76] Nørskov, J. K.; Bligaard, T.; Rossmeisl, J.; Christensen, C. H. Towards the computational design of solid catalysts. *Nature Chemistry* **2009**, *1*, 37–46.
- [77] Berland, K.; Cooper, V. R.; Lee, K.; Schröder, E.; Thonhauser, T.; Hyldgaard, P.; Lundqvist, B. I. van der Waals forces in density functional theory: a review of the vdW-DF method. *Reports on Progress in Physics* **2015**, *78*, 66501.
- [78] Göltl, F.; Sautet, P. Modeling the adsorption of short alkanes in the zeolite SSZ-13 using van der Waals DFT exchange correlation functionals: Understanding the advantages and limitations of such functionals. *The Journal of Chemical Physics* **2014**, *140*, 154105.
- [79] Kresse, G.; Furthmüller, J. Efficiency of ab-initio total energy calculations for metals and semiconductors using a plane-wave basis set. *Computational Materials Science* **1996**, *6*, 15–50.
- [80] Kresse, G.; Furthmüller, J. Efficient iterative schemes for ab initio total-energy calculations using a plane-wave basis set. *Physical Review B* **1996**, *54*, 11169–11186.
- [81] Kresse, G.; Hafner, J. Ab initio molecular dynamics for liquid metals. *Physical Review B* **1993**, *47*, 558–561.

- [82] Kresse, G.; Joubert, D. From ultrasoft pseudopotentials to the projector augmented-wave method. *Physical Review B* **1999**, *59*, 1758–1775.
- [83] Larsen, A.; Mortensen, J.; Blomqvist, J.; Jacobsen, K. The atomic simulation environment - A Python library for working with atoms. *Journal of Physics: Condensed Matter* **2017**, *29*, 273002.
- [84] Blöchl, P. E. Projector augmented-wave method. *Physical Review B* **1994**, *50*, 17953–17979.
- [85] Henkelman, G.; Uberuaga, B. P.; Jónsson, H. Climbing image nudged elastic band method for finding saddle points and minimum energy paths. *Journal of Chemical Physics* **2000**, *113*, 9901–9904.
- [86] Henkelman, G.; Jónsson, H. A dimer method for finding saddle points on high dimensional potential surfaces using only first derivatives. *The Journal of Chemical Physics* **1999**, *111*, 7010–7022.
- [87] Deshpande, S.; Kitchin, J. R.; Viswanathan, V. Quantifying Uncertainty in Activity Volcano Relationships for Oxygen Reduction Reaction. *ACS Catalysis* **2016**, *6*, 5251–5259.
- [88] Lapierre, R. B.; Rohrman, A. C.; Schlenker, J. L.; Wood, J. D.; Valyocsik, E. W.; Rubin, M. K.; Higgins, J. B.; Rohrbaugh, W. J. The framework topology of ZSM-12 - A high silica zeolite. *Zeolites* **1985**, *5*, 352–354.
- [89] Marler, B. Silica-ZSM-22: synthesis and single crystal structure refinement. *Zeolites* **1987**, *7*, 393–397.
- [90] Scott, R. P.; Cheshire, J. D. Crystal Structure of Chabazite, a Molecular Sieve. *Nature* **1958**, *180*, 1794–1796.

- [91] Jeanvoine, Y.; Ángyán, J. G.; Kresse, G.; Hafner, J. Brønsted Acid Sites in HSAPO-34 and Chabazite: An Ab Initio Structural Study. *The Journal of Physical Chemistry B* **1998**, *102*, 5573–5580.
- [92] Olson, D. H.; Kokotailo, G. T.; Lawton, S. L.; Meier, W. M. Crystal structure and structure-related properties of ZSM-5. *The Journal of Physical Chemistry* **1981**, *85*, 2238–2243.
- [93] Inazu, K.; Koyama, T.; Miyaji, A.; Baba, T. Propene production from ethene and methane using silver- and proton-exchanged zeolite catalysts. *Journal of the Japan Petroleum Institute* **2008**, *51*, 205–216.
- [94] Yoshida, H.; Hamajima, T.; Kato, Y.; Shibata, J.; Satsuma, A.; Hattori, T. Active Ag species in MFI zeolite for direct methane conversion in the light and dark. *Research on Chemical Intermediates* **2003**, *29*, 897–910.
- [95] Yumura, T.; Nanba, T.; Torigoe, H.; Kuroda, Y.; Kobayashi, H. Behavior of Ag₃ clusters inside a nanometer-sized space of ZSM-5 zeolite. *Inorganic Chemistry* **2011**, *50*, 6533–6542.
- [96] Trout, B. L.; Chakraborty, A. K.; Bell, A. T. Local spin density functional theory study of copper ion-exchanged ZSM-5. *The Journal of Physical Chemistry ...* **1996**, *100*, 4173–4179.
- [97] Groothaert, M. H.; Smeets, P. J.; Sels, B. F.; Jacobs, P. A.; Schoonheydt, R. A. Selective oxidation of methane by the bis(μ -oxo)dicopper core stabilized on ZSM-5 and mordenite zeolites. *Journal of the American Chemical Society* **2005**, *127*, 1394–1395.
- [98] Vilella, L.; Studt, F. The Stability of Copper Oxo Species in Zeolite Frameworks. *European Journal of Inorganic Chemistry* **2016**, *2016*, 1514–1520.

- [99] Mahyuddin, M. H.; Tanaka, T.; Shiota, Y.; Staykov, A.; Yoshizawa, K. Methane Partial Oxidation over $[\text{Cu}_2(\mu\text{-O})]^{2+}$ and $[\text{Cu}_3(\mu\text{-O})_3]^{2+}$ Active Species in Large-Pore Zeolites. *ACS Catalysis* **2018**, *8*, 1500–1509.
- [100] Barbosa, L.; Zhidomirov, G. M.; Van Santen, R. A. Theoretical study of methane adsorption on Zn(II) zeolites. *Physical Chemistry Chemical Physics* **2000**, *2*, 3909–3918.
- [101] Yakovlev, A. L.; Shubin, A. A.; Zhidomirov, G. M.; van Santen, R. A. DFT study of oxygen-bridged Zn^{2+} ion pairs in Zn/ZSM-5 zeolites. *Catalysis Letters* **2000**, *70*, 175–181.
- [102] Kachurovskaya, N. A.; Zhidomirov, G. M.; Hensen, E. J.; Van Santen, R. A. Cluster model DFT study of the intermediates of benzene to phenol oxidation by N_2O on FeZSM-5 zeolites. *Catalysis Letters* **2003**, *86*, 25–31.
- [103] Yakovlev, A. L.; Zhidomirov, G. M.; Van Santen, R. A. DFT calculations on N_2O decomposition by binuclear Fe complexes in Fe/ZSM-5. *Journal of Physical Chemistry B* **2001**, *105*, 12297–12302.
- [104] Lobree, L. J.; Hwang, I.-C.; Reimer, J. A.; Bell, A. T. Investigations of the State of Fe in H-ZSM-5. *Journal of Catalysis* **1999**, *186*, 242–253.
- [105] Bedard, J.; Hong, D. Y.; Bhan, A. CH_4 dehydroaromatization on Mo/H-ZSM-5: 1. Effects of co-processing H_2 and CH_3COOH . *Journal of Catalysis* **2013**, *306*, 58–67.
- [106] Bedard, J.; Hong, D.-Y.; Bhan, A. Co-processing CH_4 and oxygenates on Mo/H-ZSM-5: 2. $\text{CH}_4\text{-CO}_2$ and $\text{CH}_4\text{-HCOOH}$ mixtures. *Physical Chemistry Chemical Physics* **2013**, *15*, 12173.

- [107] Ding, W.; Li, S.; Meitzner, G. D.; Iglesia, E. Methane conversion to aromatics on Mo/H-ZSM5: structure of molybdenum species in working catalysts. *Journal of Physical Chemistry B* **2001**, *105*, 506–513.
- [108] Hwang, A.; Kumar, M.; Rimer, J. D.; Bhan, A. Implications of methanol disproportionation on catalyst lifetime for methanol-to-olefins conversion by HSSZ-13. *Journal of Catalysis* **2017**, *346*, 154–160.
- [109] Ilias, S.; Bhan, A. The mechanism of aromatic dealkylation in methanol-to-hydrocarbons conversion on H-ZSM-5: What are the aromatic precursors to light olefins? *Journal of Catalysis* **2014**, *311*, 6–16.
- [110] Lunsford, J. H. Catalytic conversion of methane to more useful chemicals and fuels: a challenge for the 21st century. *Catalysis Today* **2000**, *63*, 165–174.
- [111] Van Speybroeck, V.; Van der Mynsbrugge, J.; Vandichel, M.; Hermelsoet, K.; Lesthaeghe, D.; Ghysels, A.; Marin, G. B.; Waroquier, M. First principle kinetic studies of zeolite-catalyzed reactions relevant for the MTO process. *Journal of the American Chemical Society* **2011**, *56*, 47.
- [112] Svelle, S.; Tuma, C.; Rozanska, X.; Kerber, T.; Sauer, J. Quantum chemical modeling of zeolite-catalyzed methylation reactions: Toward chemical accuracy for barriers. *Journal of the American Chemical Society* **2009**, *131*, 816–825.
- [113] Vandichel, M.; Lesthaeghe, D.; der Mynsbrugge, J. V.; Waroquier, M.; Van Speybroeck, V. Assembly of cyclic hydrocarbons from ethene and propene in acid zeolite catalysis to produce active catalytic sites for MTO conversion. *Journal of Catalysis* **2010**, *271*, 67–78.
- [114] Ghorbanpour, A.; Rimer, J. D.; Grabow, L. C. Computational Assessment of the Dominant Factors Governing the Mechanism of Methanol Dehydration

- over H-ZSM-5 with Heterogeneous Aluminum Distribution. *ACS Catalysis* **2016**, *6*, 2287–2298.
- [115] Moses, P. G.; Nørskov, J. K. Methanol to dimethyl ether (DME) over ZSM-22. A periodic density functional theory study. *ACS Catal.* **2013**, *3*, 735–745.
- [116] Ding, B.; Huang, S.; Wang, W. Methane activation over Ag-exchanged ZSM-5 zeolites: A theoretical study. *Applied Surface Science* **2008**, *254*, 4944–4948.
- [117] Gabrienko, A. A.; Arzumanov, S. S.; Moroz, I. B.; Toktarev, A. V.; Wang, W.; Stepanov, A. G. Methane activation and transformation on Ag/H-ZSM-5 zeolite studied with solid-state NMR. *Journal of Physical Chemistry C* **2013**, *117*, 7690–7702.
- [118] Miao, S.; Wang, Y.; Ma, D.; Zhu, Q.; Zhou, S.; Su, L.; Tan, D.; Bao, X. Effect of Ag^+ Cations on Nonoxidative Activation of Methane to C₂-Hydrocarbons. *Journal of Physical Chemistry B* **2004**, *108*, 17866–17871.
- [119] Borade, R. B.; Adnot, A.; Kaliaguine, S. The effect of sodium poisoning on acid sites in ZSM-22 zeolites. *Zeolites* **1992**, *12*, 76–80.
- [120] Arvidsson, A. A.; Zhdanov, V. P.; Carlsson, P.-A.; Grönbeck, H.; Hellman, A. Metal dimer sites in ZSM-5 zeolite for methane-to-methanol conversion from first-principles kinetic modelling: is the $[\text{Cu-O-Cu}]^{2+}$ motif relevant for Ni, Co, Fe, Ag, and Au? *Catal. Sci. Technol.* **2017**, *7*, 1470–1477.
- [121] Kulkarni, A. R.; Zhao, Z. J.; Siahrostami, S.; Nørskov, J. K.; Studt, F. Mono-copper Active Site for Partial Methane Oxidation in Cu-Exchanged 8MR Zeolites. *ACS Catalysis* **2016**, *6*, 6531–6536.
- [122] Kulkarni, A. R.; Zhao, Z.; Siahrostami, S.; Nørskov, J. K.; Studt, F. Cation-

Exchanged Zeolites for the Selective Oxidation of Methane to Methanol. *Catal. Sci. Technol.* **2017**, 114–123.

- [123] Mahyuddin, M. H.; Staykov, A.; Shiota, Y.; Yoshizawa, K. Direct Conversion of Methane to Methanol by Metal-Exchanged ZSM-5 Zeolite (Metal = Fe, Co, Ni, Cu). *ACS Catalysis* **2016**, 6, 8321–8331.
- [124] Göltl, F.; Michel, C.; Andrikopoulos, P. C.; Love, A. M.; Hafner, J.; Hermans, I.; Sautet, P. Computationally Exploring Confinement Effects in the Methane-to-Methanol Conversion over Iron-Oxo Centers in Zeolites. *ACS Catalysis* **2016**, 6, 8404–8409.
- [125] Siahrostami, S.; Falsig, H.; Beato, P.; Moses, P. G.; Nørskov, J. K.; Studt, F. Exploring Scaling Relations for Chemisorption Energies on Transition-Metal-Exchanged Zeolites ZSM-22 and ZSM-5. *ChemCatChem* **2016**, 8, 767–772.
- [126] Losch, P.; Huang, W.; Vozniuk, O.; Goodman, E. D.; Schmidt, W.; Cargnello, M. Modular Pd/Zeolite Composites Demonstrating the Key Role of Support Hydrophobic/Hydrophilic Character in Methane Catalytic Combustion. *ACS Catalysis* **2019**, 4742–4753.
- [127] Petrov, A. W.; Ferri, D.; Krumeich, F.; Nachtegaal, M.; Van Bokhoven, J. A.; Kröcher, O. Stable complete methane oxidation over palladium based zeolite catalysts. *Nature Communications* **2018**, 9.
- [128] Romero, M. Á.; Lázaro, J.; Frontela, J. *Concepts of Modern Catalysis and Kinetics*; Wiley-VCH Verlag GmbH & Co. KGaA: Weinheim, FRG, 2005; pp 349–376.
- [129] Li, C.; Paris, C.; Martínez-Triguero, J.; Boronat, M.; Moliner, M.; Corma, A. Synthesis of reaction-adapted zeolites as methanol-to-olefins catalysts with

- mimics of reaction intermediates as organic structure-directing agents. *Nature Catalysis* **2018**, *1*, 547–554.
- [130] Kosinov, N.; Liu, C.; Hensen, E. J.; Pidko, E. A. Engineering of Transition Metal Catalysts Confined in Zeolites. *Chemistry of Materials* **2018**, *30*, 3177–3198.
- [131] Kosinov, N.; Coumans, F. J.; Li, G.; Uslamin, E.; Mezari, B.; Wijkema, A. S.; Pidko, E. A.; Hensen, E. J. Stable Mo/HZSM-5 methane dehydroaromatization catalysts optimized for high-temperature calcination-regeneration. *Journal of Catalysis* **2017**, *346*, 125–133.
- [132] Kosinov, N.; Wijkema, A. S.; Uslamin, E.; Rohling, R.; Coumans, F. J.; Mezari, B.; Parastayev, A.; Poryvaev, A. S.; Fedin, M. V.; Pidko, E. A.; Hensen, E. J. Confined Carbon Mediating Dehydroaromatization of Methane over Mo/ZSM-5. *Angewandte Chemie - International Edition* **2018**, *57*, 1016–1020.
- [133] Ilias, S.; Bhan, A. Mechanism of the Catalytic Conversion of Methanol to Hydrocarbons. **2013**,
- [134] Pinilla-Herrero, I.; Borfecchia, E.; Holzinger, J.; Mentzel, U. V.; Joensen, F.; Lomachenko, K. A.; Bordiga, S.; Lamberti, C.; Berlier, G.; Olsbye, U.; Svelle, S.; Skibsted, J.; Beato, P. High Zn/Al ratios enhance dehydrogenation vs hydrogen transfer reactions of Zn-ZSM-5 catalytic systems in methanol conversion to aromatics. *Journal of Catalysis* **2018**, *362*, 146–163.
- [135] Chica, A.; Corma, A. Hydroisomerization of pentane, hexane, and heptane for improving the octane number of gasoline. *Journal of Catalysis* **1999**, *187*, 167–176.

- [136] Brandenberger, S.; Kröcher, O.; Tissler, A.; Althoff, R. *Catalysis Reviews - Science and Engineering*; 2008; Vol. 50; pp 492–531.
- [137] Davis, R. J. New perspectives on basic zeolites as catalysts and catalyst supports. *Journal of Catalysis* **2003**, 216, 396–405.
- [138] Conte, M.; Lopez-Sanchez, J. A.; He, Q.; Morgan, D. J.; Ryabenkova, Y.; Bartley, J. K.; Carley, A. F.; Taylor, S. H.; Kiely, C. J.; Khalid, K.; Hutchings, G. J. Modified zeolite ZSM-5 for the methanol to aromatics reaction. *Catalysis Science and Technology* **2012**, 2, 105–112.
- [139] Li, Z.; Flytzani-Stephanopoulos, M. On the promotion of Ag-ZSM-5 by cerium for the SCR of NO by methane. *Journal of Catalysis* **1999**, 182, 313–327.
- [140] Shekhtman, S. O.; Yablonsky, G. S.; Chen, S.; Gleaves, J. T. Thin-zone TAP-reactor - theory and application. *Chemical Engineering Science* **1999**, 54, 4371–4378.
- [141] Phanawadee, P.; Shekhtman, S. O.; Jarungmanorom, C.; Yablonsky, G. S.; Gleaves, J. T. Uniformity in a thin-zone multi-pulse TAP experiment: Numerical analysis. *Chemical Engineering Science* **2003**, 58, 2215–2227.
- [142] Thirumalai, H.; Rimer, J. D.; Grabow, L. C. Quantification and Statistical Analysis of Errors Related to the Approximate Description of Active Site Models in Metal-Exchanged Zeolites. *ChemCatChem* **2019**, 11, 5055–5067.
- [143] Nosé, S. A unified formulation of the constant temperature molecular dynamics methods. *The Journal of Chemical Physics* **1984**, 81, 511–519.
- [144] Mortensen, J. J.; Kaasbjerg, K.; Frederiksen, S. L.; Norskov, J. K.; Sethna, J. P.; Jacobsen, K. W. Bayesian Error Estimation in Density Functional Theory. **2005**, 3, 1–5.

- [145] Krukau, A. V.; Vydrov, O. A.; Izmaylov, A. F.; Scuseria, G. E. Influence of the exchange screening parameter on the performance of screened hybrid functionals. *The Journal of Chemical Physics* **2006**, *125*, 224106.
- [146] Shishkin, M.; Kresse, G. Self-consistent GW calculations for semiconductors and insulators. *Physical Review B - Condensed Matter and Materials Physics* **2007**, *75*, 1–9.
- [147] Accurate quasiparticle spectra from self-consistent GW calculations with vertex corrections. *Physical Review Letters* **2007**, *99*, 14–17.
- [148] Albrecht, S.; Reining, L.; Del Sole, R.; Onida, G. Ab Initio Calculation of Excitonic Effects in the Optical Spectra of Semiconductors. *Physical Review Letters* **1998**, *80*, 4510–4513.
- [149] Electron-hole excitations in semiconductors and insulators. *Physical Review Letters* **1998**, *81*, 2312–2315.
- [150] Grimme, S. Supramolecular binding thermodynamics by dispersion-corrected density functional theory. *Chemistry - A European Journal* **2012**, *18*, 9955–9964.
- [151] Li, Y. P.; Gomes, J.; Sharada, S. M.; Bell, A. T.; Head-Gordon, M. Improved force-field parameters for QM/MM simulations of the energies of adsorption for molecules in zeolites and a free rotor correction to the rigid rotor harmonic oscillator model for adsorption enthalpies. *Journal of Physical Chemistry C* **2015**, *119*, 1840–1850.
- [152] Janda, A.; Vlasisavljević, B.; Lin, L. C.; Mallikarjun Sharada, S.; Smit, B.; Head-Gordon, M.; Bell, A. T. Adsorption thermodynamics and intrinsic activation parameters for monomolecular cracking of n-alkanes on brønsted acid sites in zeolites. *Journal of Physical Chemistry C* **2015**, *119*, 10427–10438.

- [153] Brogaard, R. Y.; Olsbye, U. Ethene Oligomerization in Ni-Containing Zeolites: Theoretical Discrimination of Reaction Mechanisms. *ACS Catalysis* **2016**, *6*, 1205–1214.
- [154] Shibata, J. Ag cluster as active species for SCR of NO by propane in the presence of hydrogen over Ag-MFI. *Journal of Catalysis* **2004**, *222*, 368–376.
- [155] Shibata, J.; Shimizu, K.-i.; Takada, Y.; Shichi, A.; Yoshida, H.; Satokawa, S.; Satsuma, A.; Hattori, T. Structure of active Ag clusters in Ag zeolites for SCR of NO by propane in the presence of hydrogen. *Journal of Catalysis* **2004**, *227*, 367–374.
- [156] Seifert, R.; Kunzmann, A.; Calzaferri, G. The Yellow Color of Silver-Containing Zeolite A. *Angewandte Chemie International Edition* **1998**, *37*, 1521–1524.
- [157] Kurnaz, E.; Fellah, M. F.; Onal, I. A density functional theory study of C-H bond activation of methane on a bridge site of M-O-M-ZSM-5 Clusters (M = Au, Ag, Fe and Cu). *Microporous and Mesoporous Materials* **2011**, *138*, 68–74.
- [158] Fellah, M. F.; Onal, I. C-H bond activation of methane on M- and MO-ZSM-5 (M = Ag, Au, Cu, Rh and Ru) clusters: A density functional theory study. *Catalysis Today* **2011**, *171*, 52–59.
- [159] Metzger, E. D.; Comito, R. J.; Hendon, C. H.; DincÇé, M. Mechanism of single-site molecule-like catalytic ethylene dimerization in Ni-MFU-4l. *Journal of the American Chemical Society* **2017**, *139*, 757–762.
- [160] Abney, C. W.; Nan, Y.; Tavlarides, L. L. X-ray Absorption Spectroscopy Investigation of Iodine Capture by Silver-Exchanged Mordenite. *Industrial & Engineering Chemistry Research* **2017**, *56*, 4837–4846.

- [161] Ito, K.; Yoshida, K.; Kittaka, S.; Yamaguchi, T. Pore Size Dependent Behavior of Hydrated Ag^+ Ions Confined in Mesoporous MCM-41 Materials under Synchrotron X-ray Irradiation. *Analytical Sciences* **2012**, 28, 639–641.
- [162] Bus, E.; Miller, J. T.; Kropf, A. J.; Prins, R.; van Bokhoven, J. A. Analysis of in situ EXAFS data of supported metal catalysts using the third and fourth cumulant. *Physical Chemistry Chemical Physics* **2006**, 8, 3248.
- [163] Gounder, R.; Iglesia, E. The Roles of Entropy and Enthalpy in Stabilizing Ion-Pairs at Transition States in Zeolite Acid Catalysis. *Accounts of Chemical Research* **2012**, 45, 229–238.
- [164] Kubas, G. J. Metal-dihydrogen and σ -bond coordination: The consummate extension of the Dewar-Chatt-Duncanson model for metal-olefin π bonding. *Journal of Organometallic Chemistry* **2001**, 635, 37–68.
- [165] Batchu, R.; Galvita, V. V.; Alexopoulos, K.; der Borght, K. V.; Poelman, H.; Reyniers, M.-F.; Marin, G. B. Role of intermediates in reaction pathways from ethene to hydrocarbons over H-ZSM-5. *Applied Catalysis A: General* **2017**, 538, 207–220.
- [166] Gounder, R.; Iglesia, E. Catalytic consequences of spatial constraints and acid site location for monomolecular alkane activation on zeolites. *Journal of the American Chemical Society* **2009**, 131, 1958–1971.
- [167] Fong, A.; Yuan, Y.; Ivry, S. L.; Scott, S. L.; Peters, B. Computational Kinetic Discrimination of Ethylene Polymerization Mechanisms for the Phillips (Cr/SiO_2) Catalyst. *ACS Catalysis* **2015**, 5, 3360–3374.
- [168] Peters, B.; Scott, S. L.; Fong, A.; Wang, Y.; Stiegman, A. E. Reexamining the evidence for proton transfers in ethylene polymerization. *Proceedings of the*

National Academy of Sciences of the United States of America **2015**, 112, E4160–E4161.

- [169] McGuinness, D. S. Olefin oligomerization via metallacycles: Dimerization, trimerization, tetramerization, and beyond. *Chemical Reviews* **2011**, 111, 2321–2341.
- [170] Franck, H.-G.; Stadelhofer, J. W. *Industrial Aromatic Chemistry*; 1988.
- [171] Tsai, T. C.; Liu, S. B.; Wang, I. Disproportionation and transalkylation of alkylbenzenes over zeolite catalysts. *Applied Catalysis A: General* **1999**, 181, 355–398.
- [172] Wittcoff, H. A.; Reuben, B. G.; Plotkin, J. S. *Industrial Organic Chemicals*; John Wiley & Sons, Inc., 2012.
- [173] *Advances in Nanoporous Materials*; Elsevier, 2010; Vol. 1; pp 97–149.
- [174] Wang, I.; Tsai, T. C.; Huang, S. T. Disproportionation of toluene and of trimethylbenzene and their transalkylation over zeolite beta. *Industrial & Engineering Chemistry Research* **1990**, 29, 2005–2012.
- [175] Young, L. B.; Butter, S. A.; Kaeding, W. W. Shape selective reactions with zeolite catalysts. III. Selectivity in xylene isomerization, toluene-methanol alkylation, and toluene disproportionation over ZSM-5 zeolite catalysts. *Journal of Catalysis* **1982**, 76, 418–432.
- [176] Zhu, Z.; Chen, Q.; Zhu, W.; Kong, D.; Li, C. Catalytic performance of MCM-22 zeolite for alkylation of toluene with methanol. *Catalysis Today* **2004**, 93–95, 321–325.
- [177] Zhang, J.; Qian, W.; Kong, C.; Wei, F. Increasing para-Xylene Selectivity in

Making Aromatics from Methanol with a Surface-Modified Zn/P/ZSM-5 Catalyst. *ACS Catalysis* **2015**, 5, 2982–2988.

- [178] Van Vu, D.; Miyamoto, M.; Nishiyama, N.; Egashira, Y.; Ueyama, K. Selective formation of para-xylene over H-ZSM-5 coated with polycrystalline silicalite crystals. *Journal of Catalysis* **2006**, 243, 389–394.
- [179] Van der Borgh, K.; Batchu, R.; Galvita, V. V.; Alexopoulos, K.; Reyniers, M.-F.; Thybaut, J. W.; Marin, G. B. Insights into the Reaction Mechanism of Ethanol Conversion into Hydrocarbons on H-ZSM-5. *Angewandte Chemie International Edition* **2016**, 55, 12817–12821.
- [180] Meshram, N. R.; Hegde, S. G.; Kulkarni, S. B. Active sites on ZSM-5 zeolites for toluene disproportionation. *Zeolites* **1986**, 6, 434–438.
- [181] Jones, A. J.; Carr, R. T.; Zones, S. I.; Iglesia, E. Acid strength and solvation in catalysis by MFI zeolites and effects of the identity, concentration and location of framework heteroatoms. *Journal of Catalysis* **2014**, 312, 58–68.
- [182] Olsbye, U.; Svelle, S.; Bjrgen, M.; Beato, P.; Janssens, T. V.; Joensen, F.; Bordiga, S.; Lillerud, K. P. Conversion of methanol to hydrocarbons: How zeolite cavity and pore size controls product selectivity. *Angewandte Chemie - International Edition* **2012**, 51, 5810–5831.
- [183] Zhao, Z.; Schipper, D. E.; Leitner, A. P.; Thirumalai, H.; Chen, J.-H.; Xie, L.; Qin, F.; Alam, M. K.; Grabow, L. C.; Chen, S.; Wang, D.; Ren, Z.; Wang, Z.; Whitmire, K. H.; Bao, J. Bifunctional metal phosphide FeMnP films from single source metal organic chemical vapor deposition for efficient overall water splitting. *Nano Energy* **2017**, 39, 444–453.
- [184] Schipper, D. E.; Zhao, Z.; Thirumalai, H.; Leitner, A. P.; Donaldson, S. L.; Kumar, A.; Qin, F.; Wang, Z.; Grabow, L. C.; Bao, J.; Whitmire, K. H. Effects

of Catalyst Phase on the Hydrogen Evolution Reaction of Water Splitting: Preparation of Phase-Pure Films of FeP, Fe₂P, and Fe₃P and Their Relative Catalytic Activities. *Chemistry of Materials* **2018**, *30*, 3588–3598.

- [185] Lewis, N. S. Research opportunities to advance solar energy utilization. *Science* **2016**, *351*, aad1920–aad1920.
- [186] McCrory, C. C. L.; Jung, S.; Peters, J. C.; Jaramillo, T. F. Benchmarking Heterogeneous Electrocatalysts for the Oxygen Evolution Reaction. *Journal of the American Chemical Society* **2013**, *135*, 16977–16987.
- [187] Jiao, Y.; Zheng, Y.; Jaroniec, M.; Qiao, S. Z. Design of electrocatalysts for oxygen- and hydrogen-involving energy conversion reactions. *Chemical Society Reviews* **2015**, *44*, 2060–2086.
- [188] Kibsgaard, J.; Tsai, C.; Chan, K.; Benck, J. D.; Nørskov, J. K.; Abild-Pedersen, F.; Jaramillo, T. F. Designing an improved transition metal phosphide catalyst for hydrogen evolution using experimental and theoretical trends. *Energy & Environmental Science* **2015**, *8*, 3022–3029.
- [189] Shi, Y.; Zhang, B. Recent advances in transition metal phosphide nanomaterials: synthesis and applications in hydrogen evolution reaction. *Chemical Society Reviews* **2016**, *45*, 1529–1541.
- [190] Callejas, J. F.; Read, C. G.; Roske, C. W.; Lewis, N. S.; Schaak, R. E. Synthesis, Characterization, and Properties of Metal Phosphide Catalysts for the Hydrogen-Evolution Reaction. *Chemistry of Materials* **2016**, *28*, 6017–6044.
- [191] Wang, F.; Sun, Y.; He, Y.; Liu, L.; Xu, J.; Zhao, X.; Yin, G.; Zhang, L.; Li, S.; Mao, Q.; Huang, Y.; Zhang, T.; Liu, B. Highly efficient and durable MoNiNC catalyst for hydrogen evolution reaction. *Nano Energy* **2017**, *37*, 1–6.

- [192] Zeng, M.; Chen, Y.; Li, J.; Xue, H.; Mendes, R. G.; Liu, J.; Zhang, T.; Rimmeli, M. H.; Fu, L. 2D WC single crystal embedded in graphene for enhancing hydrogen evolution reaction. *Nano Energy* **2017**, 33, 356–362.
- [193] Li, J.-S.; Wang, Y.; Liu, C.-H.; Li, S.-L.; Wang, Y.-G.; Dong, L.-Z.; Dai, Z.-H.; Li, Y.-F.; Lan, Y.-Q. Coupled molybdenum carbide and reduced graphene oxide electrocatalysts for efficient hydrogen evolution. *Nature Communications* **2016**, 7.
- [194] Lu, C.; Fujitsuka, M.; Sugimoto, A.; Majima, T. Unprecedented Intramolecular Electron Transfer from Excited Perylenediimide Radical Anion. *The Journal of Physical Chemistry C* **2016**, 120, 12734–12741.
- [195] Xie, Y.; Wang, J.; Zhang, Y.; Liu, X.; Wang, X.; Liu, K.; Huang, X.; Wang, Y. Quantitative profiling of spreading-coupled protein tyrosine phosphorylation in migratory cells. *Scientific Reports* **2016**, 6.
- [196] Wang, T.; Wang, X.; Liu, Y.; Zheng, J.; Li, X. A highly efficient and stable biphasic nanocrystalline Ni–Mo–N catalyst for hydrogen evolution in both acidic and alkaline electrolytes. *Nano Energy* **2016**, 22, 111–119.
- [197] Chhowalla, M.; Shin, H. S.; Eda, G.; Li, L.-J.; Loh, K. P.; Zhang, H. The chemistry of two-dimensional layered transition metal dichalcogenide nanosheets. *Nature Chemistry* **2013**, 5, 263–275.
- [198] Liu, Y.; Li, Y.; Kang, H.; Jin, T.; Jiao, L. Design, synthesis, and energy-related applications of metal sulfides. *Materials Horizons* **2016**, 3, 402–421.
- [199] Zhou, W.; Wu, X.-J.; Cao, X.; Huang, X.; Tan, C.; Tian, J.; Liu, H.; Wang, J.; Zhang, H. Ni₃S₂ nanorods/Ni foam composite electrode with low overpotential for electrocatalytic oxygen evolution. *Energy & Environmental Science* **2013**, 6, 2921.

- [200] Zhou, W.; Jia, J.; Lu, J.; Yang, L.; Hou, D.; Li, G.; Chen, S. Recent developments of carbon-based electrocatalysts for hydrogen evolution reaction. *Nano Energy* **2016**, *28*, 29–43.
- [201] Zheng, Y.; Jiao, Y.; Zhu, Y.; Li, L. H.; Han, Y.; Chen, Y.; Du, A.; Jaroniec, M.; Qiao, S. Z. Hydrogen evolution by a metal-free electrocatalyst. *Nature Communications* **2014**, *5*.
- [202] Zhao, Y.; Nakamura, R.; Kamiya, K.; Nakanishi, S.; Hashimoto, K. Nitrogen-doped carbon nanomaterials as non-metal electrocatalysts for water oxidation. *Nature Communications* **2013**, *4*.
- [203] Popczun, E. J.; McKone, J. R.; Read, C. G.; Biacchi, A. J.; Wiltrout, A. M.; Lewis, N. S.; Schaak, R. E. Nanostructured Nickel Phosphide as an Electrocatalyst for the Hydrogen Evolution Reaction. *Journal of the American Chemical Society* **2013**, *135*, 9267–9270.
- [204] Stern, L.-A.; Feng, L.; Song, F.; Hu, X. Ni₂P as a Janus catalyst for water splitting: the oxygen evolution activity of Ni₂P nanoparticles. *Energy & Environmental Science* **2015**, *8*, 2347–2351.
- [205] Tian, J.; Liu, Q.; Asiri, A. M.; Sun, X. Self-Supported Nanoporous Cobalt Phosphide Nanowire Arrays: An Efficient 3D Hydrogen-Evolving Cathode over the Wide Range of pH 0–14. *Journal of the American Chemical Society* **2014**, *136*, 7587–7590.
- [206] Callejas, J. F.; McEnaney, J. M.; Read, C. G.; Crompton, J. C.; Biacchi, A. J.; Popczun, E. J.; Gordon, T. R.; Lewis, N. S.; Schaak, R. E. Electrocatalytic and Photocatalytic Hydrogen Production from Acidic and Neutral-pH Aqueous Solutions Using Iron Phosphide Nanoparticles. *ACS Nano* **2014**, *8*, 11101–11107.

- [207] Li, D.; Baydoun, H.; Verani, C. N.; Brock, S. L. Efficient Water Oxidation Using CoMnP Nanoparticles. *Journal of the American Chemical Society* **2016**, *138*, 4006–4009.
- [208] Tan, Y.; Wang, H.; Liu, P.; Shen, Y.; Cheng, C.; Hirata, A.; Fujita, T.; Tang, Z.; Chen, M. Versatile nanoporous bimetallic phosphides towards electrochemical water splitting. *Energy & Environmental Science* **2016**, *9*, 2257–2261.
- [209] Dutta, A.; Pradhan, N. Developments of Metal Phosphides as Efficient OER Precatalysts. *The Journal of Physical Chemistry Letters* **2016**, *8*, 144–152.
- [210] Read, C. G.; Callejas, J. F.; Holder, C. F.; Schaak, R. E. General Strategy for the Synthesis of Transition Metal Phosphide Films for Electrocatalytic Hydrogen and Oxygen Evolution. *ACS Applied Materials & Interfaces* **2016**, *8*, 12798–12803.
- [211] Tegus, O.; Brück, E.; Buschow, K. H. J.; de Boer, F. R. Transition-metal-based magnetic refrigerants for room-temperature applications. *Nature* **2002**, *415*, 150–152.
- [212] Colson, A. C.; Chen, C.-W.; Morosan, E.; Whitmire, K. H. Synthesis of Phase-Pure Ferromagnetic Fe₃P Films from Single-Source Molecular Precursors. *Advanced Functional Materials* **2012**, *22*, 1850–1855.
- [213] Leitner, A. P.; Chen, J.-H.; Schipper, D. E.; Whitmire, K. H. Thin Films of (Fe_{1-x}Co_x)₃P and Fe₃(P_{1-x}Te_x) from the Co-Decomposition of Organometallic Precursors by MOCVD. *Chemistry of Materials* **2016**, *28*, 7066–7071.
- [214] Leitner, A. P.; Schipper, D. E.; Chen, J.-H.; Colson, A. C.; Rusakova, I.; Rai, B. K.; Morosan, E.; Whitmire, K. H. Synthesis of Hexagonal FeMnP

Thin Films from a Single-Source Molecular Precursor. *Chemistry - A European Journal* **2017**, *23*, 5565–5572.

- [215] Li, J.; Wu, N. Semiconductor-based photocatalysts and photoelectrochemical cells for solar fuel generation: a review. *Catalysis Science & Technology* **2015**, *5*, 1360–1384.
- [216] Schipper, D. E.; Zhao, Z.; Leitner, A. P.; Xie, L.; Qin, F.; Alam, M. K.; Chen, S.; Wang, D.; Ren, Z.; Wang, Z.; Bao, J.; Whitmire, K. H. A TiO₂/FeMnP Core/Shell Nanorod Array Photoanode for Efficient Photoelectrochemical Oxygen Evolution. *ACS Nano* **2017**, *11*, 4051–4059.
- [217] Monkhorst, H. J.; Pack, J. D. Special points for Brillouin-zone integrations. *Physical Review B* **1976**, *13*, 5188–5192.
- [218] Bengtsson, L. Dipole correction for surface supercell calculations. *Physical Review B* **1999**, *59*, 12301–12304.
- [219] Jain, A.; Ong, S. P.; Hautier, G.; Chen, W.; Richards, W. D.; Dacek, S.; Cholia, S.; Gunter, D.; Skinner, D.; Ceder, G.; Persson, K. A. Commentary: The materials project: A materials genome approach to accelerating materials innovation. *APL Materials* **2013**, *1*.
- [220] Docherty, R.; Clydesdale, G.; Roberts, K. J.; Bennema, P. Application of Bravais-Friedel-Donnay-Harker, attachment energy and Ising models to predicting and understanding the morphology of molecular crystals. *Journal of Physics D: Applied Physics* **1991**, *24*, 89–99.
- [221] Chung, D. Y.; Jun, S. W.; Yoon, G.; Kim, H.; Yoo, J. M.; Lee, K. S.; Kim, T.; Shin, H.; Sinha, A. K.; Kwon, S. G.; Kang, K.; Hyeon, T.; Sung, Y. E. Large-Scale Synthesis of Carbon-Shell-Coated FeP Nanoparticles for Robust Hy-

- drogen Evolution Reaction Electrocatalyst. *Journal of the American Chemical Society* **2017**, *139*, 6669–6674.
- [222] Santos-Carballal, D.; Roldan, A.; Grau-Crespo, R.; de Leeuw, N. H. A DFT study of the structures, stabilities and redox behaviour of the major surfaces of magnetite Fe₃O₄. *Phys. Chem. Chem. Phys.* **2014**, *16*, 21082–21097.
- [223] Nørskov, J. K.; Rossmeisl, J.; Logadottir, A.; Lindqvist, L.; Kitchin, J. R.; Bligaard, T.; Jónsson, H. Origin of the overpotential for oxygen reduction at a fuel-cell cathode. *Journal of Physical Chemistry B* **2004**, *108*, 17886–17892.
- [224] Rossmeisl, J.; Nørskov, J. K.; Taylor, C. D.; Janik, M. J.; Neurock, M. Calculated Phase Diagrams for the Electrochemical Oxidation and Reduction of Water over Pt(111). *The Journal of Physical Chemistry B* **2006**, *110*, 21833–21839.
- [225] Hunger, C.; Ojo, W.-S.; Bauer, S.; Xu, S.; Zabel, M.; Chaudret, B.; Lacroix, L.-M.; Scheer, M.; Nayral, C.; Delpech, F. Stoichiometry-controlled FeP nanoparticles synthesized from a single source precursor. *Chemical Communications* **2013**, *49*, 11788.
- [226] Dias, P. B.; de Piedade, M. E.; Simões, J. A. Bonding and energetics of phosphorus (III) ligands in transition metal complexes. *Coordination Chemistry Reviews* **1994**, *135-136*, 737–807.
- [227] Jones, P. G.; Roesky, H. W.; Grützmacher, H.; Sheldrick, G. M. Oxidative Knüpfung einer Phosphor-Phosphor-Bindung unter Einwirkung von Ag(I)- bzw. Cu(II)-Ionen: Synthese und Struktur von [(C₆H₅)Ph₂Ag{μ-(C₆H₅)₂}]₂ (AsF₆)₂, einem sechsgliedrigen Silber-Phosphor-Ring / The Oxidative Formation of a Phosphorus-Phosphorus Bond in the Presence of Ag(I) and Cu(II) Ions: Synthesis and Structure of [(C₆H₅)Ph₂Ag{μ-(C₆H₅)₂}]₂ (AsF₆)₂,

- Containing a Six-Membered Silver-Phosphorus Ring. *Zeitschrift für Naturforschung B* **1985**, 40, 590–593.
- [228] Duffy, M. P.; Ting, L. Y.; Nicholls, L.; Li, Y.; Ganguly, R.; Mathey, F. Reaction of Terminal Phosphinidene Complexes with Dihydrogen. *Organometallics* **2011**, 31, 2936–2939.
- [229] Tian, R.; Mei, Y.; Duan, Z.; Mathey, F. Simple Access to Tungsten-Stabilized Dissecondary Diphosphines. *Organometallics* **2013**, 32, 5615–5618.
- [230] Barlett, R. A.; Dias, H. V. R.; Flynn, K. M.; Hope, H.; Murray, B. D.; Olmstead, M. M.; Power, P. P. Reaction of bulky monosubstituted phosphorus(III) halides with disodium pentacarbonylchromate. Steric and electronic factors in the synthesis of $\text{Cr}(\text{CO})_5$ complexes of diphosphenes, phosphinidenes, phosphanes, diphosphanes, and cyclopolyphosphanes. *Journal of the American Chemical Society* **1987**, 109, 5693–5698.
- [231] Huttner, G.; Müller, H.-D.; Bejenke, V.; Orama, O. Die Struktur von Bis(cyclopentadienyldicarbonylmangan)-1.2-diphenyldiphosphan, $[\text{C}_5\text{H}_5(\text{CO})_2\text{Mn}]_2\text{PhP}(\text{H})\text{—}(\text{H})\text{PPh}$. *Zeitschrift für Naturforschung B* **1976**, 31, 1166–1169.
- [232] Schubert, E. H.; Sheline, R. K. The Photochemical Synthesis of Pentacarbonyliron(0) Derivatives. *Inorganic Chemistry* **1966**, 5, 1071–1074.
- [233] Weiss, E.; Stark, K.; Lancaster, J. E.; Murdoch, H. D. Olefin-eisentetracarbonyl-Komplexe mit Liganden der Malein-, Fumar-, Acryl-, Methacryl- und Zimtsure-Reihe. *Helvetica Chimica Acta* **1963**, 46, 288–297.
- [234] Blanchard, P. E. R.; Grosvenor, A. P.; Cavell, R. G.; Mar, A. X-ray Photoelectron and Absorption Spectroscopy of Metal-Rich Phosphides M_2P and M_3P ($\text{M} = \text{Cr-Ni}$). *Chemistry of Materials* **2008**, 20, 7081–7088.

- [235] Pinaud, B. A.; Benck, J. D.; Seitz, L. C.; Forman, A. J.; Chen, Z.; Deutsch, T. G.; James, B. D.; Baum, K. N.; Baum, G. N.; Ardo, S.; Wang, H.; Miller, E.; Jaramillo, T. F. Technical and economic feasibility of centralized facilities for solar hydrogen production via photocatalysis and photoelectrochemistry. *Energy & Environmental Science* **2013**, 6, 1983.
- [236] Xie, J.; Zhang, H.; Li, S.; Wang, R.; Sun, X.; Zhou, M.; Zhou, J.; Lou, X. W. D.; Xie, Y. Defect-Rich MoS₂ Ultrathin Nanosheets with Additional Active Edge Sites for Enhanced Electrocatalytic Hydrogen Evolution. *Advanced Materials* **2013**, 25, 5807–5813.
- [237] Merki, D.; Vrubel, H.; Rovelli, L.; Fierro, S.; Hu, X. Fe, Co, and Ni ions promote the catalytic activity of amorphous molybdenum sulfide films for hydrogen evolution. *Chemical Science* **2012**, 3, 2515.
- [238] Durst, J.; Siebel, A.; Simon, C.; Hasché, F.; Herranz, J.; Gasteiger, H. A. New insights into the electrochemical hydrogen oxidation and evolution reaction mechanism. *Energy Environ. Sci.* **2014**, 7, 2255–2260.
- [239] Chen, R.; Yang, C.; Cai, W.; Wang, H.-Y.; Miao, J.; Zhang, L.; Chen, S.; Liu, B. Use of Platinum as the Counter Electrode to Study the Activity of Nonprecious Metal Catalysts for the Hydrogen Evolution Reaction. *ACS Energy Letters* **2017**, 2, 1070–1075.
- [240] Zhao, Z.; Qin, F.; Kasiraju, S.; Xie, L.; Alam, M. K.; Chen, S.; Wang, D.; Ren, Z.; Wang, Z.; Grabow, L. C.; Bao, J. Vertically Aligned MoS₂/Mo₂C hybrid Nanosheets Grown on Carbon Paper for Efficient Electrocatalytic Hydrogen Evolution. *ACS Catalysis* **2017**, 7, 7312–7318.
- [241] Lv, C.; Peng, Z.; Zhao, Y.; Huang, Z.; Zhang, C. The hierarchical nanowires array of iron phosphide integrated on a carbon fiber paper as an effec-

- tive electrocatalyst for hydrogen generation. *Journal of Materials Chemistry A* **2016**, *4*, 1454–1460.
- [242] Yan, Y.; Thia, L.; Xia, B. Y.; Ge, X.; Liu, Z.; Fisher, A.; Wang, X. Construction of Efficient 3D Gas Evolution Electrocatalyst for Hydrogen Evolution: Porous FeP Nanowire Arrays on Graphene Sheets. *Advanced Science* **2015**, *2*, 1500120.
- [243] Tian, L.; Yan, X.; Chen, X. Electrochemical Activity of Iron Phosphide Nanoparticles in Hydrogen Evolution Reaction. *ACS Catalysis* **2016**, *6*, 5441–5448.
- [244] Son, C. Y.; Kwak, I. H.; Lim, Y. R.; Park, J. FeP and FeP₂ nanowires for efficient electrocatalytic hydrogen evolution reaction. *Chemical Communications* **2016**, *52*, 2819–2822.
- [245] Zhang, Y.; Zhang, H.; Feng, Y.; Liu, L.; Wang, Y. Unique Fe₂P Nanoparticles Enveloped in Sandwichlike Graphited Carbon Sheets as Excellent Hydrogen Evolution Reaction Catalyst and Lithium-Ion Battery Anode. *ACS Applied Materials & Interfaces* **2015**, *7*, 26684–26690.
- [246] Liu, M.; Yang, L.; Liu, T.; Tang, Y.; Luo, S.; Liu, C.; Zeng, Y. Fe₂P/reduced graphene oxide/Fe₂P sandwich-structured nanowall arrays: a high-performance non-noble-metal electrocatalyst for hydrogen evolution. *Journal of Materials Chemistry A* **2017**, *5*, 8608–8615.
- [247] Laursen, A. B.; Wexler, R. B.; Whitaker, M. J.; Izett, E. J.; Calvinho, K. U. D.; Hwang, S.; Rucker, R.; Wang, H.; Li, J.; Garfunkel, E.; Greenblatt, M.; Rappe, A. M.; Dismukes, G. C. Climbing the Volcano of Electrocatalytic Activity while Avoiding Catalyst Corrosion: Ni₃P, a Hydrogen Evolution

- Electrocatalyst Stable in Both Acid and Alkali. *ACS Catalysis* **2018**, *8*, 4408–4419.
- [248] Wexler, R. B.; Martirez, J. M. P.; Rappe, A. M. Active Role of Phosphorus in the Hydrogen Evolving Activity of Nickel Phosphide (0001) Surfaces. *ACS Catalysis* **2017**, *7*, 7718–7725.
- [249] Seh, Z. W.; Kibsgaard, J.; Dickens, C. F.; Chorkendorff, I.; Nørskov, J. K.; Jaramillo, T. F. Combining theory and experiment in electrocatalysis: Insights into materials design. *Science* **2017**, *355*, eaad4998.
- [250] Skúlason, E.; Karlberg, G. S.; Rossmeisl, J.; Bligaard, T.; Greeley, J.; Jónsson, H.; Nørskov, J. K. Density functional theory calculations for the hydrogen evolution reaction in an electrochemical double layer on the Pt(111) electrode. *Phys. Chem. Chem. Phys.* **2007**, *9*, 3241–3250.
- [251] Kucernak, A. R. J.; Sundaram, V. N. N. Nickel phosphide: the effect of phosphorus content on hydrogen evolution activity and corrosion resistance in acidic medium. *J. Mater. Chem. A* **2014**, *2*, 17435–17445.
- [252] Jaramillo, T. F.; Jorgensen, K. P.; Bonde, J.; Nielsen, J. H.; Horch, S.; Chorkendorff, I. Identification of Active Edge Sites for Electrochemical H₂ Evolution from MoS₂ Nanocatalysts. *Science* **2007**, *317*, 100–102.
- [253] Liao, L.; Zhu, J.; Bian, X.; Zhu, L.; Scanlon, M. D.; Girault, H. H.; Liu, B. MoS₂ Formed on Mesoporous Graphene as a Highly Active Catalyst for Hydrogen Evolution. *Advanced Functional Materials* **2013**, *23*, 5326–5333.
- [254] Jones, A. J.; Zones, S. I.; Iglesia, E. Implications of transition state confinement within small voids for acid catalysis. *Journal of Physical Chemistry C* **2014**, *118*, 17787–17800.

- [255] Li, G.; Pidko, E. A.; Van Santen, R. A.; Li, C.; Hensen, E. J. M. Stability of extraframework iron-containing complexes in ZSM-5 zeolite. *Journal of Physical Chemistry C* **2013**, *117*, 413–426.

Appendix A. Quantification and Statistical Analysis of Errors Related to the Approximate Description of Active Site Models in Metal-exchanged Zeolites

Tables and Figures

Table A.1. Initial, transition, and final states from the most preferred pathway for isolated Lewis acid sites on 5T models.

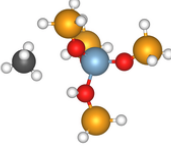
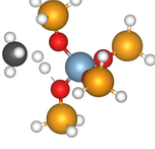

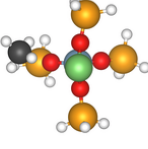
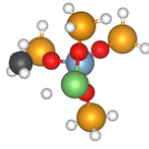
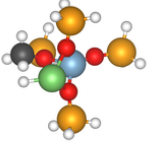
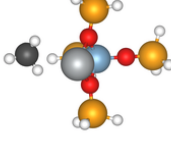
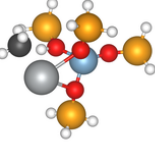
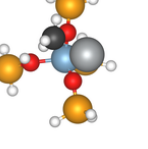
Active Species	Pathway	Initial State	Transition State	Final State
H ⁺	P1			
Li ⁺ , Na ⁺ and Ag ⁺	P1			
	P2			

Table A.1. Initial, transition, and final states from the most preferred pathway for paired Lewis acid sites on 5T models.

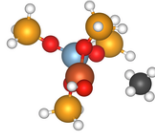
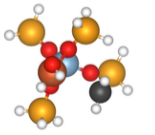
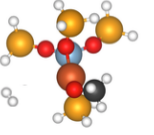
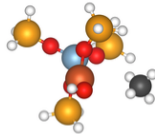
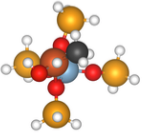
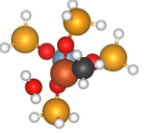
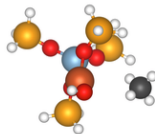
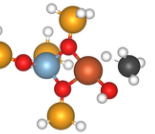
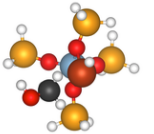
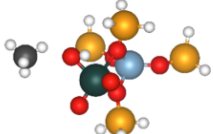
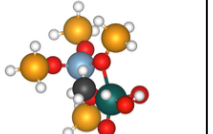
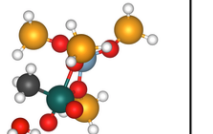
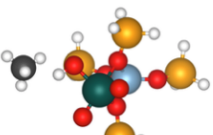
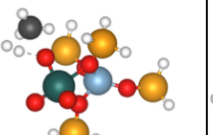
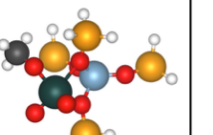
Active Species	Pathway	Initial State	Transition State	Final State
$[\text{MOH}]^+$ M: Cu, Fe, Pd	P1			
	P2			
	P3			
$[\text{MoO}_2\text{OH}]^+$	P1			
	P2			

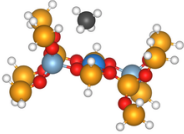
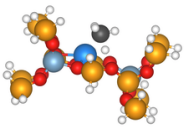
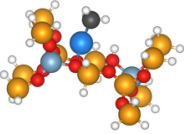
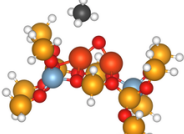
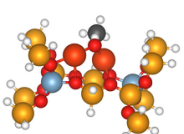
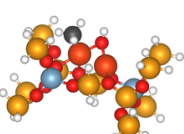
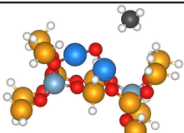
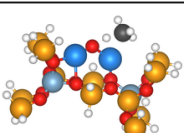
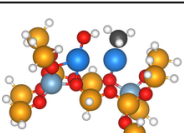
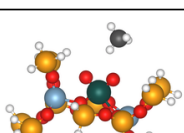
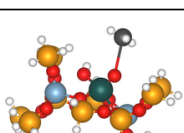
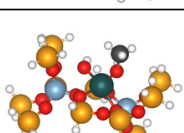
Table A.2. Energies of reaction (ΔE_{rxn}) and activation (E_a) for the preferred pathway on each Lewis acid site on (Al \times 1) zeolite models used in Figure 3.6 a.

Lewis Acid	Pathway	5T		2 \times 5T		ZSM-22		ZSM-5	
		ΔE_{rxn}	E_a	ΔE_{rxn}	E_a	ΔE_{rxn}	E_a	ΔE_{rxn}	E_a
H ⁺	P1	1.73	4.18	1.53	4.15	1.25	5.37	1.24	5.06
Li ⁺	P1	3.37							
	P2	3.8	4.9	4.22	4.99	3.83	6	3.8	6.35
Na ⁺	P1	3.36							
	P2	3.9	4.95	4.15	4.39	4.13	6.33	4.02	6.46
Ag ⁺	P1	1.18	1.69	1.3	1.62	1.44	1.63	1.38	1.62
	P2	1.87	3.56						
	P1	1.08	3.22						
[CuOH] ²⁺	P2	0.44	1.35	-0.04	1.01	0.28	1.58	-0.07	1.03
	P3	1.55	2.98						
	P1	1.38	4.77						
[ZnOH] ²⁺	P2	0.2	1.6	0.42	1.66	0.08	1.65	-0.12	1.51
	P3	1.23	3.75						
	P1	1.16	4.93						
[FeOH] ²⁺	P2	0.97	1.68	0.45	1.44	0.76	1.92	0.67	1.59
	P3	2.23	2.9						
[MoO ₂ OH] ⁺	P1	1.06	2.29	1.32	2.52	1.09	2.97	1.17	2.07
	P2	1.01	4.45						

Table A.3. Energies of reaction (ΔE_{rxn}) and activation (E_a) for the preferred pathway on each Lewis acid site on ($\text{Al} \times 2$) zeolite models used in Figure 5 b).

Species	Lewis	Pathway	2 x 5T		ZSM-22		ZSM-5	
			ΔE_{rxn}	E_a	ΔE_{rxn}	E_a	ΔE_{rxn}	E_a
H	H^+	P1	1.16	4.11	1.31	4.07	1.40	3.94
Li	Li^+	P2	4.19	4.84	3.82	4.85	4.16	4.97
Na	Na^+	P2	4.30	4.90	3.85	4.84	4.06	5.07
Ag	Ag^+	P1	1.31	1.87	1.16	1.54	1.63	1.9
Cu	$[\text{CuOH}]^+$	P1	0.49	1.61	0.13	1.23	0.28	1.53
	$[\text{Cu}]^{2+}$	P1	1.05	1.61	-0.31	0.51	-0.46	0.84
	$[\text{Cu-O-Cu}]^{2+}$	P1	-1.22	0.71	-0.66	0.85	-0.75	0.84
Zn	$[\text{ZnOH}]^+$	P1	0.51	1.72	-0.13	1.31	0.05	1.53
	$[\text{Zn}]^{2+}$	P1	0.75	1.48	-0.67	0.64	-0.72	0.72
	$[\text{Zn-O-Zn}]^{2+}$	P1	0.16	1.64	0.27	1.38	-0.07	1.45
Fe	$[\text{FeOH}]^+$	P1	1.22	2.12	0.75	1.40	0.99	1.98
	$[\text{Fe}]^{2+}$	P1	1.57	1.73	0.36	1.09	0.15	1.15
	$[\text{Fe-O-Fe}]^{2+}$	P1	0.71	1.56	0.6	1.74	0.67	1.83
Mo	$[\text{MoO}_2\text{OH}]^+$	P1	1.46	2.51	1.35	2.98	1.05	2.33
	$[\text{MoO}_2]^{2+}$	P1	2.11	3.23	2.27	2.59	1.90	3.11

Table A.4. Initial, transition, and final states of the preferred pathway for Lewis acid sites on $(Al \times 2)$ models. Visualizations for the initial, transition, and final states for $[MOH]^+$, where $M=Cu, Zn, Fe$ and $[MoO_2OH]^+$ are identical to those depicted on the 5T cluster in Table A.1

Active Species	Initial State	Transition State	Final State
M^{2+} M: Cu, Zn, Fe, Pd			
$[M-O-M]^{2+}$ M: Cu, Fe, Pd			
$[Zn-O-Zn]^{2+}$			
$[MoO_2]^{2+}$			

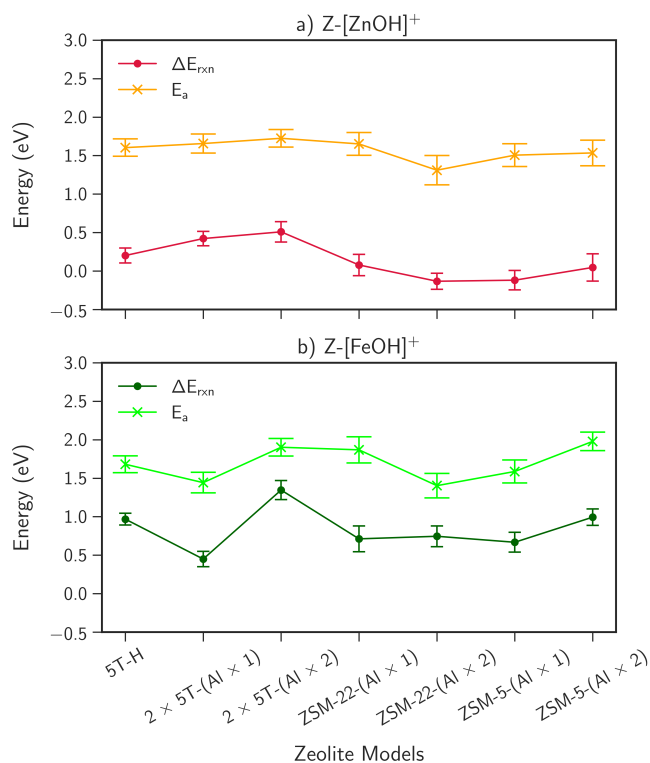


Figure A.1. Variations in ΔE_{rxn} and E_a of CH_4 across models for $[\text{ZnOH}]^+$ and $[\text{FeOH}]^+$ Lewis acids. The errorbars displayed are equivalent to one standard deviation across the mean ($\mu \pm \sigma$).

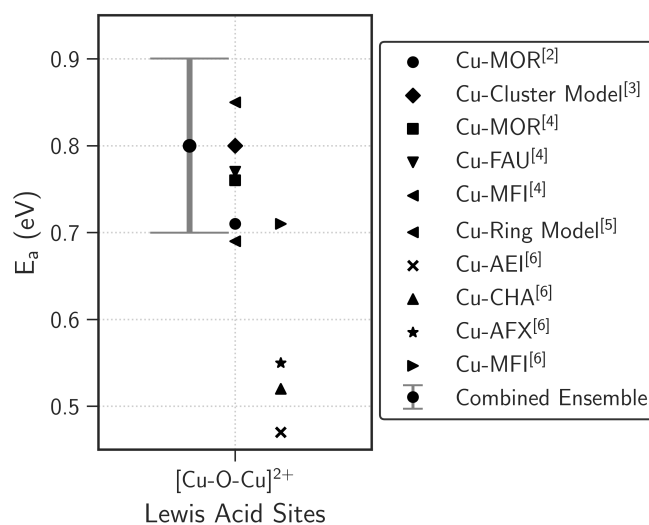


Figure A.2. Comparison of activation barriers E_a for the activation of CH_4 over $[\text{Cu-O-Cu}]^{2+}$ modeled on various zeolite models. The superscripts indicate references^{55,120–123} from which the barriers were taken.

Table A.5. Energies of reaction ΔE_{rxn} and activation E_a for Lewis acids on SSZ-13-
(Al \times 1)

Lewis Acid	Pathway	ΔE_{rxn}	E_a
H ⁺	P1	1.41	4.01
Li ⁺	P2	3.92	4.90
Na ⁺	P2	3.81	4.81
Ag ⁺	P1	1.41	1.70
[CuOH] ⁺	P2	0.14	1.22
[ZnOH] ⁺	P2	-0.28	1.49
[FeOH] ⁺	P2	0.83	1.75
[MoO ₂ OH] ⁺	P1	1.09	2.43

Table A.6. Energies of reaction ΔE_{rxn} and activation E_a for Lewis acids on SSZ-13-
(Al \times 2)

Species	Lewis Acid	Pathway	ΔE_{rxn}	E_a
H	H ⁺	P1	1.18	3.96
Li	Li ⁺	P2	3.99	5.00
Na	Na ⁺	P2	4.06	5.05
Ag	Ag ⁺	P1	1.40	1.65
Cu	[CuOH] ⁺	P1	-0.13	1.21
	[Cu] ²⁺	P1	-0.50	1.02
	[Cu-O-Cu] ²⁺	P1	-0.80	0.48
Zn	[ZnOH] ⁺	P1	0.54	1.74
	[Zn] ²⁺	P1	-0.95	1.11
	[Zn-O-Zn] ²⁺	P1	-0.53	1.34
Fe	[FeOH] ⁺	P1	0.59	1.89
	[Fe] ²⁺	P1	0.03	1.47
	[Fe-O-Fe] ²⁺	P1	0.60	1.83
Mo	[MoO ₂ OH] ⁺	P1	1.28	2.40
	[MoO ₂] ²⁺	P1	2.40	3.55

Steric Effects in Cluster Models - M^{2+} Outliers in

Figure 3.6

The outlier-like behavior of the M^{2+} Lewis acids anchored on the $2 \times 5T$ cluster models occurs due to geometric limitations and flexibility constraints in the $(2 \times 5T)-(Al \times 2)$ model. A M^{2+} cation bonded to both Al anionic sites appears to severely constrain the access of a CH_4 molecule in the process of dissociation. The fixed terminal Si atoms this model cannot stabilize the CH_4 molecule in its proximity. Consequently, CH_4 dissociation requires a concerted mechanism with a simultaneous decoupling of M^{2+} from the second Al site, as visualized in the TS in Table A.4. While the general active site geometry remains the same for ZSM-22-(Al \times 2) and ZSM-5-(Al \times 2) models, the flexibility offered by the periodic cells accommodates and stabilizes the CH_4 molecule and its fragments post dissociation more effectively, resulting in a reduction of 0.7-1.3 eV from both ΔE_{rxn} and E_a values.

Effect of Model Termination

5T-OH Cluster Models

Despite the primary dependance of CH_4 activation on the identity of the Lewis acid motif, there are variations in energies that are functions of the zeolite model and its characteristics. To further investigate these variations in energies, and motivated by the different model sizes and terminations used in literature,^{60,68,254,255} the 5T clusters were terminated with -OH groups, instead of the conventionally used H atoms. Analogously, the interconnecting Si atoms in $(2 \times 5T)$ models were terminated with -OSiH₃ groups. In theory, additional SiH₃ groups result in an apparent increase in model complexity, which could favorably

lower CH₄ dissociation energetics. The activation of CH₄ was modeled on the 5T-OH models for the preferred pathways for each Lewis acid site. The ΔE_{rxn} and E_a for each pathway on the 5T-OH cluster model is given in Table A.7, and its parity plot comparing energies obtained for the same Lewis acids and activation pathways over the 5T-H cluster is shown in Figure A.3.

Table A.7. Energies of reaction ΔE_{rxn} and activation E_a for Lewis acids on the 5T-OH cluster model.

Lewis Acid	Pathway	ΔE_{rxn}	E_a
H ⁺	P1	3.13	4.54
Li ⁺	P2	4.81	4.92
Na ⁺	P2	5.03	5.64
Ag ⁺	P1	1.82	2.16
[CuOH] ⁺	P2	0.35	1.34
[ZnOH] ⁺	P2	0.23	1.59
[FeOH] ⁺	P2	0.92	1.61
[MoO ₂ OH] ⁺	P1	1.29	2.07

A comparison of data for both models results in two clusters of data points with one showing excellent parity across both models, and the other showing large deviations. We find that the divalent Lewis acids, [CuOH]⁺, [ZnOH]⁺ and [FeOH]⁺ show little deviation, if any. In contrast, the Brønsted acid H⁺, Li⁺, Na⁺ and Ag⁺ shown in Figure A.3 become more endothermic in ΔE_{rxn} and E_a with an average increase of 0.5 eV to 1.0 eV depending on the Lewis acid. There appears to be a direct influence of these terminal OH groups on the ability of the Al site to accept protons and stabilize methyl groups post the dissociation of CH₄. This is seen in Figure A.4, which depicts the Li⁺, Na⁺ and Ag⁺ Lewis acids on a 5T-OH cluster. The extra oxygen atoms bond weakly to Li, Na and Ag, stabilizing these cations and probably reducing their activity towards CH₄ activation. The energies for divalent Lewis acids [MOH]⁺ and hexavalent [MoO₂OH]⁺ remain unchanged

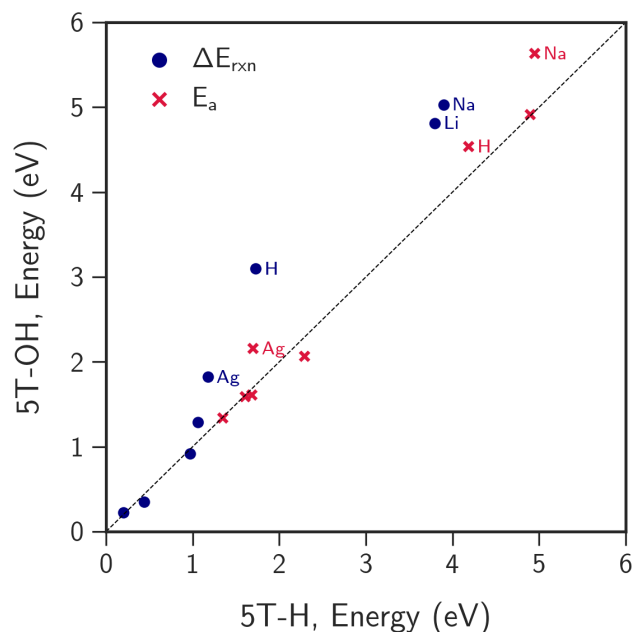


Figure A.3. Parity plot comparing the activity of Lewis acids on a 5T-H terminated cluster model and a 5T-OH terminated cluster model. Data points for ΔE_{rxn} are denoted by blue circles, E_a by red crosses, and $y = x$ parity by the dashed black line.

and are largely unaffected by the change in model terminations, and by extension, the immediate local environment around the Lewis acid site.

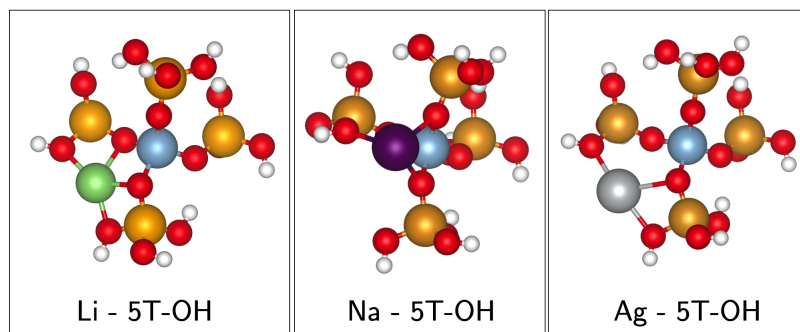


Figure A.4. Geometries of monovalent Lewis acids a) Li^+ , b) Na^+ and c) Ag^+ , showing weak bonding between terminal OH groups and the Lewis acid, in addition to the bond with the acid site.

2 × 5T Cluster Models

A (2 × 5T) cluster can be modeled as both one (Al × 1) and two acid site (Al × 2) models. Therefore, increasing the number of Si tetrahedra, coupled with Lewis acid site motifs ranging from a single atom (M^+), to a larger metal-oxo complex ($[M-O-M]^{2+}$) results in a spread of cluster model - Lewis acid combinations, which could shed some light on the effect of steric factors and choice of termination on CH_4 activation. A parity plot between (2 × 5T) and (2 × 5T)-SiH₃ data for both (Al × 1) and (Al × 2) models is shown in Figure A.5. Data for the SiH₃ terminated cluster models are also presented in Table A.8 and Table A.9. All data points are clustered around the parity line, with the largest deviations ~0.5 eV.

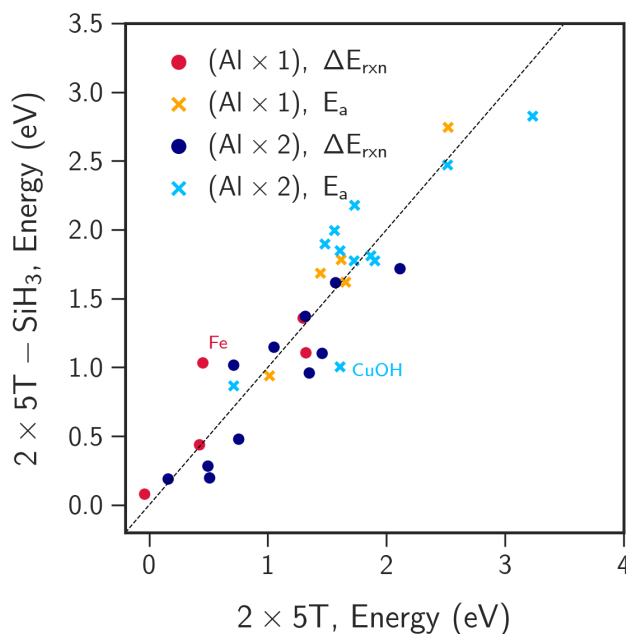


Figure A.5. Parity plot comparing the activity of a) Lewis acids on a (2 × 5T) cluster model and a (2 × 5T)-SiH₃ terminated cluster model. The $y = x$ parity is the dashed black line.

As with the 5T-OH cluster, pathways of activation that involve model framework atoms are affected, while pathways on divalent and hexavalent active site

Table A.8. Energies of reaction ΔE_{rxn} and activation E_a for Lewis acids on $(2 \times 5T)-(Al \times 1)-SiH_3$ cluster model.

Lewis Acid	Pathway	ΔE_{rxn}	E_a
H^+	P1	1.61	3.56
Li^+	P2	4.41	5.26
Na^+	P2	4.14	5.34
Ag^+	P1	1.36	1.79
$[CuOH]^+$	P2	0.08	0.94
$[ZnOH]^+$	P2	0.44	1.62
$[FeOH]^+$	P2	1.04	1.69
$[MoO_2OH]^+$	P1	1.11	2.75

Table A.9. Energies of reaction ΔE_{rxn} and activation E_a for Lewis acids on $(2 \times 5T)-(Al \times 2)-SiH_3$ cluster model.

Species	Lewis Acid	Pathway	ΔE_{rxn}	E_a
H	H^+	P1	1.37	3.89
Li	Li^+	P2	4.21	5.74
Na	Na^+	P2	4.20	5.68
Ag	Ag^+	P1	1.37	1.81
Cu	$[CuOH]^+$	P1	0.28	1.01
	$[Cu]^{2+}$	P1	1.15	1.85
	$[Cu-O-Cu]^{2+}$	P1	-0.91	0.87
Zn	$[ZnOH]^+$	P1	0.20	1.78
	$[Zn]^{2+}$	P1	0.48	1.9
	$[Zn-O-Zn]^{2+}$	P1	0.19	-
Fe	$[FeOH]^+$	P1	0.96	1.78
	$[Fe]^{2+}$	P1	1.62	2.18
	$[Fe-O-Fe]^{2+}$	P1	1.02	2.00
Mo	$[MoO_2OH]^+$	P1	1.11	2.47
	$[MoO_2]^{2+}$	P1	1.72	2.83

motifs are generally unaffected. Replacement of terminal species appears to minimally influence the activity of the Lewis acid, emphasizing the central role of the Lewis acid plays in determining the activity of a metal exchanged zeolite model.

While the OH terminations stabilized the Lewis acid site and decreased its activity towards CH₄ activation through weak bonding, the additional SiH₃ tetrahedra in the (2 × 5T)-SiH₃ model appear to constrain CH₄ access to the acid sites for monovalent metals, thus increasing the energies of reaction and activation.

Descriptive Statistics

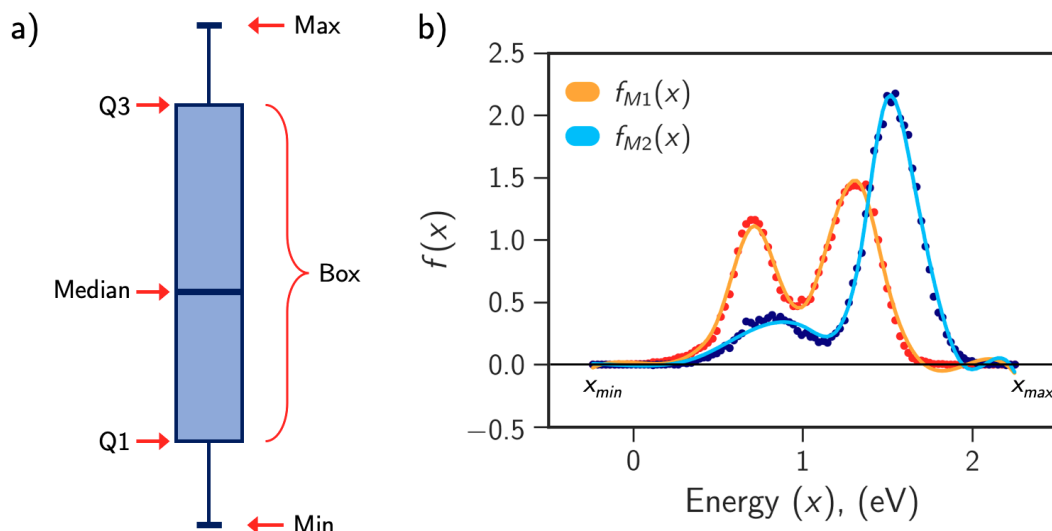


Figure A.6. a) Box plot depicting the five-number summary of a dataset, i.e. the minimum, first quartile (Q1), median, third quartile (Q3) and maximum. The range of the data is spanned between the minimum and the maximum, with outliers lying outside the range. b) Probability density functions $f_{M1}(x)$ and $f_{M2}(x)$ describing the datasets for metal exchange candidates M1 and M2.

Descriptive statistics deal with the characterization of a dataset in terms of its mean and median as measures of location, the standard deviation and interquartile range as measures of scale while also highlighting possible outliers in the data. A standardized pictorial representation of the results obtained from descriptive statistics is a box plot shown in Figure A.6. It displays the distribution of data based on the five-number summary: minimum, first quartile, median, third quartile, and maximum.

Appendix B. Effects of Catalyst Phase on the Hydrogen Evolution Reaction of Water Splitting: Preparation of Phase-pure Films of FeP, Fe₂P, and Fe₃P and their Relative Catalytic Activities

Film Deposition

Film deposition was carried out in a similar manner as previously reported.²¹³ Key differences are that the distances of the tip of the metal stage to the end of the tube and the start of the heating zone were varied according to *x* and *y* in Figure 6.1. Another key difference is that small boats/cups made

Table B.1. Film Deposition Parameters.

Material Produced	Precursor	Precursor Amount (mg)	Decomp. Temp. (Zone 1)	Decomp. Time Allowed	X (mm)	Y (mm)	Substrate(s)
FeP	2	25 (2-3 drops)	450	15 m.	75	55	FTO/Quartz
FeP	3	25 mg	350	8 h	75	55	Quartz
Fe ₂ P	1	20 mg	350	15 m	75	45	FTO/Quartz
Fe ₃ P	4	25 mg	400	3 h	75	55	FTO
FeP/Fe ₂ P Mixture	1	25 mg	450	15 m	75	45	Quartz

out of aluminum foil (1 cm deep, 1 cm in diameter) were used to weigh and transfer the precursor to the bottom of the tube, which made it easier to get the precursor to the bottom of the tube without having any to stick to the walls. This was especially helpful when working with **2** as it is a liquid. Substrates were cut into ~20.5mm x 11 mm sections and affixed to the stage with silver paste. The material production parameters are given in Table B.1. After deposition, the heating zone was shifted forward to envelop the stage and the material on the substrate allowed to anneal for two hours at the deposition temperature before slow cooling to room temperature. Note: Fe₃P was annealed for 24 h at 550° C to get a satisfactorily crystalline material, which was then used for HER testing. An aluminum foil jacket was placed over the end of the tube for Fe₃P deposition to encourage volatilization of the precursor.

Detection of Phosphine from the CVD Decomposition of **1**

300 mg of **1** was loaded into the end of the apparatus tube and the apparatus placed under high vacuum as with a typical deposition, although without the stage, and zone **2** was kept cold with liquid nitrogen. The heating zone was raised to 350° C, and the sidearm (see Figure 6.1) was immersed in liquid nitrogen, zone **2** allowed to warm to room temperature, and the valve to dynamic

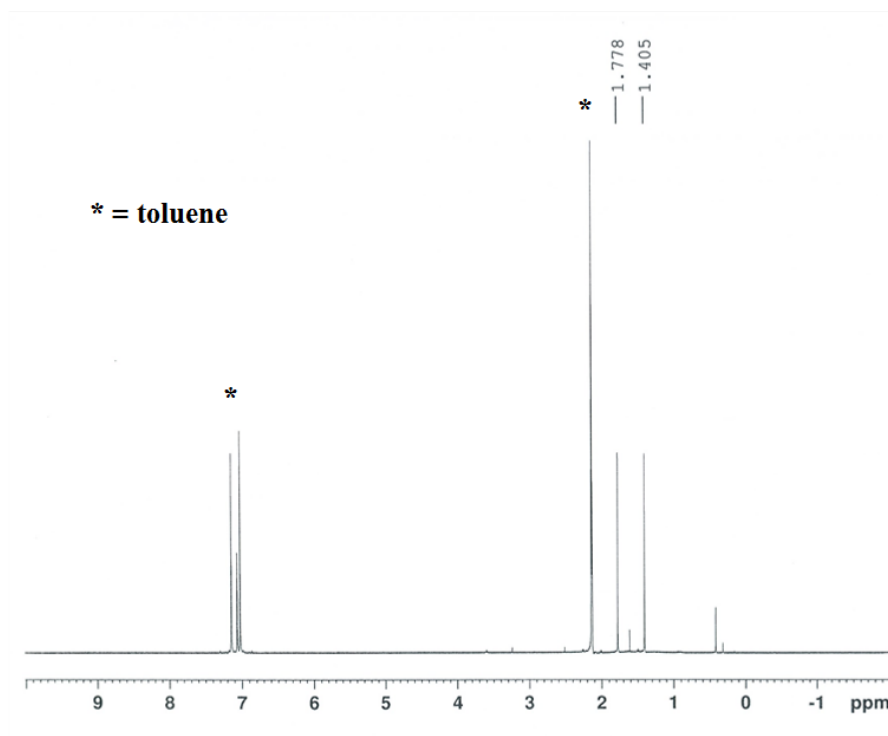


Figure B.1. ^1H NMR Spectrum of the Off-Gases of the CVD using compound **1** vacuum closed. After 20 minutes, dynamic vacuum was re-applied and zone **1** allowed to cool to room temperature. The sidearm was closed and kept at liquid nitrogen temperatures as the apparatus was closed and transferred to a Schlenk line. To the still-frozen sidearm was added approximately 3 mL d^8 -toluene via cannula, and the temperature was allowed to rise to approximately room temperature. The solution was then transferred via cannula to a septum capped NMR tube which had been flushed with nitrogen and the NMR experiments were carried out within an hour. The spectra show the presence of phosphine given the quartet at -242.78 ppm ($J_{\text{P-H}} = 186$ Hz) in the ^{31}P spectrum and the doublet at 1.592 ppm ($J_{\text{P-H}} = 186$ Hz). No other P signals could be detected.

Table B.2. Selected crystallographic data.

Compound	$\{\text{Fe}(\text{CO})_4\text{P}(\text{H})^t\text{Bu}\}_2$
Empirical Formula	$\text{C}_{16}\text{H}_{20}\text{Fe}_2\text{O}_8\text{P}_2$
Formula Weight	513.96
Temperature, K	173.15
Wavelength, Å	0.71073
Crystal System	Tetragonal
Space Group	P4_32_12
a, Å	10.2458(2)
b, Å	10.2458(2)
c, Å	21.1573(7)
α , °	90
β , °	90
γ , °	90
Volume, Å ³	2221.03(13)
Density (calculated), Mg/m ³	1.537
Absorption Coefficient, mm ⁻¹	1.487
F(000)	1052.1658
Crystal Size, mm	$0.40 \times 0.33 \times 0.30$
Theta Range for Data Collection, °	2.209 to 31.698
Index Ranges	$-15 < h < 14$; $-15 < k < 15$; $-30 < l < 31$
Reflections Collected	38368
Independent Reflections	3741 [$R(\text{int}) = 0.0295$]
Completeness to $2\theta_{\text{Max}}$	99.00%
Absorption Correction	Multi-Scan
Flack Parameter	0.51(2)
Max and Min. Transmission	1.000 and 0.197
Refinement Method	Full-Matrix Least Squares on F^2
Data / restraints / parameters	3706 / 208 / 181
Goodness-of-fit on F^2	1.098
Final R Indices [$I > 2\sigma(I)$]	0.0328
R Indices (all data)	0.0365
Largest diff. peak and hole	0.80 and -0.43 e.Å ⁻³

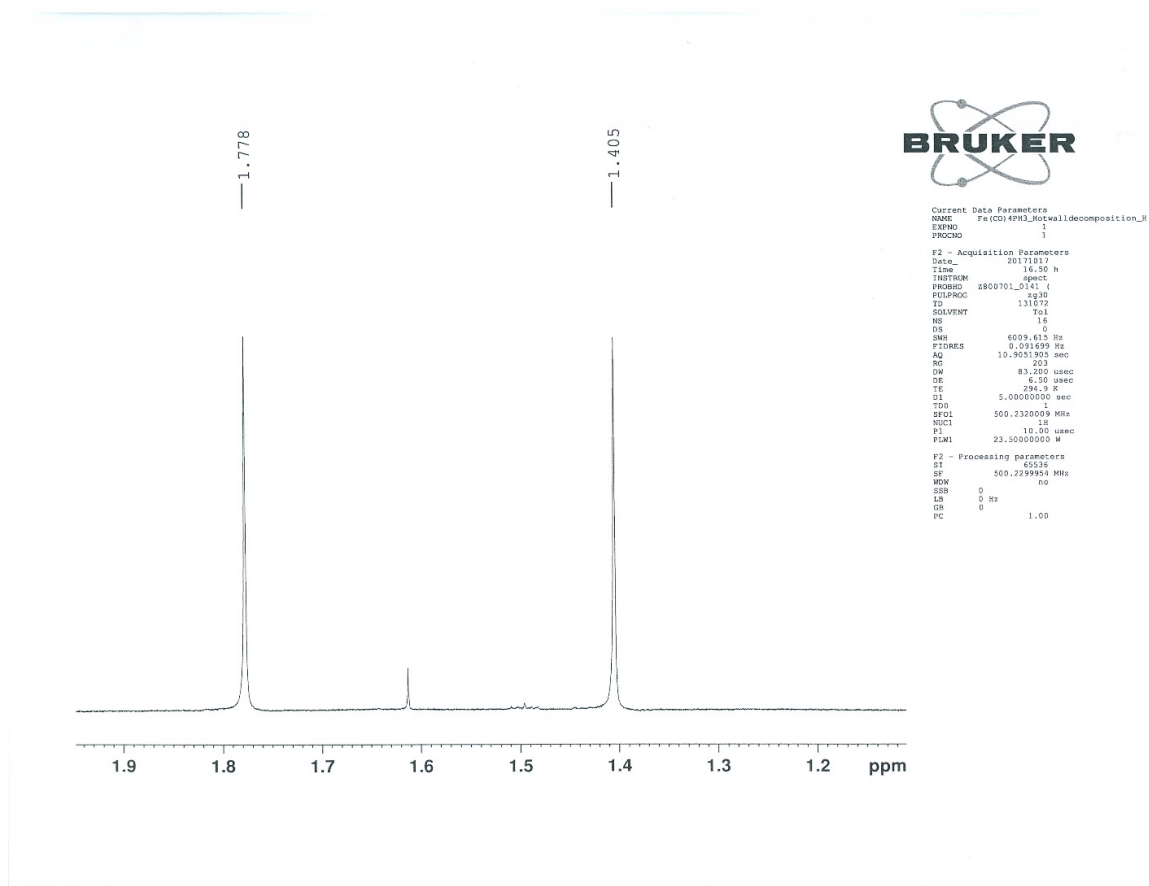


Figure B.2. ^1H NMR Spectrum in the P-H window from CVD using compound 1

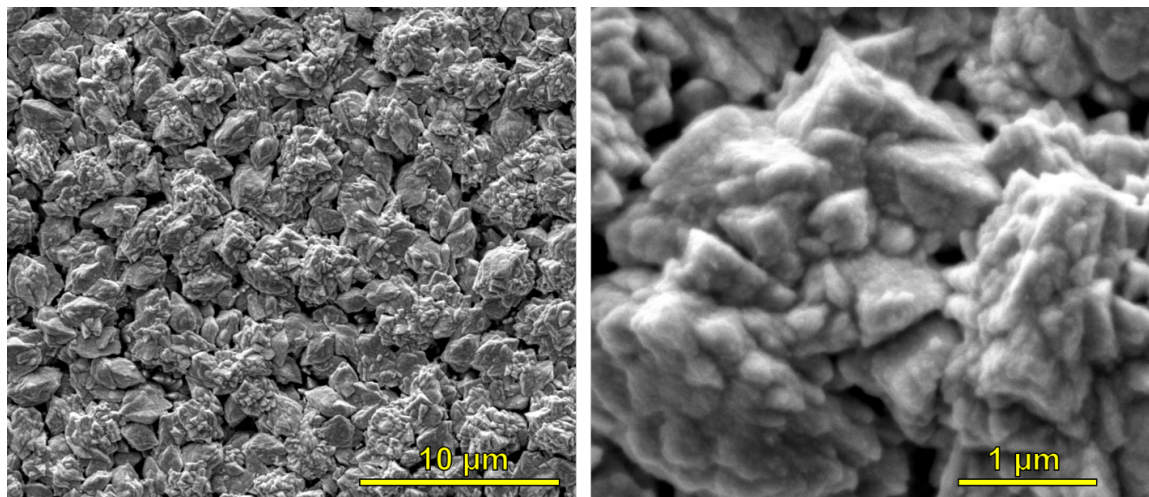


Figure B.5. SEM Images of FeP/Fe₂P mixture on quartz at two magnifications.

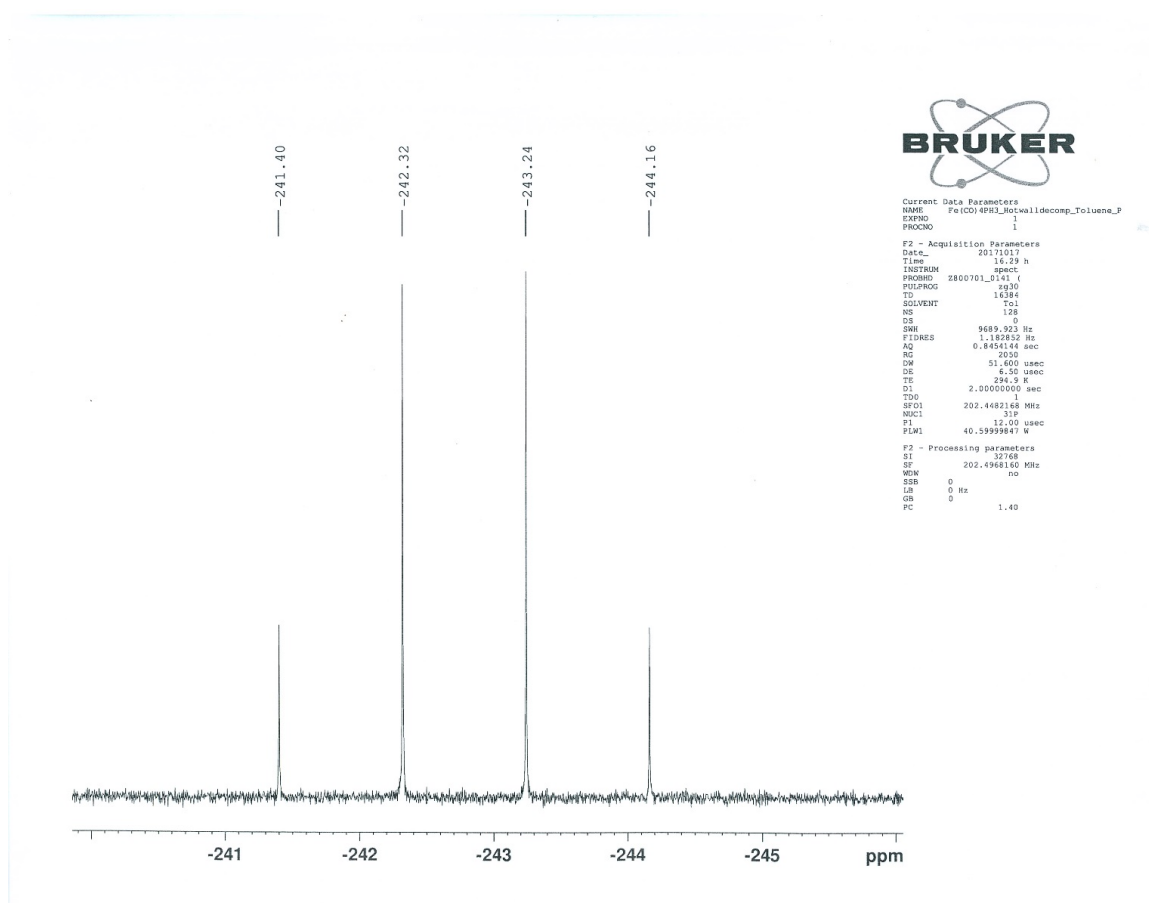


Figure B.3. ^{31}P NMR Spectrum of the Off-Gases of Compound 1 CVD Decomposition

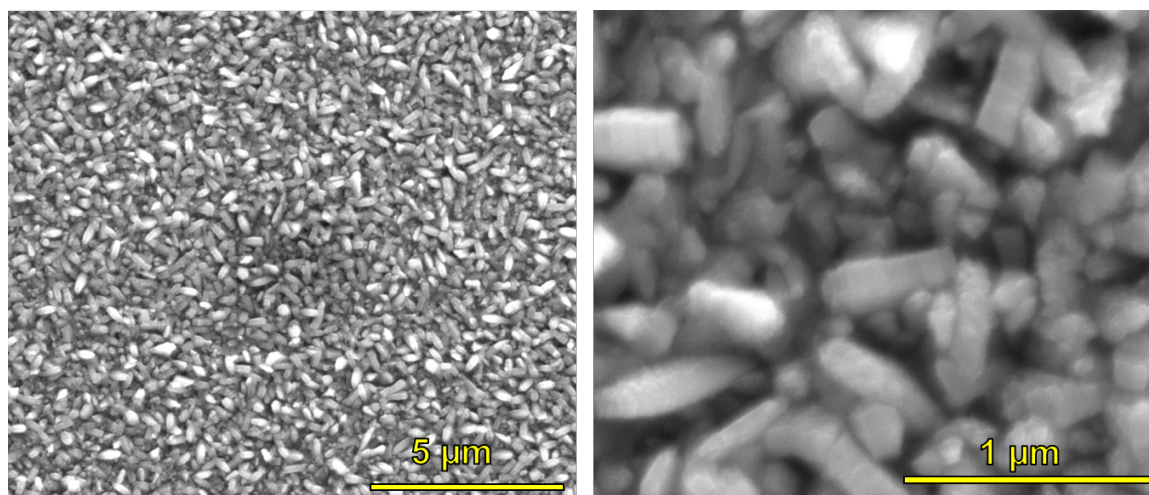


Figure B.6. SEM Images of FeP from Precursor 2 on quartz at two magnifications

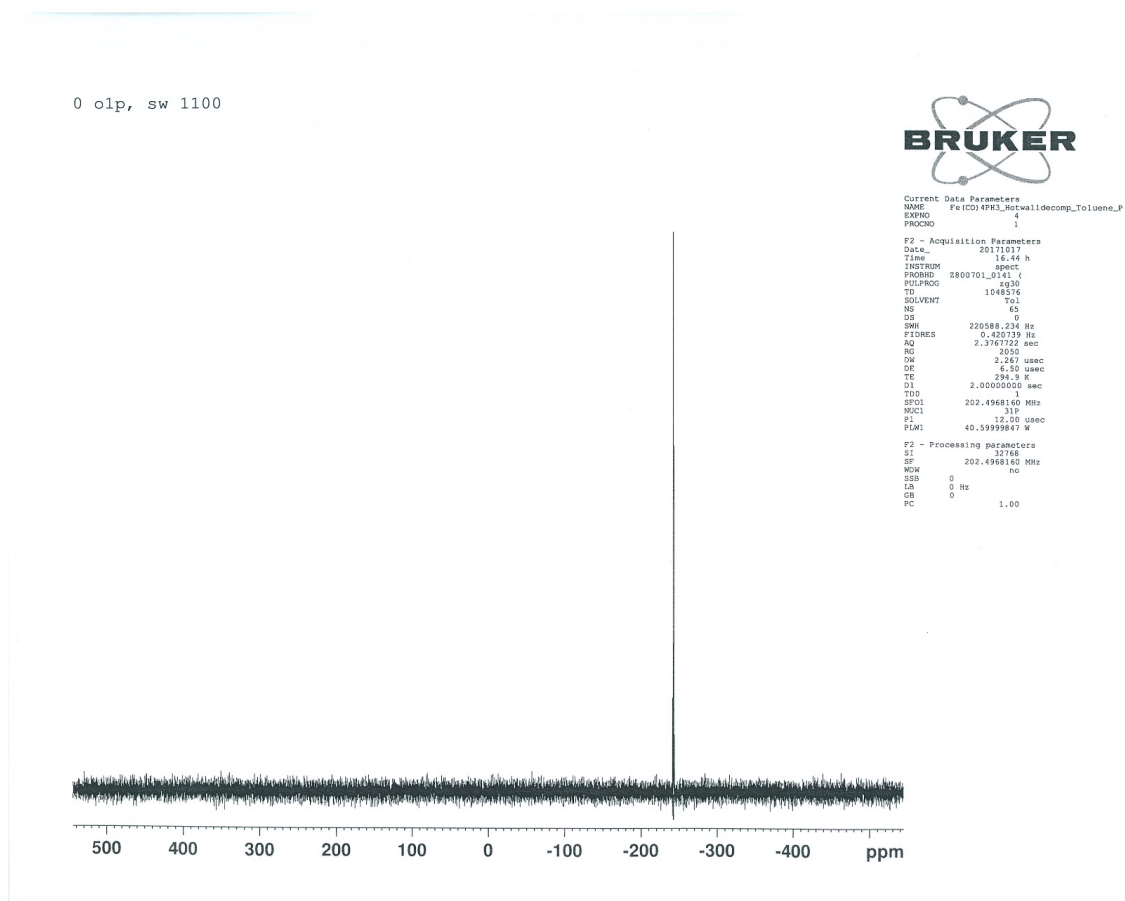


Figure B.4. ^{31}P NMR Spectrum of the Off-Gases of Compound 1 CVD Decomposition. Full window.

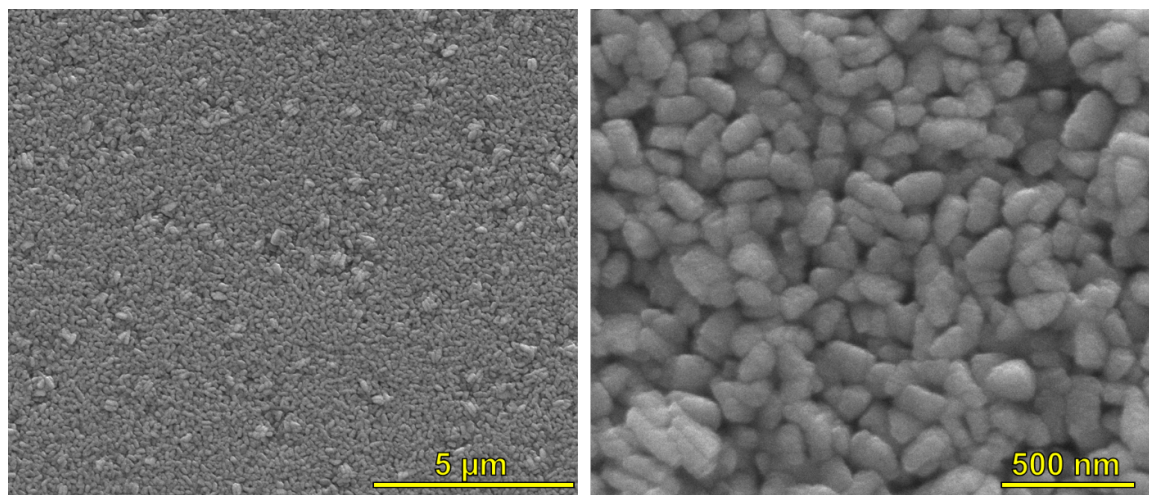


Figure B.7. SEM Images of FeP from precursor 3 on quartz at two magnifications.

Table B.3. Selected bond lengths and angles

Parameter	(Å)/(°)
Lengths:	
Fe1-P1A	2.2395(8)
Fe1-P1B	2.325(3)
P1A_a-P1A_b	2.2410(13)
P1B_a-P1B_b	2.428(7)
Angles:	
Fe1-P1A_a-P1A_b	119.92(3)
Fe1-P1B_a-P1B_b	94.0(2)

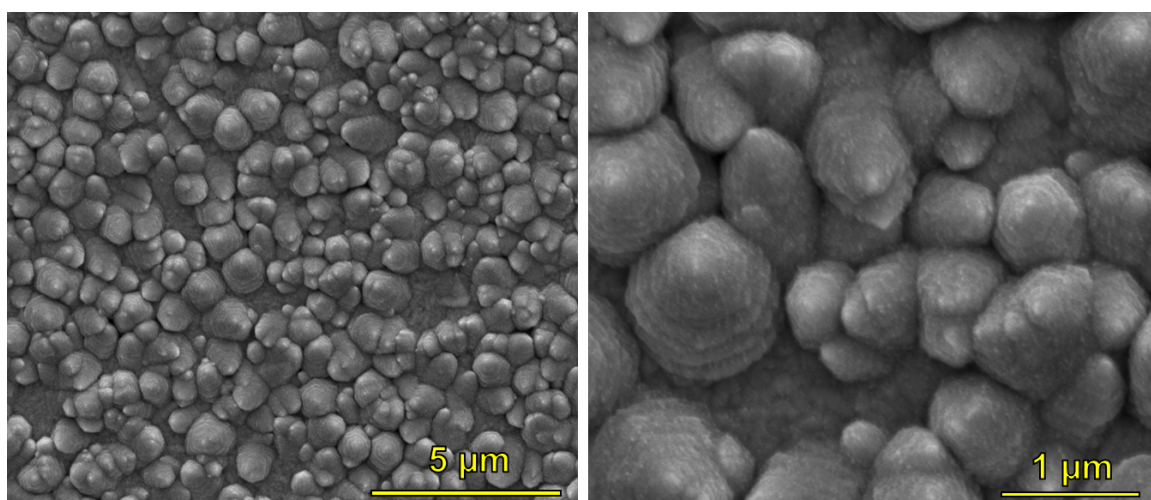


Figure B.8. SEM Images of Fe₂P on quartz at two magnifications.

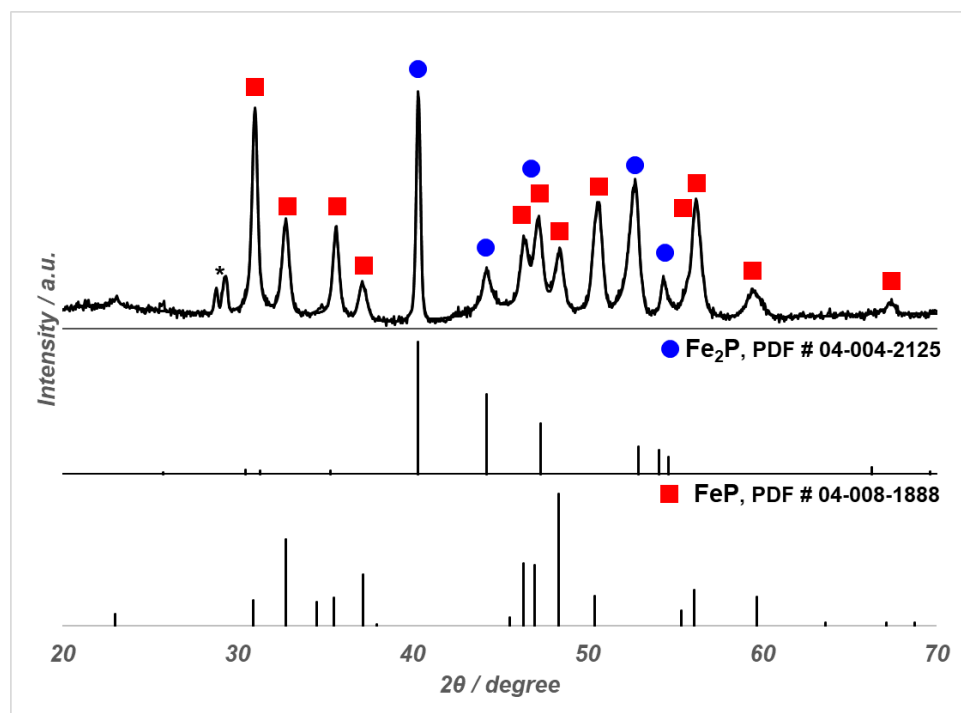


Figure B.9. XRD Pattern of FeP/Fe₂P mixture on quartz obtained from the CVD of Precursor 1 at 450° C. The asterisk denotes two peaks arising from the substrate.

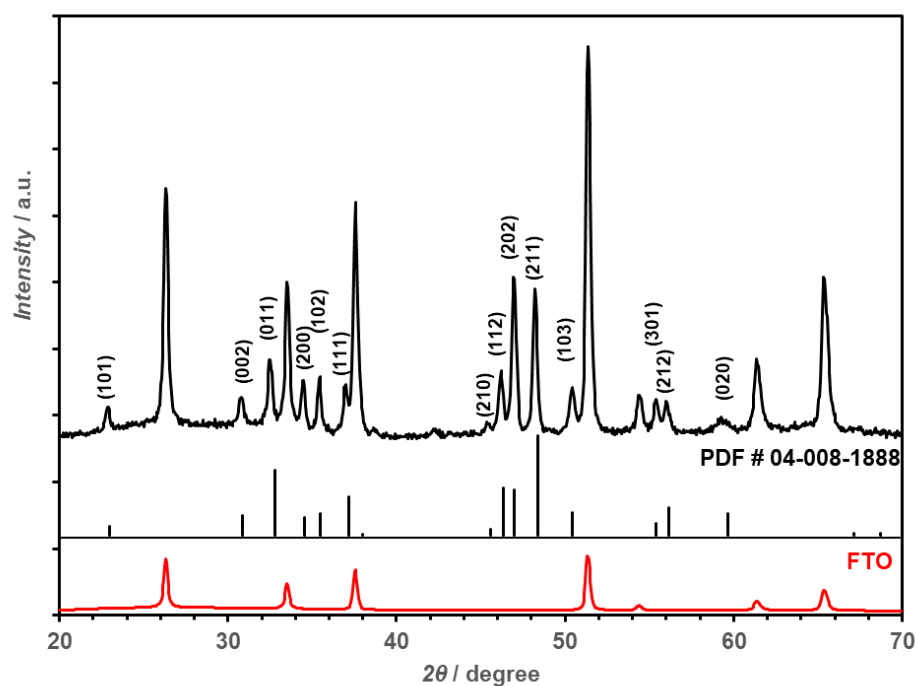


Figure B.10. PXRD of FeP on FTO from precursor 2.

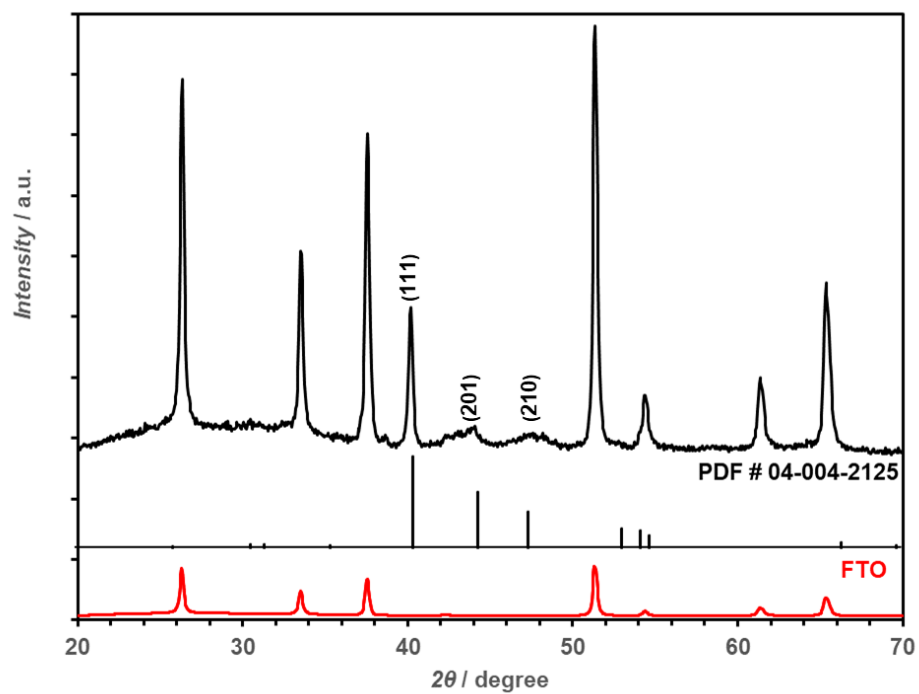


Figure B.11. PXRD of Fe_2P on FTO from precursor 1.

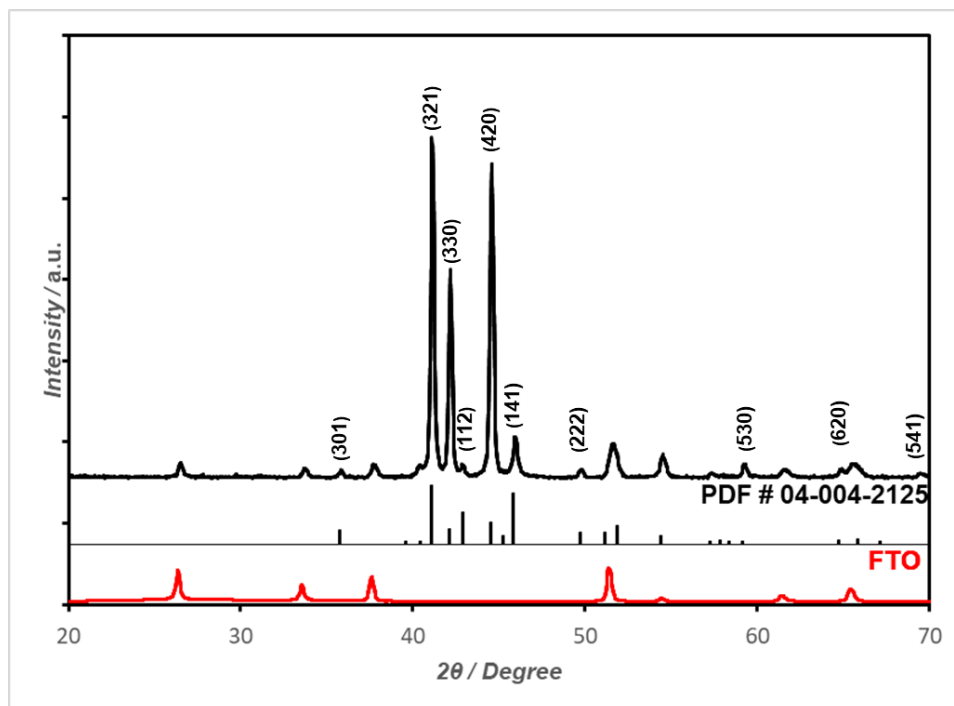


Figure B.12. PXRD of Fe_3P on FTO from precursor 4.

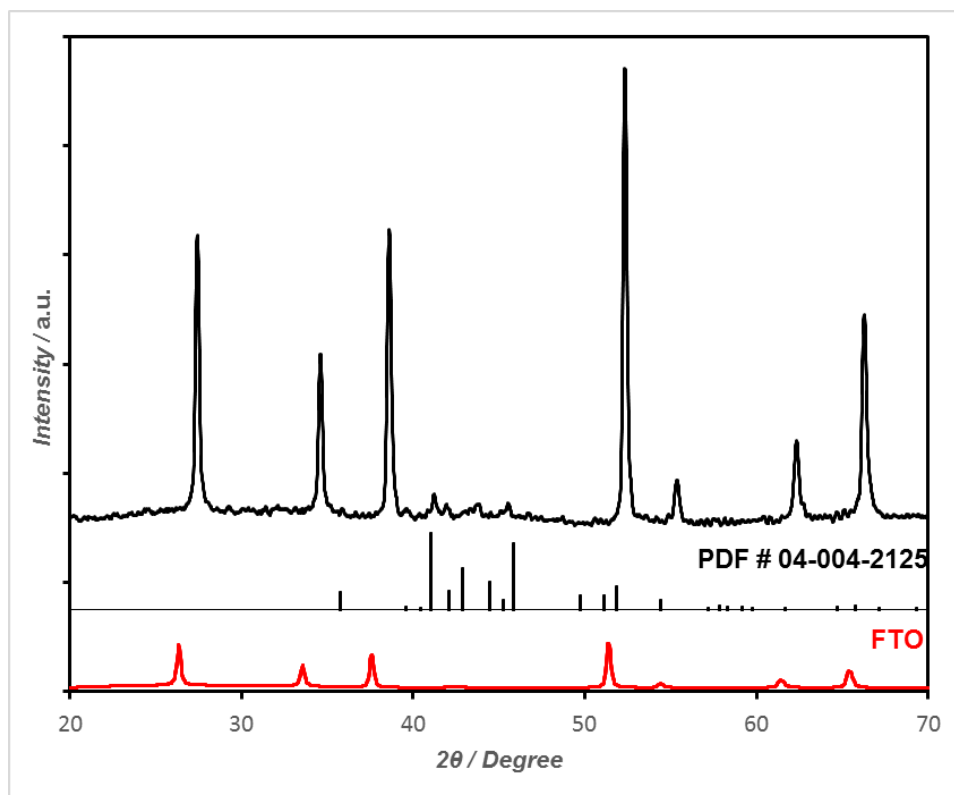


Figure B.13. PXRD of unannealed Fe_3P on FTO from precursor 4.

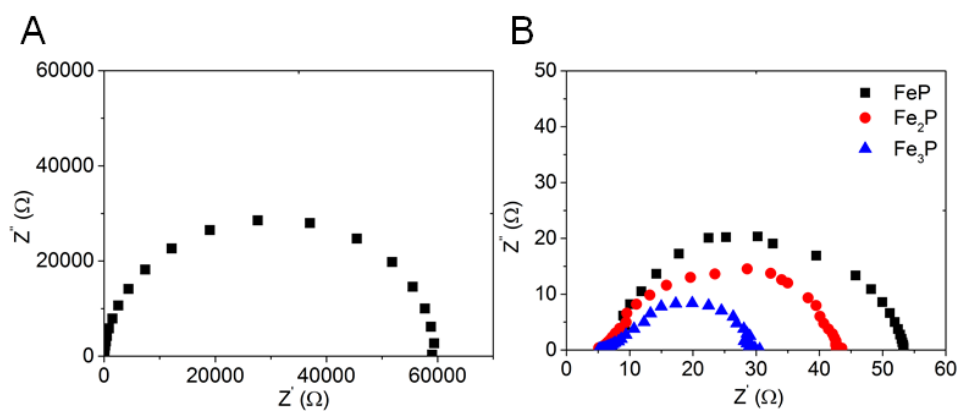


Figure B.14. Nyquist plots of bare FTO, FeP, Fe_2P and Fe_3P electrodes at the same overpotential of 160 mV.

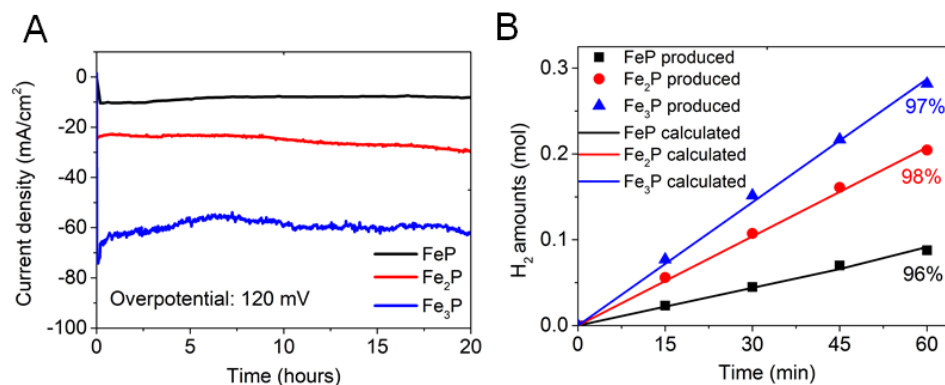


Figure B.15. (A) Time dependence of current density under static overpotential of 120 mV for FeP, Fe₂P and Fe₃P for the evaluation of the long-term stability. (B) H₂ gas amount versus electrolysis time. The Faradaic efficiency was determined by comparing measured H₂ amount to the amount calculated from the current.

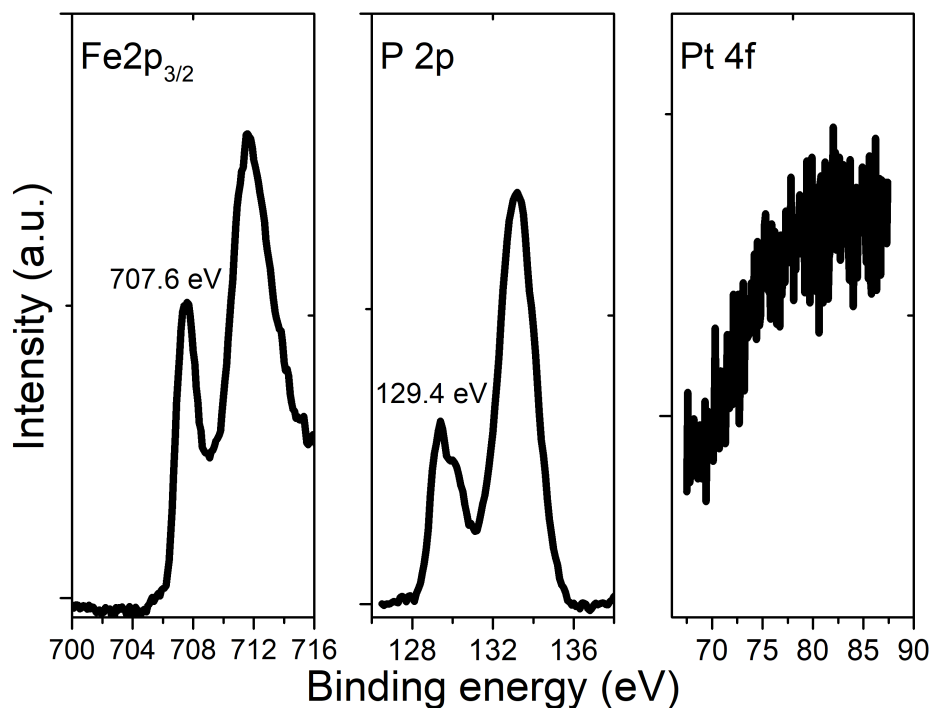


Figure B.16. Surface XPS spectra of the Fe₃P film after the HER long-term stability test.

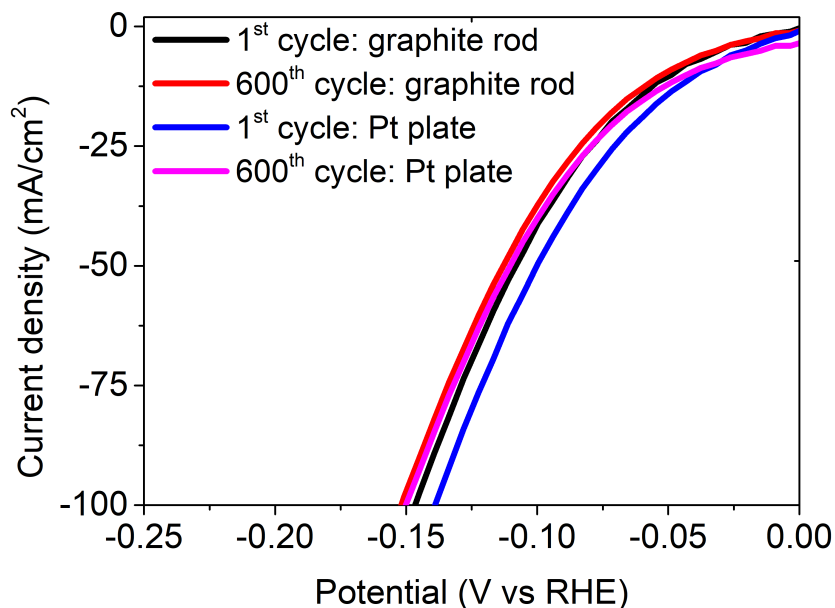


Figure B.17. The HER polarization curves of the Fe_3P film electrode on FTO with different counter electrodes at 100 mV.s in acid. Two Fe_3P electrodes were separately tested for 600 cycles at 100 mV.s in acid with Pt plate and graphite rod as the counter electrode, respectively.

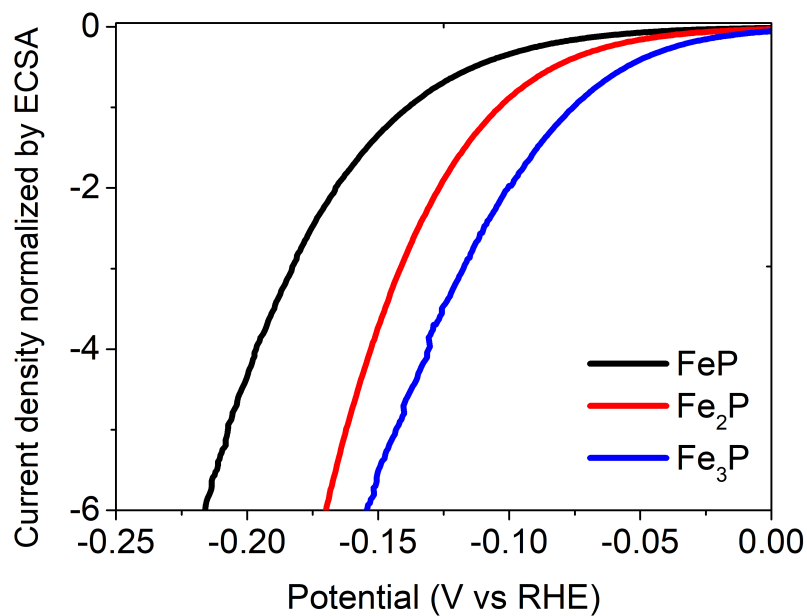


Figure B.18. The normalized polarization curves (Figure 5A) by ECSA of the FeP , Fe_2P , and Fe_3P films' electrodes.

Table B.4. The HER performance comparison of transition metal phosphides in 0.5 M H₂SO₄ solution. The overpotential is defined as the overpotential to reach a current density of 10 mA·cm⁻². FTO: Fluorine-doped Tin oxide glass; GCE: glass carbon electrode; rGO: reduced graphene oxide.

Catalyst	Substrate	Overpotential (mV)	Tafel slope (mV·dec ⁻¹)	Exchange current density (mA·cm ⁻²)	Ref.
Fe ₃ P	FTO	49	57	1.32	This work
Fe ₂ P	FTO	83	66	0.47	This work
FeP	FTO	116	76	0.24	This work
FeP nanoparticles	Ti	50		0.43	7
FeP nanotubes	Carbon cloth	88	35.5		8
FeP NWs	rGO	107	58.5		9
FeP nanowires	Carbon paper	31	53		10
FeP nanoparticles	GCE	154	65		11
FeP nanowire	Fe foil	96	39	0.17	12
Fe ₂ P nanoparticle/carbon	GCE	88	49		13
Fe ₂ P nanoparticle/rGO	GCE	101	55.2		14
Fe ₂ P	Fe foil	191	55		15
FeP ₂ nanowire	Fe foil	61	37	0.55	12
CoP nanoparticle	Ti	75	50		16
Co _x P (x=1-2) NPs	Ti	144	58		17
Co _x P (x = 1-2) NPs	Ti	110	51		18
Cu ₃ P nanowire	Cu foam	143	67	0.18	19
Ni ₂ P nanoparticle	GCE	>100	46	0.033	20

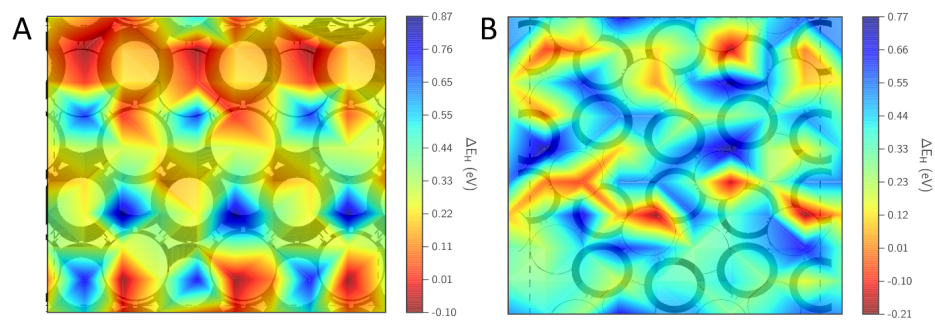


Figure B.19. Contours of H binding strength on the surfaces of a) P-terminated $\text{FeP}_{\text{P-t}}$ (011) and b) FeP (100). Fe atoms are depicted with thick boundaries, while P atoms are depicted with thin boundaries. Red areas indicate strong binding, while blue represents areas of weak binding.

